REMARKS

This amendment responds to the office action mailed on September 3, 2002. In the office action the Examiner:

- rejected claims 52-64 under 35 U.S.C. 112, second paragraph, as indefinite;

- rejected claims 1, 3-5, 28, 29, 33, 34, 54, 56, 58, and 60-65 under 35 U.S.C. 103(a) as being unpatentable over Tinkham in view of Char *et al.* (5,157,466);

- rejected claims 2, 30, 31, and 52 under 35 U.S.C. 103(a) as being unpatentable over Tinkham in view of Char *et al.* and further in view of Shnirman *et al.* (Physical Review B 57, p. 15400, 1998);

- rejected claims 6, 8-10, 35, 39, 40, 41, 53, 55, 57, and 59 under 35 U.S.C. 103(a) as being unpatentable over Tinkham in view of Char *et al.* and further in view of Baechtold *et al.* (3,953,749); and

- rejected claims 7, 11, 12-18, 36, 37, 42, 43, 45, 46, and 48-50 under 35 U.S.C. 103(a) as being unpatentable over Tinkham in view of Char *et al.*, Baechtold *et al.* and further in view of Shnirman *et al.*

After entry of this amendment, the pending claims are claims 1-18 and 28-65.

REJECTION OF CLAIMS UNDER 35 U.S.C. § 112, SECOND PARAGRAPH

The Examiner has rejected claims 52-64 under 35 U.S.C. 112, second paragraph, for three reasons. First, the Examiner indicates that it is not clear where the clockwise and counterclockwise supercurrents recited in claims 52-55 are circulating. Second, the Examiner finds that the meaning of the term "twice degenerate states," as recited in claims 56-59, is not clear. Third, the Examiner finds that the tunneling between degenerate states, as recited in claims 60 and 64, is not clear. Applicant addresses each rejection below.

CLOCKWISE AND COUNTERCLOCKWISE SUPERCURRENTS

The Examiner rejects claims 52-56 because of the recitation of clockwise and counterclockwise supercurrents that circulate in a plane in the vicinity of the clean Josephson junction. Before addressing the Examiner's specific questions regarding the clockwise and counterclockwise supercurrents, Applicant would like to discuss four references that describe such supercurrents and provide theories as to why such supercurrents form. While Applicant does not necessarily agree with each of the theories

presented in these references, the references are nevertheless presented to establish that the recitation of clockwise and counterclockwise supercurrents in claims 52 through 55 satisfy the requirements of 35 U.S.C. § 112.

The first reference is Chapter 6 of the 1999 Ph.D. dissertation of Wolfgang Belzig from Karlsruhe University (enclosed as Exhibit A). Chapter 6 of the dissertation summarizes theories behind why clockwise and counterclockwise currents arise in the vicinity of a grain boundary junction, such as the clean Josephson junction recited in claims 52-55 of the present application. Belzig states that a number of experiments have demonstrated that Cooper pairs (pairs of electrons in a superconductor) have a predominant $d_{x^2-y^2}$-wave symmetry in high-temperature (d-wave) superconductors. However, Belzig rationalizes that lattice distortions in many d-wave superconducting materials cause such materials to also have an s-wave symmetry component. Belzig hypothesizes that this admixture of d-wave and s-wave symmetry in high-temperature superconductors causes time reversal symmetry to break down in the vicinity of the grain boundary junction. This, in turn, leads to the appearance of spontaneous currents in the vicinity of the junction. These spontaneous currents flow in opposite directions on either side of the boundary. In particular, please see Belzig, p. 67-68, Section 6.2, as well as the final paragraph on p. 77.

The second reference is Il'ichev et al., arXiv:cond-mat/0102404 v3 June 2001 (enclosed as Exhibit B). Page 2, column 1, of Il'ichev provides theoretical analysis of why persistent currents circulate in the vicinity of a grain boundary junction between two d-wave superconducting materials. The theoretical analysis begins with a mathematical description of Josephson current density through a grain boundary junction. Il'ichev rationalizes that, when the difference in orientation (misorientation) between the first and second bank falls into a certain range (maximal at a misorientation angle of 45°), and when the temperature of the junction is below a particular temperature, the first harmonic of the Josephson current density is suppressed. Thus, the second harmonic of the Josephson current density essentially dominates the equation for Josephson current density through the grain boundary junction. Because the first harmonic of the Josephson current density is suppressed, the Josephson junction has a double well potential and therefore can have a doubly degenerate ground state (page 2, col. 1, last sentence of third paragraph).

Page 2, col. 1, paragraph 4, of Il'ichev states that one consequence of the suppression of the first harmonic is that time reversal symmetry is broken and small currents of equal magnitude and opposite sign flow along the interface in the left and right superconducting banks. These small currents of equal magnitude and opposite sign are <u>not</u> the Josephson current through the junction. Finally, the last paragraph of the reference states that (a) symmetric 45° junctions exhibit double degenerate ground states and (b) there is spontaneously generated flux along the interface (grain boundary) in a qubit based on an asymmetric 45° junction that should change sign between the two different ground states of the junction.

The third reference is Amin *et al.*, arXiv:cond-mat/0011416 v2, Dec. 6, 2000 (enclosed as Exhibit C). Amin *et al.* addresses *where* persistent currents (*i.e.* the clockwise and counterclockwise supercurrents) arise in grain boundary junctions between two *d*-wave superconductors or between an *s*-wave and a *d*-wave superconductor. First, Amin *et al.* provides an equation that describes the current density of such persistent currents (see Equation 4). Next, Amin *et al.* use their mathematical description of the current density of persistent currents to plot persistent current density as a function of distance from the grain boundary (Amin *et al.*, Figs. 1 and 2). For example, Fig. 1a shows that, under some circumstances, the current density of the persistent current is maximal at the grain boundary junction (Fig. 1a, x=0).

The fourth reference is Zagoskin, U.S. Patent 6,459,097 B1 (enclosed as Exhibit D). Zagoskin specifies that non-zero ground state supercurrents (*i.e.* the clockwise and counterclockwise supercurrents) arise "in the vicinity of" a grain boundary Josephson junction between an *s*-wave and a *d*-wave superconductor, see column 4, line 42. Additionally, Zagoskin specifies that these ground state supercurrents are degenerate. Finally, Zagoskin, discloses that these non-zero ground state supercurrents form the basis of a qubit for quantum computing.

With these representative references in mind, the Examiner's questions concerning clockwise and counterclockwise currents will now be discussed. First, the Examiner asks whether these supercurrents are in the mesoscopic island, circulating in the bank of superconducting material, crossing the junction, or all of the above. Amin *et al.* (Exhibit C) addresses this question by deriving equations that represent the current density of the clockwise and counterclockwise currents. Using these equations, Amin *et al.* plotted the current density of the clockwise and counterclockwise currents in

representative D-D and S-D devices. For example, Fig. 1a of Amin *et al.* shows that the supercurrents are found on both banks of a D-D (or S-D) junction as well as in the junction itself. Similarly, in the instant invention, the clockwise and counterclockwise currents are circulating in the bank, the island, and the junction itself.

Next, the Examiner asks what causes these supercurrents. There remains disagreement in the art as to what causes the claimed supercurrents. Some theories for why such supercurrents arise are outlined above in the summary of Exhibits A–D. Although the theoretical understanding of the origin of the supercurrents is unsettled, Applicants respectfully submit that the recitation of clockwise and counterclockwise supercurrents is patentable subject matter for the following reasons. First, Exhibits A–D establish that such supercurrents exist. Second, Exhibits A–D demonstrate that clockwise and counterclockwise supercurrents can be reliably created under predictable circumstances. Finally, the instant specification outlines methods by which clockwise and counterclockwise supercurrents can be usefully applied to perform quantum computation.

The Examiner further asks whether the supercurrents are due to fluctuations or differences in phase between two superconductors separated by the clean Josephson junction. Applicant does not believe that the clockwise and counterclockwise supercurrents are due to fluctuations. To the contrary, these supercurrents have been termed "persistent currents" by some references in the art. Applicant believes that the magnitude of the persistent currents are affected by the phase difference between the two superconductors separated by the clean Josephson junction. However, Applicant would like to respectfully point out that the clockwise and counterclockwise supercurrents recited in claims 52–55 are not the Josephson current through the junction. Rather, they are spontaneous currents that arise in the claimed structures and in the claimed methods.

Lastly, the Examiner asks how there can be circulation across the clean Josephson junction. Applicant again respectfully points out that the clockwise and counterclockwise supercurrents are not the Josephson current. Therefore, the phase difference across the junction does not prohibit the simultaneous circulation of both clockwise and counterclockwise supercurrents across the junction. In fact, as demonstrated by Amin *et al.* (Exhibit C), current density for the clockwise and counterclockwise supercurrents reaches a maximum at the grain boundary under the conditions set forth in the caption to Fig. 1a of Amin *et al.* (p. 2).

TWICE DEGENERATE STATES

The Examiner states that the meaning of the term "twice degenerate state," as recited in claims 56-59, is not understood. The terms "twice degenerate" and "doubly degenerate" are defined on page 6, line 20, and page 9, line 8, of the specification, on page 5 of the office action response mailed July 16, 2002 in response to the May 10, 2002 office action, U.S. Patent 6,459,097 B1 to Zagoskin, (column 6, line 33), which attached hereto as Exhibit D.

The occurrence of degeneracy in systems in accordance with the present invention relates to various aspects of the claimed structure as discussed in detail below. The d-wave superconducting material used for the bank and/or island in each of the devices recited in claims 56-59 (*e.g.*, $YBa_2Cu_3O_{7-x}$) exhibits an anisotropic order parameter that restricts supercurrent to one or more preferred directions within the material. These restricted directions are correlated with the orientation of the order parameter that is in turn correlated with the orientation of the crystal lattice of the material.

Because of the anisotropic order parameter, a Josephson junction formed out of d-wave superconducting materials can be designed to introduce a phase shift between the superconducting regions that they separate. In the structures recited in claims 56-59, the clean Josephson junction introduces a phase shift between the bulk and mesoscopic island regions of the system. Such phase shifts are recited in U.S. Patent 6,459,097 B1 to Zagoskin. In Zagoskin, the Josephson junction is comprised of s-wave and d-wave superconducting material. Applicant respectfully points out that a similar phase shift occurs in the claimed structures.

Il'ichev *et al.*, referenced above as Exhibit B, describes a system that includes a narrow Josephson junction (0.5 and 0.7 micrometers) formed in a loop with a wide Josephson junction (see Il'ichev *et al.*, Fig. 1). The system described in Il'ichev is used to explore properties of the mesoscopic Josephson junction and provides the first experimental observation of a doubly degenerate ground state energy of the system (see Il'ichev *et al.*, p. 1, second column, first complete paragraph). The doubly degenerate ground state referred to in Il'ichev *et al.* is correlated with the respective phase shift across the Josephson junction. This doubly degenerate ground state results from the fact that, although the magnitude of the phase shift is fixed, the sign of the phase shift can be either positive or negative.

If a conventional Josephson junction (S-S) was used in the Il'ichev *et al.* structure rather than the unconventional (D-D) Josephson junction, there would be no phase shift. Thus, the resulting potential landscape versus phase for the system would have only a single potential well with a ground state or minimum energy occurring at zero phase. However, when a finite (non-zero) phase shift is introduced, by using the Josephson junction described above (a D-D junction), the potential landscape versus phase forms a double well potential. This double well potential has a first minimum energy correlated with the positive phase difference and a second minimum energy correlated with the negative phase difference. Figure 5 on page 4 of Il'ichev *et al.* illustrates the free energy as a function of phase difference across the mesoscopic Josephson junction (weak link) and shows the formation of a double well energy structure with respect to phase.

Il'ichev *et al.* states that, under certain misorientation angles (the degree of misalignment between the banks on each side of a grain boundary junction), the first harmonic for the Josephson current density of a Josephson junction between d-wave superconductors is suppressed and the second harmonic dominates the current. Il'ichev *et al.* further states that the suppression of the first harmonic and the dominance of the second harmonic leads to a doubly degenerate ground state for the junction. (Il'ichev *et al.*, page 2, column 1, last sentence of the third paragraph). The doubly degenerate ground state in the Il'ichev *et al.* junction is analogous to the twice degenerate quantum state recited in claims 56-59. The recitation of degenerate ground states and the correlation to the phase difference across the junction is found in the specification of the present invention (see page 10, line 6).

TUNNELING BETWEEN DEGENERATE STATES

The Examiner has rejected claims 60 and 64 because they refer to tunneling between degenerate states. As described in Il'ichev *et al.*, for the case of a D-D junction, the potential landscape of a D-D junction or a D-S junction with respect to phase forms a double well structure having degenerate ground states. This holds true even when one of the banks is a mesoscopic island. The minimum energy levels accessible by the system (its ground state) are at the bottom of the potential wells, and are separated by a potential barrier that distinguishes them. Changing the system from one potential well to the other is physically the same as reversing the direction of the clockwise or counterclockwise supercurrent.

In classical mechanics, for a particle occupying a ground state to move to another state (*e.g.*, another ground state in a degenerate system), the particle must be given more energy than the potential barrier that separates the two states. However, if the particle is governed by quantum mechanics, it is possible for the particle to tunnel through the potential barrier separating the two states even when the particle does not have sufficient energy to pass over the potential barrier separating the two states. See, for example, Atkins, 1983, *Molecular Quantum Mechanics*, Oxford University Press, New York, pp. 41-44, which is enclosed as Exhibit E. Atkins explains that a particle (*e.g.*, a Cooper pair) may be found inside a classically forbidden region (forbidden because the particle does not have sufficient energy to be in the region). Atkins calls this effect "penetration of the barrier" or "tunneling." This type of microscopic quantum tunneling is known in the art and, for example, characterizes the Josephson effect across Josephson junctions, where Cooper pairs pass through a region of non-superconducting material via the process of quantum tunneling. In superconductors and many other systems, the same quantum mechanical behavior extends to the mesoscopic scale where mesoscopic properties of the system (made up in part by contribution from Cooper pairs) behave according to quantum mechanical rules and hence demonstrate quantum tunneling.

Tunneling is not limited to particles. The tunneling of states is well known in the field of quantum mechanics. Relevant examples of the tunneling of states, both theoretical and experimental, are found in various superconducting devices. For an example of quantum tunneling in a SQUID, see Voss *et al.*, 1981, Physical Review Letters 47, pp. 265–268 which is enclosed as Exhibit F. In particular, see last sentence of abstract and first two sentences of left column page 265. For an example related to superconducting qubits, see Zagoskin, U.S. Patent 6,459,097 B1 (column 6 line 36) (Exhibit D).

The behavior of any quantum system is defined by its Hamiltonian, which identifies the important physical characteristics of the respective system that affect its quantum state. Capacitance plays an important role in the quantum state of all superconducting systems, including Josephson junction systems. Varying the capacitance of a superconducting qubit affects the tunneling rate between degenerate states. This phenomenon is apparent from the following Hamiltonian for a Josephson junction:

$$H_{JJ} = \frac{(ne)^2}{2C} - E_J \cos(\gamma),$$

where C or capacitance is analogous to "mass" *c.f.* with the well known Hamiltonian for a simple harmonic oscillator,

$$H_{SHO} = \frac{p^2}{2m} + \frac{m\omega^2 x^2}{2}.$$

In the first Hamiltonian, e is the charge of an electron, E_J is the Josephson energy, and γ is the phase difference across the Josephson junction. In the second Hamiltonian, p is momentum, m is mass, ω is oscillation frequency, and x is position. It will be appreciated that the terms containing phase (Josephson junction) and position (simple harmonic oscillator) determine the respective potential energy profile, while the terms containing capacitance and mass contain the kinetic terms in the Josephson junction and simple harmonic oscillator Hamiltonian respectively.

Formally, this analogy of mass and capacitance can be shown by detailed analysis of a qubit, including qubits with a double well potential. In fact, "the equations of motion" for a qubit is a term of art; see Orlando *et al.*, 1999, Phys. Rev. B 60, 15398, Item IW of the information disclosure statement submitted by Applicant on March 25, 2002. Capacitance is an important parameter as disclosed in the specification of the present invention (See page 10 line 11 et seq.).

Due to the architecture of the devices recited in pending claims 60-64, the size of the mesoscopic island results in it having a small capacitance. The consequence of the mesoscopic island having a small capacitance is to increase the total energy of the qubit relative to the potential barrier height separating the potential wells in the double well potential, where each potential well contains a ground state of the system, and each ground state in turn corresponds to clockwise and counterclockwise directions of circulating supercurrent. Since the ground states of the system are quantum mechanical in nature, an increase in the energy of the qubit results in the system having a high probability to tunnel between its ground states. As such, each of the clockwise and counterclockwise circulating supercurrents possess a nonzero probability of tunneling through the potential barrier from one ground state (for example, represented by the left potential minimum of a double well potential) to another ground state (for example, represented the right potential minimum of a double well potential). Hence, the claimed system of the present invention performs quantum tunneling between its ground states without the influence of external electromagnetic energy.

CLAIM REJECTION UNDER 35 U.S.C. § 103(A)

Claims 1, 3-5, 28, 29, 33, 34, 54, 56, 58 and 60-65

The Examiner has rejected claims 1, 3-5, 28, 29, 33, 34, 54, 56, 58 and 60-65 under 35 U.S.C. 103(a) as being unpatentable over Tinkham in view of Char *et al.* (USP 5,157,466). Applicants respectfully traverse the rejection.

The instant invention is directed to novel structures used to perform quantum computing. DiVincenzo has outlined the qualities a device must have in order to perform quantum computing (DiVincenzo in *Scalable Quantum Computers*, Braunstein and Lo, eds., Wiley-VCH, 2001, Berlin, Exhibit G). One of the most fundamental requirements is for the device to have well characterized qubits. DiVincenzo states that a qubit is simply a quantum two-level system like the two spin states of a spin ½ particle, like the ground and excited states of an atom, or like the vertical and horizontal polarization of a single photon (DiVincenzo, page 3, first paragraph). The essential feature that distinguishes a qubit from a bit is that, according to the laws of quantum mechanics, the permitted states of a single qubit fill up a two-dimensional complex vector space, commonly referred to as a two dimensional Hilbert space and often represented by a Bloch sphere.

The Applicant has unexpectedly discovered that the claimed structures support a quantum two-level system. This two-level system may be used as a qubit to perform quantum calculations. Exhibits A, B, C, and D describe the special properties of D-D and D-S grain boundary junctions. In particular, according to Amin *et al.* (Exhibit C), the equilibrium phase difference φ_0 across the boundary, is generally neither 0 or π, and therefore the states within the banks on each side of the boundary with $d_1 + e^{\pm i\phi_o} d_2$ orderings are degenerate and may support spontaneous currents. (Amin *et al.*, p. 1, column 1, third full paragraph). Many researchers have studied such currents. However, as detailed in the instant specification, the Applicant exploited this phenomenon by making one of the banks separating the grain boundary junction mesoscopic. By using a mesoscopic island and a clean Josephson junction, the clockwise and counterclockwise supercurrents described in Exhibits A, B, C, and D are no longer governed by classical mechanics in the claimed structures. Rather, they are governed by the rules of quantum mechanics. Because the clockwise and counterclockwise supercurrents are governed by the rules of quantum mechanics, they can be used as qubits as described by DiVinzenco

(Exhibit G). In Applicant's invention, the clockwise supercurrents represent one state of a qubit and the counterclockwise supercurrents represent the other state of a qubit. Furthermore, because the ground states of the system are governed by the laws of quantum mechanics, the system occupying a first ground state can tunnel through the potential barrier that separates the two degenerate ground states (equal energy ground states). Thus, adopting a classical view point, by way of illustration, a Cooper pair that was initially traveling in a clockwise supercurrent has a finite probability of switching to a counterclockwise supercurrent even without the application of an external energy source.

The coexistence of currents that are traveling in opposite directions in a bank or an island is possible when the bank or island is in a superconducting state. Because of the superconducting state, the opposite currents do not interact with each other. Thus, no energy is lost and the currents can coexist for long periods of time.

With this background in mind, Applicants would like to address the specific rejections made by the Examiner. When rejecting claims under 35 USC § 103, the Examiner bears the burden of establishing a *prima facie* case of obviousness. *In re Bell*, 26 USPQ2d 1529 (Fed. Cir. 1993). To establish a *prima facie* case, the prior art reference, or references when combined, must teach or suggest each and every limitation of the claimed invention. MPEP § 706.02(j). The teaching or suggestion to make the claimed invention and the reasonable expectation of success must both be found in the prior art, not in the applicant's disclosure. *In re* Vaeck, 20 USPQ2d 1438 (Fed. Cir. 1991). There must be some motivation, suggestion, or teaching of the desirability of making the specific combination that was made by the Applicant. *In re Fine*, 837 F.2d 1071, 1075 (Fed. Cir. 1988).

In the present instance, one relevant inquiry is whether the cited art, either alone or in combination, teaches each and every limitation of the rejected claims. Another relevant inquiry is whether the prior art provides one of ordinary skill in the art with a suggestion or motivation to modify or combine the teachings of the references relied upon by the PTO to arrive at the claimed invention. As discussed in detail below, the cited art fails to satisfy either of these requirements. Therefore, the rejection should be withdrawn.

The combination of Tinkham and Char does not teach each and every limitation of the claimed invention.

One limitation of the claimed invention is a clean Josephson junction. In Applicant's response to the October 1, 2001 office action, Applicant explained that faceting (wobble) at the junction between the bank and the island must be minimized in order to support the two degenerate states in the mesoscopic island. (March 1, 2002 response, pp. 16-17). Applicant's explained that the need to minimize faceting leads to the requirement of a clean Josephson junction separating the island and the bulk regions. For this reason, a clean Josephson junction is a positively recited limitation in each of the pending claims.

Tinkham does not detail the nature of the junctions between the banks in the structures identified by the Examiner. Furthermore, the methods used by Char *et al.* to make a junction are not capable of making the claimed clean Josephson junction. The result of the fabrication method described by Char *et al.* is a dirty Josephson junction with possible uses for large junction devices.

Char *et al.* describes a method of fabrication well known in the art as bi-epitaxial grain boundary fabrication. The work of Char *et al.* was pioneering in the field and some advances have been made on the methods described therein. An example of advancements to the work of Char *et al.* is described in detail in Nicolleti *et al.*, 1996, Physica C, 269, p. 255 (attached as Exhibit H). On page 256, first column, first complete paragraph, Nicolleti *et al.* introduces bi-epitaxial layers as having first been developed by Char *et al.*, 1991, Appl. Phys. Lett., 59, 733.

The following Figure is a reproduction of Figure 8 from Nicolleti *et al.* that illustrates a characterization study comparing bi-epitaxial and bi-crystal grain boundary Josephson junctions. Specifically, the Figures illustrate the critical current (I_C) dependence on applied magnetic field (H) for a 16μm large bi-epitaxial Josephson junction and a 5μm large bi-crystal Josephson junction.
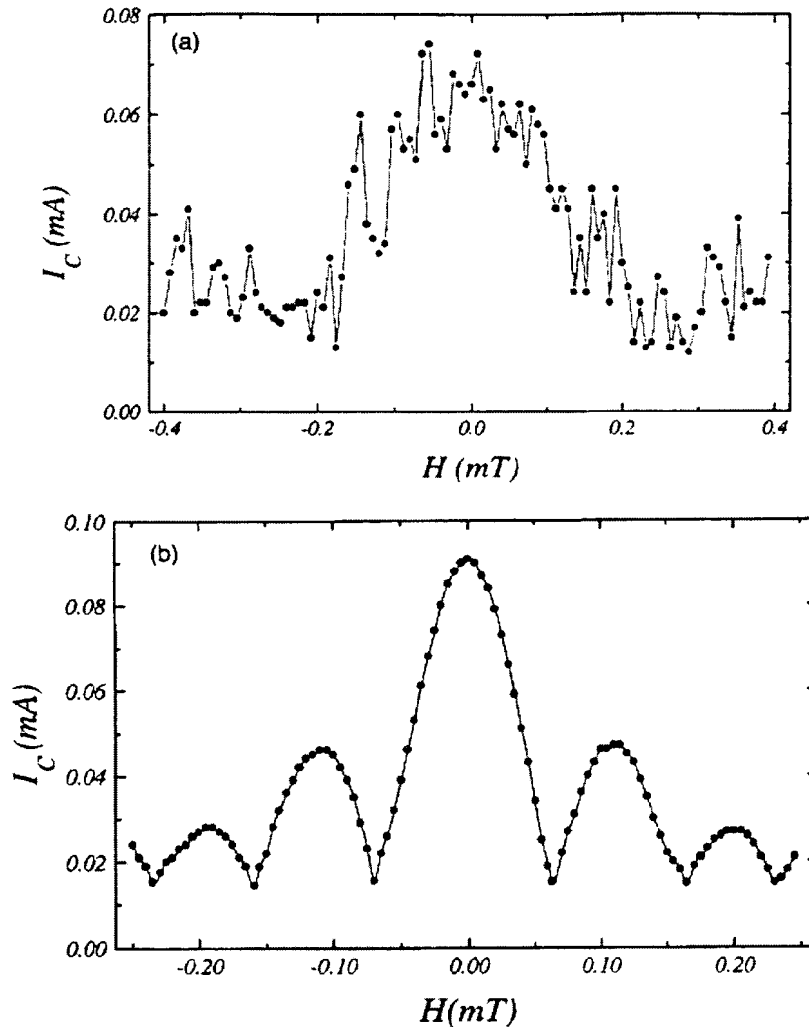
Fig. 8. I_C vs. H curve obtained on a) a 16 μm large junction fabricated on STO substrate and on b) a 5 μm large junction fabricated on 45° symmetric STO bi-crystal. The data were collected at 4.2 K.

The top curve represents a bi-epitaxial Josephson junction having randomly occurring "structural and / or morphological defects." (Nicolleti et al., p.265, column 2). The defects described are an unavoidable byproduct of the bi-epitaxial fabrication method. In complete contrast, in a clean Josephson junction, the I_C versus magnetic field (H) characteristic obeys a Fraunhofer-like behaviour. The top bi-epitaxial curve "largely deviates from the expected behavior" (Nicolleti et al., p. 266, column 1, 2nd paragraph) while the bottom bi-crystal curve demonstrates the "typical sin(x)/x pattern with symmetric periodic lobes" (ibid.).

The effect of the defects in a Josephson junction using the Char et al. bi-epitaxial technique/approach is a reduction in the current density and change in the phase along the

Josephson junction (Nicolleti *et al*, p. 266, col. 2 , first complete paragraph). Mannhart and Hilgenkamp, interpret these results as being direct evidence of faceting (wobble). See, Mannhart and Hilgenkamp, 1997, Superconductor Science and Technology 10, pp. 880–883, attached hereto as Exhibit I. In particular, see p. 881, column 1, third paragraph and Figure 2 of Exhibit I.

Bi-epitaxial technology is known to produce junctions of limited use. Bi-epitaxial grain boundary Josephson junctions are known to have a high normal resistance R_N and low $I_C R_N$ products. See, Koelle *et al.*, 1999, Reviews of Modern Physics 71, pp. 631– 686, which is attached hereto as Exhibit J. In particular, see page 643, column 2, second complete paragraph of Exhibit J. This is known by practitioners in the art who no longer use the bi-epitaxial grain boundary Josephson junctions, which are described in Char *et al.* and Nicolleti *et al*, in $YBa_2Cu_3O_{7-x}$ for SQUIDs.

In summary, the bi-epitaxial Josephson junctions described in Char *et al.* and Nicolleti *et al.* are not clean Josephson junctions as recited in the claimed invention.

There is no motivation to combine Tinkham and Char et al.

The Examiner contends that it would have been obvious to use the Char *et al.* structure for the Tinkham device to obtain a device having each of the claimed limitations because it is known to be functional. Applicant respectfully disagrees with the Examiner's analysis. *In re Fine* held that there must be some motivation, suggestion, or teaching of the desirability of making the specific combination that was made by the Applicant. *In re Fine*, 837 F.2d 1071, 1075 (Fed. Cir. 1988). As discussed below, the structures described by Char *et al.* and Tinkham have different properties and different applications. In addition, there is no suggestion in Char *et al.* and Tinkham that the references should be combined. For these reasons, Applicant contends that Tinkham and Char *et al.* cannot be combined to teach each of the limitations of the claimed invention.

The devices described by Char *et al.* and Tinkham require different functionalities to operate. The slotted dc-SQUID described in Char *et al.* is a device that converts magnetic flux into current, thus forming a sensor for magnetic fields. In operation, a potential difference is measured across the leads of the dc-SQUID that is correlated with the amount of magnetic flux that threads the dc-SQUID loop. For example, referring to Figure 14 from Char *et al.*, the potential difference would be measured between region 312 to region 310. The potential difference in the Char *et al.*

device is measured across two Josephson junctions in parallel. The Josephson junction fabrication methods described in Char *et al* are directed towards forming devices such as the slotted dc-SQUID.

In contrast, the device described in Tinkham includes two Josephson junctions in series. The passage of current or supercurrent across the island in Tinkham can be controlled. The device described in Tinkham is not useful for measuring magnetic fields and thus requires different functionality than the Char *et al.* device and structure. As a consequence of this difference, the Josephson junctions for the respective systems (Char *et al.* and Tinkham) also require different functionality.

The behavior of the device described in Tinkham depends on the ratio between the Coulomb energy E_C and Josephson coupling energy E_J. E_C depends on the capacitance of the small island as

$$E_C = \frac{(e)^2}{2C},$$

where C is the capacitance of the tunnel junctions (Tinkham, p. 249, second paragraph). E_J depends on the critical current I_C of the Josephson junctions as

$$E_J = \frac{\hbar \cdot I_C}{2e}$$

(Tinkham, p. 198, equation 6.3).
These energies depend on many aspects of the system such as the material used and the characteristics of the Josephson junctions. Since Char *et al.* only describes large-scale structures, it is not obvious what the characteristics of the Char *et al.* structure would be if it were scaled to a mesoscopic size.

For these reasons, Applicant respectfully submits that there is no motivation to combine Tinkham and Char *et al.* as required under the law. Therefore, Applicant respectfully submits that the Examiner has not satisfied the burden of establishing a *prima facie* case of obviousness.

For the reasons provided above, Applicant believes that the combination of Tinkham and Char *et al.* does not render obvious claims 1, 3-5, 28, 29, 33, 34, 54, 56, 58, or 60-65. Therefore, Applicant respectfully requests that the rejection be withdrawn.

Claims 60-63

Claims 60-63 are patentable over the combination of Tinkham and Char *et al.* for the additional reason that neither reference teaches or suggests the form of quantum tunneling recited in these claims. Claim 60 recites a supercurrent that tunnels between a first ground state and a second ground state. Tinkham and Char *et al.*, or any combination of Tinkham and Char *et al.*, do not teach or suggest a clean Josephson junction between a mesoscopic island and a bank. For this reason, the cited references fail to disclose a Josephson junction that is configured so that a supercurrent proximate to the Josephson junction alternates between a first ground state having a first magnetic moment and a second ground state having a second magnetic moment by means of quantum tunneling as recited in claim 60. Claims 61-63 depend from claim 60 and therefore are not rendered obvious by the combination of Char *et al.* and Tinkham for the same reasons.

Claims 2, 30, 31, and 52

The Examiner has rejected claims 2, 30, 31, and 52 under 35 U.S.C. 103(a) as being unpatentable over Tinkham in view of Char *et al.* (USP 5,157,466) and further in view of Shnirman *et al.*

Tinkham., either alone or in combination with Char *et al.*, does not anticipate claims 1, 28, 60 or 64 for the reasons discussed above. Shnirman merely teaches a SET capacitively coupled to a Josephson junction q-bit. As such, Shnirman *et al.* does not remedy the deficiencies identified in the combination of Tinkham and Char *et al.*. For this reason, the combination of Tinkham, Char *et al.*, and Shnirman *et al.* does not render claims 1, 28, 60 or 64 obvious. Since claims 2, 30, 31, and 52 ultimately depend from 1, 28, 60 or 64, the cited references do not anticipate these claims either. Accordingly, Applicant respectfully requests that the rejection be withdrawn.

Claims 6, 8-10, 35, 39, 40, 41, 53, 55, 57, and 59

The Examiner has rejected claims 6, 8-10, 35, 39, 40, 41, 53, 55, 57, and 59 under 35 U.S.C. 103(a) as being unpatentable over Tinkham in view of Char *et al.* (USP 5,157,466) and further in view of Baechtold *et al.* (USP 3,953,749). Tinkham, either alone or in combination with Char *et al.*, does not anticipate claims 1, 28, 60 or 64 for the reasons discussed above. Baechtold *et al.* merely teaches a binary circuit consisting of a

series/parallel arrangement of Josephson junctions. As such, Baechtold *et al.* does not remedy the deficiencies identified in the combination of Tinkham and Char *et al.*. For this reason, the combination of Tinkham, Char *et al.*, and Baechtold *et al.* does not render claims 1, 28, 60 or 64 obvious. Since claims 6, 8-10, 35, 39, 40, 41, 53, 55, 57, and 59 ultimately depend from 1, 28, 60 or 64, the cited references do not anticipate these claims either. Accordingly, Applicant respectfully requests that the rejection be withdrawn.

Claims 7, 11, 12-18, 36, 37, 42, 43, 45, 46, and 48-50

The Examiner has rejected claims 7, 11, 12-18, 36, 37, 42, 43, 45, 46, and 48-50 under 35 U.S.C. 103(a) as being unpatentable over Tinkham in view of Char *et al.*, Baechtold *et al.* and further in view of Shnirman *et al.* As previously discussed, Tinkham, either alone or in combination with Char *et al.*, does not anticipate claims 1, 28, 60 or 64. Baechtold *et al.* and Shnirman *et al.* do not remedy the deficiencies identified in the combination of Tinkham and Char *et al.* For this reason, the cited references, either alone or in any combination, do not render claims 1, 28, 60 or 64 obvious. Since claims 7, 11, 12-18, 36, 37, 42, 43, 45, 46, and 48-50 ultimately depend from claims 1, 28, 60 or 64, the references do not anticipate these claims either. Accordingly, Applicant respectfully requests that the rejection be withdrawn.

CONCLUSION

In light of the above remarks, the Applicant respectfully requests that the Examiner reconsider this application with a view towards allowance. The Examiner is invited to call the undersigned attorney if a telephone call could help resolve any remaining items.

Respectfully submitted,

PENNIE & EDMONDS LLP

By: _____
Gary S. Williams
Reg. No. 31,066

3300 Hillview Avenue
Palo Alto, CA 94304
Telephone: (650) 493-4935

APPENDIX A

AMENDED CLAIM

64. (Amended) A quantum register comprising:

a bank of a superconducting material;

a plurality of [mescopic] <u>mesoscopic</u> islands of superconducting material;

a plurality of clean Josephson junctions, wherein each Josephson junction:

is between the bank and a corresponding one of the islands ; and

is configured so that a supercurrent proximate to each Josephson junction

alternates between a first ground state having a first magnetic moment and a second

ground state having a second magnetic moment by means of quantum tunneling; and

circuitry to allow selective interruption of quantum tunneling between the first

ground state and the second ground state of the supercurrent associated with each

Josephson junction.

EXHIBIT A

CHAPTER 6 OF THE 1999 PH.D. DISSERTATION OF WOLFGANG BELZIG
FROM KARLSRUHE UNIVERSITY

Magnetische und spektrale Eigenschaften von supraleitenden Proximity-Systemen

Zur Erlangung des akademischen Grades eines

DOKTORS DER NATURWISSENSCHAFTEN

von der Fakultät für Physik der

Universität Karlsruhe (TH)

genehmigte

DISSERTATION

von

Dipl.-Phys. Wolfgang Belzig

aus München

Tag der mündlichen Prüfung:	5. Februar 1999
Hauptreferent:	Prof. Dr. Gerd Schön
1. Korreferent:	Prof. Dr. Johann Blatter
2. Korreferent:	Prof. Dr. Christoph Bruder

Magnetic and Spectral Properties of Superconducting Proximity Systems

Wolfgang Belzig

University of Karlsruhe

Chapter 6

Spontaneous time-reversal symmetry breaking at twin boundaries in high-T_C superconductors

A large number of experiments have convincingly demonstrated that Cooper pairs have basically $d_{x^2-y^2}$-wave symmetry in high-temperature superconductors [26]. In a strict sense this classification applies only to superconductors with perfectly tetragonal crystal symmetry for which the $d_{x^2-y^2}$ represents a "relative angular momentum" of the Cooper pairs with reduced symmetry. On the other hand, there is a number of slightly orthorhombically distorted systems such as $YBa_2Cu_3O_7$ (YBCO) for which the intrinsic crystal deformation removes the distinction by symmetry between this pairing states and a conventional s-wave type. We may interpret this also in the way that the orthorhombic distortion couples the two pairing channels [41, 155, 156]. Clear evidence for this kind of mixing has been found in recent c-axis Josephson experiments between YBCO and Pb [157]. In these experiments a Josephson current between a single twin domain and a s-wave superconductor was observed. If the order parameter of the twin domain would be purely d-wave the Josephson coupling would vanish due to symmetry. The reason is that the current originating from the positive lobes would exactly cancel the one from the negative lobes. Consequently, the measured current must be due to the weight difference of positive and negative lobes. This difference can be interpreted as an admixture of a subdominant s-wave component.

An interesting aspect of the s-wave admixture due to an orthorhombic distortion occurs in the vicinity of twin boundaries which separate the two degenerate orthorhombic lattice shapes (twins). A schematic picture of such a twin boundary is drawn in Fig. 6.1. Sigrist *et al.* suggested that the two order parameter components, s- and d-wave, could locally twist in a way that time reversal-symmetry $\mathcal{T}$ is broken [41]. Various physical properties are connected with this effect. In Ref. [41] it was shown on the level of Ginzburg-Landau theory
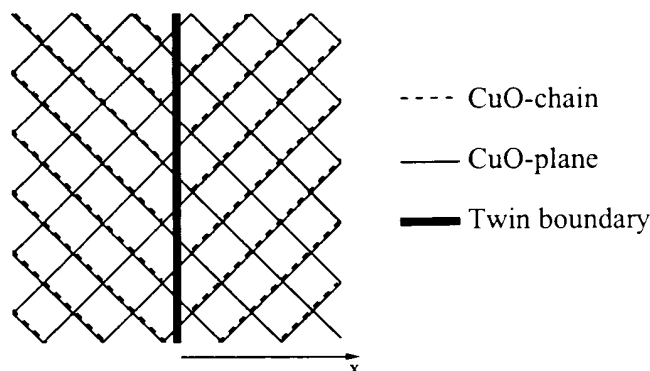
Figure 6.1: Schematic top view of a CuO plane with a twin boundary. The directions of the chains discriminates the twin domains on both sides of the twin boundary. The one-dimensional chains are interrupted at the twin boundary. Therefore, the transport through the twin boundary in the chains will be neglected in our quasiclassical model.

that the $\mathcal{T}$-violating state is accompanied by a spontaneous current flowing parallel to the twin boundary. Recently a twin boundary was studied by solving the Bogolubov-de Gennes (BdG) equations [158–160] confirming the results of the Ginzburg-Landau description and discussing the local IV-characteristics observable in a tunneling experiment. Time-reversal breaking surface states were also predicted [106] and experimentally found [100] at surfaces of YBCO.

We study a twin boundary and its properties using the quasiclassical theory of superconductivity introduced in Chapter 2. We calculate the structure of the order parameter selfconsistently at all temperatures. Our calculation includes the orthorhombic distortion in form of anisotropic quasiparticle masses. In contrast to Ref. [158], the twin boundary has no extension and is not explicitly pair breaking. In the bulk this formulation gives a mixing between s- and d-wave pairing due to the orthorhombic distortion in agreement with the other methods. For the twin boundary we show that the time-reversal symmetry is indeed broken at low enough temperature. The lower symmetry is noticeable also in the energy levels of quasiparticle bound states at the twin boundary. In the $\mathcal{T}$-invariant state there is a large density of bound states at zero energy. The breakdown of time-reversal symmetry at the twin boundary leads to the splitting of this energy level, and this effect in the local density of states is observable by scanning tunneling microscopy. This experimental technique has already been successfully used to measure the spatially resolved density of states inside vortices in classical superconductors [161, 162], in vortex lattices [163, 164] and in high-T_c superconductors [165, 166].
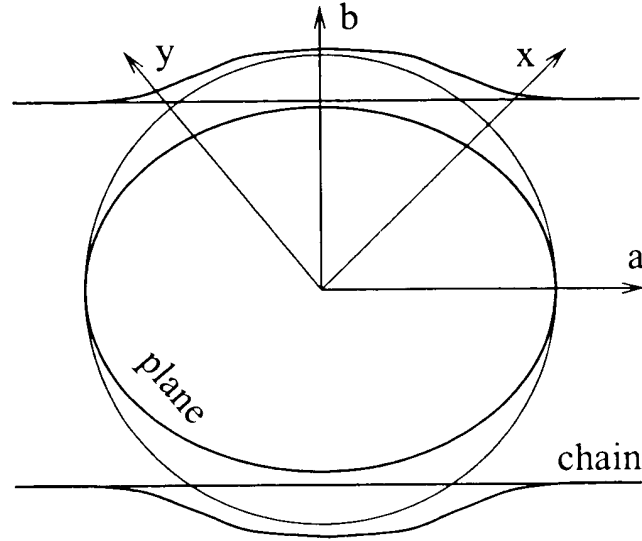
Figure 6.2: Hybridization of chain and plane Fermi surfaces. The free Fermi surfaces of the plane and the chains are drawn as thin lines. In the regions in which they overlap they hybridize leading to an avoiding of crossings. In a strict sense the hybridized Fermi surfaces cannot be associated clearly with either the chains or the planes. However, both parts of the Fermi surface retain the one- respectively two-dimensional character.

6.1 Bulk properties

In YBCO the orthorhombic symmetry reduction is partially induced by lattice deformation and mainly due to the presence of CuO-chains. The introduction of this orthorhombicity into the quasiclassical formulation is done by changing the single electron dispersion to

$$\varepsilon(\boldsymbol{k}) = \frac{\boldsymbol{k}^2}{2m} - \frac{c}{m} k_x k_y \ , \tag{6.1}$$

where the (dimensionless) constant $-1 < c < 1$ parameterizes the distortion (the sign of c defines the two twin domains). Here the x- and y-axes correspond to the direction [1,1,0] and [1,-1,0] of the tetragonal lattice. The distortion leads to a non-cylindrical FS with

$$k_{\mathrm{F}}(\theta) = \frac{k_{\mathrm{F0}}}{\sqrt{1 - c\sin 2\theta}} \ , \tag{6.2}$$

where θ is the angle between $\boldsymbol{k}$ and the k_x-direction and k_{F0} is the Fermi wave vector of the undistorted system. We will neglect all effects of electron motion in c-axis direction.

Accounting for the anisotropy the averaging over the FS has to be modified compared to the standard case,

$$\sum_{\boldsymbol{k}} \rightarrow N_0 \langle \cdots \rangle = N_0 \int_0^{2\pi} \frac{d\theta}{2\pi} n(\theta) \ . \tag{6.3}$$

Here, N_0 is the normal density of states at the Fermi energy, and

$$n(\theta) = n_{\mathrm{f}} \frac{\boldsymbol{k}_{\mathrm{F}}^2(\theta)}{m|\boldsymbol{k}_{\mathrm{F}}(\theta)\boldsymbol{v}_{\mathrm{F}}(\theta)|} = n_{\mathrm{f}} \frac{1}{1 - c\sin 2\theta} \ , \tag{6.4}$$

where n_{f} is a normalization factor. A realistic estimate for the parameter c is ~ 0.2. This has been shown in [167], where the hybridization of the chain and the plane Fermi surfaces was calculated. The resulting anisotropy of the ab-plane penetration depth was compared to experiment [168]. The anisotropy of the Fermi surface was determined to be $k_{\mathrm{Fa}}/k_{\mathrm{Fb}} \approx 1.3$, which corresponds to $c \approx 0.2$ in our model. Recently a model in which the anisotropy occurs only due to the small lattice distortions was proposed [169]. The gap anisotropy found there is, however, well described in our model with the anisotropic Fermi surface. Therefore, we will neglect all other effects related to the chains besides the modification of the dispersion.

In the following, we restrict our discussion to the s-wave and $d_{x^2-y^2}$-wave pairing channels. The pairing interaction is modeled as

$$V(\theta, \theta') = V_{\mathrm{s}} + 2V_{\mathrm{d}} \sin(2\theta) \sin(2\theta') \ , \tag{6.5}$$

where the angular dependence of the d-wave part follows from our choice of the coordinate frame. The coupling strengths $V_{\mathrm{s/d}}$ are eliminated in favor of the bare critical temperatures $T_{\mathrm{cs/d}}$ and the energy cut-off ω_c, the latter assumed to be the same for both channels. Then the coupling constants can be defined as

$$\frac{1}{N_0 V_{\mathrm{s,d}}} = \ln(T/T_{\mathrm{cs,d}}) + \sum_{n>0}^{n<\omega_c/2\pi T} \frac{1}{n + 1/2}. \tag{6.6}$$

The solution for the off-diagonal quasiclassical Green's function in the bulk is $f_\omega(\theta) = \Delta(\theta)/\Omega(\theta)$, where $\Omega(\theta) = \sqrt{\omega^2 + |\Delta(\theta)|^2}$. The gap function is a linear combination of the s- and d-wave component, $\Delta(\theta) = \Delta_{\mathrm{d}} \sin(2\theta) + \Delta_{\mathrm{s}}$. The selfconsistent calculation leads to two coupled equations for the s- and d-wave component,

$$\Delta_{\mathrm{s}} = V_{\mathrm{s}} N_0 T \sum_{\omega>0}^{\omega<\omega_c} \langle \frac{\Delta_{\mathrm{s}} + \Delta_d \sin(2\theta)}{\Omega(\theta)} \rangle \ , \tag{6.7}$$

$$\Delta_{\mathrm{d}} = V_{\mathrm{d}} 2 N_0 T \sum_{\omega>0}^{\omega<\omega_c} \langle \frac{\Delta_d \sin^2(2\theta) + \Delta_{\mathrm{s}} \sin(2\theta)}{\Omega(\theta)} \rangle \ .$$
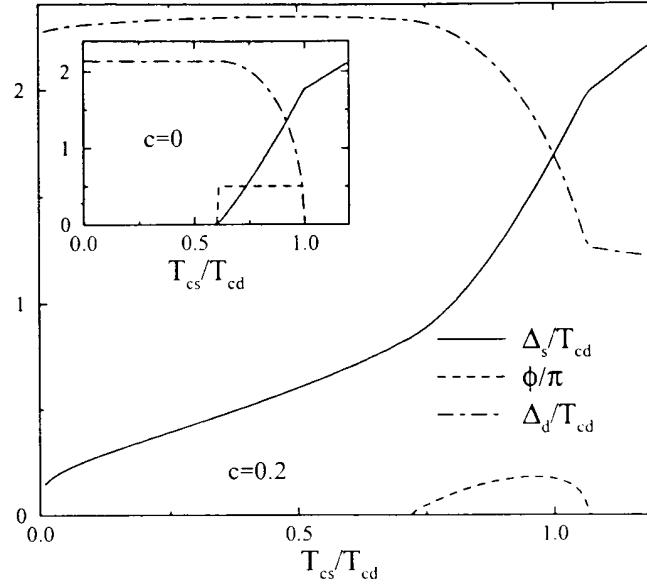
Figure 6.3: Zero-temperature properties of an orthorhombic superconductor with mixed d- and s-pairing. For different magnitudes of the orthorhombic distortion $c = 0.2$ (main graph) and $c = 0$ (inset), the two order parameters and the relative phases are shown as a function of T_{cs}/T_{cd}.

An expansion in c immediately shows that the s and d components are coupled for $c \neq 0$ and a finite value of one of the components drives the other component to be non-zero. A non-vanishing c also leads to a renormalized onset temperature for superconductivity. It is found by linearizing (6.7) under the assumption $\Delta_{s,d} \ll \omega$ and using (6.6) at $T = T_c(c)$. For a small orthorhombic distortion the critical temperature is then determined by

$$\ln\left(\frac{T_c}{T_{cd}}\right)\ln\left(\frac{T_c}{T_{cs}}\right) = \frac{\tilde{c}^2}{2}, \tag{6.8}$$

where $\tilde{c} = c\sum_{n=0}^{\omega_c/2\pi T_c}(n + 1/2)^{-1}$. If T_{cs} and T_{cd} are comparable we find the enhanced critical temperature

$$T_c(c) = \frac{1}{2}(T_{cs} + T_{cd}) + \frac{1}{2}\sqrt{(T_{cs} - T_{cd})^2 + 2\tilde{c}^2 T_{cs}T_{cd}} \ . \tag{6.9}$$

This equation establishes the bridge between our quasiclassical approach and the Ginzburg-Landau approach via Eq. (5) of Ref. [41]. The other coefficients of the Ginzburg-Landau

expansion are derived from our model in Appendix E. On the other hand, if T_{cs} and T_{cd} are not comparable the critical temperature is given by

$$T_c(c) = T_{cs,d} \left(1 + \frac{\tilde{c}^2}{2 \ln\left(T_{cd,s}/T_{cs,d}\right)} \right). \tag{6.10}$$

The resulting T_c is different from the Ginzburg-Landau result and shows explicitly, that the Ginzburg-Landau approach fails if the two coupled order parameters have strongly different coupling strengths.

The numerical results for the two order parameters and their relative phase at $T = 0$ are shown in Fig. 6.3 as a function of T_{cs}/T_{cd}. They always coexist. In contrast to the case $c = 0$, the relative phase ϕ varies continuously and is different from zero in a narrow window of values of T_{cs}/T_{cd}. The region of broken time-reversal symmetry is shrinking with increasing $|c|$, in qualitative agreement with the GL approach. In the case $c = 0$ we either find a one-component solution (i.e., the s- or the d-wave component vanishes), or both are finite and appear in the complex combination $d \pm is$, i.e. they have the relative phase $\phi = \pm\pi/2$ [170]. At $T = 0$ the complex phase occurs for $0.6 \lesssim T_{cs}/T_{cd} < 1.0$ (see the inset in Fig. 6.3).

In the following we will assume $T_{cs}/T_{cd} = 0.3$ (see Ref. [106]) and $c = 0.2$ which leads to $\Delta_s \sim 0.25\Delta_d$ and $\phi = 0$ or π (see Fig. 6.3), i.e., no bulk $\mathcal{T}$-violating state occurs in agreement with the present experimental status.

6.2   Pair potentials near a twin boundary

We will now consider a twin boundary, a boundary between two domains with the relative orientation of the crystal axes of 90°. The quasiclassical equations have to be solved along classical trajectories, which are characterized by a momentum direction on the Fermi surface k_F. At the twin boundary the k-vectors with the same k_y-component have to be matched, see Fig. 6.4. The reflection coefficient for a given k_F in the absence of a boundary potential is $R = (v_{Fx1} - v_{Fx2})^2/(v_{Fx1} + v_{Fx2})^2$. If we consider the energy dispersion given in Eq. (6.1) ($c = \text{sign}(x)|c|$), we find that $v_{Fx1} = v_{Fx2}$ for all scattering directions. Consequently we have *no normal* reflection at the twin boundary [159].

We solve the quasiclassical equations numerically in a selfconsistent way for various temperatures for a single twin boundary. Consistent with experimental observations [26, 157] we assumed that the d-wave component is identical on both sides, whereas the s-wave component changes sign.

Results for two different temperatures are shown in Figs. 6.5 and 6.6. For the higher temperature $T = 0.1T_{cd}$ the relative phase jumps from 0 to π at the twin boundary and Δ_s goes to zero directly at the twin boundary. On the other hand, for $T = 0.01T_{cd}$ we observe a
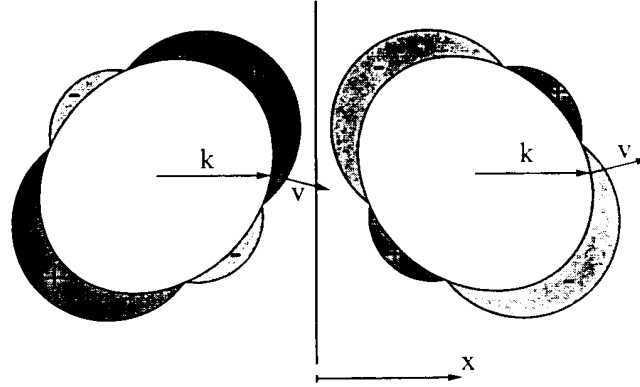
Figure 6.4: Fermi surfaces and bulk gap (shaded region) on both sides of the twin boundary. Fermi wave vectors k_F-vectors and Fermi velocities v_F for a perpendicular trajectory are indicated by arrows. The parallel components of v_F for these trajectories on both sides of the twin boundary have different sign.

local $\mathcal{T}$-violation for which the relative phase changes continuously from 0 to π with a non-vanishing s-wave pairing component. The inset in Fig. 6.6 shows $|\Delta_s|^2$ at the twin boundary as a function of temperature. It becomes finite for $T \lesssim 0.05$. A particular feature of local $\mathcal{T}$-violation is the appearance of spontaneous currents in the vicinity of the twin boundary flowing in opposite directions on both sides. These spontaneous currents at $T = 0.01 T_{cd}$ are shown in Fig. 6.7. Such spontaneous currents lead to a localized magnetization, which would be possibly observable by magnetic force microscopy [171]. Note that screening effects are not taken into account here. Typically the penetration depth is much larger than the extension of the bound states and screening effect is negligible close to the twin boundary. Hence the full magnetization should be measurable at the twin boundary.

6.3 Density of states near a twin boundary

The local density of states can be calculated by solving the Eilenberger equation for real energies. The results are given in Fig. 6.8. In the $\mathcal{T}$-invariant state a pronounced zero-energy peak occurs in the vicinity of the twin boundary. In the $\mathcal{T}$-violating state, the zero-energy peak splits into two symmetric peaks. The separation of the peaks is proportional to $\Delta_s(0)$. The local density of states can be measured by scanning tunneling microscopy. In particular, the splitting of the zero-energy peak would prove the existence of a time-reversal breaking state in YBCO [158]. The temperature at which the splitting occurs,
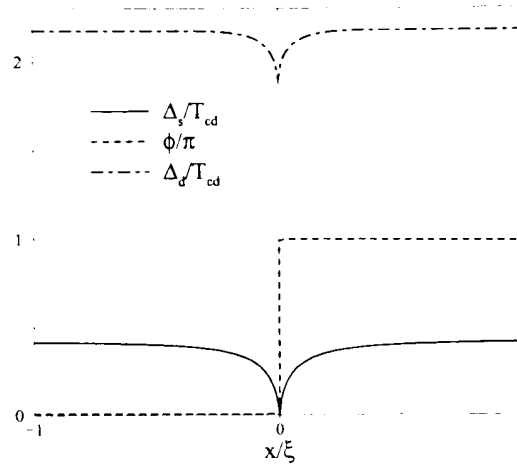
Figure 6.5: Order parameters in the vicinity of a twin boundary in the $\mathcal{T}$-invariant state for $T = 0.3T_{cd}$. The s-component goes to zero at the twin boundary and the relative phase shows a jump. The d-wave component is only slightly suppressed.
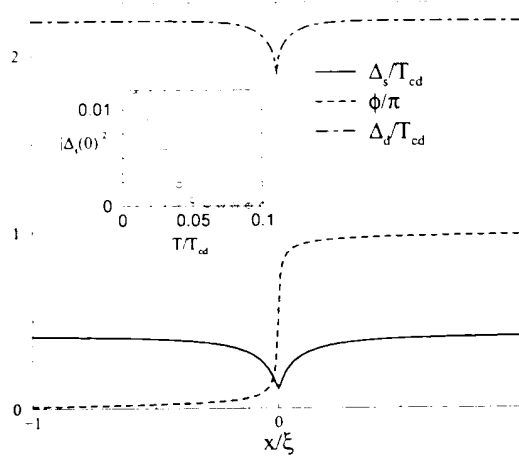

Figure 6.6: Order parameters in the vicinity of a twin boundary in the locally $\mathcal{T}$-violating state for $T = 0.01T_{cd}$. The absolute value of the s-component is finite for $x = 0$ and the relative phase changes smoothly from 0 to π. The suppression of the d-wave component is only weakly affected by the $\mathcal{T}$-violation. Inset: Modulus squared of (imaginary) s-component as a function of temperature. The second order phase transition is rounded due to numerical accuracy.
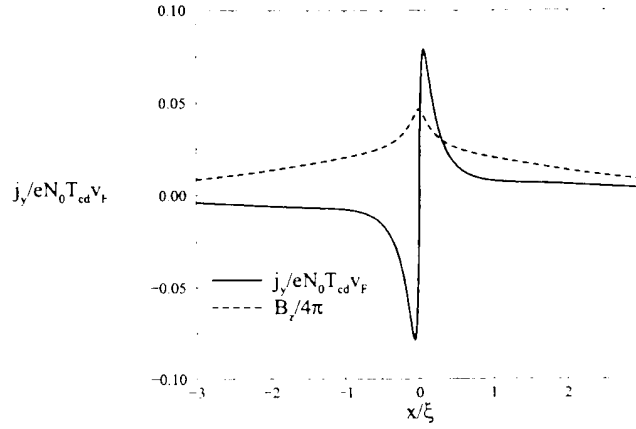
Figure 6.7: Spontaneous current and magnetic field in the $\mathcal{T}$-violating state. The current has an appreciable size of order of the depairing current. Due to the sign change of the current, the resulting magnetic induction is screened by the current on the other side of the twin boundary.

$T \sim 0.05 T_{\mathrm{cd}} \sim O(5K)$, is well within reach of current low-temperature scanning tunneling microscopy technology.

To investigate the microscopic nature of the gap feature in the local density of states and the spontaneous current it is useful to turn to an angle-resolved view of the problem. The zero-energy peak in the local density of states in the $\mathcal{T}$-invariant situation can be understood by considering classical trajectories with angles θ centered around 0, π and $\pm\pi/2$ in a range $2\delta\theta = \arcsin(\Delta_{\mathrm{s}}/\Delta_{\mathrm{d}})$. The corresponding Andreev (electron-hole) bound state for such angles is confined between two superconducting domains with a phase shift of π which leads to a zero-energy level [93]. On the other hand, broken time-reversal symmetry will generate phase shifts different from π leading to up or down shifted energy levels and the splitting of the zero-energy peak. Alternatively, this effect may be also seen as a driving mechanism: the large density of states of the zero-energy bound states at the Fermi energy gives rise to a local Fermi surface instability opening a (pseudo) gap.

How does the splitting lead to spontaneous currents? Each state (bound or extended) carries a current parallel to $\boldsymbol{v}_F(\boldsymbol{k})$. The phase gradient seen by these states leads to a shift in energy (bound states) or spectral weight (extended states). As a result left- and right-moving states are differently occupied, see Fig. 6.9. At $T = 0$ only the *right*-moving of the bound states are occupied. On the other hand, due to the shift of the spectral weight the *left*-moving continuum states give the dominant contribution of the continuum states.
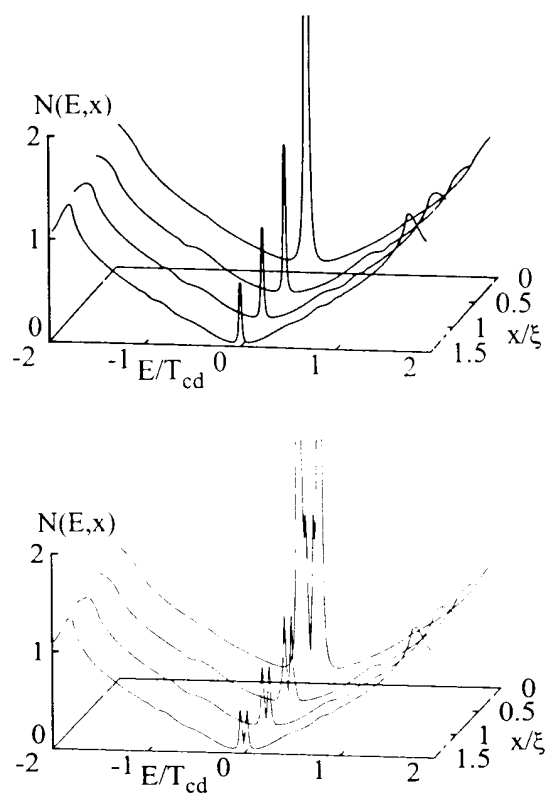
Figure 6.8: Local density of states in the vicinity of a twin boundary for $T_{cs}/T_{cd} = 0.3$ and $c = 0.2$. The two graphs correspond to $T = 0.1T_{cd}$ (upper graph) and $T = 0.01T_{cd}$ (lower graph). In the $\mathcal{T}$-invariant state there is a large peak at zero energy. The peak splits symmetrically in the $\mathcal{T}$-violating state.
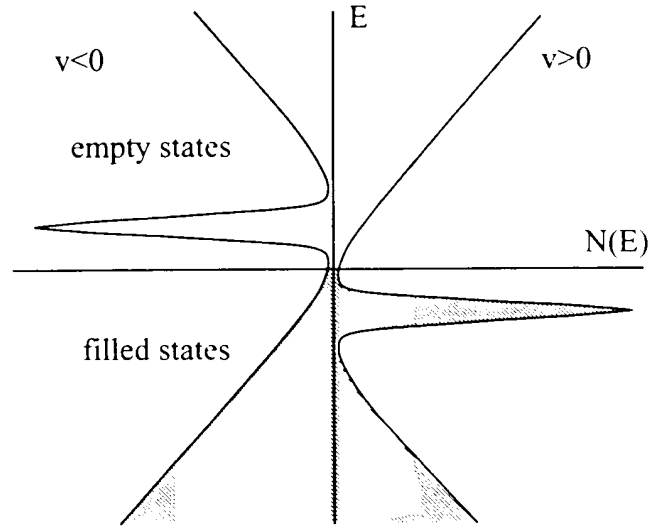
Figure 6.9: Schematic view of the angular resolved density of states at the twin boundary. Left moving ($v_y < 0$) and right moving ($v_y > 0$) are shifted in energy with opposite sign. The right moving bound states are occupied, while the left moving are empty.

They cancel the perpendicular current contribution of the bound states (as required by current conservation), leaving only a parallel component of the total current. For a simpler situation with a related mechanism, see [172]. The sign of the parallel current is different on both sides of the twin boundary due to the symmetry of the dispersion relation (the momenta and velocities for one of these states are indicated in Fig. 6.4).

In conclusion, we have studied the electronic structure of twin boundaries in orthorhombically distorted high-T_c superconductors. The orthorhombic distortion was introduced in the quasiclassical formalism of superconductivity, and the corresponding equations were solved selfconsistently. At low temperatures, we found a localized $\mathcal{T}$-violating state at the twin boundary. These localized states create spontaneous quasiparticle currents that flow in parallel to the twin boundary. In addition, we find a splitting of the zero-bias anomaly in the local density of states. Using realistic parameters we estimate that the splitting could be observed around 5K, i.e., using available low-temperature scanning tunneling microscopes. An observation of the splitting would be a unique signature of $\mathcal{T}$-violation in such systems.

EXHIBIT B

IL'ICHEV *ET AL.*, ARXIV:COND-MAT/0102404 V3 JUNE 2001

Degenerate ground state in a mesoscopic YBa$_2$Cu$_3$O$_{7-x}$ grain boundary Josephson junction

E. Il'ichev,[1] M. Grajcar,[1,2] R. Hlubina,[2] R.P.J. IJsselsteijn,[1] H.E. Hoenig,[1] H.-G. Meyer,[1] A. Golubov,[3] M.H.S. Amin,[4] A.M. Zagoskin,[4,5] A.N. Omelyanchouk,[4,6] and M.Yu. Kupriyanov[7]

[1] *Department of Cryoelectronics, Institute for Physical High Technology, P.O. Box 100239, D-07702 Jena, Germany*
[2] *Department of Solid State Physics, Comenius University, Mlynská Dolina F2, 842 48 Bratislava, Slovakia*
[3] *Department of Applied Physics, University of Twente, 7500 Æ Enschede, The Netherlands*
[4] *D-Wave Systems Inc., 320-1985 W. Broadway, Vancouver, B.C., V6J 4Y3, Canada*
[5] *Physics and Astronomy Dept., University of British Columbia 6224 Agricultural Rd., Vancouver, B.C., V6T 1Z1, Canada*
[6] *B.I. Verkin Institute for Low Temperature Physics and Engineering, 47 Lenin Ave., 310 164 Kharkov, Ukraine*
[7] *Institute of Nuclear Physics, Moscow State University, 119899 Moscow, Russia*

We have measured the current-phase relationship $I(\varphi)$ of symmetric 45° YBa$_2$Cu$_3$O$_7$ grain boundary Josephson junctions. Substantial deviations of the Josephson current from conventional tunnel-junction behavior have been observed: (i) The critical current exhibits, as a function of temperature T, a local minimum at a temperature T^*. (ii) At $T \approx T^*$, the first harmonic of $I(\varphi)$ changes sign. (iii) For $T < T^*$, the second harmonic of $I(\varphi)$ is comparable to the first harmonic, and (iv) the ground state of the junction becomes degenerate. The results are in good agreement with a microscopic model of Josephson junctions between d-wave superconductors.

The most important phenomenological difference between the high-T_c cuprates and conventional superconductors regards the orbital symmetry of the superconducting order parameter. In the cuprates the pair potential changes sign depending on the direction in momentum space according to[1,2] $\Delta(\vartheta) = \Delta_0 \cos 2(\vartheta - \theta)$, where ϑ is the angle between the wave vector and the (laboratory) x-axis, while θ is the angle between the Cu-Cu bond direction of the superconductor and the x-axis. This unconventional d-wave symmetry was predicted[3] and experimentally confirmed[1,2] to be directly measurable in the Josephson effect between a high-T_c and a conventional superconductor. Another consequence of the d-wave symmetry is that mid-gap states (MGS) with energy $\varepsilon = 0$ should form on the free surface of a d-wave superconductor if $\Delta(\vartheta)$ has opposite signs on incident and reflected electronic trajectories.[4] The MGS density must be maximal for (110)-like surfaces and this prediction has in fact been confirmed by STM microscopy on YBCO single crystals[5] which revealed the MGS contribution to the YBCO tunneling density of states. The presence of the MGS is expected to influence in a spectacular way also the Josephson effect in junctions between d-wave superconductors with different crystallographic orientations. Yet no clear manifestation of the MGS in the Josephson effect in such junctions has been observed so far, which is a challenge for the concept of d-wave superconductivity in the cuprates.

Moreover, due to possible applications in quantum computing,[6,7] there is substantial interest in Josephson junctions and circuits with a doubly degenerate ground state. Such a state was predicted in an asymmetric 45° junction ($\theta_1 = 0°$ and $\theta_2 = 45°$, the angles $\theta_{1,2}$ are defined in Fig. 1), since odd harmonics of the Josephson current $I(\varphi) = \sum_n I_n \sin n\varphi$ are suppressed by symmetry.[8,9] The current-phase relation observed in Ref. 10 indeed showed a substantial contribution of the second harmonic I_2. However, there is a finite supercurrent flowing along the interface in the ground state of asymmetric 45° junctions.[9] Therefore they do not lead to completely quiet qubits in the sense of Ref. 6.
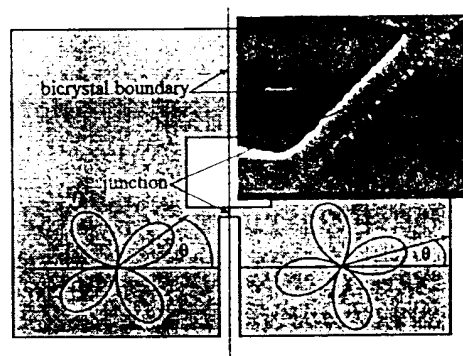

FIG. 1. Schematic picture of the RF SQUID. The YBCO thin film occupies the gray area. The inset shows an electron microscope image of the narrow grain boundary Josephson junction.

Motivated by the search for both, the MGS in high-T_c Josephson junctions and a quiet qubit, we have studied symmetric 45° junctions (i.e. junctions with $\theta_1 = -\theta_2 = 22.5°$). In this paper we report the first direct observation of several effects exclusive to such junctions: temperature controlled sign change of the first harmonic of the Josephson current, a nonmonotonic temperature dependence of the critical current, and the development of a doubly degenerate ground state of the system.

Let us start with a description of the theoretical predictions for Josephson junctions between d-wave superconductors. In symmetric short junctions the Josephson current density is conveniently described in terms of the Andreev levels in the junction as[11]

$$j(\varphi) = \frac{k_F}{\Phi_0 d} \sum_n \int_{-\pi/2}^{\pi/2} d\vartheta \cos\vartheta f\left[\varepsilon_n(\varphi,\vartheta)\right] \frac{\partial\varepsilon_n(\varphi,\vartheta)}{\partial\varphi},$$

where φ is the superconducting phase difference between the banks, Φ_0 is the magnetic flux quantum, k_F is the Fermi momentum, d is the average separation of the CuO_2 planes, $f(\varepsilon)$ is the Fermi distribution function, and $\varepsilon_n(\varphi,\vartheta)$ is the energy of the n-th Andreev level for an electron incident on the junction at an angle ϑ with respect to the boundary normal. At a given ϑ there exist only two Andreev levels with energies $\pm\varepsilon(\varphi,\vartheta)$.

The nature of the Andreev levels changes with the impact angle ϑ: (i) For $22.5° < |\vartheta| < 67.5°$, MGS are formed at $\varphi = 0$ whose energy is split by a finite phase difference φ across the contact. In this range of impact angles $\varepsilon(\varphi)$ can be qualitatively described by $\varepsilon_{MGS}(\varphi) = \Delta(\pi/4)\sin(\varphi/2)\sqrt{D(\pi/4)}$, where $0 \leq D(\vartheta) \leq 1$ is the angle-dependent barrier transparency.[12] (ii) For $|\vartheta| < 22.5°$ and $67.5° < |\vartheta| < 90°$, no MGS are formed at $\varphi = 0$ and the Andreev levels resemble those formed in a Josephson junction between s-wave superconductors. In this range of impact angles $\varepsilon(\varphi)$ can be qualitatively described by $\varepsilon_{conv}(\varphi) = \Delta(0)[1 - D(0)\sin^2(\varphi/2)]^{1/2}$.

When inserted into the equation for $j(\varphi)$, the two sets of Andreev levels yield contributions of opposite sign to the Josephson current, $I(\varphi) = I_{MGS}(\varphi) + I_{conv}(\varphi)$. Close to T_c, when $T \gg \Delta_0(T)$, we can approximately write $I_{conv} \propto D(0)(\Delta_0^2/T)\sin\varphi$ and $I_{MGS} \propto -D(\pi/4)(\Delta_0^2/T)\sin\varphi$. For a sufficiently large ratio $D(0)/D(\pi/4)$ the sign of the first harmonic at high temperatures is therefore given by the conventional contribution. Lowering the temperature to $\sqrt{D(\pi/4)}\Delta_0(T) \ll T \ll \Delta_0(T)$, I_{conv} saturates to $I_{conv} \propto D(0)\Delta_0\sin\varphi$, whereas $|I_{MGS}|$ continues to grow according to $I_{MGS} \propto -D(\pi/4)(\Delta_0^2/T)\sin\varphi$. As a result, near $T^* \sim \Delta_0 D(\pi/4)/D(0)$ the first harmonic will change sign and therefore the second harmonic will dominate the current, leading to a doubly degenerate ground state.

In a symmetric junction $\varepsilon(\varphi,\vartheta) = \varepsilon(\varphi,-\vartheta)$[12] and therefore the total current along the interface is exactly zero at any T and φ, contrasting with a finite total current in an asymmetric junction. A more detailed analysis shows that in symmetric junctions time reversal symmetry is broken and small currents of equal magnitude and opposite sign flow along the interface in the left and right superconducting banks. Thus, although they are much closer to being quiet than asymmetric junctions, even the symmetric junctions are not completely quiet.

An experimental confirmation of the above theoretical predictions requires the use of mesoscopic junctions. In fact, since the grain boundaries are faceted on a length scale $\sim 0.1~\mu m$,[13] $I(\varphi)$ of macroscopic junctions necessarily represents a nontrivial average over junctions with different misorientations. However, standard transport measurements of the critical current $I_c = \max_\varphi\{I(\varphi)\}$ are possible only at temperatures smaller than the energy of the grain boundary Josephson junction, $\sim \Phi_0 I_c/2\pi$. Therefore we have used the modified Rifkin-Deaver method[14,15] which offers a unique possibility to study $I(\varphi)$ at temperatures T much higher than the junction energy. This is achieved by connecting the banks of the junction to form a superconducting ring (or an RF SQUID) so that the phase difference across the junction is controlled by the (large) phase stiffness of the ring.
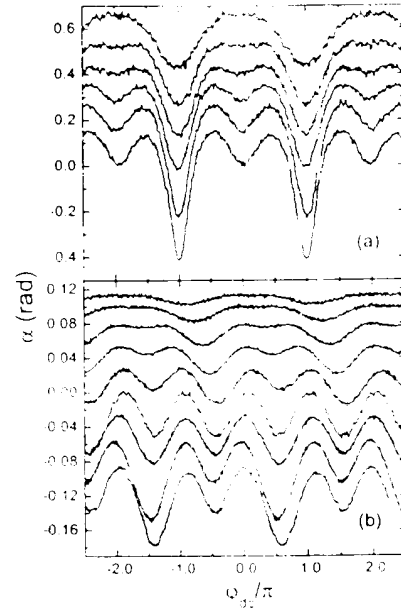

FIG. 2. The phase angle α as a function of φ measured at different temperatures for sample No. 1 (a) and No. 2 (b). From top to bottom, the data correspond to (a) $T = 30, 20, 15, 10, 4.2, 1.8$ K and (b) $T = 35, 30, 25, 20, 15, 11, 10, 5, 1.6$ K. The data are vertically shifted for clarity.

The YBCO thin films of thickness 100 nm were prepared by laser deposition on 45° symmetric bicrystal substrates. The RF SQUIDs were patterned in the shape of a square washer 3500 $\mu m \times$ 3500 μm with a hole 50 $\mu m \times$ 50 μm by electron beam lithography (see Fig. 1.). Here we present the data on two samples with critical current densities $j_c \approx 2.6 \times 10^3$ A/cm^2 for sample No. 1 and $j_c \approx 400$ A/cm^2 for sample No. 2. The estimated Josephson penetration depth λ_J is much smaller than the width of the wide junction, $w_l = 1725~\mu m$, and larger than the width of the narrow junction, $w_s = 0.7~\mu m$ and $w_s = 0.5~\mu m$ for samples No. 1 and 2, respectively. Thus the behavior of the RF SQUID is dictated by the narrow junction only. The submicron bridge was formed at a position between

the defects of the substrate which are visible in Fig. 1.

In the modified Rifkin-Deaver method,[14,15] the sample is inductively coupled to a high-quality parallel resonance circuit ($Q = 155$ and 165 for samples No. 1 and 2, respectively) driven at its resonant frequency ω_0. The angular phase shift α between the driving current and the voltage across the circuit is measured by a RF lock-in voltmeter as a function of the external magnetic flux Φ_{dc}, which is conveniently measured in the dimensionless units $\varphi_{dc} = 2\pi\Phi_{dc}/\Phi_0$. The phase difference across the junction φ was calculated from the $\alpha(\varphi_{dc})$ data using the coupling coefficient between the RF SQUID and the tank coil $k^2 = 2.6 \times 10^{-3}$ and $3.6 \cdot 10^{-3}$ for samples No. 1 and 2, respectively. After inverting the $\varphi = \varphi(\varphi_{dc})$ function, $I(\varphi)$ can be obtained from $\beta f(\varphi) = \varphi_{dc}(\varphi) - \varphi$, where $f(\varphi) = I(\varphi)/I_c$, $\beta = 2\pi L I_c/\Phi_0$, and $L = 80$ pH is the inductance of the RF SQUID. The details of the experimental method are given elsewhere.[15]
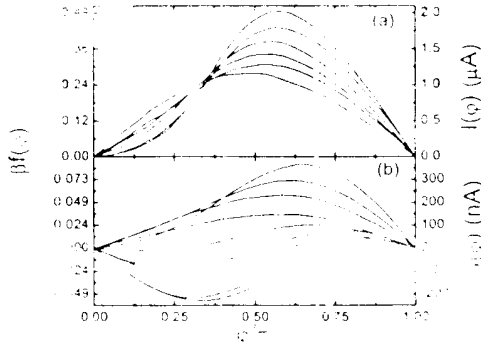

FIG. 3. $I(\varphi)$ for sample No. 1 (a) and No. 2 (b). From top to bottom at $\varphi/\pi = 0.5$, the data correspond to (a) $T = 30, 20, 15, 10, 4.2, 1.8$ K and (b) $T = 20, 25, 30, 35, 15, 11, 10, 5, 1.6$ K. The data in Fig. 3b correspond to $T = 20, 25, 30, 35$ were multiplied by a factor 1 for clarity.

The measured $\alpha(\varphi_{dc})$ curves shown in Fig. 2 exhibit local minima at low T when φ_{dc} is a multiple of 2π. This is qualitatively different from what has been observed before for 45° symmetric grain boundary Josephson junctions on samples with $w_s > 1$ μm where no such minima were found.[16] We believe that the difference is caused by the existence of the bicrystal boundary defects with a typical distance ~ 1 μm (see Fig. 1), which cannot be avoided for large junctions.

The Josephson current calculated from the measured $\alpha(\varphi_{dc})$ data is shown in Fig. 3. Note the anomalous form of $I(\varphi)$ at low temperatures. The anomalies in sample No. 2 are much more pronounced than in sample No. 1. We believe this is a combined effect of smaller junction cross-sections and higher junction quality, as evidenced by the much smaller values of I_c in sample No. 2. In Fig. 4 we plot the first two harmonics I_1 and I_2 for the sample No. 2. The most striking result is that for $T^* \approx 12$ K, I_1 changes sign. In the same temperature region where I_1 starts to exhibit a downturn, the value of $|I_2|$ rises from

the negligible high-T values to values comparable to $|I_1|$ at low T, suggesting a common origin of both phenomena. Furthermore, Fig. 4 shows that close to T^*, there is a local minimum of the critical current I_c as a function of T, which is associated with the sign change of I_1. These results are in a qualitative agreement with theoretical predictions for $I(\varphi)$ of 45° junctions with ideally flat interfaces.[17,8]

We can reconstruct the free energy F of the junction as a function of φ from $F(\varphi) = (\Phi_0/2\pi) \int_0^\varphi d\phi I(\phi)$. The result is shown in Fig. 5. Note that for $T \leq 15$ K, the free energy minimum of the sample No. 2 moves away from $\varphi = 0$, and the $F(\varphi)$ curve exhibits two degenerate minima at $\varphi = \pm\varphi_0$, as observed previously in Ref. 10 on asymmetric 45° junctions, see Fig. 5.
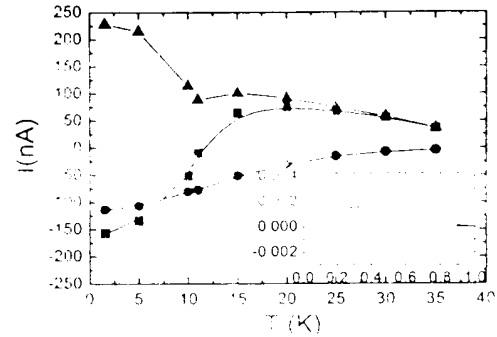

FIG. 4. The critical current I_c (triangles) and the harmonic components I_1 (squares) and I_2 (circles) of the Josephson current as a function of temperature for sample No. 2. The data are obtained by the Fourier analysis of $I(\varphi)$ shown in Fig. 3b. Inset: Theoretical prediction for the temperature dependence of j, j_1, and j_2 for a junction with $\mathcal{D} = 0.3$ and $\rho = 0.3$. The current densities are plotted in units of the Landau critical current density, the temperature is in units of T_c.

In Fig. 4 we compare the experimental data with a theoretical treatment based on the quasiclassical Eilenberger equations which was introduced in the s-wave case in Ref. 18 and will be described in detail elsewhere. Within our approach the junction is described by two phenomenological parameters, the junction transparency $\mathcal{D}$ and the roughness parameter $0 < \rho < \infty$. The temperature dependence of I_1, I_2, and I_c is fit well by our theory with $\mathcal{D} = 0.3$ and $\rho = 0.3$. The theoretical j_c is reported in Fig. 4 in units of the Landau critical current density $j_0 = k_F\Delta_0/\Phi_0 d$, where Δ_0 is the gap parameter at the interface. The experimental critical current density j_c for 45° junctions is smaller than j_c^{bulk} by a factor[13] $\sim 10^{-5} - 10^{-4}$. Remarkably, the absolute value of j_c is also well described by $\mathcal{D} = 0.3$ and $\rho = 0.3$. In fact, in 45° junctions Δ_0 can be estimated from[13] $\Delta_0 \sim I_c R_N \sim 10^{-1} - 1$ meV, and therefore $j_0/j_c^{\text{bulk}} \sim \Delta_0/\Delta_0^{\text{bulk}} \sim 10^{-2} - 10^{-1}$. Together with the theoretical result $j_c/j_0 \sim 10^{-3}$, this explains the experimental ratio j_c/j_c^{bulk}.

3

FIG. 5. Free energy $F(\varphi)$ as a function of the phase difference across the weak link. The zero of energy has been set so that $F(0) = 0$. (a) Asymmetric 45° grain boundary (Ref. 10). Top to bottom curves correspond to $T = 30$, 20, 15, 10, and 1.2 K respectively. (b) Symmetric 45° grain boundary (present work). Top to bottom curves correspond to $T = 20$, 15, 11, 10, 5, and 1.6 K, respectively.

Before concluding let us point out that a large I_2 can be expected also in a real-space scenario, in which it is predicted that due to surface roughness and/or twinning of the superconducting bank, a spontaneous magnetic flux is generated along the interface [19,20] We are not aware of any prediction of a sign change of I_1 within the real-space scenario. But we can rule it out also in a different way, on very general grounds. I_1 corresponds to a $F_1 \cos \varphi$ term in the free energy, where $F_2 = -\Phi_0/4\pi)I_2$. In the real-space scenario, F_2 is the free energy due to the formation of spontaneous magnetic domains. Taking $I_2 = 120$ nA for the sample No. 2 at low T, we estimate $F_2/k_B \approx 1.3$ K. However, since the associated pattern of phase differences along the junction is not controlled by external circuit (unlike the average phase difference across the junction), thermal fluctuations would smear the I_2 component at $T > F_2/k_B$, in disagreement with experiment.

In conclusion, we have found that symmetric 45° junctions exhibit doubly degenerate ground states. Therefore they are of potential use in superconducting qubit fabrication. The qubits based on asymmetric 45° junctions are not quiet,[6] since there exists spontaneously generated flux along the interface[21] which should change sign between the two different ground states of the junction. The qubits based on symmetric junctions might be close to being completely quiet, since their spontaneously generated flux is unmeasurably small.[21] The key technological question is how to increase the energy barrier between the two degenerate minima at $\varphi = \pm\varphi_0$. An interesting possibility seems to be to increase the barrier transparency by an appropriate doping of the grain boundary.[22]

[1] D. J. Van Harlingen, Rev. Mod. Phys. **67**, 515 (1995).

[2] C. C. Tsuei and J. R. Kirtley, Rev. Mod. Phys. **72**, 969 (2000).

[3] M. Sigrist and T. M. Rice, J. Phys. Soc. Jpn. **61**, 4283 (1992).

[4] C. R. Hu, Phys. Rev. Lett. **72**, 1526 (1994).

[5] L. Y. T. Wei et al., Phys. Rev. Lett. **81**, 2542 (1998).

[6] J. B. Ioffe et al. Nature **398**, 679 (1999).

[7] A. Blais and A. M. Zagoskin, Phys. Rev. A **61**, 042308-1 (2000).

[8] S. Kashiwaya and Y. Tanaka, Rep. Prog. Phys. **63**, 1641 (2000).

[9] ... ... (1997).

[10] E. Il'ichev et al. Phys. Rev. B 60, 3096 (1999).

[11] ... ... (1998).

[12] Yu. S. Barash, Phys. Rev. B **61**, 678 (2000).

[13] H. Hilgenkamp, J. Mannhart, and B. Mayer, Phys. Rev. B **53**, 14586 (1996).

[14] R. Rifkin and B. ... (1976).

[15] E. Il'ichev et al. Applied ... Physics **38**, 507 (1998).

[16] E. Il'ichev et al., Phys. Rev. Lett. **81**, 894 (1998).

[17] Y. Tanaka and S. Kashiwaya, Phys. Rev. B **53**, R11 957 (1996).

[18] A. N. Omelyanchouk, R. deBruyn Ouboter, and C. J. Muller, Low Temp. Physics **20**, 398 (1994).

[19] A. J. Millis, Phys. Rev. B **49**, 15 408 (1994).

[20] R. G. Mints, Phys. Rev. B **57**, R322 (1998).

[21] J. Mannhart et al., Phys. Rev. Lett. **77**, 2782 (1996).

[22] G. Hammerl et al., Nature **407**, 162 (2000).

EXHIBIT C

AMIN *ET AL.*, ARXIV:COND-MAT/0011416 V2, DEC. 6, 2002

Mechanisms of Spontaneous Current Generation in an Inhomogeneous d-Wave Superconductor

M.H.S. Amin[a], A.N. Omelyanchouk[b], and A.M. Zagoskin[a,c]

[a] D-Wave Systems Inc., 320-1985 W. Broadway, Vancouver, B.C., V6J 4Y3, Canada
[b] B.I. Verkin Institute for Low Temperature Physics and Engineering,
Ukrainian National Academy of Sciences, Lenin Ave. 47, Kharkov 310164, Ukraine
[c] Physics and Astronomy Dept., The University of British Columbia,
6224 Agricultural Rd., Vancouver, B.C., V6T 1Z1, Canada.

A boundary between two d-wave superconductors or an s-wave and a d-wave superconductor generally breaks time-reversal symmetry and can generate spontaneous currents due to proximity effect. On the other hand, surfaces and interfaces in d-wave superconductors can produce localized current-carrying states by supporting the T-breaking combination of dominant and subdominant order parameters. We investigate spontaneous currents in the presence of both mechanisms and show that at low temperature, counter-intuitively, the subdominant coupling *decreases* the amplitude of the spontaneous current due to proximity effect. Superscreening of spontaneous currents is demonstrated to be present in any d-d (but not s-d) junction and surface with $d + id$ order parameter symmetry. We show that this superscreening is the result of contributions from the local magnetic moment of the condensate to the spontaneous current.

(November 12, 2002)

The time-reversal symmetry (T) breaking on surfaces and interfaces of superconductors with d-wave orbital pairing has been intensively investigated in the last years both in theory and experiment [1-8]. Several mechanisms of T-breaking have been proposed, which fall in two categories: appearance of subdominant order parameter and proximity effect [2,3].

In the first case the surface interface suppresses the dominant order parameter ($d_{x^2-y^2}$ in YBCO [4]). If pairing into channels is nonzero, the dominant order and the corresponding, smaller critical temperature T_{c2}. The combination of breaks surface current $d_{x^2-y^2} \pm is$ or $d_{x^2-y^2} \pm id_{xy}$ combinations are predicted. Recent observations of peak splitting in surface tunneling experiments [5] and spontaneous fractional flux 0.1-0.2 Φ_0) near the "green phase" inclusions in YBCO [6] agree with this picture.

The other possibility arises in a junction between two d-wave superconductors with different orientations of the order parameter [7]. In this case the two order parameters necessary to form a T-breaking state, $d_{1,2}$, are supplied by the bulk superconductors. The equilibrium phase difference across the boundary, ϕ_0, is generally neither 0 nor π, and therefore the states with $d_1 + e^{\pm i\phi_0}d_2$ orderings are degenerate and may support spontaneous currents. The same mechanism applies in case of a boundary between an s- and a d-wave superconductor [8].

In order to investigate the interplay of both mechanisms, in this letter we consider d-d and s-d interfaces as well as (110)-surface of a d-wave superconductor. We will see that generally the spontaneous currents due to proximity effect are suppressed by the existence of subdominant order parameter. There is also an important

distinction between the d-d and s-d cases: In the former case the superconductor may have local orbital and magnetic moments, contributing to the non-dissipative current. In the latter case such a contribution is absent. Our results indicate that in a clean d-d junction all of the spontaneous current can be attributed to this "molecular currents" mechanism. We also show that this effect suppression of spontaneous current d-d junctions of coherent pendent

We use cal Eilenberger equations for Green's functions integrated

above ω is the Matsubara frequency and

$$\widehat{G}_\omega(\mathbf{v}_F, \mathbf{r}) = \begin{pmatrix} g_\omega & f_\omega \\ f_\omega^\dagger & g_\omega \end{pmatrix}, \quad \widehat{\Delta}(\mathbf{v}_F, \mathbf{r}) = \begin{pmatrix} 0 & \Delta \\ \Delta^\dagger & 0 \end{pmatrix}.$$

Here $\widehat{G}_\omega$ is the matrix Green's function and Δ is the superconducting order parameter. They both are functions of Fermi velocity $\mathbf{v}_F$ and position $\mathbf{r}$. We also need to satisfy the normalization condition $g_\omega = \sqrt{1 - f_\omega f_\omega^\dagger}$. In general case Δ depends on the direction of the vector $\mathbf{v}_F$ and is determined by the self-consistency equation

$$\Delta(\mathbf{v}_F, \mathbf{r}) = 2\pi N(0) T \sum_{\omega > 0} V \quad f_-(\mathbf{v}'_F, \mathbf{r}) \quad _\theta. \quad (2)$$

where V is the interaction potential. In our calculations we will consider is the 2D density of states and $< ... > \int_0 \frac{d\theta}{2\pi}$ is the averaging over directions of 2D vector $\mathbf{v}_F = (v_F \cos\theta, v_F \sin\theta)$.
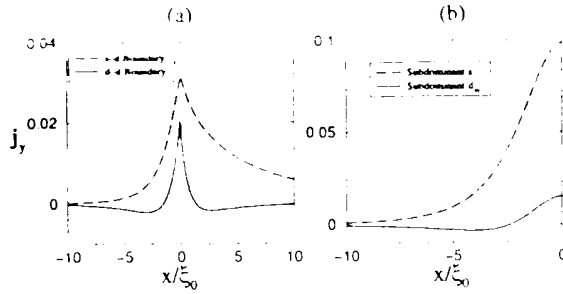
FIG. 1. (a) Spontaneous current for d-d and s-d junctions. The boundary is located at $x = 0$. Calculations are done at $t = T/T_c = 0.05$, with $T_{c2} = 0.05T_c$ for the d-d case and $T_{cs} = 0.1T_c$ and $T_{c2} = 0.05T_c$ for the s-d junction (b) Spontaneous current at the (110)- surface of a d-wave superconductor at $t = 0.05$ with $T_{c2} = T_{cs} = 0.1T_c$ for both s or d_{xy} subdominant order parameters.

In general it is possible to obtain a mixture of different symmetries of the order parameter, $\Delta(\theta) = \Delta_{x^2-y^2}(\theta) + \Delta_{xy}(\theta) + \Delta_s$ where $\Delta_{x^2-y^2}(\theta) = \Delta_1 \cos 2\theta$, $\Delta_{xy}(\theta) = \Delta_2 \sin 2\theta$ and Δ_s are the $d_{x^2-y^2}$, d_{xy}, and the s-wave components of the order parameter respectively. The corresponding interaction potential, $V_{\theta\theta'} = V_{d1} \cos 2\theta \cos 2\theta' + V_{d2} \sin 2\theta \sin 2\theta' + V_s$, must be substituted in the self-consistency equation (2) for the order parameter in each channel. The current density $\mathbf{j}(\mathbf{r})$ is found from the solution of the matrix equation (1) as

$$\mathbf{j}(\mathbf{r}) = -4\pi e N(0)T \sum_{\omega > 0} < \mathbf{v}_F g_\omega(\mathbf{v}_F, \mathbf{r}) >_\theta. \qquad (3)$$

Here we consider three cases, (i) boundary between two semi-infinite d-wave superconductors with crystalographic orientations with respect to the boundary given by angles χ_l and χ_r ("d-d interface"), (ii) boundary between an s-wave and a d-wave superconductor with $45°$ orientation ("$45°$ s-d interface"), and (iii) (110)-surface of a d-wave superconductor. In all three cases it is possible to have time reversal symmetry breaking ground state. The direction and magnitude of the spontaneous current depends on the relative phases of the order parameters.

Assuming constant order parameters on both sides of an interface, one can obtain an analytical (non-selfconsistent) expression for the current density

$$\mathbf{j}(x) = 4\pi e N(0)T \sin \phi \qquad (4)$$
$$\sum_{\omega > 0} \langle \frac{\mathbf{v}_F \Delta_l \Delta_r \text{sign}(\cos \theta)}{\Omega_l \Omega_r + \omega^2 + \Delta_l \Delta_r \cos \phi} e^{-2|x|\Omega /|v \cos\theta|} \rangle_\theta,$$

where l (r) labels left (right) side of the interface, and $\Omega_i = \sqrt{\omega^2 + |\Delta_i|^2}$. This expression is valid for arbitrary symmetry of the order parameters $\Delta_{l,r}$. For a d-d interface we have $\Delta_l = \Delta_0(T) \cos 2(\theta - \chi_l)$ and $\Delta_r = \Delta_0(T) \cos 2(\theta - \chi_r)$ where $\Delta_0(T)$ depends on the superconducting coupling and temperature.

Our numerical calculations were based on Schopohl-Maki parameterization of Green's functions [11] ,
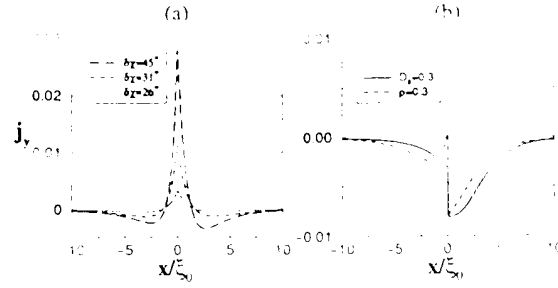
FIG. 2. (a) Spontaneous currents for d-d_{xy} junctions with different misorientation angles. (b) Spontaneous current at imperfect ($0°$-$45°$) junctions. Solid line: junction with transparency $D_0 = 0.3$. Dashed line: junction with roughness $\rho = 0.3$. All calculations are done at $t = 0.1$.

$$g = \frac{1 - aa^\dagger}{1 + aa^\dagger}, \qquad f = \frac{2a}{1 + aa^\dagger}, \qquad f^\dagger = \frac{2a^\dagger}{1 + aa^\dagger},$$

which transforms Eq. (1) into

$$\mathbf{v}_F \cdot \nabla a = 2\omega a - \Delta^* a^2 + \Delta \qquad (5)$$
$$-\mathbf{v}_F \cdot \nabla a^\dagger = 2\omega a^\dagger - \Delta a^{\dagger 2} + \Delta^*. \qquad (6)$$

For positive v_x, Eq. (5) (Eq. (6)) is stable if the boundary condition at $x = -\infty$ ($+\infty$) is chosen. The opposite is true for negative v_x. We use the solutions in a homogeneous system, $a = \Delta/(\omega + \Omega)$ and $a^\dagger = \Delta^*/(\omega + \Omega)$ as boundary conditions at $\pm\infty$. The values of a ($a^\dagger$) at all other points on the trajectory are then easily found. The self-consistency is introduced through iterations, assuming a constant order parameter in either half of the system for the first iteration.

Fig. 1a shows the spatial distribution of the spontaneous current in d-d and s-d junctions. The left superconuctor is a d-wave superconductor with $45°$ crystal orientation with respect to the boundary. The right side is either an s-wave or a d-wave superconductor aligned with the boundary. The current distribution is qualitatively different in s-d and d-d junctions. In the d-d case, the current density is at maximum in a layer of width of about coherence length, $\xi_0 = v_F/\pi\Delta$, along the boundary; there also exists a counter-flow, spread over about $10\xi_0$ on either side of the boundary. The total current in y-direction is zero within the numerical accuracy, *independently* on the right and left sides of the junction. This effect can be called "superscreening", since the resulting magnetic field of the spontaneous current is cancelled on the scale of $\sim 10\xi_0 \ll \lambda_L, \lambda_J$, the London and Josephson magnetic penetration depths. Note that this has nothing to do with the Meissner screening; it appears without taking into account the vector potential of the magnetic field of the current (and makes it unnecessary) [12]. On the contrary, in the s-d junction the counter-flows are absent (unless the Meissner effect is taken into account [8]).

The same situation takes place near the surface, if the subdominant pairing is present. Fig. 1b shows the cur-
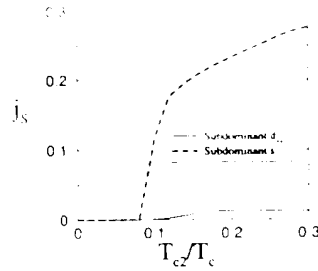
2

FIG. 3. The effect of subdominant interaction on the spontaneous current j_s ($\equiv j_y(x=0)$) at the surface of a d wave superconductor. A second order phase transition happens at $T_{c2} = T$. $1T_c$

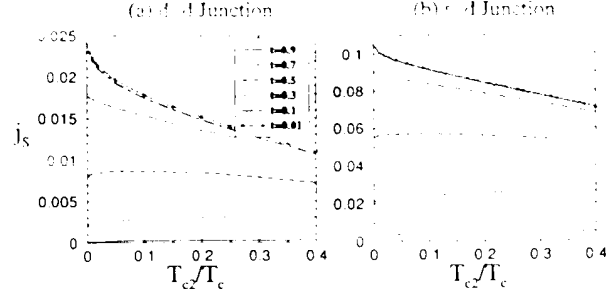FIG. 4. Suppression of spontaneous current by subdominant order parameter. (a) A d-d grain boundary. (b) An s-d interface. In the s-d case, we have taken the same T_c for both sides and also $T_{cs} = T_{c2}$.

r distribution at the (110)-surface of a d-wave superconductor. If d_{xy} is the leading subdominant order parameter, the form of the current distribution is similar to the one in the d-d boundary. The superscreening is absent if the subdominant order parameter is s-wave.

The superscreening effect can be obtained analytically from the non-selfconsistent expression (4) in case of 0-45° junction. The nullification of the total current results from integrating the spontaneous current

$$\int_0^\infty dx j_y(x) \propto \langle \frac{\Delta_l \Delta_r \sin\theta \ \text{sign}(\cos\theta)}{\Omega_l \Omega_r + \omega^2 + \Delta_l \Delta_r \cos\varphi} \frac{v_F |\cos\theta|}{\Omega_r} \rangle_\theta \sin\varphi$$

which is zero after angle averaging. Our numerical calculations however show that in clean boundary junctions the total current is zero (within the numerical accuracy) even after self-consistent calculation and at all other misorientation angles (see Fig. 2a).

To understand the situation, let us recall that in a system with local magnetic moment density $\mathbf{m}(\mathbf{r})$ the "molecular currents" flow with density $\mathbf{j}(\mathbf{r}) = c\nabla \times \mathbf{m}(\mathbf{r})$. In a superconductor with order parameter $d_{x^2-y^2} + e^{i\phi_0}d_{xy}$ local orbital/magnetic moment density

$$\mathbf{m}(\mathbf{r}) \propto \hat{\mathbf{z}} \int_0^{2\pi} \frac{d\theta}{2\pi} \left(\Delta_1(x)\cos 2\theta + \Delta_2(x)e^{-i\phi_0}\sin 2\theta \right)$$
$$\times \frac{1}{i} \frac{\partial}{\partial\theta} \left(\Delta_1(x)\cos 2\theta + \Delta_2(x)e^{i\phi_0}\sin 2\theta \right)$$
$$= 2\Delta_1(x)\Delta_2(x)\hat{\mathbf{z}}\sin\phi_0.$$

The contribution to the spontaneous current is thus $\mathbf{j}(\mathbf{r}) \propto \nabla \times \mathbf{m}(\mathbf{r}) \parallel \hat{\mathbf{y}}$. Notice that the same expression is obtained from the Ginzburg-Landau equations [13] ($\mathbf{j} \propto \nabla \times (\hat{\mathbf{z}} \ \text{Im} \ d_1(\mathbf{r})d_2(\mathbf{r})^*)$). The total current in y-direction due to this mechanism is $I_{\text{total}} \propto \int_\Omega dS \cdot \nabla \times \mathbf{m} = \oint_{\partial\Omega} dl \cdot \mathbf{m} = 0$, where Ω is a cross section perpendicular to the junction from $x = -\infty$ to ∞ and $\partial\Omega$ is its boundary. The latter integral is obviously zero because $dl \cdot \mathbf{m} = 0$ ($\mathbf{m} \parallel \mathbf{z}$) everywhere except where the contour closes ($x = \pm\infty$), but there $\mathbf{m} = 0$. This is certainly not the case in s-d junctions (cf. Fig. 1). (Of course, since

the Meissner currents must be taken into account in this case, the results presented in Fig. 1 are valid only if the system size is much less than the London penetration depth.)

We also calculate the spontaneous current for an imperfect boundary, i.e a boundary with arbitrary transparency D_0 and also with finite roughness ρ. We use Zaitsev's boundary condition [14,15] to incorporate the finite transparency effect. For surface roughness we assume a thin layer with scattering centers at the junction [16]. We take the mean free path l and the layer thickness d to zero while keeping $\rho \equiv d/l$ finite. The details of calculations will be given in a separate publication. Here we only present the results of our calculation for asymmetric (0°-45°) d-d junction in Fig. 2b. As is clearly seen, the spontaneous currents now does not necessarily have a counterflow (at small ρ or $D_0 \leq 1$ there will be some counterflow), and the exact superscreening no longer takes place. They are now carried merely by Andreev bound states at the interface, the same as in s-d or SND [8] junctions. Although near realistic surfaces/interfaces with d-d ordering the superscreening is not complete, the magnetic fields created by the spontaneous currents are nevertheless suppressed on very short distances. This can be practically important for attempting to build a "quiet" qubit based on such junctions [17].

Fig. 3 presents the spontaneous current as a function of the subdominant critical temperature T_{c2} at the (110)-surface of a d-wave superconductor. One notices that the spontaneous current vanishes when $T_{c2} < T$. In fact, at temperatures below $T = T_{c2}$ the subdominant order parameter starts to appear at the surface through a second-order phase transition. Spontaneous symmetry breaking and generation of the spontaneous current are the consequences of the emergence of this second order parameter. The symmetry of the subdominant order parameter is dictated by whichever channel (s or d_{xy}) has stronger interaction potential.

In the d-d and s-d interfaces on the other hand, the subdominant order parameter is induced by the proximity to a different superconductor. One important difference is
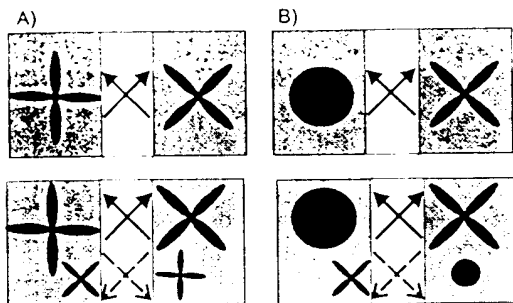
FIG. 5. The DND and SND model of a T-breaking junction. (a) DND junction. The normal region contains current-carrying Andreev bound states (arrows); in equilibrium net current across the boundary is zero, while the spontaneous currents flow along the normal layer (above). If subdominant order parameter is present, the additional set of Andreev levels in equilibrium carries spontaneous current in the opposite direction (below). The model gives the same predictions for SND case (b).

that unlike the surface case, at the d-d or s-d interfaces the presence of the subdominant order parameter is not necessary for generation of spontaneous current. From Eqs. (3) and (1) we see that it is the Green's function (the pairing *amplitude*), not the order parameter (pairing *potential*), which determines the current. In fact, the presence of subdominant order parameter does not always increase the spontaneous current. At low temperatures, it actually *decreases* the spontaneous current [18]. This counter-intuitive effect is displayed in Fig. 4 in which the spontaneous current is plotted as a function of T_{c2}. The temperature used in the calculations is $t = 0.1$ and we take the same T_c for both d and s-wave superconductors. Increasing T_{c2} increases the interaction in the subdominant channel and therefore the magnitude of the subdominant order parameter. The spontaneous current on the other hand decreases with increasing T_{c2}. The situation is the same for both d-d and s-d interfaces.

The decrease of the spontaneous currents when there is interaction in the subdominant channel may seem paradoxical. Nevertheless it is easy to understand in the DND-model of T-breaking junction. [8,19] (Fig. 5). First consider the case without subdominant order parameters. The spontaneous currents in this model flow exclusively within the normal layer and are carried by "zero" and "π"- Andreev bound states, which connect the lobes of d-wave order parameter with the same and opposite signs respectively: in equilibrium there is no net current across the boundary. Now let us assume that the subdominant order parameters are present. Due to continuity, they must have the same phase as the dominant order parameter on the other side (Fig. 5). Therefore now we will have two extra sets of current-carrying Andreev states, the ones linking the *subdominant* order parameters, and it is obvious that the spontaneous currents they carry will always flow opposite to the currents carried by the "dominant-dominant" states.

In conclusion, we have investigated the spontaneous currents near the surface and d-d and s-d boundaries in d-wave superconductors. We obtained the contributions to the spontaneous currents due to the proximity effect and due to the subdominant order parameter generation, and found that at interfaces the latter generally decreases the magnitude of the effect. In d-d junctions, we separated the contribution from the local orbital/magnetic moment of the condensate; this contribution dominates spontaneous currents in clean d-d junctions, which explains the superscreening of the spontaneous currents in such systems.

[1] M. Sigrist, Progr. Theor. Phys. **99**, 899 (1998).

[2] M. Fogelström and S.-K. Yip, Physical Review B **57**, R14060 (1998).

[3] T. Löfwander, V.S. Shumeiko, and G. Wendin, preprint (cond-mat/0008235).

[4] I. Iguchi et al., Phys. Rev. B **62**, R6131 (2000).

[5] M. Covington et al., Phys. Rev. Letters **79**, 277 (1997); L.H. Greene at al., Physica B **280**, 159 (2000).

[6] F. Tafuri and J.R. Kirtley, preprint (cond-mat/0003106).

[7] S. Yip, J. Low Temp. Phys **91** 203 (1993); T.P. Devereaux and P. Fulde, Phys. Rev. B **47**, 14 638 (1993); Y. Tanaka, Phys. Rev. Letters **72** 3871 (1994).

[8] A. Huck, A. von Otterlo, and M. Sigrist, Phys. Rev. B **56**, 14 163 (1997).

[9] E.M. Lifshits and L.P. Pitaevskii, Statistical physics, p.2 (Teoreticheskaia fizika, v.IX). Oxford ; New York : Pergamon Press (1980); §54.

[10] G. Eilenberger, Z. Phys. **214** 195 (1968).

[11] N. Schopohl and K. Maki, Phys. Rev. B **52**, 490 (1995); N. Schopohl, preprint (cond-mat/9804064).

[12] A similar distribution of spontaneous current density on (110) surfaces and interfaces of d-superconductors was obtained in [2] (Fig.4a).

[13] D.B. Bailey, M. Sigrist and R.B. Laughlin Phys. Rev. B **55**, 15239, (1997).

[14] A.V. Zaitsev, JETP **59** 1015 (1984).

[15] S.-K. Yip, J. Low Temp. Phys. **109** 547 (1997).

[16] F.J. Guletto, G. Keiselmann, and D. Rainer, in *Proceedings of the 17th International Conference on Low Temperature Physics*, (North Holland, Amsterdam, 1984) p.1027; A.A. Golubov, and M. Yu. Kupriyanov, preprint (cond-mat/9901318).

[17] L.B. Ioffe et al. Nature **398**, 679 (1999).

[18] Subdominant pairing potential also suppresses the Josephson current. See Y. Tanaka and S. Kashiwaya Phys. Rev. B **58** 2948 (1998).

[19] A.M. Zagoskin, J Phys.: Cond. Matter **9**, L419 (1997).

EXHIBIT E

ATKINS, 1983, *MOLECULAR QUANTUM MECHANICS*, OXFORD UNIVERSITY PRESS, NEW YORK, PP. 41-44

So far we have considered the case when the energy of the particle is specified exactly. But suppose the particle had been prepared, as in real life, with an imprecisely specified energy. What is the form of its wavefunction? Since the energy is imprecise, the wavefunction has to be expressed as a superposition of wavefunctions, each one corresponding to a different energy. That is, we form a *wavepacket*. For example, suppose the particle corresponds to a bullet fired towards positive x, then we know that its wavefunction must be a superposition of functions of the form e^{ikx} with a range of values of k corresponding to the range of momenta (or kinetic energies) over which the preparation of the state is uncertain (e.g. uncertainties in the explosion characteristics of the gunpowder). We know that bullets appear to move, and this is a signal that we are dealing with time-dependent behaviour. Therefore we need to express the superposition in terms of time-dependent wavefunctions.

We have already seen how to add the time-dependent phase factor to wavefunctions of definite energy (p. 30). In the present case we know that a wavefunction e^{ikx} corresponds to an energy $E = k^2\hbar^2/2m$, and so its full, time-dependent form is

$$\Psi_k(x, t) = A e^{ikx} e^{-iEt/\hbar} = A e^{ikx - ik^2\hbar t/2m}. \tag{3.1.6}$$

The superposition corresponding to the wavepacket prepared when the trigger was pulled is a sum of such functions, each one weighted with some coefficient, which we write $g(k)$, called the *shape function* of the packet. Since k is a continuously variable parameter the sum is really an integral over k, and so the wavepacket has the mathematical form

$$\Psi = \int g(k)\Psi_k(x, t)\, dk. \tag{3.1.7}$$

The pictorial form of such a packet is shown in Fig. 3.2(a). You can see that on account of the interference between the waves, at one instant it has a strong amplitude at one point of space (inside the barrel), but because the time-dependent factor affects the phases of the waves forming the superposition, the region of constructive interference changes with time, Fig. 3.2(b). It is not hard to believe that the centre of the packet moves to the right (towards the target), and this is confirmed by the mathematical analysis of its motion given in Appendix 3 (the packet also spreads). The classical motion of a particle (such as a bullet) is captured by the motion of the wavepacket, and once again we see how classical mechanics emerges as an imprecise form of quantum mechanics. In the present case, the imprecision is in the specification of the initial conditions, the state of preparation, of the projectile. This aspect will recur throughout this chapter.

3.2 Potential barriers and tunnelling

A highly instructive extension of the results for free translational motion is to the case where the potential energy varies as depicted in

(a)

(b)
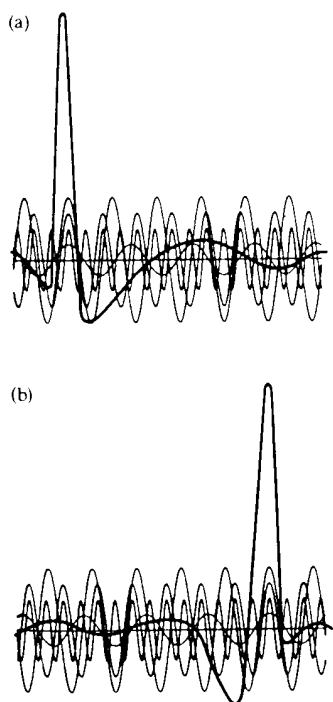
Fig. 3.2. A wavepacket (a) initially and (b) later.

Fig. 3.3(a). This can be regarded as an idealization of a particle penetrating a thin foil. Classically we know what happens: if the particle is shot from the left, it will penetrate only if its initial energy is greater than the potential energy it possesses when embedded in the foil, otherwise it will be reflected. But what does quantum mechanics predict?

The Schrödinger equation for the problem falls apart into three equations, one for each of the zones. The hamiltonians for each zone are

Zone A: $H = -(\hbar^2/2m)(\mathrm{d}^2/\mathrm{d}x^2)$, $x < 0$ (3.2.1a)

Zone B: $H = -(\hbar^2/2m)(\mathrm{d}^2/\mathrm{d}x^2) + V$, $0 \leq x \leq l$ (3.2.1b)

Zone C: $H = -(\hbar^2/2m)(\mathrm{d}^2/\mathrm{d}x^2)$ $x > l$.   (3.2.1c)

The corresponding equations each have the form for free-particle motion (but with $E - V$ in place of E for Zone B). Therefore we can write down the solutions by referring to eqn (3.1.2):

Zone A: $\psi = A e^{ikx} + B e^{-ikx}$, $k = (2mE/\hbar^2)^{\frac{1}{2}}$,   (3.2.2a)

Zone B: $\psi = A' e^{ik'x} + B' e^{-ik'x}$, $k' = \{2m(E - V)/\hbar^2\}^{\frac{1}{2}}$,   (3.2.2b)

Zone C: $\psi = A'' e^{ikx} + B'' e^{-ikx}$, $k = (2mE/\hbar^2)^{\frac{1}{2}}$.   (3.2.2c)

We shall concentrate on the case when E is less than V, so that classically the particle cannot penetrate the barier. This has an immediate and important effect on the form of the wavefunction for Zone B, because when $E < V$, k' is imaginary. Therefore, if we write $k' = i\kappa$ where κ is the real quantity $\{2m(V - E)/\hbar^2\}^{\frac{1}{2}}$, we find

Zone B: $\psi = A' e^{-\kappa x} + B' e^{\kappa x}$,   (3.2.3)

which is a mixture of decaying and increasing exponential functions: *a wavefunction does not oscillate when $E < V$*.

If the barrier is infinitely wide (when the foil is armour plate) the increasing exponential must be ruled out because it leads to an infinite amplitude, which conflicts with the Born interpretation. Therefore inside a barrier like that shown in Fig. 3.3(b) the wavefunction must be simply a *decaying* exponential function $e^{-\kappa x}$. The important point is that the amplitude is not zero inside the barrier, and so *the particle may be found inside a classically forbidden region*. This effect is called *penetration* of a barrier. The rapidity with which the wavefunction decays to zero depends sharply on the mass of the particle and the value of $V - E$, and macroscopic particles have wavefunctions that decay so quickly with distance that for all practical purposes they do not penetrate the classically forbidden zone. An electron or a proton, on the other hand, may penetrate a forbidden zone to an appreciable extent. For example, a 1 eV electron (an electron accelerated through a potential difference of 1 V and therefore having an energy $E = e \times (1 \text{ V}) = 1.6 \times 10^{-19} \text{ C V} = 1.6 \times 10^{-19} \text{ J}$) incident on a potential barrier equivalent to 2 V (and therefore to a potential energy $3.2 \times 10^{-19} \text{ J}$
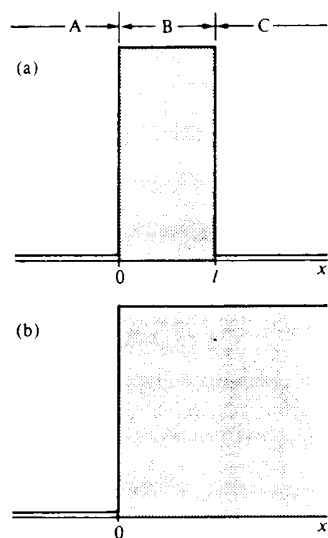
Fig. 3.3. (a) A potential barrier; (b) an infinitely thick wall.

when the electron is inside it) has a wavefunction that decays with distance as $e^{-5.12(x/nm)}$, and so it has decayed to $1/e$ of its initial value only after 0.20 nm, or about the diameter of an atom. Hence penetration can have very important effects on processes at surfaces (e.g. electrodes) and for all events on an atomic scale.

When the barrier is not of infinite width, the increasing exponential component of the Zone B wavefunction is not ruled out because it does not necessarily rise to an infinite amplitude before the potential has dropped back to zero again. Therefore the coefficient B' is not necessarily zero. The values of the coefficients are established by using the other criteria for acceptable wavefunctions set out in Chapter 2, and in particular the requirement that they and their slopes be continuous. This continuity condition lets us match the wavefunction at the points where the zones meet, and therefore to find values for the coefficients. For example, the continuity of the amplitudes at $x = 0$ and at $x = 1$ leads to the two conditions

$$A + B = A' + B'; \qquad A'e^{-\kappa l} + B'e^{\kappa l} = A''e^{ikl} + B''e^{-ikl}. \qquad (3.2.4a)$$

and the continuity of the slopes at the same two points leads to

$$ikA - ikB = -\kappa A' + \kappa B'; \qquad -\kappa A'e^{\kappa l} + \kappa B'e^{\kappa l} = ikA''e^{ikl} - ikB''e^{ikl}$$
$$(3.2.4b)$$

which is almost enough to determine the six coefficients.

Consider the case where particles are prepared with a momentum carrying them towards the right. Then we can immediately infer that the coefficient B'' must be zero, because the wavefunction $B''e^{-ikx}$ denotes the presence of particles travelling to the left on the right-hand side of the barrier, and there can be no such particles. There may be particles on the left of the barrier travelling to the left, because the barrier reflects the incoming particles. We can therefore identify the coefficient B as determining (via $|B|^2$) the probability that the prepared state particles are *reflected* from the barrier, and the coefficient A'' as the probability (via $|A''|^2$) that the particle *penetrates* the barrier and emerges on the other side to travel there with momentum $k\hbar$ to the right. We shall use the relations between the coefficients established above to compute the ratio $|A''|^2/|A|^2 = P$, the *transmission probability*, the probability that a particle incident on the left of the barrier emerges on the right.

The calculation involves elementary manipulations of the relations in eqn (3.2.4); the result is that

$$P = 1/(1 + G); \qquad G = \frac{(e^{\kappa l} - e^{-\kappa l})^2}{4(E/V)(1 - E/V)}, \qquad \kappa = \{2m(V - E)/\hbar^2\}^{\frac{1}{2}}.$$
$$(3.2.5)$$

The important feature of this result is that P may be non-zero; that is, the particle may tunnel through the barrier, even though E is less than V. This phenomenon is an entirely quantum mechanical property, and depends on the fact that a wavefunction does not fall abruptly to zero

inside a region where its potential energy exceeds its total energy. Its amplitude may be non-zero on the other side of the barrier, where it may burst into undamped oscillation again.

Tunnelling is sharply dependent on the mass of the particle and the height of the barrier relative to the incident energy. The behaviour of P for a proton and a deuteron is shown in Fig. 3.4. The diagram also shows how P depends on the energy when $E > V$ so that the particle would, according to classical mechanics, certainly be able to surmount the barrier and therefore have a transmission probability of unity. (The calculation carries through in the same way as before, but k' is no longer imaginary.) The interesting feature is that $P < 1$ in the quantum calculation, and even though the energy is sufficient to carry the particle over the barrier, there is a high probability that the particle will be reflected. Therefore, although quantum mechanics predicts an enhanced tunnelling when $E < V$, it predicts an enhanced reflection, a kind of *antitunnelling*, when $E > V$. This is reminiscent of the way that light reflects from an abrupt change of refractive index at the interface of two transparent media: the wave nature of the incident state is manifesting itself in the same way in the two cases.

Tunnelling is an important property of electrons, protons, and deuterons, and has a number of effects in chemistry. Although the potential energies then have a more complex position dependence than the one we have treated, the broad conclusions are the same: only light particles tunnel significantly, and then only if the barrier is neither too high nor too wide.

3.3 Particle in a box

Now we turn to the case where the particle is confined by walls to a region of space of length L. The walls can be represented by a potential energy that is zero inside the region, but which rises sharply to infinity at the edges, Fig. 3.5. This is the *one-dimensional square well*, or the *particle in a box*, the squareness referring to the steepness with which the potential energy of the particle goes off to infinity at the edges of the box. Since the particle is confined, its energy is quantized. We shall see how the boundary conditions select the permissible energies.

The hamiltonian operator for the infinitely deep square well is

$$H = -(\hbar^2/2m)(d^2/dx^2) + V(x);$$

$$V(x) = \begin{cases} 0 & \text{for } 0 \le x \le L \\ \infty & \text{for } x < 0 \text{ and } x > L. \end{cases}$$

(3.3.1)

Because the potential energy of a particle that touches the walls is infinitely great, it cannot penetrate them. This remark is justified by the behaviour of the wavefunction in the previous section where we saw that there is no penetration of an infinitely high barrier. It follows that the hamiltonian for the region where the potential energy is not infinite, and therefore the only region where the wavefunction is

Fig. 3.4. Tunnelling probabilities for protons and deuterons ($V = 5$ eV, $l = 0.1$ nm).

EXHIBIT F

VOSS *ET AL.*, 1981, PHYSICAL REVIEW LETTERS 47, PP. 265–268

Macroscopic Quantum Tunneling in 1-μm Nb Josephson Junctions

Richard F. Voss and Richard A. Webb

IBM Thomas J. Watson Research Center, Yorktown Heights, New York 10598

The probability distributions for switching out of the superconducting state of low-current-density 1-μm Nb Josephson junctions with capacitance ≈0.1 pF have been measured as a function of temperature T down to 3 mK. Below 100 mK the distribution widths become independent of T. The results are in excellent agreement with predictions for the quantum tunneling of the (macroscopic) junction phase that include the reduction of tunneling rates due to dissipation.

At high temperatures a macroscopic system in a metastable state undergoes transitions to a lower energy state via thermal excitation over the intervening barrier. At sufficiently low T, however, transitions can only occur via a quantum mechanical tunneling through the barrier. This latter process, known as macroscopic quantum tunneling (MQT), is of great theoretical and experimental interest.[1-9] Both Josephson junctions and superconducting loops containing a junction have been proposed as possible experimental systems for the study of these transitions. Unlike microscopic tunneling, MQT involves the collective behavior of many degrees of freedom and macroscopic dissipation is expected to play an important role.[3-5] Although recent experiments on superconducting loops (rf SQUID's) have been interpreted in terms of MQT,[7,8] such interpretations are doubtful. Not only are the measurements rather indirect, but the Josephson elements (point contacts) are not well characterized and the effects require much higher tunneling rates than expected for a reasonable choice of junction parameters. On the other hand, preliminary measurements on high-current-density junctions[9] from 1.5 to 4.2 K show temperature-dependent rates smaller than expected from a simple WKB calculation. In this Letter, we show that careful measurements on well characterized low-current-density Josephson junctions down to 3 mK give tunneling rates in excellent agreement with theoretical predictions[3,4] that include a reduction due to dissipation.

The classical equation of motion of a Josephson junction of critical current I_c (supercurrent $I_0 \sin\theta$ where θ is the phase difference across the junction) shunted by a resistance R and capacitance C and driven by an external constant current I can be written in the form

$$C\ddot{s} + \frac{\dot{s}}{R} + \frac{\partial U(s)}{\partial s} = 0. \tag{1}$$

The junction voltage $V = \varphi_0 \dot{\theta}/2\pi = \dot{s}$, where φ_0 is the flux quantum. This formulation corresponds to the motion of a particle of mass C in the one-dimensional potential

$$U(s) = \frac{I_c \varphi_0}{2\pi}\left[\frac{2\pi s x}{\varphi_0} + \cos\left(\frac{2\pi s}{\varphi_0}\right)\right].$$

For $x = I/I_c < 1$, $U(s)$ consists of a series of wells separated by barriers of height

$$H(x) = (I_c \varphi_0/\pi)[(1 - x^2)^{1/2} - x\cos^{-1}x] - \hbar\omega_0/2,$$

which is reduced by the zero-point energy $\hbar\omega_0/2$. The natural frequency of the particle in the well, ω_0, is related to the Josephson frequency $\omega_J = (2\pi I_c/\varphi_0 C)^{1/2}$ of the junction by $\omega_0 = \omega_J(1 - x^2)^{1/4}$. Confinement in a single well corresponds to the superconducting state of the junction. For $\beta_c = (\omega_J RC)^2 = 2\pi I_c R^2 C/\varphi_0 \gtrsim 1$, the motion is underdamped and a transition out of the well leads to continuous motion of the particle down the potential and a switching to the finite voltage state in the junction.

At high temperatures the transition rate out of the metastable state is dominated by thermal activation over the barrier $H(x)$. The thermal rate,

$$\tau_{th}^{-1} = (\omega_0/2\pi)\exp[-H(x)/k_B T], \tag{2}$$

has been well verified[10] for junctions above 1.5 K. As $T \to 0$ the transition rate is dominated by the quantum mechanical tunneling of the macroscopic junction phase. Path integral techniques[3,4] can be used to calculate the tunneling rate and the result can be cast in the form

$$\tau_{MQT}^{-1} = \frac{\omega_0}{2\pi}\left(\frac{b}{2\pi}\right)^{1/2} e^{-b}, \tag{3}$$

where

$$b = \frac{\alpha H(x)}{\hbar\omega_0} + \frac{A(\Delta s)^2}{\hbar R}. \tag{4}$$

The first term in Eq. (4) is the usual tunneling exponent (in a form similar to the WKB calculation[2] for the superconducting ring) while α is a factor depending on the shape of the barrier ($\alpha = 7.2$ for a cubic potential appropriate to a junction[4] with I near I_c). The second term represents the lowest-order dissipative corrections, where A is a numerical factor of order unity and Δs is the distance under the barrier. Near its maximum $U(s) \approx H(x) - \omega_0^2 C s^2/2$, $(\Delta s)^2 \approx 8H(x)/\omega_0^2 C$, and

$$b \approx (7.2 + 8A/\omega_0 RC)H(x)/\hbar\omega_0. \tag{5}$$

In the absence of dissipation, we expect a transition from thermal activation to tunneling when $k_B T \approx \hbar\omega_0/7$. In the above formulation dissipation reduces the crossover temperature. Although increases with dissipation have also been predicted,[5] Eqs. (3) and (5) provide a convenient framework for comparison with experiment.

The junctions used in the experiment were patterned on Si chips with use of electron beam lithography in a crossed strip geometry with an overlap area of $1\mu m.^2$ Both base and counter electrodes were made of electron beam evaporated Nb with $T_c \approx 9$ K. An rf plasma discharge was used to grow the oxide tunnel barrier. Similar junctions have been extensively studied for dc SQUID's and other applications.[11] The capacitance of the junctions is estimated both from dc SQUID resonances[12] and oxide studies[13] to be 0.1 ± 0.2 pF. The junctions had a uniform critical current density as evidenced by the fact that I_c could be modulated to near zero with a magnetic field.

The samples were placed inside the copper mixing chamber of a dilution refrigerator to ensure maximum thermal coupling. A low-frequency sinusoidal current (amplitude $\approx 2I_c$) was applied to the junction and the distribution of currents at which the junction switched out of the superconducting state was measured. Extensive efforts were made to isolate the sample from external noise. Connections to room-temperature electronics were made through cooled 2-kΩ resistors. The large cable capacitance together with the 2-kΩ resistors and large sample impedance gave electrical cutoff frequencies $\lesssim 1$ kHz. The computerized measurement apparatus was located outside the screened room that contained the refrigerator and a series of isolation amplifiers and filters. The low current densities and slow (10–20 Hz) current sweeps ensured that the junctions were at the bath temperature in the superconducting state with no dissipation prior to

switching. In fact, measurements using the same apparatus on other samples (two-dimensional arrays of 20 000 1-μm Nb junctions) of comparable impedance and I_c on the same chip showed temperature-dependent effects well below 20 mK.

Typical distributions consisted of 200 000 events measured over about five hours at constant temperature. Figure 1 shows a series of switching probability distributions $P(I)$ versus applied current I at various T for a junction with a maximum $I_c \approx 1.6$ μA. As T is lowered $P(I)$ narrows and moves to higher I. All $P(I)$ have a characteristic asymmetry with a tail at low I and a more abrupt cutoff at high I as expected from theory. With the measurement of the complete $P(I)$ we could ensure that neither low-frequency noise [which would smear out $P(I)$ to approach a Gaussian distribution] nor external transients [$P(I)$ independent of I at low I] influenced the switching.

The inset shows the highly hysteretic ($\beta_c \approx 50$) I-V characteristic of the sample at 95 mK. As is common in all-Nb junctions, the samples had a significant normal conductance, similar to an external shunt, in parallel with the usual tunneling currents. Although undesirable for many digital applications, this temperature-independent (below 2 K) conductance provided a well-defined R [appropriate for Eq. (1)] that we shall use for comparison with theory.

The measured $P(I)$ can be related[10] to the transition rate $\tau^{-1}(I)$ by

$$P(I) = \tau^{-1}(I)|dI/dt|^{-1}[1 - \int_0^I P(i)di].$$
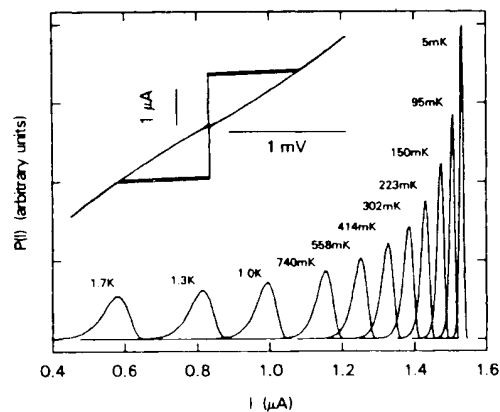

FIG. 1. Switching distribution $P(I)$ vs I out of the superconducting state for a 1-μm Nb junction at various T. Inset shows four traces of the I-V charactistic at 95 mK.

Figure 2(a) shows $\tau^{-1}(I)$ calculated from the measured $P(I)$ of the junction in Fig. 1. Figure 2(b) shows $\tau^{-1}(I)$ calculated from the $P(I)$ for a junction with an order of magnitude smaller I_c and smaller damping ($\beta_c \approx 5000$). In both cases, $\ln\tau^{-1}(I)$ is roughly proportional to I. As T decreases $\tau^{-1}(I)$ moves to higher I and the slope of $\ln\tau^{-1}(I)$ increases. For $T \lesssim 100$ mK there is little change in either the slope shown in Fig. 2 or the width of $P(I)$. I_c, however, continues to increase slightly as T is lowered.

The I_c of each junction is estimated by fitting the high-T $\tau^{-1}(I)$ to Eq. (2). Such fits are very sensitive to small changes in I_c and are accurate to within 5%. For the high-I_c junction we find I_c = 1.62 μA and for the low-I_c junction I_c = 162 nA. These fits are shown as the solid lines marked "thermal" in Fig. 2. Since the Nb $T_c \approx 9$ K and the measured R was independent of T for $T \lesssim 2$ K, we believe that I_c is also independent of T in this range.

Using the above values of I_c with $C = 0.1$ pF we can estimate the tunneling rates from Eq. (3). The estimates without dissipation [$A = 0$ in Eq. (5)] are shown as the dashed lines in Fig. 2. In Fig. 2(a) the measured low-temperature rates fall significantly below this prediction, while in Fig. 2(b) the estimate is fairly accurate. The results are thus consistent with the effect of increased dissipation giving a smaller rate. Indeed, if we treat the numerical factor A in Eq. (5) as an adjustable parameter, excellent agreement of the data is found for $A \approx 4.5$. This tunneling rate, corrected for dissipation ($A = 4.5$), is shown as the dotted lines in Fig. 2.

An alternate method of displaying the data is presented in Fig. 3 which shows the width of the distribution $P(I)$, $\Delta I = \langle (I - \langle I \rangle)^2 \rangle^{1/2}$, vs T. As expected ΔI [which is proportional to the inverse slope of $\ln\tau^{-1}(I)$ vs I] becomes independent of T at low T. Also shown are the expected theoretical widths for thermal activation [Eq. (2)] and MQT tunneling with ($A = 4.5$) and without ($A = 0$) damping from Eqs. (3) and (5). It should be emphasized that there is little freedom in determining the junction parameters I_c, C, and R and that the only really adjustable parameter is the damping factor A (which has little effect on the low-I_c junction).

We believe that the measurements presented here are the first compelling evidence for the existence of quantum tunneling of a macroscopic variable. In fact, the low-I_c, high-β_c sample

FIG. 2. Transition rates $\tau^{-1}(I)$ from the measured $P(I)$ for two junctions. (a) $I_c \approx 1.62$ μA, $R \approx 320$ Ω. (b) $I_c \approx 162$ nA, $R \approx 10$ kΩ. High-T theoretical thermal rates are shown as solid lines; MQT rates without damping are shown as dashed lines, with damping as dotted lines.
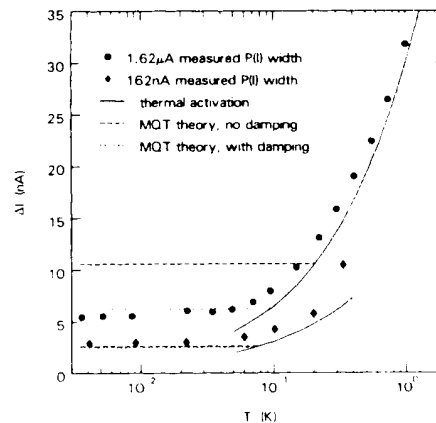
FIG. 3. Measured $P(I)$ widths $\Delta I = \langle (I - \langle I \rangle)^2 \rangle^{1/2}$ vs T for the two junctions. Theoretical predictions for thermal activation and MQT rates with and without damping are also shown.

267

shows a behavior close to the undamped predictions, while the higher-I_c sample demonstrates the reduction of tunneling rates due to dissipation. This reduction is consistent with the temperature-dependent rates found in high-current-density junctions.[9] The use of well characterized junctions [independent estimate of C and direct measurement of $R(T)$], the extension to very low temperatures, and the detailed measurement of $P(I)$ were important in being able to rule out extraneous effects and interpret the data within a theoretical framework. Although the observed reduction in tunneling rate ($A \approx 4.5$) is slightly greater than the expected $A \approx 1$, the magnitude is still reasonable. It is possible that the appropriate R in Eq. (5) is not the measured dc resistance near the origin (as used here) but either the high-frequency resistance or the quasiparticle resistance above the gap (in which case $A \approx 1.5$). Additional theoretical work is needed both on the effect of nonlinear and frequency-dependent damping and on the actual form of the crossover from thermal activation to macroscopic tunneling.

We acknowledge helpful discussions with A. J. Leggett, S. Kirkpatrick, and Y. Imry as well as the expertise of R. Laibowitz and S. Raider in preparing the all-Nb junctions.

[1]A. J. Leggett, J. Phys. (Paris), Colloq. 39, C6-1264 (1978).

[2]J. Kurkijarvi, in *Proceedings of the Second International Conference on Superconducting Quantum Interference Devices and Third Workshop on Biomagnetism, Berlin, Germany, 6–9 May 1980*, edited by W. de Gruyter (Physikalische–Technische Bundesanstalt, Berlin, 1980), p. 247.

[3]A. O. Caldeira and A. J. Leggett, Phys. Rev. Lett. 46, 211 (1981); A. O. Caldeira, Ph.D thesis, University of Sussex, 1980 (unpublished).

[4]A. J. Leggett, in Proceedings of the Sixth International Conference on Noise in Physical Systems, Gaithersburg, Maryland, 1981 (to be published).

[5]A. Widom, G. Megaloudis, J. E. Sacco, and T. D. Clark, Nuovo Cimento 61B, 112 (1981).

[6]I. Affleck, Phys. Rev. Lett. 46, 388 (1981).

[7]W. den Boer and R. de Bruyn Ouboter, Physica (Utrecht) 98B+C, 185 (1980).

[8]R. J. Prance et al., Nature (London) 289, 543 (1981).

[9]E. L. Jackel et al., Bull. Am. Phys. Soc. 26, 382 (1981).

[10]T. A. Fulton and L. N. Dunkelberger, Phys. Rev. B 9, 4760 (1974).

[11]R. F. Voss, R. B. Laibowitz, S. I. Raider, and J. Clarke, J. Appl. Phys. 51, 2306 (1980).

[12]R. F. Voss et al., IEEE Trans. Magn. 17, 395 (1981).

[13]J. Magerlein, IEEE Trans. Magn. 17, 286 (1981).

Evidence for Elastic Disorder in the Elastically Ordered Phase of KCN

Harold T. Stokes

Department of Physics and Materials Research Laboratory, University of Illinois, Urbana, Illinois 61801

and

Thomas A. Case and David C. Ailion

Department of Physics, University of Utah, Salt Lake City, Utah 84112
(Received 12 March 1981)

We have obtained evidence from ^{13}C NMR measurements that the CN$^-$ ion in the elastically ordered phase of KCN is misoriented slightly with respect to the orthorhombic b axis. This misorientation varies randomly over the lattice, averaging to zero on a macroscopic scale. The misorientations are manifested through small-angle CN$^-$ reorientations which contribute to the spin-lattice relaxation time T_1 of the ^{13}C nuclei, via dipolar interactions and chemical shift anisotropy.

PACS numbers: 76.60.Es, 61.50.-f, 61.16.Hn

Potassium cyanide (KCN) exhibits an elastically ordered phase (below 168 °K) in which the CN$^-$ molecules are aligned parallel to the b axis in an orthorhombic crystal structure[4,2] (see Fig. 1). In this phase, the CN$^-$ molecules are disordered with respect to head-to-tail alignment and undergo random head-to-tail reorientations. The structure and dynamics of this system have been of considerable interest in recent years.[3-7]

We have studied this system by NMR of ^{13}C and from our results have been forced to conclude that, in the elastically ordered phase of KCN, *small*-angle reorientations as well as head-to-tail reorientations are taking place. This effect arises from the head-to-tail disorder of the CN$^-$ molecules. Since the CN$^-$ molecule is slightly different with respect to head and tail, this disorder breaks the orthorhombic symmetry of the

EXHIBIT G

DIVINCENZO IN *SCALABLE QUANTUM COMPUTERS*, BRAUNSTEIN AND LO, EDS., WILEY-VCH, 2001, BERLIN

Samuel L. Braunstein,
Hoi-Kwong Lo (eds.)
Pieter Kok (ass. ed.)

Scalable
Quantum Computers

Paving the Way
to Realization

The Physical Implementation of Quantum Computation

DAVID P. DIVINCENZO

IBM T. J. Watson Research Center, Yorktown Heights, NY 10598 USA

Abstract

After a brief introduction to the principles and promise of quantum information processing, the requirements for the physical implementation of quantum computation are discussed. These five requirements, plus two relating to the communication of quantum information, are extensively explored and related to the many schemes in atomic phys…, quantum optics, nuclear and electron magnetic resonance spectroscopy, super…ducting electro… …d q…um dot physics, for achieving quantum … …uting.

1. … …

The advent of quantum information processing, as an abstract concept, has given birth to a great deal of new thinking, of a very concrete form, about how to create physical computing devices that operate in the hitherto unexplored quantum mechanical regime. The efforts … underway to produce working laboratory devices that perf… this profoundly new … …

In this chapter I provide an overview of the common objectives of the investigations reported in the remainder of this special issue. The scope of the approaches, proposed and underway, to the implementation of quantum hardware is remarkable, emerging from specialties in atomic physics [1], in quantum optics [2], in nuclear [3] and electron [4] magnetic resonance spectroscopy, in superconducting device physics [5], in electron physics [6], and in mesoscopic and quantum dot research [7]. This amazing variety of approaches has arisen because, as we will see, the principles of quantum computing are posed using the most fundamental ideas of quantum mechanics, ones whose embodiment can be contemplated in virtually every branch of quantum physics.

The interdisciplinary spirit which has been fostered as a result is one of the most pleasant and remarkable features of this field. The excitement and freshness that has been produced bodes well for the prospect for discovery, invention, and innovation in this endeavor.

2. Why *Quantum* Information Processing?

The shortest of answers to this question would be, why not? The manipulation and transmission of information is today carried out by physical machines (computers, routers, scanners, etc.), in which the embodiment and transformations of this information can be described using the language of classical mechanics. But the final physical theory of the … … quantum mechanics … there … … that machines follow … …ine laws of quantum mechanics should have … … computational power as classical machines; indeed, since Newtonian mechanics emerges as a special limit of quantum mechanics … …

similar line of reasoning, it may well be asked whether machines embodying the principles of other refined descriptions of nature (perhaps general relativity or string theory) may have even more information processing capabilities; speculations exist about these more exotic possibilities, but they are beyond the scope of the present discussion.

But computing with quantum mechanics really deserves a lot more attention than wormhole computing or quantum-gravity computing; quantum computing, while far in the future from the perspective of CMOS roadmaps and projections of chip fab advances, can certainly be seen as a real prospect from the perspective of research studies in quantum physics. It does not require science fiction to envision a quantum computer; the proposals discussed later in this issue paint a rather definite picture of what a real quantum computer will look like.

So, how much is gained by computing with quantum physics over computing with classical physics? We do not seem to be near to a final answer to this question, which is natural since even the ultimate computing power of classical machines remains unknown. But the answer as we know it today has an unexpected structure; it is not that quantum tools simply speed up all information processing tasks by a uniform amount. By a standard complexity measure (i.e., the way in which the number of computational steps required to complete a task grows with the "size" n of the task), some tasks are not sped up at all [10] by using quantum tools (e.g., obtaining the nth iterate of a function $f(x)$ [11]), some are sped up moderately (locating an entry in a database of n entries [12]), and some are apparently sped up exponentially (Shor's algorithm for factoring an n-digit number [13]).

In other types of information processing tasks, particularly those involving communication [14], both quantitative and qualitative improvements are seen [15]: for certain tasks (choosing a time and date for an appointment between two parties from out of a list) there is a reduction in the amount of communication if quantum rather than classical states are transmitted [16]. For some tasks (the "set disjointness problem", related to the appointment-finding problem above and to the Deutsch-Jozsa computation) the reduction of required communication is exponential [17]. Finally, there are tasks that are doable in the quantum world that have no counterpart classically: quantum cryptography provides an absolute secrecy of communication between parties that is impossible classically [18]. And for some games, winning strategies become possible with the use of quantum resources that are not available otherwise [19, 20].

This issue, and this chapter, are primarily concerned with the "hows" of quantum computing rather than the "whys," so we will leave behind the computer science after this extremely brief mention. There is no shortage of other places to obtain more information about these things; I recommend the recent articles by Aharonov [21] and by Cleve [22]; other general introductions [23] will give the reader pointers to the already vast specialized literature on this subject.

3.   Realizing Quantum Computation

Let me proceed with the main topic: the physical realization of quantum information processing. As a guide to the remainder of the special issue, and as a means of reviewing the basic steps required to make quantum computation work, I can think of no better plan than to review a set of basic criteria that my coworkers and I have been discussing over the last few years [24] for the realization of quantum computation (and communication), and to assess the current state of the art for the various physical implementations that are being explored.

So, without further ado, here are the

Five (plus two) requirements for the implementation of quantum computation

1. A scalable physical system with well characterized qubits

For a start, a physical system containing a collection of qubits is needed. A qubit (or, more precisely, the embodiment of a qubit) is [25] simply a quantum two-level system like the two spin states of a spin 1/2 particle, like the ground and excited states of an atom, or like the vertical and horizontal polarization of a single photon. The generic notation for a qubit state denotes one state as $|0\rangle$ and the other as $|1\rangle$. The essential feature that distinguishes a qubit from a bit is that, according to the laws of quantum mechanics, the permitted states of a single qubit fills up a two-dimensional complex vector space; the general state is written $a|0\rangle + b|1\rangle$, where a and b are complex numbers, and a normalization convention $|a|^2 + |b|^2 = 1$ is normally adopted. The general state of two qubits, $a|00\rangle + b|01\rangle + c|10\rangle + d|11\rangle$, is a four-dimensional vector, one dimension for each distinguishable state of the two systems. These states are generically *entangled*, meaning that they cannot be written as a product of the states of two individual qubits. The general state of n qubits is specified by a 2^n-dimensional complex vector.

A qubit being "well characterized" means several different things. Its physical parameters should be accurately known, including the internal Hamiltonian of the qubit (which determines the energy eigenstates of the qubit, which is often, although not always, taken the $|0\rangle$ and $|1\rangle$ states), the presence of and couplings to other states of the qubit, the interactions with other qubits, and the couplings to external fields that might be used to manipulate the state of the qubit. If the qubit has third, fourth, etc., levels, the computer's control apparatus should be designed so that the probability of the system ever going into these states is small. The smallness of this and other parameters will be determined by the quantum error correction, which will be discussed under requirement 3.

Recognizing a qubit can be trickier than one might think. For example, one might consider a pair of one-electron quantum dots that share a single electron between them as a two-level system. One is certainly sure that we can describe the presence of the electron on each dot by $|0\rangle$ and $|1\rangle$, and it is well known experimentally how to put this system into the "entangled" state $1/\sqrt{2}(|01\rangle + |10\rangle)$ in which the electron is in a superposition of being on the left dot and the right dot. But it is fallacious to consider this as a two-qubit system; while the states $|00\rangle$ and $|11\rangle$ are other allowed physical states of the dots, super-selection principles forbid the creation of entangled states involving different particle numbers such as $1/\sqrt{2}(|00\rangle + |11\rangle)$.

It is therefore false to consider this as a two-qubit system, and, since there are not two qubits, it is nonsense to say that there is entanglement in this system. It is correct to say that the electron is in a superposition of different quantum states living on the two different dots. It is also perfectly correct to consider this system to be the embodiment of a *single* qubit, spanned by the states (in the misleading notation above) $|01\rangle$ ("electron on the right dot") and $|10\rangle$ ("electron on the left dot"). Indeed, several of the viable proposals, including the ones by Schön, Averin, and Tanamoto in this special issue, use exactly this system as a qubit. However, false lines of reasoning like the one outlined here have sunk various proposals before they were properly launched (no such abortive proposals are represented in this book, but they can be found occasionally in the literature).

An amazing variety of realizations of the qubit are represented in this volume. There is a very well developed line of work that began with the proposal of CIRAC and ZOLLER [1] for an ion trap quantum computer, in which, in its quiescent state, the computer holds the qubits in pairs of energy levels of ions held in a linear electromagnetic trap. Various pairs of energy levels (e.g., Zeeman degenerate ground states, as are also used in the NMR systems) give a more precise readout of a (one) state. The [27] use similar atomic energy levels of neutral species. These are

als use other auxiliary qubits such as the position of atoms in a trap or lattice, the presence or absence of a photon in an optical cavity, or the vibrational quanta of trapped electrons, ions or atoms (in the Platzman proposal below [6] this is the primary qubit). Many of the solid-state proposals exploit the fact that impurities or quantum dots have well characterized discrete energy level spectra; these include the spin states of quantum dots (see chapters by Loss [7] and Imamoglu [2]), the spin states of donor impurities (see Kane [4]), and the orbital or charge states of quantum dots (see Tanamoto [7]). Finally, there are a variety of interesting proposals which use the quantized states of superconducting devices, either ones involving the (Cooper-pair) charge (see Schön, Averin), or the flux (see Mooij) [5].

2. The ability to initialize the state of the qubits to a simple fiducial state, such as $|000\ldots\rangle$
This arises first from the straightforward computing requirement that registers should be initialized to a known value before the start of computation. There is a second reason for this initialization requirement: quantum error correction (see requirement 3 below) requires a continuous, fresh supply of qubits in a low-entropy state (like the 0 state). The need for a continuous supply of 0s, rather than just an initial supply, is a real headache for many proposed implementations. But since it is likely that a demonstration of a substantial degree of quantum error correction is still quite some time off, the problem of continuous initialization does not have to be solved very soon. Still, experimentalists should be aware of the speed with which a qubit can be zeroed will eventually be a very important issue. If the time it takes to do this initialization is relatively long compared with gate-operation times (see requirement 4), then the quantum computer will have to equipped with some kind of "qubit conveyor belt", on which qubits in need of initialization are carried away from the region in which active computation is taking place, initialized qubits on the "belt", then brought back to the active place. or the initialization is to be done in place (qubits could be envisioned in requirement 5 for the case of low quantum-efficiency measurements [28].)

There are two main approaches to initializing qubits to a standard state; the system can be "naturally" cooled when the ground state of its Hamiltonian is the state of interest, or the standard state can be achieved by a measurement which projects the system either into the state desired or another state which can be rotated into it. These approaches are not fundamentally different from one another, since the projection procedure is a form of cooling; for instance, the laser cooling techniques used routinely now for the cooling of ion states to near their ground state in a trap [1] are closely connected to the fluorescence techniques used to measure the state of these ions. A more "natural" kind of cooling is advocated in many of the electron spin resonance based techniques (using quantum dots or impurities) [7, 4] in which the spins are placed in a strong magnetic field and allowed to align with it via interaction with their heat bath. In this kind of approach the time scale will be a problem. Since the natural thermalization times are never shorter than the decoherence time of the system, this procedure will be too slow for the needs of error correction and a "conveyor belt" scheme would be required. Cooling by projection, in which the Hamiltonian of the system and its environment are necessarily perturbed strongly, will have a time scale dependent on the details of the setup, but potentially much shorter than the natural relaxation times. One cannot say too much more at this point, as the schemes for measurement have in many cases not been fully implemented (see requirement 5). In the NMR quantum computer implementations to date (see Cory below), cooling of the initial state has been foregone; however, it is acknowledged that once these cooling schemes are implemented (a nontrivial thing to do) then there can be a scalable scheme for quantum computing.

3. Long...

decoherence times. decoherence times describe the amount of time a quantum system is coupled with its environment. The (somewhat overly) simplified definition of this time is that it is

esence
ctrons,
of the
terized
ters by
nd the
iety of
r ones

00...)
uld be
on for
uires a
1 fo-
y ...
... f
... n
... d
ime it
s (see
"qubit
tion in

... e
...

est, or
er into
e not
cool-
of ion
scence
ling is
dots or
wed to
le will
erence
and a
milto-
a time
natural
easure-
NMR
state
... d
calable

ontact
at it is

the characteristic time for a generic qubit state $|\psi\rangle = a\,|0\rangle + b\,|1\rangle$ to be transformed into the mixture $\rho = |a|^2\,|0\rangle\langle 0| + |b|^2\,|1\rangle\langle 1|$. A more proper characterization of decoherence, in which the decay can depend on the form of the initial state, in which the state amplitudes may change as well, and in which other quantum states of the qubit can play a role (in a special form of state decay called "leakage" in quantum computing [29, 30]), is rather more technical than I want to get here; but see Refs. [31] and [32] for a good general discussion of all these. Even the simplest discussion of decoherence that I have given here should also be extended to include the possibility that the decoherence of neighboring qubits is correlated. It seems safest to assume that they will be neither completely correlated nor completely uncorrelated, and the thinking about error correction has taken this into account.

Decoherence is very important for the fundamentals of quantum physics, as it is identified as the principal mechanism for the emergence of classical behavior. For the same reason, decoherence is very dangerous for quantum computing, since if it acts for very long, the capability of the quantum computer will not be so different from that of a classical machine. The decoherence time must be long enough that the uniquely quantum features of this style of computation have a chance to come into play. How long is "long enough" is also indicated by the results of quantum error correction, which I will summarize shortly.

I have indicated that the "relevant" decoherence times should be long enough. This emphasizes that a quantum particle can have many decoherence times pertaining to different degrees of freedom of that particle. But many of these can be irrelevant to the functioning of this particle as a qubit. For example, the rapid decoherence of an electron's position state in a solid state environment does not preclude its having a very long spin coherence time, and it can be arranged that this is the only time relevant for quantum computation. Which times are relevant is determined by the choice of the qubit basis states 0 and 1; for example, if these two states correspond to different spin states but identical orbital states, then orbital decoherence will be irrelevant.

One might worry that the decoherence time necessary to do a successful quantum computation will scale with the duration of the computation. This would place incredibly stringent requirements on the physical system implementing the computation. Fortunately, in one of the great discoveries of quantum information theory (in 1995–1996), it was found that error correction of quantum states is possible [33] and that this correction procedure can be successfully applied in quantum computation [34], putting much more reasonable (although still daunting) requirements on the needed decoherence times.

In brief, quantum error correction starts with coding: as in binary error correction codes, in which only a subset of all boolean strings are "legal" states, quantum error correction codes consist of legal states confined to a subspace of the vector space of a collection of qubits. Departure from this subspace is caused by decoherence. Codes can be chosen such that, with a suitable sequence of quantum computations and measurements of some ancillary qubits, the error caused by decoherence can be detected and corrected. As noted above, these ancillary qubits have to be continuously refreshed for use. I will not go much farther into the subject here, see [31] for more. It is known that quantum error correction can be made fully fault tolerant, meaning that error correction operations can be successfully intermingled with quantum computation operations, that errors occurring during the act of error correction, if they occur at a sufficiently small rate, do no harm, and that the act of quantum computation does not itself cause an unreasonable proliferation of errors.

These detailed analyses have indicated the time needed for decoherence that is barely acceptable for fault-tolerant quantum computation. The result is that, if the decoherence time is 10^4–10^5 times the "clock time" of the quantum computer, that is, the time for the ... ... quantum ... ... with the truth, or rather ... ... with ... ... do not have such long decoherence times. But sometimes they do, and our search for a successful physical implementation must turn towards these. At least this result says that

the required decoherence rate does not become ever smaller as the size and duration of the quantum computation grows. So, once the desired threshold is attainable, decoherence will not be an obstacle to scalable quantum computation.

Having said this, it must be admitted that it will be some time before it is even possible to subject quantum error correction to a reasonable test. Nearly all parts of requirements 1–5 must be in place before such a test is possible. And even the most limited application of quantum error correction has quite a large overhead: roughly 10 ancillary qubits must be added for each individual qubit of the computation. Fortunately, this overhead ratio grows only logarithmically as the the size of the quantum computation is increased.

In the short run, it is at least possible to design and perform experiments which measure the decoherence times and other relevant properties (such as the correlation of decoherence of neighboring qubits) of candidate implementations of qubits. With such initial test experiments, caution must be exercised in interpreting the results, because decoherence is a very system-specific phenomenon, depending on the details of all the qubits' couplings to various environmental degrees of freedom. For example, the decoherence time of the spin of an impurity in the bulk of a perfect semiconductor may not be the same as its decoherence time when it is near the surface of the solid, in the immediate neighborhood of device structures designed to manipulate its quantum state. Test experiments should probe decoherence in as realistic a structure as is possible.

4. A "universal" set of quantum gates

This requirement is of course at the heart of quantum computing. A quantum algorithm is typically specified [8] as a sequence of unitary transformations $U_1, U_2, U_3, \ldots$, each acting on a small number of qubits, typically no more than three. The most straightforward transcription of this into a physical apparatus is to identify Hamiltonians which generate these unitary transformations, viz. $U_1 = e^{iH_1 t_1}$, $U_2 = e^{iH_2 t_2}, \ldots, e^{iH_n t_n}$, etc.; then, the physical apparatus should be designed so that H_1 can be turned on from time 0 to time t, then turned off, and H_2 turned on from time t to time $2t$.

Would that life were so simple! In reality what can be done is much less, but much less can be sufficient. Understanding exactly how much less is still enough, is the main complication of this requirement. In all the physical implementations discussed in this volume, only particular sorts of Hamiltonians can be turned on and off: in most cases, for example, only two-body (two-qubit) interactions are considered. This immediately poses a problem for a quantum computation specified with three-qubit unitary transformations; fortunately, of course, these can always be re-expressed in terms of sequences of one- and two-body interactions [35], and the two-body interactions can be of just one type [36], the "quantum XOR" or "cNOT". There are some implementations in which multi-qubit gates can be implemented directly [37].

However, this still leaves a lot of work to do. In some systems, notably in NMR (see Cory), there are two-body interactions present which cannot be turned *off*, as well as others which are switchable. This would in general be fatal for quantum computation, but the particular form of the fixed interactions permit their effects to be annulled by particular "refocusing" sequences of the controllable interactions, and it has recently been discovered [38] that these refocusing sequences can be designed and implemented efficiently.

For many other systems, the two-body Hamiltonian needed to generate directly the cNOT unitary transformation is not available. For example, in the quantum-dot proposal described by Loss below [7], the only two-body interaction which should be easily achievable is the exchange interaction between neighboring spins, $H \propto S_i \cdot S_{i+1}$, in the Imamoglu chapter [2], the attainable interaction is of the XY type, i.e. $H \propto S_{ix}S_{jx} + S_{iy}S_{jy}$. An important observation is that with these particular interactions (which are assumed controllable) any desired cNOT transformation can be synthesized [39]. It is incumbent on each implementation pro-

posal to exhibit such a sequence for producing the cNOT using the interactions that are naturally realizable.

Often there is also some sophisticated thinking required about the time profile of the two-qubit interaction. The naive description above uses a "square pulse" time profile, but often this is completely inappropriate; for instance, if the Hamiltonian can also couple the qubit to other, higher-lying levels of the quantum system, often the only way to get the desired transformation is to turn on and off the interaction smoothly and slowly enough that an adiabatic approximation is accurate [29, 30] (in a solid-state context, see also [40]). The actual duration of the pulse will have to be sufficiently long that any such adiabatic requirement is satisfied; then typically only the time integral $\int dt\, H(t)$ is relevant for the quantum gate action. The overall time scale of the interaction pulse is also controlled by the attainable maximum size of the matrix elements of $H(t)$, which will be determined by various fundamental considerations, like the requirement that the system remains in the regime of validity of a linear approximation, and practical considerations, like the laser power that can be concentrated on a particular ion. Given these various constraints, the "clock time" of the quantum computer will be determined by the time interval needed such that two consecutive pulses have negligible overlap.

Another consideration, which does not seem to present a problem with any current implementation scheme but which may be an issue in the future, is the classicality of the control apparatus. We say that the interaction Hamiltonian $H(t)$ has a time profile which is controlled externally by some "classical" means, that is, by the intensity of a laser beam, the value of a gate voltage, or the current level in a wire. But each of these control devices is made up themselves of quantum mechanical parts. When we require that these behave classically, we mean that their action should proceed without any entanglement developing between these control devices and the quantum computer. Estimates indicate that this entanglement can indeed be negligible, but this effect needs to be assessed for each individual case.

In many cases it is impossible to turn on the desired interaction between a pair of qubits; for instance, in the ion-trap scheme, no direct interaction is available between the ion-level qubits [1]. In this and in other cases, a special quantum subsystem (sometimes referred to as a "bus qubit") is used which can interact with each of the qubits in turn and mediate the desired interaction; for the ion trap, this is envisioned to be the vibrational state of the ion chain in the trap; in other cases it is a cavity photon whose wavefunction overlaps all the qubits. Unfortunately, this auxiliary quantum system introduces new channels for the environment to couple to the system and cause decoherence, and indeed the decoherence occurring during gate operation is of concern in the ion-trap and cavity-quantum electrodynamics schemes.

Some points about requirement 4 are important to note in relation to the implementation of error correction. Successful error correction requires fully parallel operation, meaning that gate operations involving a finite fraction of all the qubits must be doable simultaneously. This can present a problem with some of the proposals in which the single "bus qubit" is needed to mediate each interaction. On the other hand, the constraint that interactions are only among nearest neighbors in a lattice, as in many of the solid-state proposals, does allow for sufficient parallelism [41].

Quantum gates cannot be implemented perfectly; we must expect both systematic and random errors in the implementation of the necessary transformations. Both types of errors can be viewed as another source of decoherence and discussed error correction techniques are effective for producing reliable computations from unreliable gates, if the unreliability is

gate operation or so. It might be hoped that systematic errors could be corrected by careful calibration; but this will surely not always be the case. It seems harder to give a

good rule for how much systematic error is tolerable, the conservative estimates give a very, very small number (the square of the above) [31], but on the other hand there seems to be some evidence that certain important quantum computations (e.g., the quantum Fourier transform) can tolerate a very high level of systematic error (over- or under-rotation). Some types of very large errors may be tolerable if their presence can be detected and accounted for on the fly (we are thinking, for example, about charge switching in semiconductors or superconductors).

Error correction requires that gate operations be done on coded qubits, and one might worry that such operations would require a new repertoire of elementary gate operations for the base-level qubits which make up the code. For the most important error correction techniques, using the so called "stabilizer" codes, this is not the case. The base-level toolkit is exactly the same as for the unencoded case: one-bit gates and cNOTs, or any gate repertoire that can produce these, are adequate. Sometimes the use of coding can actually *reduce* the gate repertoire required: in the work on decoherence free subspaces and subsystems, codes are introduced using blocks of three and four qubits for which two-qubit exchange interactions alone are enough to implement general quantum computation [42, 43]. This simplification could be very useful in the quantum-dot [7] or semiconductor impurity [4] implementations.

5. A qubit-specific measurement capability

Finally, the result of a computation must be read out, and this requires the ability to measure specific qubits. In an ideal measurement, if a qubit's density matrix is $\rho = p\,|0\rangle\langle 0| + (1-p)\,|1\rangle\langle 1| + \alpha\,|0\rangle\langle 1| + \alpha^*\,|1\rangle\langle 0|$, the measurement should give outcome "0" with probability p and "1" with probability $1-p$ independent of α and of any other parameters of the system, including the state of nearby qubits, and without changing the state of the rest of the quantum computer. If the measurement is "non-demolition", that is, if in addition to reporting outcome "0" the measurement leaves the qubit in state $|0\rangle\langle 0|$, then it can also be used for the state preparation of requirement 2; but requirement 2 can be fulfilled in other ways.

Such an ideal measurement as I have described is said to have 100% quantum efficiency; real measurements always have less. While the fidelity of a quantum measurement is not captured by a single number, the single quantum-efficiency parameter is often a very useful way to summarize it, just as the decoherence time is a useful if incomplete summary of the damage caused to a quantum state by the environment.

While quantum efficiency of 100% is desirable, much less is needed for quantum computation; there is, in fact, a tradeoff possible between quantum efficiency and other resources which results in reliable computation. As a simple example, if the quantum efficiency is 90%, then, in the absence of any other imperfections, a computation with a single-bit output (a so-called "decision problem", common in computer science) will have 90% reliability. If 97% reliability is needed, this can just be achieved by rerunning the calculation three times. Much better, actually, is to "copy" the single output qubit to three, by applying two cNOT gates involving the output qubit and two other qubits set to $|0\rangle$, and measuring those three. (Of course, qubits cannot be "copied", but their value in a particular basis can.) In general, if quantum efficiency q is available, then copying to somewhat more than $1/q$ qubits and measuring all of these will result in a reliable outcome. So, a quantum efficiency of 1% would be usable for quantum computation, at the expense of hundreds of copies/remeasures of the same output qubit. (This assumes that the measurement does not otherwise disturb the quantum computer. If not, then the probabilities are further complicated.)

Indeed quantum efficiencies almost much less than than 1% can be the basis for useful quantum computation: this is the "bulk" model of NMR (see Cory and [3]), where macroscopic numbers of copies of the same quantum computer (different molecules in solu-

tion) run simultaneously, with the final measurement done as an ensemble average over the whole sample. These kinds of weak measurements, in which each individual qubit is hardly disturbed, are quite common and well understood in condensed-matter physics.

If a measurement can be completed quickly, on the timescale of 10^{-4} of the decoherence time, say, then its repeated application during the course of quantum computation is valuable for simplifying the process of quantum error correction. On the other hand, if this fast measurement capability is not available, quantum error correction is still possible, but it then requires a greater number of quantum gates to implement.

Other tradeoffs between the complexity and reliability of quantum measurement vs. those of quantum computation have recently been explored. It has been shown that if qubits can be initialized into pairs of maximally entangled states, and two-qubit measurements in the so-called Bell basis ($\Psi^{\pm} = |01\rangle \pm |10\rangle$, $\Phi^{\pm} = |00\rangle \pm |11\rangle$) are possible, then no two-qubit quantum gates are needed, one-bit gates alone suffice [44]. Now, often this tradeoff will not be useful, as in many schemes a Bell measurement would require two-bit quantum gates.

But the overall message, seen in many of our requirements, is that more and more, the theoretical study of quantum computation has offered a great variety of tradeoffs for the potential implementations: if X is very hard, it can be substituted with more of Y. Of course, in many cases both X and Y are beyond the present experimental state of the art; a thorough knowledge of these tradeoffs is very useful for devising a rational plan for the pursuit of future experiments.

4.   **Desiderata for Quantum Communication**

For computation alone, the five requirements above suffice. But the advantages of quantum information processing are not manifest solely, or perhaps even principally, for straightforward computation only. There are many kinds of information processing tasks, reviewed briefly at the beginning, that involve more than just computation, and for which quantum tools provide a unique advantage.

The tasks we have in mind here all involve not only computation but also communication. The list of these tasks that have been considered in the light of quantum capabilities, and for which some advantage has been found in using quantum tools, is fairly long and diverse: it includes secret key distribution, multiparty function evaluation as in appointment scheduling, secret sharing, and game playing [14].

When we say communication we mean quantum communication: the transmission of intact qubits from place to place. This obviously adds more features that the physical apparatus must have to carry out this information processing. We formalize these by adding two more items to the list of requirements:

6. *The ability to interconvert stationary and flying qubits*

7. *The ability to faithfully transmit flying qubits between specified locations*

These two requirements are obviously closely related, but it is worthwhile to consider them separately, because some tasks need one but not the other. For instance, quantum cryptography [18] involves only requirement 7; it is sufficient to create and detect flying qubits directly.

I have used the jargon "flying qubits" [2], which has become current in the discussion of quantum communication. Using this term emphasizes that the optimal embodiment of a qubit that can readily transmit from place to place may be different from the one for the stationary qubit for reliable quantum computation. It is widely supposed that some photon states, with the qubit encoded either in the polarization or in the time of arrival of the photon, will be the flying qubit of choice, and indeed, the well developed tech-

nology of light transmission through optical fibers provides a very promising system for the transmission of qubits. I would note, though, that my colleagues and I have raised the possibility that electrons traveling though solids could provide another realization of the flying qubit [14, 45].

Only a few completely developed proposals exist which incorporate requirements 6 and 7. Of course, there are a number of quite detailed studies of 7, in the sense that experiments on quantum cryptography have been very concerned with the preservation of the photon quantum state during transmission through optical fibers or through the atmosphere. However, these studies are rather disconnected from the other concerns of quantum computing. Requirement 6 is the really hard one; to date the only theoretical proposal sufficiently concrete that experiments addressing it have been planned is the scheme produced by Kimble and coworkers [46] for unloading a cavity photon into a traveling mode via atomic spectroscopy, and loading it by the time-reversed process. Other promising concepts, like the launching of electrons from quantum dots into quantum wires such that the spin coherence of the electrons is preserved, need to be worked out more fully.

5.   Summary

So, what is the "winning" technology going to be? I don't think that any living mortal has an answer to this question, and at this point it may be counterproductive even to ask it. Even though we have lived with quantum mechanics for a century, our study of quantum effects in complex artificial systems like those we have in mind for quantum computing is in its infancy. No one can see how or whether all the requirements I have can be met, or of whether there are new tradeoffs, not envisioned in our present theoretical discussions but suggested by further experiments, that might take our investigations in an entirely new path.

Indeed, the above discussion, and the other chapters of this special issue, really do not cover all the foreseeable approaches. I will mention two of which I am aware: first, another computational paradigm, that of the cellular automaton, is potentially available for exploitation. This is distinguished from the above "general purpose" approach in that it assumes that every bit pattern throughout the computer will be subjected to the same evolution rule. It is known that general-purpose computation is performable, although with considerable overhead, by a cellular automaton. This is true as well for the quantum version of the cellular automaton, as LLOYD [47] indicated in his original work. New theoretical work by BENJAMIN [48] shows very explicitly how relatively simple local rules would permit the implementation of some quantum computations. This could point us perhaps towards some sort of polymer with a string of qubits on its backbone that can be addressed globally in a spectroscopic fashion. Experiments are not oriented towards this at the moment, but the tradeoffs are very different, and I don't believe it should be excluded in the future.

Second, even more speculative, but very elegant, is the proposal of KITAEV [49] to use quantum systems with particular kinds of topological excitations, for example nonabelian anyons, for quantum computing. It is hard to see at the moment how to turn this exciting proposal into an experimental program, as no known physical system is agreed to have the appropriate topological excitations. But further research in, for example, the quantum Hall effect might reveal such a system, more likely, perhaps, is that further understanding of this approach, and that of Freedman and his colleagues [50], will shed more light on doing quantum computing using the "standard" approach being considered in this book.

I am convinced of one thing: the study of quantum information science will continue to spur a large number of the most important and interesting developments for many years to come.

Acknowledgments

References

[1] J. I. CIRAC and P. ZOLLER, Phys. Rev. Lett. **74**, 4091 (1995); T. PELLIZZARI, S. A. GARDINER, J. I. CIRAC, and P. ZOLLER, Phys. Rev. Lett. **75**, 3788 (1995); C. MONROE, D. M. MEEKHOF, B. E. KING, W. M. ITANO, and D. J. WINELAND, *Demonstration of a fundamental quantum logic gate*, Phys. Rev. Lett. **75**, 4714 (1995); A. SORENSEN and K. MOLMER, Phys. Rev. Lett. **82**, 1971 (1999); S. SCHNEIDER, D. F. V. JAMES, and G. J. MILBURN, *Method of quantum computation with 'hot' trapped ions*, quant-ph/9808012.

[2] Q. A. TURCHETTE, C. J. HOOD, W. LANGE, H. MABUCHI, and H. J. KIMBLE, *Measurement of conditional phase shifts for quantum logic*, Phys. Rev. Lett. **75**, 4710 (1995); A. IMAMOGLU, D. D. AWSCHALOM, G. BURKARD, D. P. DiVINCENZO, D. LOSS, M. SHERWIN, and A. SMALL, Phys. Rev. Lett. **83**, 4204 (1999) (quant-ph/9904096).

[3] N. GERSHENFELD and I. CHUANG, SCIENCE **275**, 350 (1997); D. CORY, A. FAHMY, and T. HAVEL, Proc. Nat. Acad. Sci. **94** (5), 1634 (1997).

[4] B. KANE, NATURE **393**, 133 (1998); R. VRIJEN et al., *Electron spin resonance transistors for quantum computing in silicon-germanium heterostructures*, Phys. Rev. A, in press (quant-ph 9905096).

[5] D. AVERIN, Solid State Commun. **105**, 659 (1998); A. SHNIRMAN, G. SCHÖN, and Z. HERMON, Phys. Rev. Lett. **79**, 2371 (1997); J. E. MOOIJ, T. P. ORLANDO, L. LEVITOV, L. TIAN, C. H. VAN DER WAL, and S. LLOYD, Science **285**, (1999).

[6] P. M. PLATZMAN and M. I. DYKMAN, Science **284**, 1967 (1999).

[7] D. LOSS and D. P. DiVINCENZO, Phys. Rev. A **57**, 120 (1998) (cond-mat/9701055); M. SHERWIN, A. IMAMOGLU, and T. MONTROY, *Quantum computation with quantum dots and terahertz cavity quantum electrodynamics*, Phys. Rev. A **60**, 3508 (1999) (quant-ph/9903065); T. TANAMOTO, Phys. Rev. A **61**, 022305 (2000) (quant-ph/9902031).

[8] D. DEUTSCH, Proc. R. Soc. London A **400**, 97 (1985); **425**, 73 (1989).

[9] R. P. FEYNMAN, Int. J. Theor. Phys. **21**, 467 (1982); Found. Phys. **16**, 507 (1986). See also *Feynman Lectures on Computation*, eds. A. J. G. Hey and R. Allen (Perseus Press, 1996).

[10] R. BEALS, H. BUHRMAN, R. CLEVE, M. MOSCA, and R. DE WOLF, *Quantum lower bounds by polynomials*, Proc. of the 39th Annual Symposium on the Foundations of Computer Science (IEEE Press, Los Alamitos, 1998), p. 352; quant-ph/9802049.

[11] Y. OZHIGOV, *Quantum computer cannot speed up iterated applications of a black box*, quant-ph/9712051; B. Terhal, PhD Thesis, University of Amsterdam, 1999.

[12] L. K. GROVER, *Quantum mechanics helps in searching for a needle in a haystack*, Phys. Rev. Lett. **79**, 325 (1997).

[13] P. W. SHOR, *Polynomial time algorithms for prime factorization and discrete logarithms on a quantum computer*, SIAM J. Comput. **26**, 1484 (1997), and references therein.

[14] D. P. DiVINCENZO and D. LOSS, *Quantum Computers and Quantum Coherence*, J. Magnetism Magn. Matl. **200**, 202–218 (1999).

[15] R. CLEVE and H. BUHRMAN, Phys. Rev. A **56**, 1201 (1997).

[16] H. BUHRMAN, R. CLEVE, and A. WIGDERSON, *Quantum vs. Classical Communication and Computation*, in *Proc. of the 30th Ann. ACM Symp. on the Theory of Computing* (ACM Press, 1998), p. 63; eprint quant-ph/9802040.

[17] A. AMBAINIS, L. SCHULMAN, A. TA-SHMA, U. VAZIRANI, and A. WIGDERSON, *The quantum communication complexity of sampling*, in *Proc. of the 39th Annual Symposium on the Foundations of Computer Science* (IEEE Press, Los Alamitos, 1998), see http://www.icsi.berkeley.edu/~amnon/Papers/scps.

[18] C. H. BENNETT and G. BRASSARD, *Quantum Cryptography: Public Key Distribution and Coin Tossing*, in Proc. of the International Conference on Computers, Systems and Signal Processing, Bangalore, India (IEEE, New York, 1984), p. 175.

[19] D. A. Meyer, *Quantum strategies*, Phys. Rev. Lett. **82**, 1052 (1999) (quant-ph/9804010); J. Eisert, M. Wilkens, and M. Lewenstein, *Quantum games and quantum strategies*, Phys. Rev. Lett. **83**, 3077 (1999) (quant-ph/9806088); L. Goldenberg, L. Vaidman, and S. Wiesner, *Quantum gambling*, Phys. Rev. Lett. **82**, 3356 (1999) (quant-ph/9808001).

[20] A. M. Steane and W. van Dam, *Physicists Triumph at 'Guess my Number'*, Physics Today **53** (2), 35–39 (2000).

[21] D. Aharonov, *Quantum Computation* in *Annual Reviews of Computational Physics*, vol. VI (ed. Dietrich Stauffer, World Scientific, Singapore, 1998) (quant-ph/9812037).

[22] R. Cleve, *An Introduction to Quantum Complexity Theory*, to appear in *Collected Papers on Quantum Computation and Quantum Information Theory* (eds. C. Macchiavello, G. M. Palma, and A. Zeilinger, World Scientific, 2000) (quant-ph/9906111).

[23] C. H. Bennett, Physics Today **48** (10), 24 (1995); D. P. DiVincenzo, Science **270**, 255 (1995); D. P. DiVincenzo, Proc. R. Soc. London A **454**, 261 (1998) (and quant-ph/9705009); A. Barenco, Contemp. Phys. **37**, 375 (1996); A. Steane, Rep. Prog. Phys. **61**, 117 (1998); C. H. Bennett and P. W. Shor, IEEE Trans. Info. Theory **44**, 2724 (1998).

[24] D. P. DiVincenzo, *Mesoscopic Electron Transport*, eds. L. Sohn, L. Kouwenhoven, and G. Schön (Vol. 345, NATO ASI Series E, Kluwer, 1997) p. 657 (cond-mat/9612126); D. P. DiVincenzo and D. Loss, *Superlattices and Microstructures* **23**, 419 (1998) (cond-mat/9710259); D. P. DiVincenzo and D. Loss, J. Magn. Mag. Matl. **200**, 202 (1999) (cond-mat/9901137).

[25] B. Schumacher, Phys. Rev. A **54**, 2614 (1996).

[26] G. K. Brennen, C. M. Caves, P. S. Jessen, and I. H. Deutsch, Phys. Rev. Lett. **82**, 1060 (1999).

[27] D. Jaksch, H. J. Briegel, J. I. Cirac, C. Gardiner, and P. Zoller, Phys. Rev. Lett. **82**, 1975 (1999).

[28] I am grateful to R. Schoelkopf and M. Devoret for clarifying discussion on these points.

[29] M. B. Plenio and P. L. Knight, Phys. Rev. A **53**, 2986 (1996).

[30] M. B. Plenio and P. L. Knight, Proc. Roy. Soc. Lond. A**453**, 2017–2041 (1997).

[31] J. Preskill, Proc. R. Soc. Lond. A **454**, 385 (1998) (quant-ph/9705031).

[32] M. A. Nielsen and I. L. Chuang, *Quantum Computation and Quantum Information* (Cambridge University Press, 2000); see also M. A. Nielsen, C. M. Caves, B. Schumacher, and H. Barnum, Proc. R. Soc. Lond. A **454**, 277–304 (1998) (quant-ph/9706064).

[33] P. Shor, in *Proceedings of the 35th Symposium on the Foundations of Computer Science* (IEEE Press, Los Alamitos, CA, 1996) (quant-ph/9605011); D. Aharonov and M. Ben-Or, in *Proceedings of the 29th Annual ACM Symposium on the Theory of Computing* (ACM Press, New York, 1997) (quant-ph/9906129); E. Knill, R. Laflamme, and W. Zurek, Science **279**, 342 (1998). These results are reviewed in [31].

[35] D. P. DiVincenzo, *Two-bit gates are universal for quantum computation*, Phys. Rev. A **51**, 1015 (1995) (cond-mat/9407022).

[36] A. Barenco, C. H. Bennett, R. Cleve, D. P. DiVincenzo, N. Margolus, P. Shor, T. Sleator, J. A. Smolin, and H. Weinfurter, *Elementary gates for quantum computation*, Phys. Rev. A **52**, 3457 (1995) quant-ph/9503016.

[37] K. Molmer and A. Sorensen, Phys. Rev. Lett. **82**, 1835 (1999).

[38] D. W. Leung, I. L. Chuang, F. Yamaguchi, and Y. Yamamoto, *Efficient implementation of selective recoupling in heteronuclear spin systems using Hadamard matrices*, quant-ph/9904100.

[39] G. Burkard, D. Loss, D. P. DiVincenzo, and J. A. Smolin, Phys. Rev. B **60**, 11404 (1999); cond-mat/9905230.

[40] G. Burkard, D. Loss, D. P. DiVincenzo, Phys. Rev. B **59**, 2070 (1999); cond-mat/9808026.

[41] D. Gottesman, *Fault-Tolerant Quantum Computation with Local Gates*, J. Mod. Optics **47**, 333 (2000); quant-ph/9903099.

[42] D. Bacon, J. Kempe, D. A. Lidar, and K. B. Whaley, *Universal fault-tolerant computation on decoherence-free subspaces*, quant-ph/9909058.

[43] D. P. DiVincenzo, G. Burkard, D. Loss, and E. V. Sukhorukov, *Quantum computation and spin electronics* in *Quantum Mesoscopic Phenomena and Mesoscopic Devices in Microelectronics*, eds. I.O. Kulik and R. Ellialtioglu (NATO Advanced Study Institute, Turkey, June 13–25, 1999), to be published; cond-mat/9911245.

[44] D. Gottesman and I. L. Chuang, Nature **402**, 390 (1999).

[45] D. Loss and E. V. Sukhorukov, Phys. Rev. Lett. **84**, 1035 (2000).

[46] J. I. Cirac, P. Zoller, H. J. Kimble, and H. Mabuchi, Phys. Rev. Lett. **78**, 3221 (1997) (quant-ph/9611017).

[47] S. Lloyd, Science **261**, 1569 (1993); **263**, 695 (1994).

[48] S. Benjamin, Phys. Rev. A **61**, 020301(R) (2000) (quant-ph/9909007).

[49] A. Yu. Kitaev, *Fault-tolerant quantum computation with anyons*, quant-ph/9707021; see J. Preskill, in *Introduction to Quantum Computation and Information* (eds. H.-K. Lo, S. Popescu, and T. Spiller, World Scientific, Singapore, 1998) pp. 213–269 (quant-ph/9712048).

[50] M. H. Freedman, M. Larsen, and Z. Wang, *A modular functor which is universal for quantum computation*, quant-ph/0001108; M. H. Freedman, *Poly-locality in quantum computing*, quant-ph/0001077; M. H. Freedman, A. Yu. Kitaev, and Z. Wang, *Simulation of topological field theories by quantum computers*, quant-ph/0001071.

EXHIBIT H

NICOLLETI *ET AL.*, 1996, PHYSICA C, 269, P. 255

Bi-epitaxial YBCO grain boundary Josephson junctions on SrTiO₃ and sapphire substrates

S. Nicoletti [a,*], H. Moriceau [b], J.C. Villegier [a], D. Chateigner [c], B. Bourgeaux [c], C. Cabanel [d], J.Y. Laval [d]

[a] *DRFMC / SPSMS – CEA Grenoble, 38054 Grenoble Cedex 09 France*
[b] *LETI / DMITEC, 38054 Grenoble Cedex 09 France*
[c] *CNRS-Laboratoire de Cristallographie, BP 166, 38042 Grenoble Cedex 09 France*
[d] *Laboratoire de Physique du Solide UPR 5 CNRS-ESPCI, 10, rue Vauquelin, 75231 Paris Cedex 05 France*

Abstract

This paper deals with YBCO Josephson junctions based on artificially generated in-plane bi-epitaxial grain boundaries fabricated on SrTiO₃ and buffered R-plane sapphire. The grain boundary was obtained by partly interposing a MgO seed layer between a bare or even-buffered substrate and a CeO₂ layer [1]. The devices were produced by patterning the overhanging YBCO film in a form of stripes across the grain boundary occurring at the interface between the two regions.

The samples were structurally and electrically characterized. As shown by X-ray diffraction analyses and high resolution electron microscopy, the structural perfection of the YBCO film decreases as the complexity of the stacking sequence increases. The fabricated junctions behave according to the Resistively Shunted Junction model for both the samples on SrTiO₃ and on Al₂O₃. Under microwave irradiation, the devices displayed several Shapiro steps while their critical currents were deeply modulated under magnetic field.

By comparing the transport properties of the devices with the structural properties of the YBCO film on the different stacking sequences, we found a strong correlation between the normalized resistance $R_N A$ and the degree of structural disorder in the superconducting film.

Keywords: Grain boundary; Texturing; Thin films; Weak links; Josephson effect

1. Introduction

Large angle grain boundaries (GB) are well known to behave like a weak link with RSJ behavior [2]. The fabrication of complex devices based on GB junctions actually represents one of the most viable ways to develop superconducting electronic circuits. In this aim the control of artificial GBs in the YBCO films is essential.

GB junctions obtained on bi-crystal substrates show good junction quality and reproducibility and among the best performances [3] but the intrinsic restrain of the GB location at the bi-crystal interface seriously limit their integration in any large scale technological process. Moreover, this technique is

* Corresponding author. Permanent address: CNR-Istituto LAMEL, Via Gobetti 101, I-40129 Bologna, Italy. Fax: +39 51 6399216; e-mail: nicoletti@area.bo.cnr.it.

well assessed for SrTiO$_3$ (STO) or MgO [4] but for other substrates of technological interest, such as Al$_2$O$_3$ (ALO), several problems are still present.

A possible way to overcome these problems is the fabrication of artificially engineered bi-epitaxial GB [1,5,6], where a suitable sequence of epitaxial layers locally induce a 45° rotation of the crystal lattices across the grain boundary. This behavior, first shown at Conductus [1], has to be related to an "abnormal" epitaxial in plane coincidence between the MgO and the CeO$_2$ crystal lattices where MgO is a very thin "seed" film independent of the underlying substrate. It is worth noting that the use of commercially available, low cost epitaxial quality R-plane sapphire substrates, should be envisaged for any application where high dielectric constant and low losses are required. However, for this kind of substrates, severe film-substrate interactions occurring above 650°C require a buffer layer as a barrier against the diffusion.

In this paper we report the fabrication and the characterization of bi-epitaxial 45° GB Josephson junctions on SrTiO$_3$ (STO) or Al$_2$O$_3$ (ALO) substrates. This work is focused on the MgO–CeO$_2$ seed layers deposition and on the CeO$_2$/YBCO/STO multilayer buffer for the sapphire substrates suitable for a collective fabrication of artificially engineered GB with good reproducibility of the process. Emphasis is made on the structural properties of the stacking sequence and on their influence on the electrical performances of the final device.

2. Experimental

The films depositions were carried out by Pulsed Laser Deposition (PLD) from sintered massive targets. The PLD apparatus used is based on an excimer laser ($\lambda = 248$ nm, $\tau_{pulse} = 30$ ns). The deposition chamber is equipped with four targets and with a load lock, allowing multilayer processes without breaking vacuum or atmosphere. All the deposition parameters are controlled by a personal computer insuring good reproducibility. A detailed description of the deposition apparatus was reported elsewhere [7].

It is well known that in the temperature range of the YBCO deposition, STO is chemically stable while sapphire presents a severe interdiffusion be-

tween the substrate and the superconducting film. To obtain both a suitable crystal lattice and a barrier against the mutual diffusion a CeO$_2$/YBCO/STO trilayer was first deposited on the sapphire substrates. This multilayer structure was chosen to overcome the limitations in the stacking sequence. The STO thin films do not grow epitaxialy nor on R-plane ALO neither on CeO$_2$ films, giving several orientations and a large fraction of amorphous material. The deposition of the CeO$_2$/YBCO/STO tri-layer allows an epitaxial growth along the whole structure of the buffer layer as well as a suitable substrate surface for the fabrication of the bi-epitaxial GB.

In order to fabricate artificially engineered bi-epitaxial grain boundaries, a ~ 5 nm thick MgO seed layer and a ~ 11 nm thick CeO$_2$ buffer layer were first deposited onto a bare (or buffered) substrate under the same processing conditions. These two intermediate layers were therefore removed on part of the substrate by Xe ion milling on a photolithographically defined geometry. These procedures lead to a smooth and sharp interface where the grain boundary is located. Then a second ~ 18 nm CeO$_2$ buffer layer and the superconducting YBCO film were deposited. The PLD process parameters for each deposition step are summarized in Table 1 while Fig. 1(a,b) shows the stacking sequence followed during the fabrication process for STO and ALO, respectively. To define the contact pads, a 200 nm thick gold layer was subsequently sputtered through a mechanical mask. The devices were patterned in form of stripes defined across the GB by standard photolithographic technique followed by Xe ion milling.

The films obtained were structurally characterized by X-ray diffraction analysis (XRD) in both the Bragg–Brentano and Schulz [8] configurations using the Cu-Kα radiation and by Transmission Electron Microscopy (TEM). Using XRD, we measured the θ–2θ scans, and pole figures on the part of the sample where the MgO is present and on the part of the sample where the MgO was removed. By means of these analyses we first determined the in-plane epitaxial relationships and then, considering the pole dispersion taken at their full width half maximum (FWHM), we evaluated the degree of orientation. The experimental setup and the axes resolutions were described elsewhere [9] as well as the calcula-

tion procedure to obtain the volume fraction related to a given peak [10].

The samples on STO were observed on cross-sections, by high resolution electron microscopy (HTEM). In order to prepare these specimens, two flakes heterostructures were glued together with an epoxy charged with a very fine alumina powder (0.5 μm). The obtained disks were cut with their faces perpendicular to the [100] axis of the substrate.

Then they were mechanically thinned to $\cong 15$ μm and ion milled at low temperature to electron transparency. Cross-sections were observed at 200 keV on a Philips CM20UT.

The electrical characterization was performed by placing the samples on a cryogenic probe for testing under magnetic field as well as under microwave irradiation. The probe was inserted in a double magnetic shielded dewar allowing the measurements from

Table 1
Deposition parameters used during the fabrication of bi-epitaxial grain boundaries

Material	Sub-layer or substrate	Temperature (°C)	Laser energy (J/cm^2)	Pulse rate (Hz)	Oxygen pressure (Pa)	Deposition rate (nm/pulse)	Thickness (nm)
CeO$_2$	R-Al$_2$O$_3$	780	2.0	1	40	0.05	20
YBCO	CeO$_2$	650	2.0	2	40	0.06	30
SrTiO$_3$	YBCO	780	2.6	5	32	0.02	50
MgO	SrTiO$_3$	600	2.6	5	2.5	0.009	5
CeO$_2$-I	MgO	780	2.0	10	40	0.05	11
CeO$_2$-II	CeO$_2$-I/SrTiO$_3$	780	2.0	10	40	0.05	18
YBCO	CeO$_2$	750–780	2.0	2	40	0.055	200
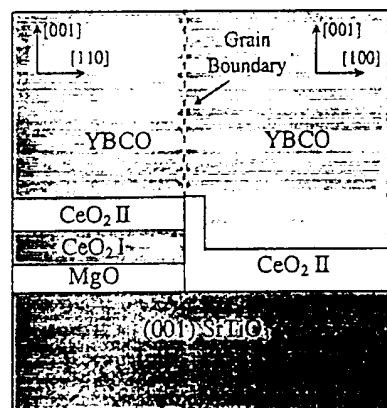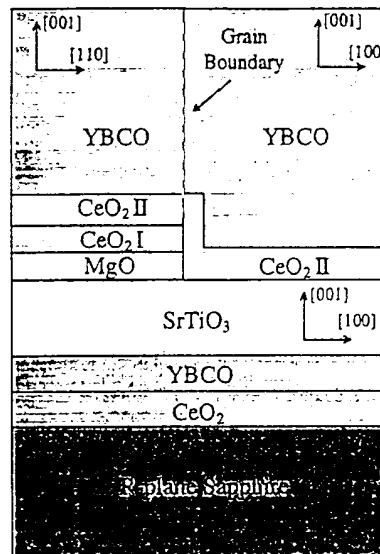
Fig. 1. Schematic representation of the stacking sequence followed during the grain boundary fabrication on a) SrTiO$_3$ and b) R-plane sapphire substrates, respectively.

room temperature to liquid helium temperature. The data were collected by taking as a general criterion for the J_c evaluation the current value corresponding to a 10 μV voltage drop across the junction.

3. Results and discussion

3.1. Structural characterization

The XRD θ–2θ scans allow the determination of the crystalline planes parallel to the sample surface. In Figs. 2 and 3 we report the θ–2θ diffraction patterns of two different samples deposited on STO and ALO substrates, respectively. To facilitate the comparison, the patterns collected on the whole stacking sequence were shifted with regard to those collected on the side where the MgO/CeO$_2$ bi-layer was etched. Two general features can be observed. First, as indicated by the strong (00l) reflections, the YBCO and the MgO layers are mainly grown [001] oriented. The presence of the characteristic BaCeO$_3$

(BCO) reflections indicates that some reactions occur at the interface between YBCO and CeO$_2$ layers.

The CeO$_2$ layers behave differently, depending on the substrate side. As shown by the diffraction patterns of Fig. 2, on STO substrate we can identify two different behaviors: on bare substrate, the CeO$_2$ is (001)-oriented even after the ion etching. Where MgO is present underneath the CeO$_2$ layer, we observe a strong reflection at $2\theta \cong 29.5$. This additional peak can be attributed either to (111) reflection of CeO$_2$ or to the (200 + 112) reflections from the BCO. Furthermore, the growth of this phase seems to be competing with the growth of the BCO phase, as evidenced by the (004 + 220) reflection of this latter phase which decreases considerably in intensity when (111)-CeO$_2$ increases (4 layers side). This is consistent with less YBCO/CeO$_2$ interaction when the etching procedure has been applied (less crystalline disorder in the CeO$_2$ layer in the absence of MgO). The poor crystallinity of CeO$_2$ and BCO, whatever the substrate and the sample side, is revealed by comparing the enlargement of their peaks with those of the YBCO in the θ–2θ spectra. The (111)-CeO$_2$ and (200 + 112)-BCO reflections are too
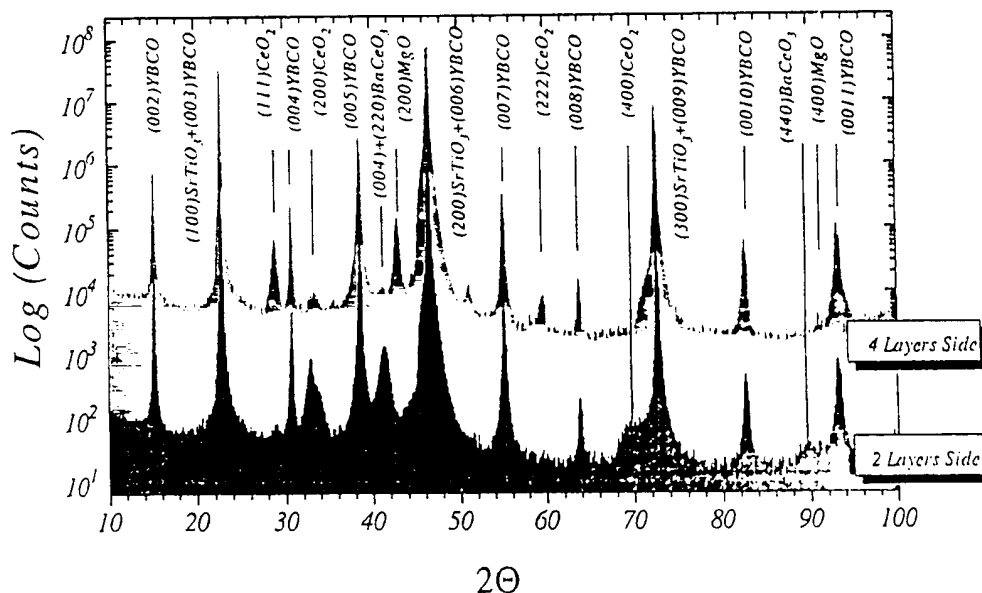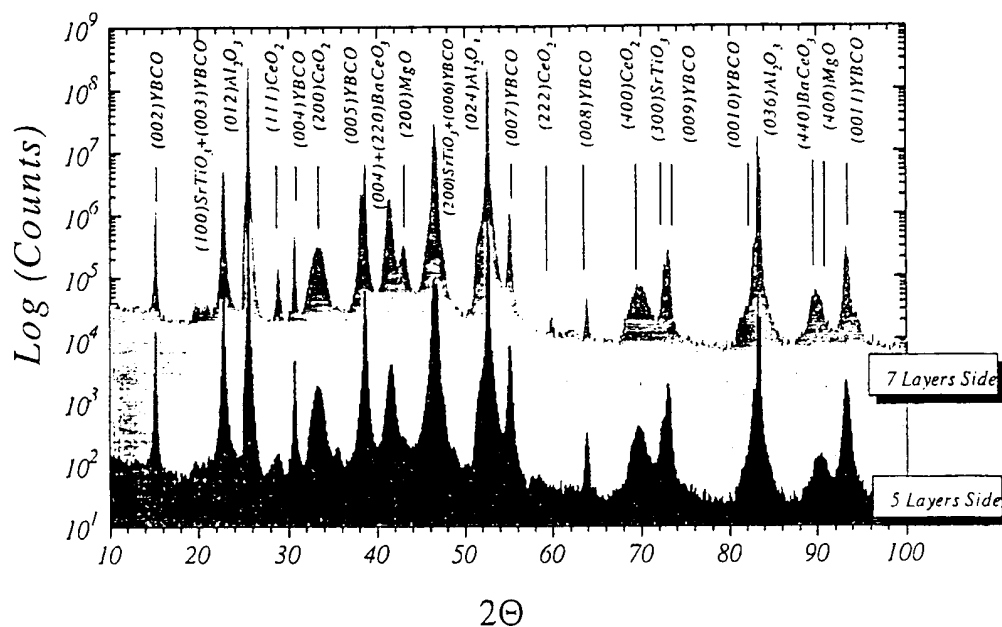

Fig. 2. θ–2θ diffraction patterns collected on both halves of a sample fabricated on SrTiO$_3$ substrate. The pattern collected on the whole stacking sequence is [4 layers side] shifted with regards to that collected on the side without the MgO/CeO$_2$ bi-layer [2 layers side].

close (28.5–29.5 in θ) to be distinguished taking into account the peak width.

As reported in Fig. 3, the same set of peaks was found on sapphire substrate, with the exception of those coming from the substrate itself. Taking into account that a buried double layer of $CeO_2/YBCO$ is first deposited on this substrate, we attribute the (004 + 220)-BCO peak (present on both sides) to this first deposited layer. Since this deep layer partially shadows the duality between the (111)-CeO_2 and the (004 + 220)-BCO peaks, we can assume a similar behavior for this stacking sequence.

Fig. 4 shows HREM cross-section images corresponding to the grown heterostructures a) without the MgO layer and b) with the MgO layer, respectively. From Fig. 4a we found, for both the CeO_2 and YBCO grown on STO, the same orientation relationships already detected by X-ray analyses. The YBCO layer grows with the same orientation as the substrate. The STO/CeO_2 interface is fairly abrupt whereas the $CeO_2/YBCO$ interface is highly perturbed as a result a preferential thinning on the

YBCO side; the thickness of the CeO_2 layer is found to be equal to 11 nm. The BCO phase, observed by X-ray, was not detected in this region. This behavior can be explained by assuming that the BCO is present only as islands.

From the micrograph 4b we found that the YBCO layer is 45° rotated along the c axis, whenever a MgO layer is intercalated in the growth process. The MgO and CeO_2 layers are 4 nm and 30 nm thick, respectively. The interfaces are well defined and sharp. However, in the CeO_2 layer we can distinguish two different zones. Close to the MgO interface, the presence of Moiré patterns reveals slight local variations of the lattice parameters and a fairly perturbed layer. Nevertheless the lattice parameter length indicates an (00l)-oriented growth. Otherwise, close to the YBCO interface, the lattice parameter changes, indicating the formation of a different phase. This phase can be identified as either (111)-oriented CeO_2 or (200)-oriented BCO. Since the thickness almost coincides with that expected for the topmost CeO_2 layer and the (111)-phase admits the growth of

Fig. 3. θ–2θ diffraction patterns collected on both halves of a sample fabricated on Al_2O_3 substrate. The pattern collected on the whole stacking sequence [7 layers side] is shifted with regards to that collected on the side without the MgO/CeO_2 bi-layer [5 layers side].

the (00*l*)-YBCO layer along the suitable in-plane orientation, we attribute the peak located at $2\theta \cong 29.5$ to this phase.

In Fig. 5 we report a ϕ-scan of a STO sample while Fig. 6 displays the pole figure of an ALO sample. Each sample were scanned on both sides. In
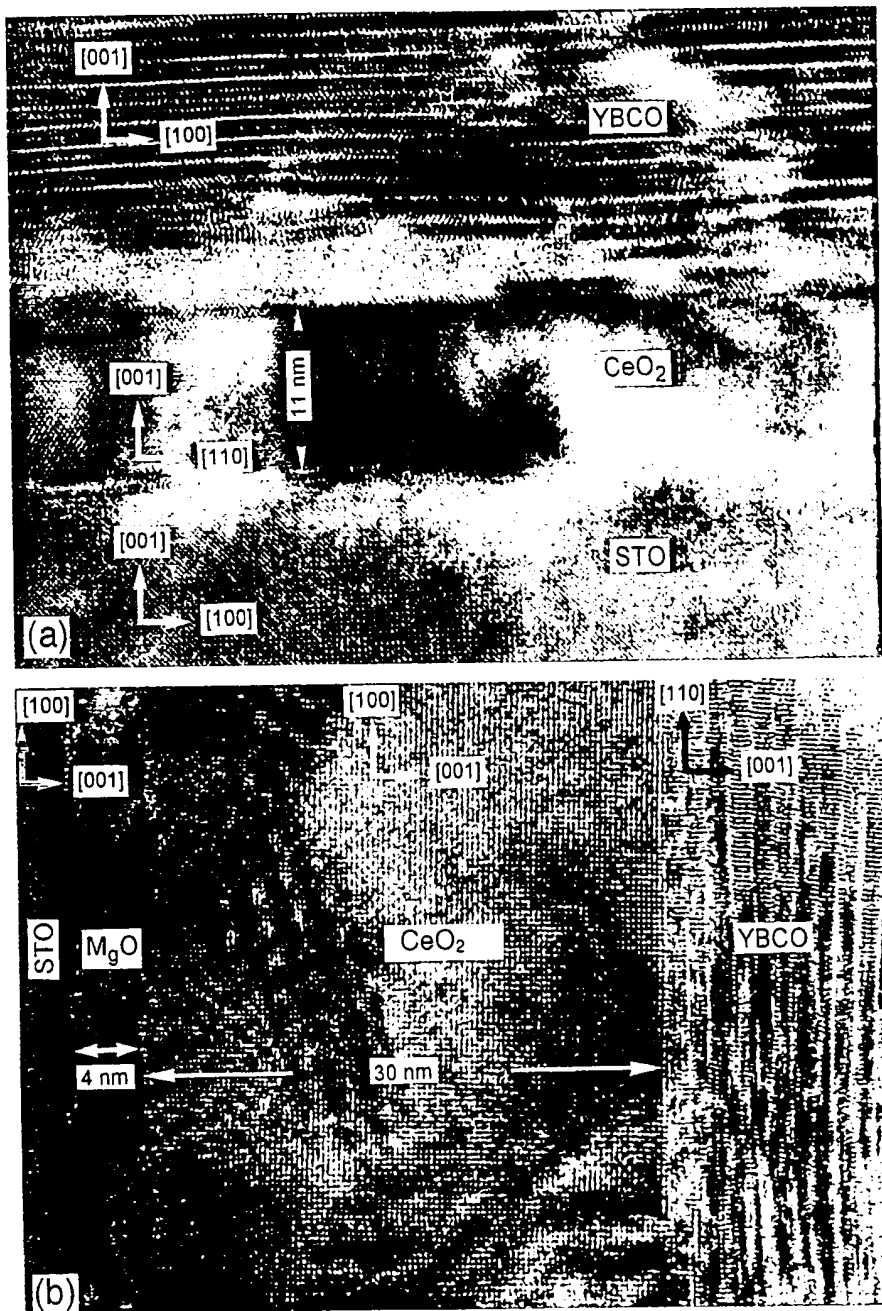

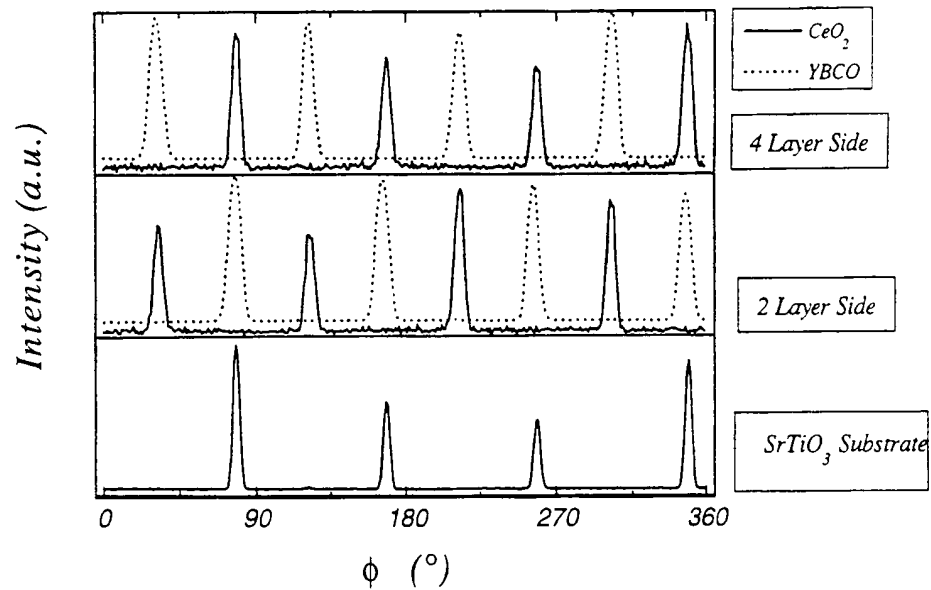Fig. 4. HREM cross view of a) the YBCO/CeO$_2$ and b) the YBCO/CeO$_2$/MgO multilayers structure on a SrTiO$_3$ substrate.

Fig. 5. ϕ-scan diffraction pattern of the {204}-CeO2 and {108}-YBCO reflections taken separately on both sides of an SrTiO$_3$ sample. The diffraction pattern of {204} of the substrate is reported for comparison, in the bottom of the figure.
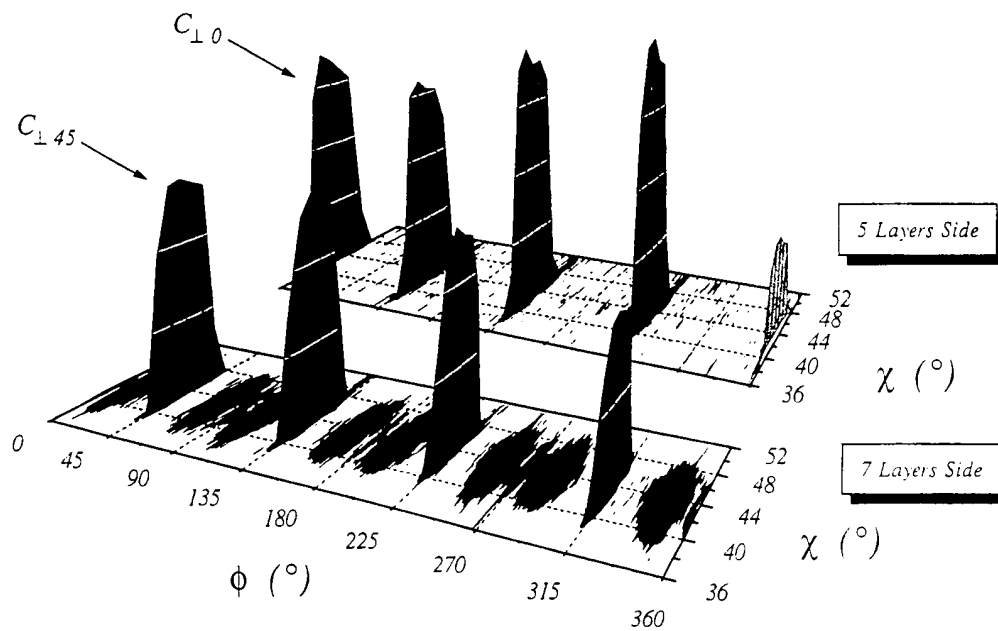
Fig. 6. Pole figure diffraction pattern of the {103}-YBCO reflection taken separately on both sides of a sample fabricated on sapphire substrate.

Table 2
Epitaxial relationships between substrates and deposited layers

Substrate material	Relationship	Sample area without the MgO seed layer	Sample area with the MgO seed layer
$SrTiO_3$	Perpendicular to the substrate surface	$[001]YBCO\|\|[001]CeO_2\|\|[001]SrTiO_3$	$[001]YBCO\|\|[001]CeO_2\|\|[001]MgO\|\|[001]SrTiO_3$
	Parallel to the substrate	$[100]YBCO\|\|[110]CeO_2\|\|[100]SrTiO_3$	$[110]YBCO\|\|[100]CeO_2\|\|[100]MgO\|\|[100]SrTiO_3$
Al_2O_3	Perpendicular to the substrate surface	$[001]YBCO\|\|[001]CeO_2\|\|[001]SrTiO_3\|\|[001]YBCO\|\|$ $[001]CeO_2\|\|[012]^* Al_2O_3$	$[001]YBCO\|\|[001]CeO_2\|\|[001]MgO[001]SrTiO_3\|\|[001]YBCO\|\|$ $[001]CeO_2\|\|[012]^* Al_2O_3$
	Parallel to the substrate surface	$[100]YBCO\|\|[110]CeO_2\|\|[100]SrTiO_3\|\|[100]YBCO\|\|$ $[110]CeO_2\|\|[021]Al_2O_3$	$[110]YBCO\|\|[100]CeO_2\|\|[100]MgO[100]SrTiO_3\|\|[100]YBCO\|\|$ $[110]CeO_2\|\|[021]Al_2O_3$

the case of STO (Fig. 5), as expected from the cell match between the different layers, the relationships are fully respected for both sides of the GB. The $C_{\perp 0}^{\text{YBCO}}$ relationship is the only one present when the MgO is absent (2 layers), while when it is present (4 layers) $C_{\perp 45}^{\text{YBCO}}$ is fully achieved. In the case of ALO (Fig. 6), $C_{\perp 0}^{\text{YBCO/STO}}$ is also fully respected when MgO is absent (5 layers), but persists at a level

of 1–2% in volume on the 7 layers side of the sample. The buried YBCO layer deposited together with CeO_2 and STO to buffer the ALO can account for this residual orientation. The $C_{\perp 45}^{\text{YBCO}}$ attempted relationship dominates with ~ 94% in volume on this side of the GB, even if we can observe the presence of $C_{\perp \phi}^{\text{YBCO}}$ orientations with $8° \leq \phi \leq 30°$ of about 3–4% in volume.
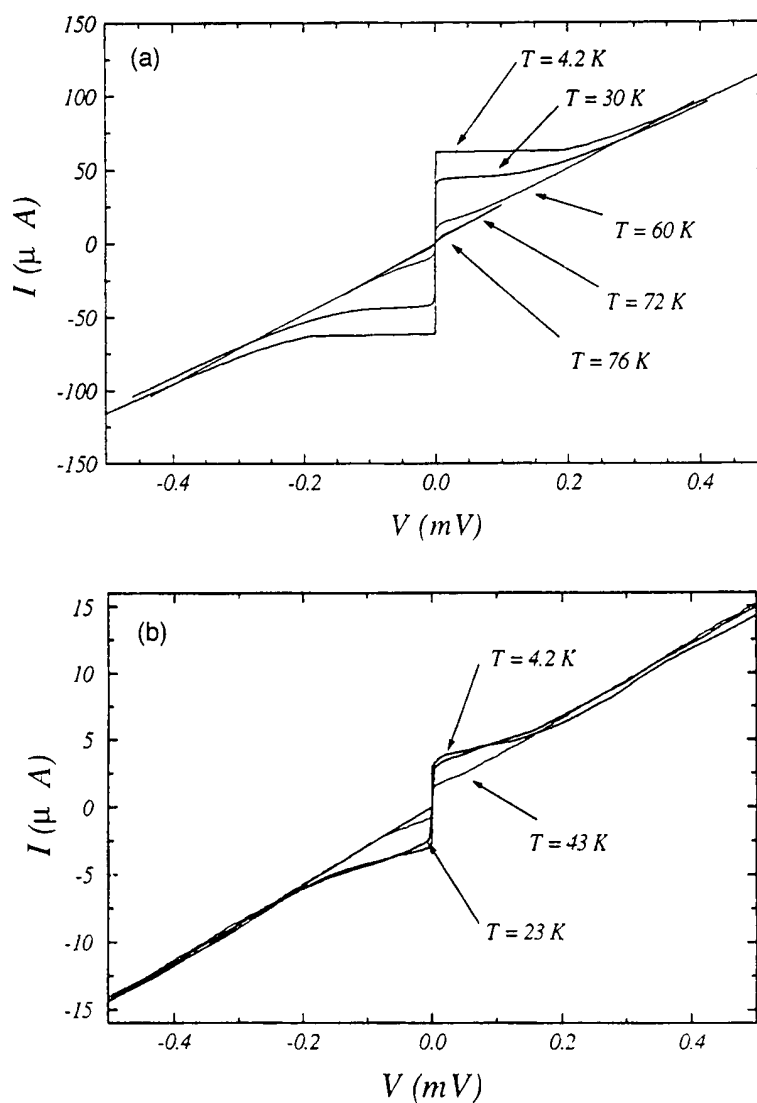
Fig. 7. I–V characteristic of a 16 μm large junction taken at different temperatures for a sample fabricated on a) SrTiO$_3$ and on b) sapphire, respectively.

Table 3
T_c and FWHM values of the (103) YBCO pole figures collected on the different stacking sequence

	SrTiO$_3$		Al$_2$O$_3$	
	Without MgO	With MgO	Without MgO	With MgO
T_c	91	86	85	82.5
FWHM$_\phi$	2.0°	2.5°	1.6°	1.4°
FWHM$_\chi$	4.0°	4.0°	6.8°	7.2°

A detailed analysis carried out on the whole multilayer structure gives, for the different layers, the epitaxial relationships reported in Table 2. As expected, on one part of the sample, the topmost CeO$_2$ and YBCO layers are 45° in-plane rotated with respect to the other part. This behavior leads to the formation of the artificial GB located at the interface between the unetched and the etched side of the sample. Table 3 reports the peak extensions (FWHM) in the pole figure together with the T_c values of the YBCO films deposited over the different stacking sequence. By comparing similar FWHM's for both sides of each sample, the FWHM$_\phi$ values show that the epitaxial relationships are respected in the order of 2°. On the other hand, looking at samples fabricated on different substrates, we note that the diffraction peaks obtained on ALO are wider than those obtained on STO, indicating a degree of structural perfection substantially lower for the YBCO deposited on the former substrate. Since the YBCO obtained on CeO$_2$ buffered sapphire generally exhibit excellent structural properties [11], the origin of disorder probably reside in the complex stacking sequence which involve several layers. It is worth noting that for YBCO on bare STO, FWHM's of 1.53° in χ and of 0.95° in ϕ are currently obtained [10]. In this latter case the FWHM$_\chi$ is nearly doubled compared to the former STO substrate sample. This is attributed to the twin formation in the rhombohedral structure of the ALO giving rise to the formation of faceting at the surface, which is propagated in the stack. This behavior is clearly visible, for example, on the surface of LaAlO$_3$. On such a substrate, FWHM$_\chi$ as great as 10° have been already observed even with no FWHM$_\phi$ more than 2° [10].

3.2. Electrical characterization

As reported in Table 3, all the films exhibit a T_c higher than 80 K but two different behaviors can be observed. First, the T_c of the samples deposited on STO substrates are always higher than those on ALO. Meanwhile, the YBCO film deposited on the side where the MgO is present has a T_c slightly lower than the T_c of the other side, independently of the substrate nature. The correlation with the degree of the structural perfection became evident by comparing the FWHM of each set of peaks. As shown in Table 3, the larger the peaks the lower the T_c. Furthermore, due to the lattice mismatch with the other materials considered here, the MgO layer, even if thin, is the source of further structural disorder in the overhanging layers.

In Fig. 7 (a,b) we report the I–V characteristics taken at different temperatures for a typical junction fabricated on STO and on sapphire substrates, respectively. Under the application of a microwave irradiation the junctions show several Shapiro steps. As already reported, by changing the radiation intensity, the critical current of the junction follows the Bessel behavior as a function of the power [6]. The obtained I–V characteristics of the junctions exhibit

Table 4
Electrical parameters of the Josephson junctions fabricated on SrTiO$_3$ and R-plane Al$_2$O$_3$ at different temperatures. For comparison, same preliminar results obtained on a junction fabricated on a 45° bi-crystal substrate are reported

Substrate	T (K)	J_C (A/cm^2)	$R_N A$ ($\Omega \cdot \mu$m^2)	$I_C R_N$ (μV)
SrTiO$_3$ bi-epitaxial	4.2	3.1×10^3	9.1	282
	30	1.9×10^3	9.0	170
	60	3.8×10^2	8.2	31
	76	2.5	7.9	2
Al$_2$O$_3$ bi-epitaxial	4.2	1.4×10^2	56	60
	23	9.4×10^1	58	54
	42	1.2×10^1	60	7.5
SrTiO$_3$ 45° bicrystal	4.2	6.6×10^3	3.0	221
	30	6.1×10^3	2.9	193
	60	1.1×10^3	2.5	31
	77	3.8×10^1	2.5	1.1

RSJ behavior independently of the substrate type. As reported in Table 4, the normalized resistance, taken on the device biased at 2 mV (i.e. far above $I_C R_N$), do not change significantly with the temperature. By comparing the values for our two samples with those measured on a series of junctions fabricated on a 45° tilted STO bi-crystal, we note that, for the bi-epitaxial GB junctions, the $R_N A$ values are always higher. With respect to the latter values, $R_N A$ about three times and one order of magnitude for the devices on STO and sapphire substrate, respectively. This behavior indicates either a more insulating barrier or a thicker barrier correlated with structural and/or morphological defects.
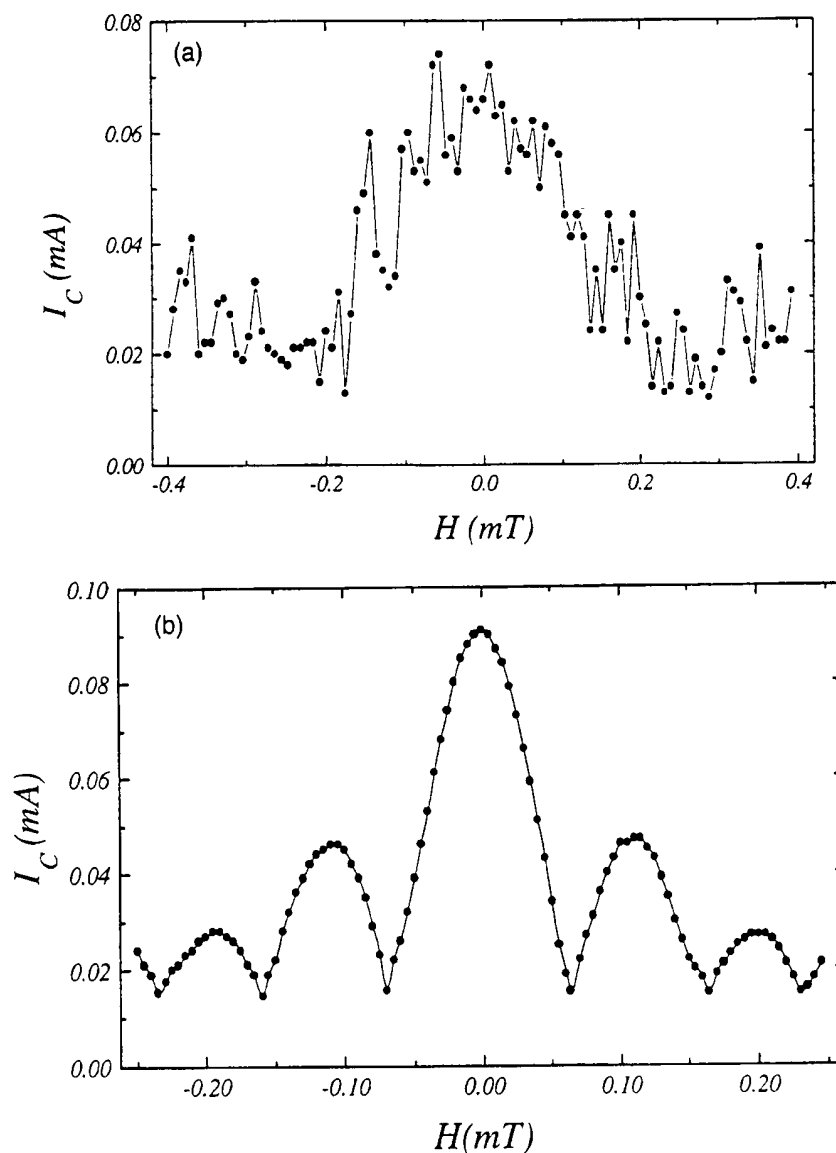
Fig. 8. I_C vs. H curve obtained on a) a 16 μm large junction fabricated on STO substrate and on b) a 5 μm large junction fabricated on 45° symmetric STO bi-crystal. The data were collected at 4.2 K.

To account for the weak link behavior of the GB two models are currently proposed: the model of the Insulating Barrier at the GB interface presented by Gross et al. [12] and the Two Channels model presented separately by Moeckley et al. [13] and by Sarnelli [14]. In these models, the weak link behavior of the GB is correlated to a defective layer at the interface between the two grains. Actually, the origin of this layer is generally ascribed to deviations from the bulk stoichiometry or to the structural disorder associated with the GB itself, but this occurrence is still unproven [15]. The reduction of J_C across the GB is therefore correlated with the spatial extent of this region or, in other words, with the effective thickness of the barrier in the Josephson junction. In this general frame, as much as the YBCO layer itself is defective as much as the interface is defective and as much as the order parameter will be reduced across the GB. Hence, we can explain the electrical behavior of our devices by considering the results of Table 3. The effective thickness of the barrier is correlated with the degree of structural perfection YBCO of the electrodes close to the GB. Consequently, as the structural perfection of the superconducting layer decreases the R_N of the junction increases.

In Fig. 8 we report a typical I_C vs. H curve obtained respectively on a 16 μm large junction fabricated on STO substrate and on a 5 μm large junction fabricated on 45° symmetric STO bi-crystal. The data were collected at 4.2 K. Since the Josephson penetration depth λ_J, as calculated from Table 4, is about 5.5 μm for the bi-epitaxial sample and about 3.8 μm for the bi-crystal sample, we expect, for these devices, the typical Fraunhofer-like I_C vs. H pattern for small uniform junctions ($w/\lambda_J \leq 4$) [16]. As it can be seen from these figures, for the bi-epitaxial I_C is modulated by the magnetic field, but the diffraction pattern largely deviates from the expected behavior. Meanwhile, the curve obtained on the bi-crystal junction shows the typical $\sin(x)/x$ pattern with symmetric periodic lobes.

As already discussed by Copetti et al. [17] and by Hilgenkamp et al. [18], the non-periodical dependence of I_C on the magnetic field and the strong reduction of J_C in GB-based devices can be well accounted for by considering the mutual occurrence of the $d_{x^2-y^2}$ symmetry of the order parameter in

HT$_C$ materials and the microscopic faceting structure of the GB. Moreover, following the discussion carried out in these references, a similar behaviour is expected for symmetric GBs. On the contrary, our data show that a periodic pattern can be obtained even for high angle GBs.

On the other hand, Itzler and Tinkham recently discussed the role of random occurring defects inside the barrier on the electrical behavior of the junction under magnetic field [19]. They were able to demonstrate that the pinning of the Josephson vortices by the defects can interact with the electrical behavior of the device. The action is double: they reduce the carried current and they change the phase along the junction. Therefore, the I_C vs. H pattern is significantly modified by the presence of these pinned vortices in the barrier.

Since the electrical and magnetic performances of the devices increases as the structural perfection of YBCO layer increases, our results are in better agreement with this second model.

4. Conclusions

YBCO Josephson junctions, based on artificially generated in-plane bi-epitaxial grain boundaries, on SrTiO$_3$ and buffered R-plane sapphire were fabricated and characterized. The obtained devices followed the Resistively Shunted Junction model independently off the substrate type, showing Shapiro steps under microwave irradiation and critical current modulation under magnetic field. By comparing the obtained results with those obtained on a 45° bi-crystal, the Josephson current density of the junctions fabricated on sapphire substrates were largely depressed, while those of the devices on STO was only slightly below.

X-ray diffraction and High Resolution Electron Microscopy analyses showed that the structural and textural perfection of the YBCO film decreases as the complexity of the stacking sequence increases. The critical temperature is shown to be correlated to the orientation deviations.

Taking into account the structural properties of the YBCO film on the different stacking sequences, we can explain the behavior of our devices by treating the GB as a conventional Josephson struc-

ture where the barrier transparency is correlated with the degree of structural and textural perfection of each electrode, justifying the correlation between the normalized junction resistance $R_N A$ and the degree of disorder in the superconducting electrodes.

Acknowledgements

References

[1] K. Char, M.S. Colclough, S.M. Garrison, N. Newman and G. Zaharchuk, Appl. Phys. Lett. 59 (1991) 733.

[2] P. Chaudhari, J. Mannhart, D. Dimos, C.C. Touri, J. Chi, M.M. Oprysko and M. Scheuermann, Phys. Rev. Lett. 60 (1988) 1653.

[3] R. Gross, Proc. Int. Workshop on HTS Electron Devices, Whistler Mountain, Canada (1994), 19 and refs. therein reported.

[4] A. Beck, A. Stenzel, O. Froelich, R. Gerber, R. Gerdermann, L. Alff, B. Mayer, R. Gross, A. Marx, J.C. Villegier and H. Moriceau, IEEE Trans. Applied Superconductivity 5 (1995) 2192.

[5] F. Wang, G. Kunkel, C. Copetti, H. Kohlstedt and R. Wördenweber, Proc. EUCAS'93, ed. K. Sremyhrdt (DGM, Göttingen, 1993).

[6] S. Nicoletti, H. Moriceau, J.C. Villegier and D. Chateigner, Physica C 242 (1995) 99.

[7] J.C. Villegier, H. Moriceau, H. Boucher, R. Chicault, L. Di Cioccio, A. Jäger, M. Schwerdtfeger, M. Vabre and C. Villard, IEEE Trans. Magn. 27 (1991) 1552.

[8] L.G. Schulz, J. Appl. Phys. 20 (1949) 1030.

[9] M. Pernet, D. Chateigner and P. Germi, J. Alloys & Comp. 195 (1993) 149.

[10] D. Chateigner, Ph.D. Thesis, Université Joseph Fourier, 1994.

[11] L. Correra, S. Nicoletti, F. Arcidiacono and S. Neri, in ESPRIT BRA Project no. 6625 "X Band SRO" – Final Report.

[12] R. Gross and B. Mayer, Physica C 180 (1991) 235.

[13] B.H. Moeckley and R.A. Buhrman, IEEE Trans. on Appl. Sup. 5 (1995) 3414.

[14] E. Sarnelli, Interface Science 1 (1993) 287.

[15] See for example: A. Alarco, E. Olsson, Z.G. Ivanov, D. Winkler, E.A. Stepantsov, O.I. Lebedev, A.L. Vasiliev, A.Ya. Tzalenchuk and N.A. Kiselev, Physica C 247 (1995) 263.

[16] Physic and Applications of the Josephson Effect, A. Barone and G. Paternó (Wiley, New York, 1982).

[17] C.A. Copetti, F Rüders, B. Oelze, Ch. Buchal, B. Kabius and J.W. Seo, Physica C 253 (1995) 63.

[18] H. Hilgenkamp, J. Mannhart and B. Mayer, Phys. Rev. B (to be published).

[19] M.A. Itzler and M. Tinkham, Phys. Rev. B 53 (1996) 11949.

EXHIBIT J

KOELLE *ET AL.*, 1999, REVIEWS OF MODERN PHYSICS 71, PP. 631–686

Molecular Quantum Mechanics

SECOND EDITION

P. W. ATKINS

High-transition-temperature superconducting quantum interference devices

D. Koelle

II. Physikalisches Institut, Lehrstuhl für Angewandte Physik, Universität zu Köln, D-50937 Köln, Germany

R. Kleiner

Physikalisches Institut III, Universität Erlangen-Nürnberg, D-91058 Erlangen, Germany

F. Ludwig

Physikalisch-Technische Bundesanstalt, Section Cryosensors, D-10587 Berlin, Germany

E. Dantsker* and John Clarke

Physics Department, University of California, Berkeley, and Materials Sciences Division, Lawrence Berkeley National Laboratory, Berkeley, California 94720

The advent of high-T_c superconductors gave great impetus to the development of thin-film superconducting quantum interference devices (SQUIDs) for operation at temperatures up to the boiling point of liquid nitrogen, 77 K. The spectral density of the white flux noise can be calculated analytically for rf SQUIDs and by computer simulation for dc SQUIDs; however, observed noise spectral densities are typically an order of magnitude higher. Low-frequency $1/f$ noise from thermally activated vortex motion is a much bigger issue in high-T_c SQUIDs at 77 K than in low-T_c SQUIDs because of the low flux-pinning energies in high-T_c superconductors. The magnitude of the noise depends strongly on the quality of the thin films, and much effort has been expended to improve techniques for depositing $YBa_2Cu_3O_{7-x}$ (YBCO) on lattice-matched single-crystal substrates. Substantial effort has also been invested in the development of new types of Josephson junctions, of which grain-boundary junctions are the most widely used in SQUIDs. Appropriate electronic read-out schemes largely eliminate $1/f$ noise from fluctuations in the junction critical current in both rf and dc SQUIDs. Typical levels of white flux noise are a few $\mu\Phi_0 \, Hz^{1/2}$ (Φ_0 is the flux quantum). Magnetometers—consisting of a superconducting flux transformer coupled to a SQUID—achieve a white magnetic-field noise as low as 10 fT $Hz^{1/2}$, increasing to typically 30 fT $Hz^{1/2}$ at 1 Hz. When these devices are operated in an unshielded environment, it is important to minimize the motion of trapped vortices and induced supercurrents, which can greatly increase the $1/f$ noise. The ambient noise is far greater than the intrinsic noise of the devices, but can be substantially reduced by various gradiometer configurations. There is now considerable effort to apply high-T_c SQUIDs in magnetocardiology, nondestructive evaluation, microscopy, and geophysics. [S0034-6861(99)00403-1]

CONTENTS

*Current address: TRW, Electronics & Technology Division, Redondo Beach, California 90278.

I. INTRODUCTION

The discovery of superconductivity in ceramic oxides (Bednorz and Müller, 1986) such as $YBa_2Cu_3O_{7-x}$ (YBCO) (Wu *et al.*, 1987) with transition temperatures (T_c) above the boiling point of liquid nitrogen (77 K) generated a worldwide furor to develop new superconducting technologies for both large- and small-scale applications. This frenzy of activity was of course driven by the perception that superconductors cooled in liquid nitrogen at 77 K would quickly become much more widely applicable than superconductors cooled in liquid ^{4}He at 4.2 K. There are two broad reasons behind this perception: liquid nitrogen is much cheaper than liquid helium, and, for a given heat load, liquid nitrogen boils away much more slowly than liquid helium. It was immediately apparent that small-scale devices would require the development of thin-film techniques, and to provide a framework for this research many groups focused on the superconducting quantum interference device (SQUID). Thus at a very early stage of the field Koch *et al.* (1987) and subsequently Nakane *et al.* (1987) fabricated the first thin-film dc SQUIDs: the first rf SQUIDs appeared a little later (Colclough *et al.*, 1987; Zimmerman *et al.*, 1987), although they were actually formed from bulk YBCO. There were several good reasons for choosing the SQUID as a vehicle for the development of this new technology. Low-T_c SQUIDs are by far the most widely used superconducting thin-film devices at liquid ^{4}He temperatures, and it was a natural assumption that this trend would continue at liquid N_2 temperatures. Furthermore, the SQUID incorporates most of the components needed for a broader range of electronic devices. The first is a photolithographically patterned thin film with high crystalline quality and a transition temperature essentially equal to that of the bulk material. A second, essential component is the Josephson junction (Josephson, 1962), for which one would like a process that yields highly reproducible parameters. A third ingredient is an interconnect technology, that is, a multiple-level process that enables one to fabricate crossovers—two intersecting superconducting films separated by an insulating layer—and *vias*—superconducting contacts through the insulating layer.

Progress in high-T_c dc and rf SQUIDs over the last decade has been dramatic, and the purpose of this review is to give a perspective on the current state of the art.

The dc SQUID (Jaklevic *et al.*, 1964) consists of two Josephson junctions connected in parallel on a superconducting loop. When the magnetic flux Φ threading the loop is changed monotonically, the maximum supercurrent the SQUID can sustain (the critical current) is modulated with a period of one flux quantum, $\Phi_0 \equiv h/2e$. Provided the current-voltage (I-V) characteristic is nonhysteretic (Sec. II.A), this modulation results in a concomitant modulation of the voltage across the SQUID when it is biased with a constant current greater than the maximum critical current. In essence, the SQUID is a flux-to-voltage transducer, characterized by the transfer coefficient $|\partial V/\partial \Phi|_I$. The flux resolution of the SQUID is determined by its intrinsic noise, which has a spectral density that is white at frequencies above a certain threshold and that scales approximately as $1/f$ at frequencies f below the threshold. In low-T_c SQUIDs the threshold frequency can be 0.1 Hz or lower, while, as we shall see, in high-T_c SQUIDs it can be substantially higher. In Secs. II.B and C, we outline the theory of operation of the dc SQUID and solve its equations of motion numerically for both the transfer function and white noise. From the results of our simulations we discuss the optimum choice of parameters for operation at 77 K.

The rf SQUID (Zimmerman *et al.*, 1970; Mercereau, 1970; Nisenoff, 1970) involves a single Josephson junction that interrupts a superconducting loop. This loop is inductively coupled to the inductor of an LC-resonant circuit that is driven by an rf current at or near its resonant frequency, which ranges from 20 MHz to 10 GHz. The amplitude of the rf voltage across the tank circuit is periodic in the magnetic flux in the SQUID with period Φ_0, so that, after demodulating this voltage, one obtains a quasistatic voltage that is periodic in Φ just as for the dc SQUID. For operation at 4.2 K the rf SQUID has been largely abandoned in favor of the dc SQUID, but the advantage in sensitivity of the latter device at 77 K is much narrower. In Secs. II.D–F, we outline the theory of operation and noise limitations of the rf SQUID.

Low-T_c SQUIDs have been used as sensors in a broad range of applications, including biomagnetism, nondestructive evaluation, geophysics, susceptometers, voltmeters, scanning SQUID microscopes, and nuclear magnetic and nuclear quadrupole resonance (Weinstock, 1996). Of these, the largest number of SQUIDs are deployed in multichannel systems for magnetoencephalography and, to a lesser extent, magnetocardiology. A major requirement for biomagnetic measurements is high magnetic-field sensitivity at frequencies down to 1 Hz. Although this requirement is readily met with niobium based SQUID magnetometers, which achieve a sensitivity of a few fT Hz$^{1/2}$, the issue of $1/f$ noise in high-T_c SQUIDs has been a major challenge, and will emerge repeatedly throughout this review. There are two separate sources of $1/f$ noise (Koch *et al.*, 1983): fluctuations in the critical current of the junction(s) and the ther-

mally activated hopping of flux vortices among pinning sites in the thin-film loop. Fortunately, as will be described, $1/f$ noise due to critical-current fluctuations in both dc and rf SQUIDs can be largely eliminated electronically by means of appropriate schemes (Secs. V.B and VII.C). In the case of low-T_c SQUIDs, $1/f$ noise from vortex motion is rarely a problem, but for high-T_c SQUIDs it is a major issue. The reason is simple: flux-pinning energies are lower and thermal energies are higher. At an early stage, Ferrari *et al.* (1988, 1989) used a low-T_c dc SQUID to show that vortex motion in unpatterned high-T_c films indeed produced copious levels of $1/f$ flux noise and that the level diminished dramatically as the microstructural quality of the film was improved. This theme is first raised in Sec. III, in which we briefly review issues concerning the fabrication of thin films. We confine our discussion to YBCO, the only material that has been used for practical devices. Of the possible substrate materials only a handful are admissible. Pulsed laser deposition, sputtering, and recently, coevaporation have emerged as the deposition techniques of choice. Issues of patterning and multilayer processing as well as $1/f$ noise are also discussed in this section.

The other major challenge in the development of SQUIDs, and indeed for high-T_c electronics circuits in general, has been the need to develop an appropriate technology for Josephson junctions (Sec. IV). Many approaches have been tried, ranging from a single layer of YBCO in which grain-boundary junctions are formed along the misorientation boundary of a bicrystal substrate or at a step edge milled in a substrate, to multilayers in which insulating or metallic barriers are formed between two YBCO films. It seems fair to say that the ideal technology has not yet been invented. For virtually all applications, the figure of merit is the I_0R product, where I_0 is the critical current and R is the resistance for currents much greater than I_0. Although one might hope to achieve values of several millivolts at 77 K, in practice the highest values achieved to date are more like 300 μV. For SQUIDs, the technique most widely used today is the grain-boundary junction formed on either a bicrystal or a step edge.

Section V reviews practical high-T_c dc SQUIDs. The two widely used readout schemes, flux modulation and direct readout, are briefly described, and the use of bias reversal to eliminate the $1/f$ noise due to critical-current fluctuations is outlined. Achieved levels of white noise and $1/f$ noise are summarized in a series of figures. For reasons that are not well understood, the levels of white noise are generally higher than the predictions of the computer model described in Sec. II.

Although dc SQUIDs are exquisitely sensitive to changes in magnetic flux—typical devices have a white noise of a few $\mu\Phi_0$ Hz $^{1/2}$—their small area implies that they are relatively insensitive to changes in magnetic field. To increase this sensitivity, as described in Sec. VI, one almost invariably couples the SQUID to a flux transformer that increases its effective area. Broadly speaking, there are two classes of such magnetometers.

In the first, the so-called directly coupled magnetometer, a large pickup loop—perhaps 10 mm across—is patterned in the same layer as the SQUID so that the supercurrent produced by an applied magnetic field is injected directly into the body of the SQUID. This scheme has the advantage that it involves only a single superconducting layer but suffers from the disadvantage that the inductances of the pickup loop and SQUID are mismatched, thereby reducing the flux-coupling efficiency of the transformer. The mismatch is overcome in the second approach, mimicking that used for low-T_c magnetometers, in which a pickup loop is connected to a multiturn input coil that in turn is inductively coupled to the SQUID. The flux transformer can be either deposited directly onto the SQUID or deposited on a separate substrate and coupled to the SQUID in a flip-chip arrangement. This flux transformer matches the inductance of the pickup loop to the SQUID, but the multilayer structure required for the input coil complicates the fabrication. The best of these magnetometers have achieved a white noise below 10 fT Hz $^{1/2}$. An alternative, multilayer magnetometer is the fractional-turn SQUID described in Sec. VI.D.

Section VII is concerned with practical rf SQUIDs, usually fabricated from single layers of YBCO. As discussed in Sec. II, the inductance of the rf SQUID can be somewhat larger than its dc counterpart, enabling one to obtain a higher effective area. Early devices consisted of square washers with step-edge, grain-boundary junctions, and were operated at typically 150 MHz. The sensitivity has been improved by increasing the frequency substantially; as shown in Sec. II, the spectral density of the flux noise is expected to scale inversely with the rf frequency. In the best device reported to date, the white noise was 16 fT Hz $^{1/2}$. Section VII.C describes how the $1/f$ noise due to critical-current fluctuations is eliminated by the combination of rf biasing and flux modulation.

Sections VIII and IX are concerned with using SQUID magnetometers in real-world environments. Most notably in biomagnetism, one needs to measure a tiny magnetic signal against a magnetically noisy background. The standard approach to this problem is to use a spatial gradiometer, usually in conjunction with a magnetically shielded room. The gradiometer discriminates against distant noise sources in favor of a nearby signal source. Given the lack of a suitable high-T_c superconducting wire, two approaches have been adopted (Sec. VIII): electronic subtraction of the signals from two or more spatially separated magnetometers, usually to form axial gradiometers, and the use of planar, thin-film gradiometers that measure off-diagonal gradients. Section IX is largely concerned with the operation of magnetometers or gradiometers in the ambient magnetic field of the earth, which has two deleterious effects. The additional vortices created by the penetration of the earth's field into the thin films can greatly increase the level of $1/f$ noise. Fortunately, this problem can be largely alleviated by making the thin-film structures sufficiently narrow, if necessary, by patterning slots or holes

in them. A related problem is hysteresis produced by the entry of vortices when the device is rotated in the earth's field. Flux entry can be greatly reduced, fortunately, by patterning straight, near-vertical edges which provide high edge-pinning forces. Other issues discussed in Sec. IX include rf interference and temperature fluctuations.

In Sec. X we briefly review several applications of high-T_c SQUIDs, which are still in their infancy. Nonetheless, impressive progress has been made in biomagnetism, particularly magnetocardiology, and useful demonstrations have been made in both nondestructive evaluation and scanning SQUID microscopy. Prototype geophysical systems have been successfully deployed. Section XI contains our conclusions.

Writing this review brought home to us the enormous amount of effort that has been expended in developing the technology of high-T_c SQUIDs, and the vastness of the literature. Regrettably, it was out of the question to list more than a fraction of the publications in the space of this review. We have attempted to give a broad perspective on the field, but we are acutely aware that our choice of topics is subjective and far from exhaustive.

II. THEORY

A. Resistively shunted junction model

The Josephson junction (Josephson 1962, 1965; Barone and Paterno, 1982) consists of two weakly coupled superconducting electrodes separated—in the case of the low-T_c tunnel junction—by a thin insulating barrier. Cooper pairs tunneling through the barrier constitute a supercurrent $I = I_0 \sin \delta$, where I_0 is the critical current and δ is the difference between the phases of the order parameters in the two superconductors. For zero applied current, the two electrodes are coupled by an energy $I_0 \Phi_0 / 2\pi$. In the absence of thermal fluctuations, the voltage V across the barrier is zero for $I < I_0$; for $I > I_0$ a voltage is developed and δ evolves with time as $\dot{\delta} = 2eV/\hbar = 2\pi V/\Phi_0$. At least for low-$T_c$ junctions, the current-voltage characteristics are well explained by the resistively and capacitively shunted junction (RCSJ) model (McCumber, 1968; Stewart, 1968). In this model, the Josephson element is in parallel with a resistance R (which may be an external shunt) and a capacitance C. For SQUIDs, one generally needs nonhysteretic I-V characteristics, a requirement that is met if $\beta_c \equiv 2\pi I_0 R^2 C/\Phi_0 < 1$. In the limit $\beta_c \ll 1$, which as we shall see is often the case for high-T_c junctions, the RCSJ model reduces to the RSJ model and the I-V characteristic in the absence of thermal noise is given by $V = R(I^2 - I_0^2)^{1/2}$ for $I \geq I_0$.

Particularly in the case of devices operating at 77 K, however, noise has an appreciable effect, and is added to the model by associating a Nyquist noise current I_N with spectral density $S_I(f) = 4k_B T/R$ with the shunt resistor. This noise term rounds the I-V characteristic at low voltages and reduces the apparent critical current (Ambegaokar and Halperin, 1969). To maintain a reasonable
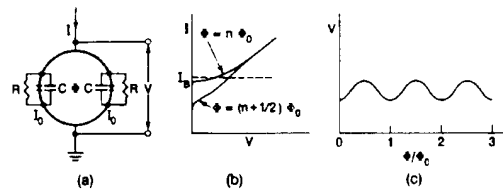

FIG. 1. The dc SQUID: (a) schematic, (b) I-V characteristic, (c) V vs Φ/Φ_0 at constant bias current I_B.

degree of Josephson coupling one requires the noise parameter $\Gamma \equiv 2\pi k_B T/I_0 \Phi_0 = I_{th}/I_0 \ll 1$; at 77 K, $I_{th} \approx 3.3 \,\mu$A.

B. dc SQUID: Overview

The dc SQUID (Jaklevic *et al.*, 1964) consists of two Josephson junctions connected in parallel on a superconducting loop of inductance L [Fig. 1(a)]. If one biases the SQUID with a constant current $I_B(> 2I_0)$ the voltage V across the SQUID oscillates with a period Φ_0 as one changes the external magnetic flux Φ [Figs. 1(b) and (c)]. To measure small changes in Φ ($< \Phi_0$) one generally chooses the bias current to maximize the amplitude of the voltage modulation and sets the external flux at $(2n-1)\Phi_0/4$ ($n = 0,1,2,\ldots$), so that the flux-to-voltage transfer coefficient $|\partial V/\partial \Phi|_I$ is a maximum, which we denote as V_Φ. Thus the SQUID produces a maximum output voltage signal $\delta V = V_\Phi \delta\Phi$ in response to a small flux signal $\delta\Phi$. For frequencies f well below the Josephson frequency $f_J = V/\Phi_0$, the two independent Nyquist noise currents in the shunt resistors produce a white voltage noise across the SQUID with a spectral density $S_V(f)$ (Tesche and Clarke, 1977) and a white current noise around the SQUID loop with a spectral density $S_J(f)$; in fact, these two noise terms are partially correlated (Tesche and Clarke, 1979). The intrinsic white flux noise of the SQUID is given by $S_\Phi(f) = S_V(f)/V_\Phi^2$; it is often convenient to introduce a noise energy per unit bandwidth $\varepsilon(f) = S_\Phi(f)/2L$. We note that noise imposes a second constraint on the parameters, namely that the magnetic energy per flux quantum $\Phi_0^2/2L$ must be substantially greater than $k_B T$. We can express this requirement as $\Gamma \beta_L = L/L_{th} < 1$, where we define $\beta_L = 2LI_0/\Phi_0$, and $L_{th} \equiv \Phi_0^2/4\pi k_B T = 321$ pH at 77 K. As we shall see, this restriction, which can also be written as $\Phi_0^2/2L > 2\pi k_B T$, will play a key role in our choice of parameters.

There have been extensive computer simulations of dc SQUIDs operated at 4.2 K (Tesche and Clarke, 1977, 1979; Bruines *et al.*, 1982; Voss, 1981; de Waal *et al.*, 1984; Ryhänen *et al.*, 1989). These simulations show that the minimum noise energy is obtained for $\beta_L \approx 1$ and that, for a representative value of the noise parameter $\Gamma \approx 0.05$, $V_\Phi \approx R/L$, $S_V(f) \approx 16k_B TR$ and $\varepsilon \approx 9k_B TL/R \approx 9k_B T\Phi_0/2I_0 R$. Thus ε inevitably increases with temperature and, for optimized parameters, scales as $1/I_0 R$. In addition to the white noise, there is usually low-

frequency $1/f$ noise generated by both $1/f$ noise in the critical current and by the motion of flux vortices trapped in the body of the SQUID. We defer the issue of $1/f$ noise to Sec. V.D, and turn our attention to optimizing the parameters of the SQUID at 77 K with regard to white noise.

C. dc SQUID: Transfer function and thermal noise

It is straightforward to show that the phase differences $\delta_1(t)$ and $\delta_2(t)$ across the two junctions obey the following equations (Tesche and Clarke, 1977):

$$\frac{\hbar C}{2e}\ddot{\delta}_1 + \frac{\hbar}{2eR}\dot{\delta}_1 + I_0 \sin \delta_1 + I_{N1} = \frac{I}{2} + J, \tag{2.1}$$

$$\frac{\hbar C}{2e}\ddot{\delta}_2 + \frac{\hbar}{2eR}\dot{\delta}_2 + I_0 \sin \delta_2 + I_{N2} = \frac{I}{2} - J, \tag{2.2}$$

$$\delta_1 - \delta_2 = \frac{2\pi}{\Phi_0}(\Phi - LJ), \tag{2.3}$$

and

$$\dot{\delta}_1 + \dot{\delta}_2 = \frac{4eV}{\hbar}. \tag{2.4}$$

The Langevin Eqs. (2.1) and (2.2) are coupled via the circulating current J, which is related to the external flux Φ in Eq. (2.3). Equation (2.4) expresses the voltage across the SQUID as the rate of the change of the phase differences. In all our simulations we set $\beta_c = 0.5$; the results change only slightly for the smaller values of β_c that we expect for many high-T_c junctions operated at 77 K. To find the transfer function we set $\Phi = \Phi_0/4$, integrate Eqs. (2.1)-(2.3) numerically over 10^4 to 10^6 time units ($\Phi_0/2\pi I_0 R$), and use Eq. (2.4) to obtain the average voltage across the SQUID (Kleiner, 1996). We compute $\partial V/\partial \Phi$ as a function of I to find the maximum value V_Φ. To explore the dependence on the inductance L, it is convenient to plot V_Φ vs $\Gamma\beta_L \equiv L/L_{th} \equiv (4\pi k_B T/\Phi_0^2)L$. The range of interest for $\Gamma\beta_L$ extends from well below 0.05 to unity. For convenience, we start from $\Gamma\beta_L = (0.05)2^{-2} = \frac{1}{80}$ and increase $\Gamma\beta_L$ in powers of $2^{1/2}$ up to $(0.05)2^{9/2}\approx 1.13$. For $T = 77$ K this corresponds to inductances between 4 and 362 pH, while for $T = 4.2$ K the corresponding range is 74 pH to 6.7 nH. For most high-T_c devices $\Gamma\beta_L \gtrsim 0.1$, whereas for typical low-T_c devices $\Gamma\beta_L \ll 0.05$.

On calculating the dimensionless transfer function $v_\phi \equiv V_\Phi \Phi_0/I_0 R$ vs $\Gamma\beta_L$ for values of β_L ranging from 0.6 to 4 one finds that, although v_ϕ for a given value of $\Gamma\beta_L$ decreases with β_L, its functional dependence on $\Gamma\beta_L$ is essentially the same for all values of β_L. Thus, on normalizing curves of v_ϕ vs $\Gamma\beta_L$ to their value at, say, $\Gamma\beta_L = \frac{1}{80}$, one obtains a universal curve $g(\Gamma\beta_L) = v_\phi(\beta_L;\Gamma\beta_L)/v_\phi(\beta_L;\Gamma\beta_L = \frac{1}{80})$, which is independent of β_L. Note that the value of $\Gamma\beta_L = \frac{1}{80}$ is an arbitrary but convenient choice suggested by the smallest value of $\Gamma\beta_L$ used in the simulations. We denote the normalization factor $v_\phi(\beta_L;\Gamma\beta_L = \frac{1}{80})$ as $f(\beta_L)$. Figure 2 shows
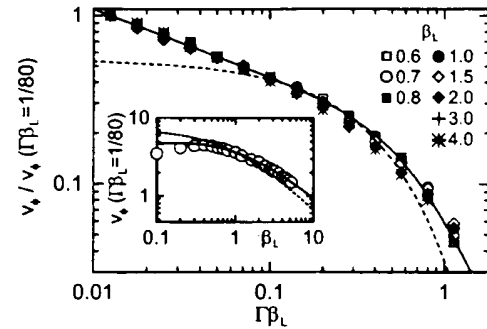

FIG. 2. Computed normalized transfer function $v_\phi/v_\phi(\beta_L;\Gamma\beta_L = \frac{1}{80})$ vs $\Gamma\beta_L$ for $\beta_c = 0.5$. Solid line corresponds to Eq. (2.5), dashed line to $(4/7.3)\exp(-2.75\Gamma\beta_L)$. Inset shows $v_\phi(\beta_L;\Gamma\beta_L = \frac{1}{80})$ vs β_L; solid line corresponds to Eq. (2.6), dashed line to $7.3/(1+\beta_L)$.

the normalized curve $g(\Gamma\beta_L)$ vs $\Gamma\beta_L$ for eight values of β_L ranging from 0.6 to 4.0. As discussed, the results collapse onto a single curve. The solid line in Fig. 2 is an empirical fit to the computed values

$$g(\Gamma\beta_L) = v_\phi(\beta_L;\Gamma\beta_L)/v_\phi(\beta_L;\Gamma\beta_L = 1/80)$$
$$= [(80\Gamma\beta_L)^{0.4} + 0.35(4\Gamma\beta_L)^{2.5}]^{-1}. \tag{2.5}$$

For $\Gamma\beta_L \leq 0.2$, Eq. (2.5) can be approximated as $g(\Gamma\beta_L)\approx (80\Gamma\beta_L)^{-0.4}$. The inset of Fig. 2 shows $f(\beta_L)$ vs β_L for the fixed value $\Gamma\beta_L = 1/80$ for $0.1\leq\beta_L\leq 5.2$. For $\beta_L \geq 0.5$, the range of experimental interest, one can fit the transfer function with the expression

$$f(\beta_L) = v_\phi(\beta_L;\Gamma\beta_L = 1/80) = 7.3\beta_L^{0.15}/(1+\beta_L), \tag{2.6}$$

shown as a solid line in the inset. With the aid of the factorization $v_\phi = f(\beta_L)g(\Gamma\beta_L)$, these two curves, or Eqs. (2.5) and (2.6), enable one to calculate v_ϕ immediately for any value of β_L and $\Gamma\beta_L$ within the specified ranges. Note that v_ϕ, calculated numerically, decreases for $\beta_L < 0.4$. This decrease is not reproduced by Eq. (2.6). Furthermore, since the SQUID will no longer function when Γ becomes much greater than unity, the range of validity of Eqs. (2.5) and (2.6) is restricted to $\Gamma \leq 1$, that is $\Gamma\beta_L \leq \beta_L$. Note that in the range $\Gamma\beta_L \leq 0.2$, where $g(\Gamma\beta_L)\approx (80\Gamma\beta_L)^{-0.4}$, we can also factorize v_ϕ as $\hat{f}(\beta_L)\hat{g}(\Gamma)$, where $\hat{f}(\beta_L) = f(\beta_L)/\beta_L^{0.4}$ and $\hat{g}(\beta_L) = (80\Gamma)^{-0.4}$. Thus for $\Gamma\beta_L \leq 0.2$ the variables β_L and $\Gamma\beta_L$ are not the only possible choices for factorization. In order to confirm the validity of Eq. (2.6) for larger values of β_L, we also calculated v_ϕ for $\beta_L = 20$ and $\Gamma\beta_L = 1/80$. The numerical result is $v_\phi\approx 0.6$ whereas Eq. (2.6) yields 0.55.

It is of interest to compare our results with the expression of Enpuku, Doi *et al.* (1995) and Enpuku, Tokita *et al.* (1995),

$$v_\phi = \frac{4}{1+\beta_L}\exp\left(-\frac{3.5\pi^2(\delta\Phi_n)^2}{\Phi_0^2}\right)$$
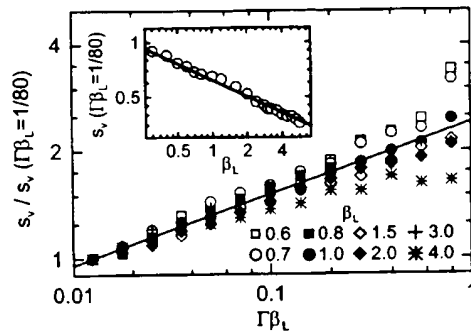$$\approx \frac{4}{1+\beta_L}\exp(-2.75\Gamma\beta_L), \tag{2.7}$$

FIG. 3. Computed normalized voltage noise power $s_v/s_v(\beta_L;\Gamma\beta_L \ \frac{1}{80})$, vs $\Gamma\beta_L$ for β_c 0.5. Solid line shows $s_v(\beta_L;\Gamma\beta_L)/s_v(\beta_L;\Gamma\beta_L \ \frac{1}{80})$ $(80\Gamma\beta_L)^{0.2}$. Inset shows $s_v(\beta_L;\Gamma\beta_L \ \frac{1}{80})$ vs β_L, solid line is $s_v(\beta_L;\Gamma\beta_L \ \frac{1}{80})$ $0.62\beta_L^{0.3}$.

FIG. 4. Computed normalized flux noise power $s_\phi/s_\phi(\beta_L;\Gamma\beta_L \ \frac{1}{80})$ vs $\Gamma\beta_L$ for β_c 0.5. Solid line corresponds to Eq. (2.8). Inset shows $s_\phi(\beta_L;\Gamma\beta_L \ \frac{1}{80})$ vs β_L. Solid line corresponds to Eq. (2.9).

where $(\delta\Phi_n)^2$ k_BTL is the mean square flux noise. This expression also factorizes into two terms, which depend on β_L and $\Gamma\beta_L$, respectively. Equation (2.7) agrees well with our results for intermediate values of β_L and $\Gamma\beta_L$, but underestimates v_ϕ outside this region. For example, for β_L 1 the agreement is better than 5% for 0.09 $\Gamma\beta_L$ 0.35. The dashed line in Fig. 2 is given by $(4/7.3)\exp(\ 2.75\Gamma\beta_L)$, and the dashed line in the inset of Fig. 2 corresponds to $7.3/(1\ \beta_L)$. The prefactor $(\frac{7.3}{4})$ was chosen to obtain the best agreement with our simulations for β_L 1. Similar results have been found by Koch (1994), Keene *et al.* (1995), and Foglietti *et al.* (1995).

We turn now to the voltage noise at frequencies well below the Josephson frequency, where its spectral density is white. Using Eqs. (2.1)–(2.4) we compute the Fourier transform of the time-varying voltage across the SQUID and hence the dimensionless power spectrum $s_V(f)$ $2\pi S_V(f)/I_0R\Phi_0$. We set Φ $\Phi_0/4$, vary the bias current so that V_ϕ takes its maximum value and calculate $S_V(f)$. In Fig. 3 we plot $s_v(\beta_L;\Gamma\beta_L)/s_v(\beta_L;\Gamma\beta_L \ \frac{1}{80})$ vs $\Gamma\beta_L$ for eight values of β_L. For a given value of β_L, the noise power increases with $\Gamma\beta_L$. However, the overall variation in $s_v(\beta_L;\Gamma\beta_L)$ is weak: within a factor of 2, $s_v\approx 1$ or $S_V\approx I_0R\Phi_0/2\pi$. In contrast to the transfer function (Fig. 2), there is no universal behavior for the noise power, although roughly speaking, s_v scales as $(80\Gamma\beta_L)^{0.2}$ (line in Fig. 3). The inset to Fig. 3 shows $s_v(\beta_L;\Gamma\beta \ \frac{1}{80})$ vs β_L. For fixed $\Gamma\beta_L$, β_L is proportional to I_0/T; the decrease in noise with increasing β_L thus reflects either the decrease in temperature if I_0 is fixed or the increase in I_0 if T is fixed. The line is a fit to $s_v(\beta_L;\Gamma\beta_L \ \frac{1}{80})$ $0.62\beta_L^{0.3}$; within the range 0.2 β_L 5.2, we can approximate $s_v\approx 1.5\beta_L^{0.3}(\Gamma\beta_L)^{0.2}$. For Γ 0.05 and β_L 1 we find s_v 0.82, in excellent agreement with the result of Tesche and Clarke (1977), $S_V \approx 16k_BTR$. (To make the comparison, note that s_v $(2\pi/I_0R\Phi_0)16k_BTR$ 16Γ 0.8.)

We find the flux noise of the dc SQUID from the relation $S_\Phi(f)$ $S_V(f)/V_\phi^2$ or $s_\phi(f)$ s_v/v_ϕ^2 $(2\pi I_0R/\Phi_0^3)S_\Phi(f)$. Figure 4 shows $s_\phi(\beta_L;\Gamma\beta_L)/$
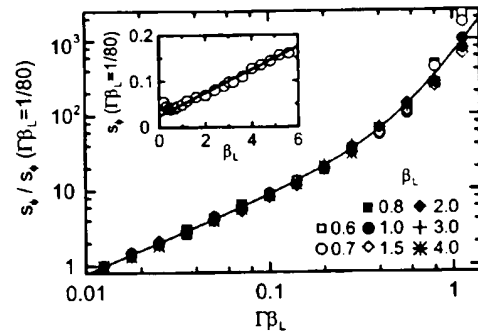
$s_\phi(\beta_L;\Gamma\beta_L \ \frac{1}{80})$ vs $\Gamma\beta_L$, obtained from the results in Figs. 2 and 3. The computed data very nearly follow a universal curve, because of the universal, strong dependence of v_ϕ on $\Gamma\beta_L$ and the weak dependence of s_v. For 0.01 $\Gamma\beta_L$ 1 we can fit the curve reasonably well by the expression

$$s_\phi(\beta_L;\Gamma\beta_L)/s_\phi(\beta_L;\Gamma\beta_L \ \tfrac{1}{80})$$
$$0.8[80\Gamma\beta_L \ (1 \ 4\Gamma\beta_L)^{4.1} \ 1]. \qquad (2.8)$$

For $\Gamma\beta_L$ 0.1, $s_\phi(\beta_L;\Gamma\beta_L)/s_\phi(\beta_L;\Gamma\beta_L \ \frac{1}{80})$ reduces to approximately $80\Gamma\beta_L$, while for larger values of $\Gamma\beta_L$ it increases rapidly because of the rapid drop in v_ϕ. In the inset to Fig. 4 we plot $s_\phi(\beta_L;\Gamma\beta_L \ \frac{1}{80})$ vs β_L, together with the fitted curve

$$s_\phi(\beta_L;\Gamma\beta_L \ \tfrac{1}{80}) \ (1 \ \beta_L)/40. \qquad (2.9)$$

Note that the increase of $s_\phi(\beta_L;\Gamma\beta_L \ \frac{1}{80})$ for β_L 0.5, which arises from the decrease of $v_\phi(\beta_L;\Gamma\beta_L \ \frac{1}{80})$, is not reproduced by Eq. (2.9). Thus, for the range $\Gamma\beta_L$ 0.1 and β_L 0.5, we find $s_\phi\approx 2(1 \ \beta_L)\Gamma\beta_L$ or S_Φ $\approx 4(1 \ \beta_L)\Phi_0k_BTL/I_0R$. For β_L 1, this result becomes $16k_BTL^2/R$, in excellent agreement with the value of Tesche and Clarke (1977). As an example, from Fig. 4 for $\beta_L\Gamma$ 0.1 and β_L 1 we find $s_\phi\approx 0.4$; with I_0R 200 μV, this value corresponds to S_Φ ≈ 0.6 10 $^{12}\Phi_0^2$ Hz ^{1}.

Finally, we derive the noise energy $\varepsilon(f)$ $S_\Phi(f)/2L$; in dimensionless units, e $\varepsilon I_0R/2\Phi_0k_BT$ $s_\phi/2\Gamma\beta_L$. Figure 5 shows $e(\beta_L;\Gamma\beta)/e(\beta_L;\Gamma\beta_L \ \frac{1}{80})$ vs $\Gamma\beta_L$, obtained from the results in Figs. 2 and 3. For $\Gamma\beta_L$ 0.2, the reduced noise energy is almost constant, while for higher values of $\Gamma\beta_L$ it increases rapidly. The rapid increase in noise energy arises from the rapid degradation of the transfer function over the same values of $\Gamma\beta_L$ (Fig. 2). In the inset of Fig. 5 we plot $e(\Gamma\beta_L$ 1/80) as a function of β_L: the dependence is linear for β_L 0.5, and to a good approximation $e(\beta_L;\Gamma\beta_L$ 1/80)$\approx(1 \ \beta_L)$ for β_L 0.5. For a SQUID with Γ 0.05 and β_L 1, Tesche and Clarke (1977) find $\varepsilon\approx 9k_BTL/R$, corresponding to e $\varepsilon I_0R/2\Phi_0k_BT\approx 9LI_0/2\Phi_0$ $9\beta_L/4$ 2.25. From Fig. 5, we predict $e\approx 2$, in good agreement,
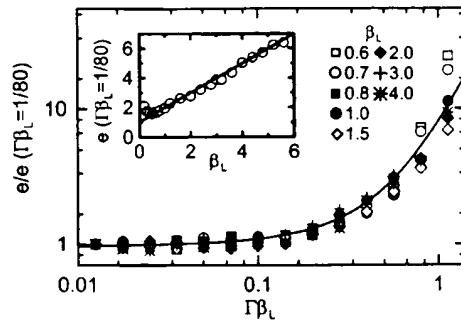
FIG. 5. Computed normalized energy resolution $e/e(\beta_L:\Gamma\beta_L$ $\frac{1}{80})$ vs $\Gamma\beta_L$ for β_c 0.5. Solid line corresponds to Eq. (2.8) divided by $(80\Gamma\beta_L)$. Inset shows $e(\beta_L:\Gamma\beta_L$ $\frac{1}{80})$ vs β_L, solid line is the function $(1 \beta_L)$.

and observe that this value remains valid for $\Gamma\beta_L$ 0.2. More generally, for $\Gamma\beta_L$ 0.2 and for an arbitrary value of β_L we find $e\approx(1 \beta_L)$ or $\varepsilon\approx2(1 \beta_L)\Phi_0 k_B T/I_0 R$.

This concludes our description of the signal and noise theory for the dc SQUID. The results dictate the range of parameters required to achieve near optimal performance. Low-T_c SQUIDs are usually optimized under the constraint $I_0 R^2$ constant (Tesche and Clarke, 1977), in order to keep β_c fixed. For a given value of L we then have $I_0 \propto \beta_L$ and $R \propto I_0^{-1/2}$, so that $I_0 R \propto \beta_L^{1/2}$. Since $e \propto (1 \beta_L)$ we find $\varepsilon \propto (1 \beta_L)\beta_L^{1/2}$, which has a minimum at β_L 1. The situation for high-T_c SQUIDs is more complicated. One way to optimize the SQUID is to vary the junction width on a given substrate. We then have $I_0 R$ constant, and the dependence of ε on β_L can be scaled from the plots in Fig. 5; in this case, the minimum is at $\beta_L \approx 0.5$. However, we again emphasize that this value is at the lower end of the validity of our equations. A discussion of smaller values would be purely academic, since one generally couples the SQUID to a pickup loop with an inductance that is much higher than the SQUID inductance L (Sec. VI). Thus, to reduce the inductance mismatch, there is a strong incentive to make L as high as possible. As a result, values of β_L 1 would require values of Γ that are outside the validity of our equations. An alternative philosophy is to fix the junction area and to vary the critical current, for example, by changing the barrier thickness. Since for many high-T_c junctions $I_0 R \propto j_c^{1/2}$ (Sec. IV), this approach leads to $I_0 R^2$ constant as for low-T_c SQUIDs, so that β_L 1 is the optimum value.

Figure 5 shows clearly that the reduced noise energy increases rapidly once $\Gamma\beta_L$ L/L_{th} is raised above about 0.15; for T 77 K, this constraint implies L 50 pH. However, one can use higher inductances either by adding a damping resistor across the SQUID loop (Enpuku, Sueoka *et al.*, 1985; Enpuku, Muta *et al.*, 1985; Enpuku, *et al.*, 1993; Enpuku, 1993) and/or a third Josephson junction (Enpuku, 1993; Enpuku *et al.*, 1994; Enpuku, Doi *et al.*, 1995). It is shown that with these additional circuit elements one may increase the SQUID inductance up to 500 pH. Recently, high-T_c SQUIDs

with integrated damping resistors have been studied by Kang *et al.* (1997), and three-junction SQUIDs have been investigated by Schultze, Ijsselsteijn *et al.* (1997). In both cases, an enhanced voltage modulation was observed. However, for the three-junction SQUID, large modulation was obtained only over a few periods and the authors concluded that this SQUID has no advantage over the conventional SQUID.

Finally, the fact that ε scales as $1/I_0 R$ emphasizes the need to develop junction technologies with the largest possible value of $I_0 R$. In particular, one would like a type of junction in which I_0 and R can be varied independently. For example, for L 40 pH, the requirement β_L 1 leads to I_0 25 μA; increasing $I_0 R$ solely by increasing I_0 will not lead to significantly enhanced performance.

D. rf SQUID: Overview

The rf SQUID (Mercereau, 1970; Nisenoff, 1970; Zimmerman *et al.*, 1970) consists of a single Josephson junction integrated into a superconducting loop that is inductively coupled to the inductance L_T of an LC-resonant (tank) circuit [inset Fig. 6(b)]. The tank circuit is driven by an rf current, and the resultant rf voltage is periodic in the flux applied to the SQUID with period Φ_0. Detailed reviews have been written by many authors (for example, Jackel and Buhrman, 1975; Ehnholm, 1977; Likharev and Ulrich, 1978; Likharev, 1986; Ryhänen *et al.*, 1989; Clarke, 1996).

The total flux Φ_T in the SQUID is related to the applied flux Φ by

$$\Phi_T \quad \Phi \quad L I_0 \sin(2\pi\Phi_T/\Phi_0). \qquad (2.10)$$

We see immediately that Eq. (2.10) can exhibit two distinct kinds of behavior [Fig. 6(a)]. For β_L $2\pi L I_0/\Phi_0$ 1, the slope $d\Phi_T/d\Phi$ $[1 \beta_L \cos(2\pi\Phi_T/\Phi_0)]^{-1}$ is everywhere positive and the Φ_T vs Φ curve is nonhysteretic. On the other hand, for β_L 1, there are regions in which $d\Phi_T/d\Phi$ is positive, negative, or divergent so that the Φ_T vs Φ curve becomes hysteretic. Radio frequency superconducting quantum interference devices have been operated in both modes. In the hysteretic mode the SQUID makes transitions between quantum states and dissipates energy at a rate that is periodic in Φ. This periodic dissipation in turn modulates the quality factor Q of the tank circuit, so that when it is driven on resonance with a current of constant amplitude the rf voltage is periodic in Φ. In the case β_L 1, the nondissipative mode, the SQUID behaves as a parametric inductance, modulating the effective inductance and hence the resonant frequency of the tank circuit as the flux is varied. Thus when the tank circuit is driven at constant frequency, the variations in its resonant frequency cause the rf voltage to be periodic in Φ.

Historically, it appears that most low-T_c rf SQUIDs were operated in the hysteretic mode, although as we shall see, there are advantages to the nonhysteretic mode. However, the theory of noise in the nondissipa-
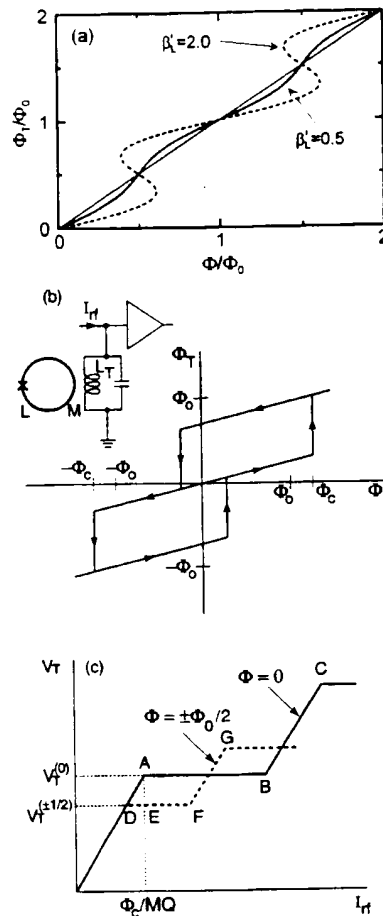
FIG. 6. The rf SQUID: (a) Normalized total flux Φ_T/Φ_0 vs normalized applied flux Φ/Φ_0 for β_L 0.5,2. (b) Total flux Φ_T vs applied flux Φ for rf SQUID with LI_0/Φ_0 $\frac{5}{4}$, showing transitions between quantum states in absence of thermal noise as Φ is increased and subsequently decreased. Inset shows rf SQUID inductively coupled to the inductor of a resonant circuit. (c) Peak rf voltage V_T across tank circuit vs peak rf current I_{rf} in absence of thermal noise for Φ 0 (solid line) and Φ $\Phi_0/2$ (dashed line).

tive regime was worked out in the late 1970s, just as dc SQUIDs began largely to replace rf SQUIDs. As a result, the importance of the nonhysteretic rf SQUID was not widely exploited experimentally. The advent of 77 K operation has changed this situation dramatically, largely due to the systematic experimental effort of the group at Jülich and the very recent theoretical work of Chesca (1998). In the following two sections we briefly outline the theory of the dissipative and nondissipative rf SQUIDs.

E. rf SQUID: Hysteretic mode

For the case β_I 1, the unstable nature of the Φ_T vs Φ curve in Fig. 6(a) causes the SQUID to make transi-

tions between stable quantum states as Φ is changed [Fig. 6(b)]. For example, when Φ is increased from 0, there is a transition from the k 0 flux state to the k 1 state at a critical flux (neglecting fluctuations) Φ_c LI_0. In rf operation, a current $I_{rf} \sin \omega_{rf} t$ is applied to the resonant circuit. The peak voltage V_T across the resonant circuit increases linearly with I_{rf} until, for Φ 0, I_{rf} Φ_c/MQ, at which value

$$V_T^{(0)} \omega_{rf} L_T \Phi_c / M, \tag{2.11}$$

where M $\kappa(L L_T)^{1/2}$. At this point [A in Fig. 6(c)] the SQUID makes a transition to the k 1 or 1 state. As the SQUID traverses the hysteresis loop, energy ΔE is extracted from the tank circuit. Because of this loss, the peak flux on the next half cycle is less than Φ_c, and no transition occurs. The tank circuit takes many cycles to recover sufficient energy to induce a further transition, which may be into either the k 1 or 1 states. If we now increase I_{rf}, transitions are induced at the same values of I_T and V_T but, because energy is supplied at a higher rate, the stored energy builds up more rapidly after each energy loss ΔE, and transitions occur more frequently. At B, a transition is induced on each positive and negative rf peak, and a further increase in I_{rf} produces the "riser" BC. At C, transitions from the k 1 states to the k 2 states occur, and a second step begins. A plot of the peak values $V_T^{(0)}$ vs I_{rf} produces the "steps and risers" shown in Fig. 6(c).

If we now apply an external flux $\Phi_0/2$, the hysteresis loops in Fig. 6(b) are shifted by this amount, and one finds

$$V_T^{(1/2)} \omega_{rf} L_T (\Phi_c \Phi_0/2)/M. \tag{2.12}$$

As I_{rf} is increased, this voltage remains constant until the point F, at which the SQUID traverses the hysteresis loop corresponding to the k 0 k 1 transitions once per rf cycle. A further increase in I_{rf} produces the riser FG; at G, corresponding to a peak rf flux (Φ_c $\Phi_0/2$), transitions k 0 k 1 begin. Thus an applied flux other than $n\Phi_0$ (n is an integer) causes the step AB to split as shown in Fig. 6(c).

The model outlined above enables us to calculate the transfer function at values of I_{rf} that maintain the SQUID biased on a step: the change in V_T as we increase Φ from 0 to $\Phi_0/2$ is $V_T^{(0)}$ $V_T^{(1/2)}$ $\omega_{rf} L_T \Phi_0/2M$, so that for small changes in flux in the range 0 Φ $\Phi_0/2$ we find V_Φ $\omega_{rf} L_T/M$. At first sight, this result seems to imply that V_Φ can be increased indefinitely by reducing κ. This is not the case, since one must ensure that the point F in Fig. 6(c) lies to the right of E, that is, DF must exceed DE. To calculate DF we note that the power dissipated in the SQUID is zero at D and approximately $I_0\Phi_0\omega_{rf}/2\pi$ at F, since the energy dissipated per rf cycle is approximately $I_0\Phi_0$ for a device with $LI_0 \approx \Phi_0$. Thus, taking account of the fact that the rf currents and voltages are peak values, we find ($I_{rf}^{(F)}$ $I_{rf}^{(D)}$) $V_T^{(1/2)}/2 \approx I_0\Phi_0\omega_{rf}/2\pi$. Furthermore, we can easily see that $I_{rf}^{(E)}$ $I_{rf}^{(D)}$ $\Phi_0/2MQ$. Assuming LI_0

$\approx \Phi_0$ and using Eq. (2.12), we can write the requirement that DF exceeds DE in the form

$$\kappa^2 Q \quad \pi/4. \tag{2.13}$$

Taking $\kappa \approx 1/Q^{1/2}$, we find that the expression for V_Φ becomes

$$V_\Phi \approx \omega_{rf}(QL_T/L)^{1/2} \approx \omega_{rf}(L_T/L)^{1/2}/\kappa. \tag{2.14}$$

We note that V_Φ scales with ω_{rf} and as $L^{-1/2}$.

A detailed theory has been developed for noise in the hysteretic rf SQUID operating at liquid helium temperatures (Kurkijärvi, 1972, 1973; Jackel and Buhrman, 1975; Giffard et al., 1976; Ehnholm, 1977; Hollenhorst and Giffard, 1980; Ryhänen et al., 1989). Although in a noise-free model the steps are flat, thermal noise causes them to tilt to a slope η. In addition, thermal noise induces voltage noise on the step arising from fluctuations in the value of flux at which transitions between flux states occur. The corresponding intrinsic flux noise of the SQUID is (Kurkijärvi, 1973)

$$S_\Phi^i(f) \approx \frac{(LI_0)^2}{\omega_{rf}} \left(\frac{2\pi k_B T}{I_0 \Phi_0} \right)^{4/3}. \tag{2.15}$$

In the case of helium-cooled rf SQUIDs in which the tank circuit voltage is detected with a room-temperature amplifier, there is a second, extrinsic contribution to the flux noise. This arises in part because the noise temperature of the rf amplifier is above the bath temperature and in part because a fraction of the coaxial line connecting the tank circuit to the amplifier is at room temperature. We can represent these two contributions by an effective noise temperature T_a^{eff}, enabling us to write the noise energy due to intrinsic and extrinsic noise sources as (Jackel and Buhrman, 1975; Giffard et al., 1976)

$$\varepsilon \approx \frac{LI_0^2}{2\omega_{rf}} \left(\frac{2\pi k_B T}{I_0 \Phi_0} \right)^{4/3} \quad \frac{2\pi \eta k_B T_a^{eff}}{\omega_{rf}}. \tag{2.16}$$

Equation (2.16) makes two important points. First, ε scales as $1/\omega_{rf}$, up to a limiting value R/L. Second, for low-T_c SQUIDs, the extrinsic noise energy generally dominates the intrinsic noise: if we take the representative values T 4 K, Γ 0.1, η 0.2, β_L 2π and T_a^{eff} 100 K, we find that the extrinsic noise energy is about 20 times the intrinsic value. Thus, although we should be wary of extrapolating these results to 77 K where, to our knowledge, there are no simulations or calculations, the overall noise energy of the hysteretic rf SQUID should not increase very much as we raise the temperature from 4 K to 77 K. This result is in contrast to the dc SQUID, which for properly designed circuitry is limited largely by intrinsic noise at 4.2 K, so that the overall noise energy will increase significantly as the temperature is raised to 77 K.

F. rf SQUID: Nonhysteretic mode

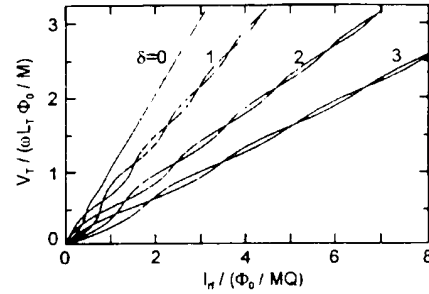To give an approximate account of the operation of the nonhysteretic rf SQUID we follow the description of

FIG. 7. Tank circuit voltage V_T vs rf drive current I_T for four values of the tuning parameter δ $[2(\omega_{rf} \quad \omega_0)/\omega_0]Q$ and for Φ $0, \Phi_0/2$. Curves plotted for $\kappa^2 Q \beta_L$ $\pi/2$ (Hansma, 1973).

Hansma (1973), which is valid in the limits β_L 1, where the total magnetic flux threading the SQUID is nearly equal to the applied flux, and ω_{rf} $I_0 R/\Phi_0$. More general treatments are given, for example, by Jackel and Buhrman (1975), Erne et al. (1976), Danilov et al. (1980), Likharev (1986), and Ryhänen et al. (1989).

In the presence of a static flux Φ and rf flux $\Phi_{rf} \sin \omega_{rf} t$, the current in the SQUID loop is

$$I \quad I_0 \sin[(2\pi/\Phi_0)(\Phi \quad \Phi_{rf} \sin \omega_{rf} t)]$$

$$(2\pi LI_0 \quad \Phi_0). \tag{2.17}$$

The oscillating component of this current induces a current I_i $(M/Z)dI/dt$ into the tank circuit, where Z R_T $i[\omega_{rf}(L_T \quad M^2/L) \quad 1/\omega_{rf}C_T]$ is its impedance; the inductance of the tank circuit is modified by the contribution M^2/L from the SQUID. If we assume that the rf frequency is near resonance and that Q is reasonably large, we can neglect all frequency components other than the fundamental. Expanding the right-hand side of Eq. (2.17) in terms of the Bessel function J_1, we find the induced current

$$I_i \quad \frac{2\kappa^2 QLI_0}{M(1 \quad \delta^2)^{1/2}} \cos\left(\frac{2\pi\Phi}{\Phi_0} \right) J_1\left(\frac{2\pi\Phi_{rf}}{\Phi_0} \right) \sin(\omega_{rf} t \quad \theta). \tag{2.18}$$

Here, δ $2[(\omega_{rf} \quad \omega_0)/\omega_0]Q$ is the normalized difference between the rf frequency and the tank-circuit resonant frequency ω_0, and θ $\tan^{-1} \delta$ $\pi/2$.

The rf flux applied to the SQUID is $MI_T \sin \omega_{rf} t$, where I_T is the amplitude of the total current in the inductor which, in addition to the induced current given by Eq. (2.18), also contains a component of amplitude $QI_{rf}/(1 \quad \delta^2)^{1/2}$ produced by the external rf current. From Eq. (2.18) we see that the total current leads the induced current by a phase angle θ. The amplitudes of the total and external rf currents are related by

$$I_{rf} \quad \frac{(1 \quad \delta^2)^{1/2}}{Q} \left\{ \left[\frac{2\kappa^2 QLI_0}{(1 \quad \delta^2)^{1/2}M} \cos\left(\frac{2\pi\Phi}{\Phi_0} \right) \right. \right.$$

$$\left. \left. J_1\left(\frac{2\pi MI_T}{\Phi_0} \right) \quad I_T \cos\theta \right]^2 \quad I_T^2 \sin^2\theta \right\}^{1/2}. \tag{2.19}$$

Figure 7 shows plots of V_T vs I_{rf} for Φ 0 and $\Phi_0/2$ for

four values of the tuning parameter δ. We see that the response is insensitive to the flux in the SQUID for δ 0; thus the tank circuit for the nonhysteretic SQUID is operated off resonance. For a given value of δ, the response shows a series of oscillations as I_{rf} is increased, arising from the oscillations of the Bessel function. The maximum peak-to-peak modulation of V_T at fixed I_{rf} is of the order of $2\kappa^2 Q L I_0(\omega_{rf} L_T/M)$, so that

$$V_\Phi \approx (2/\pi)\kappa^2 Q\beta_L \omega_{rf}L_T/M$$

$$\approx (2/\pi)(\kappa^2 Q\beta_L)\omega_{rf}(L_T/L)^{1/2}/\kappa. \qquad (2.20)$$

This transfer function exceeds that of the hysteretic rf SQUID [Eq. (2.14)] by a factor of order $\kappa^2 Q\beta_L$, which can be made larger than unity for the nonhysteretic case by choosing $\kappa^2 Q$ 1.

The intrinsic noise energy of low-T_c, nonhysteretic, rf SQUIDs has been calculated by several authors, and is approximately $3k_B T/(\beta_L)^2\omega_c$ (Likharev, 1986), where the drive frequency is set equal to ω_c R/L, the cutoff frequency of the SQUID. A noise energy as low as $20\hbar$ has been achieved by Kuzmin *et al.* (1985).

As a preamble to the discussion of nonhysteretic high-T_c SQUIDs, we note that Falco and Parker (1975) successfully observed flux modulation in an rf SQUID at 2 K with a supercurrent as low as 50 nA. The corresponding value of the noise parameter Γ $2\pi k_B T/I_0\Phi_0$ was about 1.7; at this high value, they were unable to observe any trace of supercurrent in an isolated junction. Thus it is evident that one can expect to operate an rf SQUID with substantially higher values of Γ than is the case for the dc SQUID (see Sec. II.C). Although this important fact has been known experimentally for many years, only very recently has the work of Chesca (1998) provided a quantitative explanation. In contrast to previous theories of the rf SQUID in which one regards thermal noise as a perturbation on a noise-free system, Chesca solves the Smoluchowski equation for the situation in which thermal fluctuations dominate. Thus both the signal produced by the SQUID and the noise are found in a unified calculation that yields analytical results. For the case $\beta_L \le 1$ and ω_{rf} R/L, Chesca finds

$$\varepsilon \approx 3\Gamma^2\left(1 \quad \frac{T_k}{T}\frac{1}{\kappa^2 Q}\frac{R/L}{\omega_{rf}}\right)\frac{\exp(L/L_{th})}{L/L_{th}}\frac{k_B T L_{th}}{R}. \qquad (2.21)$$

Here, L_{th} $(\Phi_0/2\pi)^2/k_B T$ and T_k is the effective noise temperature of the tank circuit, including any contribution from the preamplifier. If one assumes L/L_{th} $\beta_L\Gamma$ 1 and that $\kappa^2 Q$ can be made sufficiently large that $(T_k/T)(R/\omega_{rf}L)/\kappa^2 Q$ 1, Eq. (2.21) can be written in the alternative forms

$$\varepsilon \approx 3k_B T/(\beta_L)^2(R/L) \qquad (2.22a)$$

$$\approx 3k_B T\Phi_0/2\pi\beta_L I_0 R. \qquad (2.22b)$$

Interestingly, Eq. (2.22a) is identical to the result found perturbatively for the rf SQUID for low values of Γ. The value for ε in Eq. (2.22b) is equal to $3/4\pi\beta_L(1 \quad \beta_L)$ times that for the dc SQUID in the limit $\Gamma\beta_L$ 0.2.
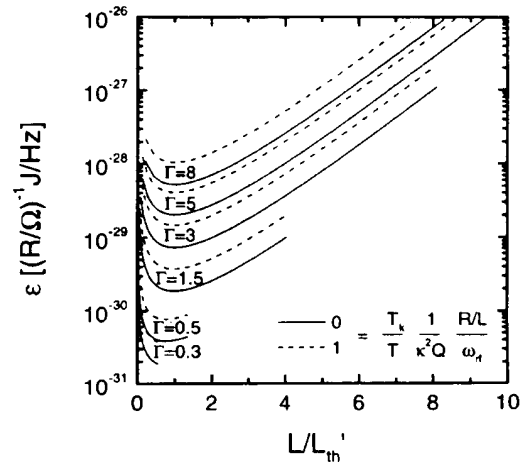

FIG. 8. ε vs L/L_{th} for nonhysteretic rf SQUID at 77 K (Chesca, 1998).

Equation (2.21) is plotted in Fig. 8 for the two cases $(T_K/T)(1/\kappa^2 Q)(R/\omega L_{rf})$ 0 and 1, and for six values of Γ. One concludes from these plots that the optimal values are (Chesca, 1998)

$$\beta_L \quad 1 \quad \text{if } \Gamma\le 1, \qquad (2.23a)$$

$$\beta_L \quad 1/\Gamma \quad \text{if } \Gamma\ge 1. \qquad (2.23b)$$

We note that for the lowest value of Γ plotted, 0.3, the curve is cut off at $\beta_L\Gamma$ L/L_{th} 0.55, at which value the noise energy approaches 10^{-31} JHz^{-1} for R 1 Ω. For the case $\Gamma\ge 1$, the noise energy is higher and the optimal SQUID inductance is approximately $L_{th}\approx 100$ pH at 77 K. Again, this value is about two times higher than for the dc SQUID at 77 K. One consequence of this result is that one can expect to use rf SQUIDs with an area about two times higher than dc SQUIDs.

III. THIN FILMS: FABRICATION AND 1/f NOISE

In this section, we discuss issues related to the fabrication of epitaxial thin films for high-T_c SQUIDs and flux-coupling input circuits. Key requirements for the films are high crystalline quality and either elimination or efficient pinning of flux vortices, in order to achieve both good electrical transport properties and low levels of 1/f noise. For some structures, for example, multiturn flux transformers (Sec. VI.C) or multiloop magnetometers (Sec. VI.D), one requires two or more superconducting films separated by an insulating layer. Hence all layers must be of high crystalline quality. To achieve heteroepitaxial growth of such multilayer structures, it is essential that the various films have comparable lattice constants and thermal-expansion coefficients, that they are chemically compatible at the relatively high deposition temperatures, typically 700 800 °C, and that they can be deposited with sufficiently smooth surfaces to al-

low subsequent layers to grow with high structural and electrical integrity and without electrical shorts between them. Moreover, one must be able to pattern the films without introducing a significant deterioration in their properties.

A. Materials

Despite the wide variety of high-T_c compounds, work on SQUIDs has been mostly restricted to YBCO. This is largely because only YBCO films with their c axis normal to the substrate ("c-axis films") have been shown to have sufficiently strong flux pinning at 77 K to ensure both high critical-current densities in the ab plane— several 10^6 A cm^{-2}—and acceptably low levels of $1/f$ noise. Furthermore, because of the worldwide effort that has been focused on YBCO, its physical properties and growth mechanisms are well understood and high-quality thin films can be grown *in situ* by a variety of deposition techniques on a number of substrate materials. As a result, it seems unlikely that YBCO will be supplanted as the superconductor of choice, although NdBa$_2$Cu$_3$O$_{7-x}$ is worthy of consideration because of its superior stability.

There are a number of substrates suitable for growing high-quality YBCO films (for a discussion see Scheel *et al.*, 1991; Somekh and Barber, 1992, Braginski, 1993, 1996; Wellstood *et al.*, 1994; Phillips, 1996). To fabricate low-noise SQUIDs, one usually chooses substrates that are closely lattice matched to YBCO and have comparable thermal expansion coefficients, notably (100) SrTiO$_3$, LaAlO$_3$, and NdGaO$_3$, thus allowing the YBCO films to grow with a high degree of crystallographic perfection. In addition, MgO substrates are frequently used since they are relatively inexpensive and allow one to grow YBCO films with acceptable electrical properties.

B. Thin-film deposition

Among the many different techniques used to deposit YBCO *in situ* (for reviews, see Somekh and Barber, 1992; Phillips, 1993; Wellstood *et al.*, 1994), those most commonly applied to SQUID fabrication are pulsed laser deposition and sputtering, although a few groups have successfully used coevaporation. All of these techniques produce smooth YBCO films with excellent electrical properties. Typical YBCO films, 100–300 nm thick, grown on lattice-matched substrates such as SrTiO$_3$ (STO), have critical current densities at 77 K of $(2-5) \times 10^6$ A cm^{-2}. The surface roughness of the best films, usually determined by atomic force microscopy, is below 10 nm and the half-width of the x-ray rocking curve (005 line) is typically 0.1–0.3°. The critical-current densities in such films are two orders of magnitude higher than in high-quality YBCO single crystals, indicating that a high density of defects, which provide strong pinning sites, must be present.

To deposit Ag or Au layers for contact pads, one can use thermal evaporation, electron-beam evaporation,

sputtering, or ion-beam-assisted deposition, usually with the substrate at room temperature. To achieve a low metal/YBCO contact resistance ($\leq 10^{-6}\ \Omega\ cm^2$) one should deposit the metal layer either *in situ* or after only a brief exposure to air (Russek *et al.*, 1994, 1996). If the YBCO film is stored in air for any length of time or exposed to photoresist, low-energy Ar-ion-beam cleaning of the surface and/or postannealing in oxygen at 400–500 °C is necessary to achieve a low contact resistance.

C. Patterning

Patterning techniques that are well established in semiconductor and low-T_c superconductor technology are not necessarily applicable to YBCO thin films. One immediate problem is that contact of YBCO with water or water-soluble chemicals degrades the superconducting properties. Second, the use of dry-etching methods in a vacuum can lead to a significant heating of the sample and thus to oxygen loss at the edges. Given these limitations, however, a number of techniques have been used successfully to pattern YBCO films down to submicrometer dimensions without degrading their properties; for reviews, see Braginski (1993) and Wellstood *et al.* (1994).

Conventional photomasking followed by dry etching is the most widely used technique for patterning SQUID devices based on YBCO films or multilayers. However, sometimes special masks are used, especially for step-edge and ramp-edge junctions (Sec. IV) and for patterning submicrometer structures (Barth *et al.*, 1993; Schneider *et al.*, 1993; van der Harg *et al.*, 1995). Among dry-etching methods, the most commonly used is Ar-ion beam milling. To minimize damage to the YBCO, one restricts the beam energies to between 350 and 500 eV, the latter being the most common value, and the beam current density to below 1 mA/cm^2. To reduce heating of the film, it is also important to cool the sample, either with water or particularly for submicrometer dimensions, preferably with liquid nitrogen. Alff *et al.* (1992) and Schneidewind *et al.* (1995) reported systematic studies of the effects of ion-beam voltage, current density and sample cooling on the dependence of the critical-current density on the linewidth of YBCO films. Generally, for high-quality, c-axis YBCO films, the edges are damaged over a length of much less than 1 μm provided the sample is water-cooled and the beam energy and current density do not exceed the values given above.

D. Multilayer processing

All multilayer structures for multiturn flux transformers, integrated magnetometers and multiloop SQUIDs involve a YBCO/insulator/YBCO trilayer. Of course, additional layers might be advantageous, for example, a superconducting ground plane. However, although integrated magnetometers with up to 15 epitaxial layers have been made (Lee *et al.*, 1991), it is difficult to maintain high crystalline quality throughout so many layers

as is required for low levels of $1/f$ noise. Thus we confine our attention to trilayers. The insulator is generally one of the substrate materials listed in Sec. III.A; the most widely used is $SrTiO_3$. As an alternative to the various insulating materials, $PrBa_2Cu_3O_{7-x}$ (PBCO) has been used in the fabrication of multiturn flux transformers (Keene *et al.*, 1993; Keene, Goodyear *et al.*, 1994).

An important issue related to the integrity of the insulator is the oxygen content of the lower YBCO film. To ensure proper oxygenation of a single YBCO film it is usually sufficient to vent the deposition chamber with 0.5–1 atm. O_2 and to cool the sample from the deposition temperature to room temperature in about 30 min. The use of this process after the deposition of a high-quality insulating layer on a YBCO film can result in a reduced transition temperature because the insulator inhibits the necessary oxygen diffusion (Humphreys *et al.*, 1991; Ludwig, Koelle *et al.*, 1995; Ockenfuß *et al.*, 1995). To reoxygenate the lower YBCO film fully, one can either increase the annealing time considerably (Ludwig, Koelle *et al.*, 1995) or perform the annealing in an oxygen plasma rather than in molecular O_2 (Yanamoto *et al.*, 1991; Humphreys *et al.*, 1991; Ockenfuß *et al.*, 1995).

In actual multilayer devices, the need to pattern each layer separately, usually with photolithographic processing, greatly complicates matters. Multiturn flux transformers, integrated magnetometers and multiloop SQUIDs all contain the basic elements of a superconducting interconnect technology: *crossovers* and *vias*. In these structures, one has to produce edges over which subsequent layers grow with high crystalline quality; in particular, the growth of YBCO over edges steeper than 45° results in grain boundaries and thus leads to a reduction in critical current (Jia *et al.*, 1991).

Various processes suitable for multilayer magnetometers were developed and have been extensively reviewed (Wellstood *et al.*, 1994; Braginski, 1996). In the process that was used to fabricate most of the low-noise multilayer magnetometers discussed in Secs. VI.C and VI.D, each layer is patterned by Ar-ion beam etching. To obtain the gently sloped edges on the lower layers, essential for the epitaxial growth of subsequent layers, one usually bakes the photoresist after development, yielding to a significant rounding of the edges (David *et al.*, 1994). The subsequent Ar-ion milling at an angle of typically 45–60° produces edges on the patterned film with ramp angles below 20°. Another key issue is the protection of the surface of the lower YBCO film, since photoresist attacks the YBCO surface thus degrading the growth of subsequent layers (Ludwig, Koelle *et al.*, 1995). To protect the YBCO, one commonly deposits an *in situ* $SrTiO_3$ layer, 20–50 nm thick, over the lower YBCO film, thus preventing its contact with photoresist (Missert *et al.*, 1993). Alternatively, a brief Ar-ion beam etch has been used to clean the surfaces before the deposition of the next layer (Keene, Goodyear *et al.*, 1994; Shen *et al.*, 1995). With these techniques, critical-current densities up to 3×10^6 A cm^{-2} for crossovers (Ludwig, Koelle *et al.*, 1995) and above 1×10^6 A cm^{-2}

for vias (DiIorio, Yoshizumi, Yang, Maung, Zhang, and Power, 1993; Keene *et al.*, 1993) have been achieved in separate test structures at 77 K.

E. 1/f Noise in YBCO films

As we pointed out earlier, the main requirement for YBCO films used in SQUIDs is a low level of the magnetic flux noise generated by the thermally activated motion of flux vortices. To optimize the deposition process one should, in principle, measure the flux noise of each YBCO film. To our knowledge, such noise measurements have been performed only by the Berkeley group. As a simpler alternative, many groups measure the critical-current density j_c as an estimate of the flux pinning, but one must be careful in drawing conclusions about flux noise from measurements of j_c. These measurements are generally performed with strong driving forces applied by currents, and thus provide information on the pinning of the vortex lattice, that is, on the pinning *forces*. In contrast, flux noise measurements, performed in weak magnetic fields (below 10^{-4} T) reflect the dynamics of weakly interacting vortices in the superconducting sample and probe their pinning *energies*. For example, Ludwig, Koelle *et al.* (1995) found that *ex situ* YBCO/SrTiO$_3$/YBCO trilayers exhibited relatively high levels of flux noise despite the fact that similar test structures had high critical-current densities in both YBCO films. Furthermore, flux noise measurements on YBCO single crystals irradiated with protons or heavy ions indicated that protons proved to be more effective in reducing the flux noise while both produced comparable increases in critical-current density (Shaw *et al.*, 1996).

To study the flux noise in high-T_c thin films and single crystals, Ferrari *et al.* (1988, 1989, 1994) measured their fluctuating magnetization using a low-T_c, thin film SQUID in the shape of a 1-mm-square washer. The SQUID was operated in a flux-locked loop with a typical flux noise of $2\mu\Phi_0$ Hz$^{1/2}$ at 1 Hz. The experiment was designed to allow tight inductive coupling between the SQUID, maintained at or near 4.2 K, and the sample, the temperature of which could be raised to above T_c. Subsequently, the availability of high-T_c SQUIDs with low levels of $1/f$ noise allowed the measurement of the flux noise of high-T_c films in liquid nitrogen more straightforwardly by mounting them directly on such a SQUID, patterned into a 0.5-mm-square washer, with a typical flux noise of $15\mu\Phi_0$ Hz$^{1/2}$ at 1 Hz (Koelle *et al.*, 1993; Ludwig, Koelle *et al.*, 1995, Ludwig, Dantsker, Koelle, Kleiner, Miklich, and Clarke, 1995).

In their early work, Ferrari *et al.* (1988) found that the $1/f$ flux noise of a YBCO thin film decreases dramatically as the crystalline quality of the sample improves. For example, for a polycrystalline YBCO film they found a flux-noise power of $3 \times 10^{-4} \Phi_0^2$/Hz at 1 Hz and 40 K, whereas values below $10^{-10} \Phi_0^2$/Hz at 1 Hz and 77 K were obtained for high-quality epitaxial YBCO films (Shaw *et al.*, 1996). On the other hand, for YBCO single crystals, the flux-noise power at 1 Hz was more than a factor of 50 higher than the latter value, even after the

incorporation of artificial defects by proton irradiation (Shaw *et al.*, 1996). This result indicates that there must be a high density of effective, intrinsic pinning sites in high-quality (that is, magnetically quiet) epitaxial YBCO films, but unfortunately, little is known about their nature. Thus a film with low $1/f$ flux noise may have pinning sites with high activation energies or short hopping distances, or a combination of both; alternatively, the sample may simply contain fewer vortices. Studies in which various parameters controlling sample quality are systematically and independently varied are very much needed to shed light on these issues. Furthermore, the microstructural quality of patterned film edges may also be crucial, although its impact on $1/f$ noise has yet to be clarified.

The general tendencies observed for single YBCO films also apply to multilayers. Since the upper YBCO film in patterned YBCO/insulator/YBCO trilayers tends to be of poorer quality than a single YBCO film, its flux noise is generally higher. Nevertheless, Ludwig, Koelle *et al.* (1995) and Ludwig, Dantsker, Koelle, Kleiner, Miklich, and Clarke (1995) have demonstrated that a careful optimization of the multilayer fabrication process allows one to fabricate *ex situ* trilayers with low levels of $1/f$ flux noise.

Last, the level of $1/f$ noise in a given film generally increases strongly with the ambient magnetic field in which it is cooled unless its linewidth is made sufficiently narrow. These issues are deferred to Sec. IX.

IV. HIGH-T_C JOSEPHSON JUNCTIONS

The requirements for a successful junction technology include a nonhysteretic I-V characteristic, with properties close to the predictions of the RSJ model, a high $I_0 R$ product, controllable and reproducible parameters (I_0, R, C), high yield, high stability under room-temperature storage and thermal cycling, and low $1/f$ noise. These requirements are very well satisfied in low-T_c junctions by the Nb-Al$_2$O$_3$-Nb trilayer technology (Gurvitch *et al.*, 1983). Unfortunately, a comparable high-T_c technology does not yet exist, for the following reasons: First, in contrast to Nb, high-T_c materials require epitaxial growth, imposing severe constraints on the choice of materials and processing techniques. Second, again in contrast to Nb, the superconducting coherence length ξ is both short and highly anisotropic, typically 2 nm in the *ab*-plane and 0.2 nm in the *c*-axis direction. As a result, the properties of high-T_c materials are highly susceptible to structural and chemical changes on atomic length scales; in particular, the superconducting order parameter can be strongly suppressed at a superconductor-insulator interface, in turn reducing the $I_0 R$ product substantially (Deutscher and Müller, 1987). Thus the superconducting electrodes need to have perfect crystallinity, and a well-defined interface has to be achieved within a single unit cell. Third, the barrier materials are generally oxides close to a metal-insulator transition with a complex crystal structure and a strong sensitivity to defects on an atomic length scale.

As a result, transport across the barrier is highly dependent on microstructural imperfections in the barrier and at its interface with the electrodes. Thus a well-defined barrier with high crystalline quality and homogeneity is required.

In the following we review those types of high-T_c junctions which have been most successfully used in SQUIDs. We divide them into two classes (Gross *et al.*, 1997): junctions with intrinsic interfaces and junctions with extrinsic interfaces. We do not discuss a third class, junctions without interfaces (weakened structures), since these have not been used widely in practical devices.

A. Junctions with intrinsic interfaces

The strong anisotropy of high-T_c superconductors with respect to both crystal structure and transport properties provides the basis for new types of weak links exploiting *intrinsic* interfaces and/or barriers. This new class of Josephson junctions, which has no analog in low-T_c superconductors, involves either the weak coupling in the *ab* plane between two superconducting grains with different orientations, the so-called grain-boundary junctions (GBJ's), or the intrinsic Josephson effect in the *c*-axis direction. While the feasibility of intrinsic Josephson junctions (Kleiner *et al.*, 1992; Kleiner and Müller, 1994) for SQUIDs has not been demonstrated, GBJ's were the basis of the first dc SQUIDs fabricated from polycrystalline thin films of YBCO (Koch *et al.*, 1987). Although grain sizes and orientations were uncontrolled, these devices provided the first evidence that high-T_c grain boundaries act as junctions and may be used in SQUIDs. Shortly after, junctions and dc SQUIDs were fabricated across single grain boundaries in epitaxial YBCO films on polycrystalline STO substrates (Tsuei *et al.*, 1989; Hagerhorst *et al.*, 1989); Subsequently, engineered GBJ's were developed, and the most important types are bicrystal, and step-edge GBJ's [Fig. 9(a) and (b)]. Although important historically, biepitaxial GBJ's (Char *et al.*, 1991) are no longer used for SQUIDs, because of their small $I_c R$ products. For reviews on GBJ's see Gross (1994) and Gross *et al.* (1995).

1. Bicrystal grain-boundary junctions

The key to both the development of a useful high-T_c Josephson junction technology and the understanding of transport across grain boundaries was provided by the pioneering work at IBM, Yorktown Heights on bicrystal GBJ's (Chaudhari *et al.*, 1988; Dimos *et al.*, 1988; Mannhart *et al.*, 1988, Dimos *et al.*, 1990; Gross *et al.*, 1990a, 1990b, 1991). These junctions are fabricated by the epitaxial growth of a high-T_c thin film on a bicrystal substrate with a predetermined misorientation angle θ [Fig. 9(a)]. In contrast to other GBJ fabrication techniques, this method can be used to obtain arbitrary misorientation angles and geometries, such as [001] and [100] tilt or [100] twist grain boundaries (Dimos *et al.*, 1990), enabling a systematic study of transport across high-T_c grain boundaries. Their straightforward fabrication
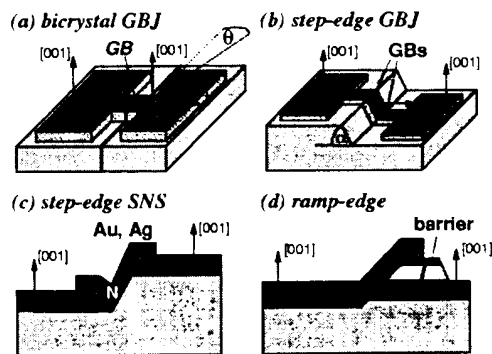
FIG. 9. Types of high-T_c Josephson junctions.

makes these junctions the most reliable and successful currently available, both for SQUIDs and more generally for any application which does not require many junctions at arbitrary positions on the substrate. Any substrate which supports the epitaxial growth of high-T_c films is suitable, including $SrTiO_3$ (Dimos *et al.*, 1988), YSZ (Ivanov *et al.*, 1991), Si (Chen *et al.*, 1991), $NdGaO_3$ (Quincey, 1994), MgO (Beck *et al.*, 1995), $LaAlO_3$ (Chen *et al.*, 1996), and r plane Al_2O_3 (Sapphire) (Vale *et al.*, 1997). Most work on bicrystal junctions has involved YBCO, but other superconductors have been investigated, including $Bi_2Sr_2CaCu_2O_8$ (Mayer *et al.*, 1993), $Tl_2Ba_2CaCu_2O_8$ (Kawasaki *et al.*, 1993), $HgBa_2CaCu_2O_6$ (Gupta *et al.*, 1994), and $La_{1.85}Sr_{0.15}CuO_4$ (Beck *et al.*, 1996).

Bicrystal junctions generally exhibit characteristics reasonably close to the RSJ model, provided θ exceeds a critical value, about $10°$ for YBCO (Dimos *et al.*, 1990; Gross, 1994). The critical-current density j_c for YBCO junctions decreases exponentially with increasing θ (Gross and Mayer, 1991; Ivanov *et al.*, 1991) This behavior is explained in part by the faceting of the grain boundary combined with d-wave pairing symmetry (Hilgenkamp *et al.*, 1996); however, it seems likely that a further contribution arises from an increase of the barrier thickness with increasing θ. For fixed θ, the critical-current density can be changed by more than one order of magnitude by appropriate annealing in oxygen (Kawasaki *et al.*, 1992), implying that the barrier thickness or height depends on oxygen content. Most SQUIDs have been made on $24°$ or $36°$ bicrystals, but recently $30°$ bicrystals have also become commercially available. At 77 K the $I_0R(j_c\rho_n)$ product of such junctions made from c-axis YBCO films on $24°$ bicrystals is typically 0.1-0.3 mV; comparable values have recently been reported on $30°$ bicrystals (Minotani, Kawakami *et al.*, 1997; Beyer *et al.*, 1998). The corresponding critical-current density j_c is of the order of 10^4 A/cm^2 at 77 K and the temperature-independent specific resistance-area product ρ_n is about 10^{-8} Ω cm^2. Although standard deviations in I_0R of around 20% have been reported for junctions on a given bicrystal (Miklich *et al.*, 1993), the

parameters often vary much more widely because of variations in the quality of the bicrystal substrate (McDaniel *et al.*, 1997).

2. Step-edge grain-boundary junctions

The step-edge GBJ, which is also widely used, is based on the fact that an epitaxially grown, c-axis YBCO film changes its orientation at a steep step in the substrate or deposited dielectric [Fig. 9(b)]. This technique, initially realized by Simon *et al.* (1991), was subsequently refined by several groups (Herrmann *et al.*, 1991; Sun, Gallagher, Callegari *et al.*, 1993; Herrmann *et al.*, 1995; Pettiette-Hall *et al.*, 1995; Yi *et al.*, 1996). Common substrate materials are $SrTiO_3$ and $LaAlO_3$. For large step angles (α $70°$) the two grain boundaries grow with different orientations, causing the lower junction to have a much lower critical-current density than the upper junction (Jia *et al.*, 1992). Thus, at least for currents not too far above I_0, the junction properties are determined solely by the lower grain boundary.

The substrate steps are aligned along major cubic axes of the substrate, and are usually patterned by standard lithography and Ar-ion milling so that their location can be chosen at will. This advantage over the bicrystal technique enables one to fabricate more complex circuits. Even for SQUIDs which require only one or two junctions, this flexibility in layout can be important, for example, for minimizing parasitic inductances.

It has been proposed that the grain boundaries formed at step edges behave as junctions because of their defect structure (Herrmann *et al.*, 1995), since $90°$ grain boundaries in planar films do not exhibit such behavior. Thus the properties of step-edge junctions depend strongly on the microstructure of the milled step and on the film-growth conditions, leading to greater spreads in parameters than for bicrystal junctions. The use of carbonlike diamond masks and very low milling rates improve the definition of the steps, and hence their reproducibility (Sun, Gallagher, Callegari *et al.*, 1993; Yi *et al.*, 1996). Dillmann *et al.* (1996) have used annealing processes to trim the parameters of their junctions. For a detailed review of the fabrication of step-edge junctions for SQUIDs, see Braginski (1996).

B. Junctions with extrinsic interfaces

This class of junctions involves a thin, deposited interlayer of insulating or normal material between two superconducting electrodes. Hence extrinsic interfaces are involved, and the control of their properties requires an advanced fabrication technology, usually involving the heteroepitaxial growth of high-T_c and interlayer materials. The transport and noise properties of these junctions are even less well understood than those for GBJ's. Although low-noise SQUIDs based on these junctions have been reported, the absence of reproducible fabrication processes has hindered their widespread use. Figures 9(c) and (d) illustrate two possible configurations:

the step-edge junction with a non-epitaxial noble-metal interlayer, and the ramp-edge junction with an epitaxially grown interlayer.

1. Step-edge SNS junctions

DiIorio *et al.* (1991), DiIorio, Yoshizumi, Yang, Maung, Zang, and Power (1993), and DiIorio *et al.* (1995) introduced the SNS junction illustrated in Fig. 9(c), and systematic studies of their properties have been carried out at NIST (Ono *et al.*, 1991, 1993; Rosenthal *et al.*, 1993; Reintsema *et al.*, 1995) and FZ Jülich (Grove *et al.*, 1996; Bode *et al.*, 1996). In principle, fabrication is simple: one cuts a steep step in the substrate, 50–100 nm high, using photolithography and Ar-ion milling, and deposits a high-T_c film directionally, so that the film does not grow on the step. Without breaking vacuum, one fills the gap by directional deposition of a Au or Ag layer, which makes contact to the a-b planes of the high-T_c films.

Very high I_0R products, up to 1 mV at 77 K, and high normal resistance, above 10 Ω for 4–8 μm widths, have been reported. However, the transport and noise properties are still unsettled issues. The I-V characteristics often exhibit excess current. The normal resistance appears to be determined by the boundary resistance at the SN interfaces, and various models for the transport have been suggested, for example, SINIS (Reintsema *et al.*, 1995) or ScNS (Bode *et al.*, 1996); *c* denotes point contacts at the SN interfaces. The major problem appears to be the lack of control of the interface properties which determine R and are most likely responsible for the large spreads in I_0. These difficulties have hindered the widespread application of this type of junction to SQUIDs.

2. Ramp-edge Josephson junctions

These junctions require the fabrication of an epitaxial trilayer with two superconducting electrodes separated by a thin barrier layer. Current transport is along the a-b planes of the c-axis oriented electrode films, taking advantage of the larger coherence length along this direction. One fabricates a ramp-edge junction [Fig. 9(d)] by first depositing a YBCO film and covering it with a thick, insulating film. Next, one patterns a ramp with a shallow angle (typically 10° to 20°) using ion milling or anisotropic wet etching, and finally deposits the barrier material and top electrode *in situ*. The top electrode effectively shields the magnetic-field component normal to the film surface. Hence ramp-edge junctions may offer an important advantage over planar GBJ's for operation in magnetically unshielded environments. Furthermore, ramp-edge junctions may be more robust against aging and thermal cycling compared to GBJ's since the barrier/interfaces are not directly exposed to the environment.

Gao *et al.* (1990, 1992) pioneered ramp-edge junctions with YBCO electrodes and a $PrBa_2Cu_3O_7$ barrier. Subsequently, many other barrier materials such as ruthenates or doped YBCO have been investigated (see, for example, Gross *et al.*, 1997 and references therein). The key requirement is a lower electrode with a smooth ramp edge of excellent crystalline quality to support the growth of a thin, homogenous barrier. Thus any damage caused by milling the ramp or by its exposure to air has to be healed prior to deposition of the barrier. The need to pattern the ramp with an *ex situ* process can be avoided by patterning the lower electrode with a micro-shadow mask (Strikovskiy and Engelhardt, 1996).

Ramp-edge junctions with Ca- or Co-doped YBCO barriers show behavior close to proximity effect coupling (Kleinsasser and Delin, 1995; Delin and Kleinsasser, 1996), with low or negligible interface resistance, but with junction resistances too low for SQUID applications. On the other hand, for ruthenate or PBCO barriers the junction resistance is dominated by interface resistance rather than the intrinsic barrier resistivity, and transport is explained via tunneling through localized states in the barrier or interface, which has a high defect density (Dömel *et al.*, 1995; Satoh *et al.*, 1995; Schilling, 1997). Using bromine etching to form the ramp, Faley, Poppe, Jia *et al.* (1995) fabricated a quasiplanar junction with PBC(Ga)O barriers that exhibited negligible interface resistance; hence the resistance of these junctions scaled with barrier thickness. Junctions 5 μm wide and with barriers 20 nm thick exhibited I-V characteristics close to that of the RSJ model with $I_0R \sim 200\,\mu$V and $R \sim 1\,\Omega$ at 77 K, making them good candidates for SQUIDs.

C. Discussion of high-T_c junctions

For most high-T_c junctions, one finds the following common properties:

(i)   They are internally shunted and at 77 K produce I-V characteristics reasonably close to the RSJ model. The most common deviation from the RSJ characteristic is an excess supercurrent. Possible candidates for its origin are a nonsinusoidal current-phase relation (Ilichev *et al.*, 1998), superconducting shorts through the barrier, or Andreev reflection at the barrier interfaces (Alff *et al.*, 1998). At lower temperatures, that is, higher critical currents, the characteristics may become hysteretic, implying that even at 77 K β_c may not be too much below unity.

(ii) The critical-current density generally increases linearly with decreasing temperature, while, at least for GBJ's, the resistance-area product ρ_n is nearly independent of temperature (Gross, 1994).

(iii) The I_0R ($j_c\rho_n$) products are smaller than the gap voltage, typically below 300 μV at 77 K. Values of $j_c\rho_n$ up to about 1 mV at 77 K have been reported for some junctions, but always seem to be associated with large excess currents. Grain-boundary junctions (Gross, Chaudhari, Kawasaki *et al.*, 1990; Russek *et al.*, 1990; Hermann *et al.*, 1991) and junctions with artificial barriers show a scaling $j_c\rho_n \propto (j_c)^p$, where $p \approx 0.5$ over seven orders of
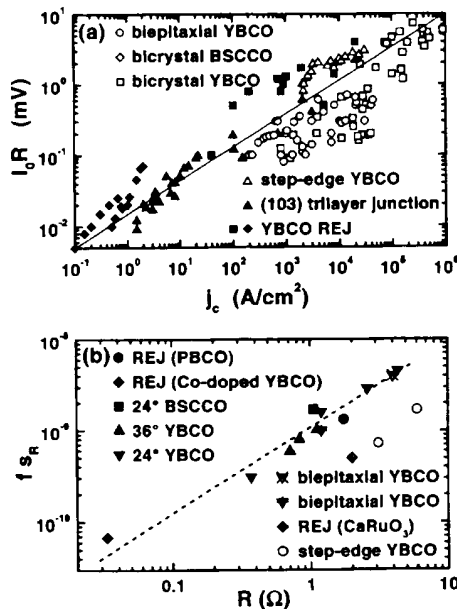
FIG. 10. Scaling behavior of various high-T_c Josephson junctions: (a) I_0R product vs critical current-density j_c at 4.2 K; a line with slope 0.5 has been drawn through the data (Gross *et al.*, 1997); (b) fs_R vs normal resistance R; the dashed line is a guide to the eye (Marx and Gross, 1997).

magnitude in j_c, as shown in Fig. 10(a) (Gross, 1994; Gross *et al.*, 1997, and references therein).

(iv) Most junctions exhibit large levels of low-frequency $1/f$ noise arising from fluctuations of the critical current and the junction resistance (Kawasaki *et al.*, 1992; Miklich *et al.*, 1992; Marx, Fath *et al.*, 1995). The normalized spectral densities $s_I \equiv S_{I_0}/I_0^2$ and $s_R \equiv S_R/R^2$ for critical-current and resistance fluctuations are temperature independent and proportional to the junction resistance (Marx and Gross, 1997), as shown in Fig. 10(b). Defining $S_{I_0}/I_0^2 \equiv a^2/f$ one finds typically $a^2 \approx 10^{-8} R/\Omega$, which is about three orders of magnitude larger than for Nb junctions with shunt resistances of a few ohms (Foglietti *et al.*, 1986; Savo *et al.*, 1987). Furthermore, the relation $(s_I/s_R)^{1/2} \approx 1/(1-p)$ observed for GBJ's (Gross, 1994, Marx, Fath *et al.*, 1995) strongly suggests that the low-frequency noise and scaling of I_0R have the same microscopic origin.

The universal scaling of $j_c\rho_n$, s_I, and s_R is an important feature of high-T_c junctions because it may be the key to understanding their transport and noise properties and offers the possibility of adjusting important junction parameters for optimum SQUID performance. The fact that both GBJ's and junctions with artificial barriers have the same scaling suggests a common transport mechanism governed by thin interface layers. However, the details of this mechanism are still controversial.

Since proximity effect coupling cannot explain the observed transport properties for the vast majority of junctions, several models have been proposed that include the effects of a boundary resistance between S and N layers (SNIS, SINIS) (Kupriyanov and Likharev, 1990) or of constrictions (ScNS, SNcNS) (Aminov *et al.*, 1996; Golubov and Kupriyanov, 1996). On the other hand, for grain-boundary junctions it has been proposed that resonant tunneling of quasiparticles via localized states in an insulating barrier acts as an intrinsic normal shunt (Gross and Mayer, 1991). This model, known as the intrinsically shunted junction model, naturally explains the low I_0R product in terms of an intrinsic shunt due to a high density of localized states. The universal scaling of I_0R with j_c suggests that the density of localized states is about the same in all junctions. The trapping and release of charge carriers in localized states lead to fluctuations in the local barrier height which cause I_0 and R to fluctuate with antiphase correlation (Marx, Alff *et al.*, 1995), thus explaining the high level of $1/f$ noise in junctions with a high density of localized states. The same scaling of I_0R with j_c is predicted by a channel model (Moeckly *et al.*, 1993) in which the Josephson current in GBJ's is restricted to narrow superconducting filaments in a weakly conducting medium. However, this model cannot account for the observed phase correlation of I_0 and R fluctuations, since the superconductive and resistive channels are spatially separated.

The scaling behavior described above has important consequences for the optimization of SQUIDs. At T = 77 K, j_c is typically 10^4 A/cm^2 for 24° YBCO grain boundaries, corresponding to $I_0R \approx 100 \mu$V. Hence for junctions of width w and thickness $d \approx 200$ nm critical currents of about 20μA$(w/\mu$m$)$ are typical. Thus to achieve $\beta_L \approx 1$ for an inductance $L \approx 50$ pH one requires $w \sim 1 \mu$m, close to the minimum linewidth achievable with photolithography. Increasing I_0R with oxygen annealing or reducing the misorientation angle may not be very useful unless one can achieve submicron patterning without significant damage to the edges of the film. We note that for $p \approx 0.5$, an increase in I_0R by a factor of 3 requires an increase in j_c by an order of magnitude. An alternative to submicron patterning may be thinning of the film in the junction region; however, this approach is not applicable to all types of junctions, may be detrimental to the junction properties, and can contribute a significant kinetic inductance.

Clearly, it is highly desirable to have a lower critical-current density for the same I_0R product, but this would require reduction of the density of localized states which, in turn, would result in an increase of ρ_n for fixed j_c. Even if this goal could be achieved, since $\beta_c \propto j_c \rho_n^2 C_s$ increases with ρ_n^2 for fixed j_c and C_s, such junctions may become hysteretic at 77 K. In contrast, a change in $I_0R \propto j_c^{1/2}$ causes $j_c\rho_n^2$ to be constant and leaves β_c approximately unchanged (neglecting the change in the specific capacitance C_s with effective barrier thickness). Although junctions with high values of ρ_n are occasionally reported in the context of high performance
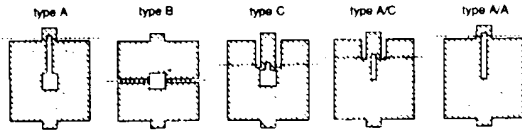
FIG. 11. Five configurations of planar dc SQUID fabricated at Berkeley. Dashed lines indicate the bicrystal boundary along which the junctions are formed. Outer dimension is typically 500 500 μm^2.

dc SQUIDs (Lee *et al.*, 1995; Glyantsev *et al.*, 1996), detailed data on their transport characteristics have not been presented.

For the optimization of SQUIDs a detailed knowledge of the junction transport mechanism may not be necessary. However, control of the junction parameters is essential, and may only be possible if the transport mechanism is understood. This, in turn, may require the fabrication of junctions with well-defined interfaces and barriers. Such a technology is not yet at hand: spreads in I_0 and R are typically 20% on chip and usually much higher from chip to chip. Although these large spreads may be unacceptable for applications which require many junctions, they have not prevented the fabrication of low noise SQUIDs. Nevertheless, to allow a more systematic study of SQUID performance and to clarify discrepancies between experimental results and theory for high-T_c dc SQUIDs (Sec. V.C), a more reproducible technology is highly desirable. To complicate the issue, integrated SQUID magnetometers may require the incorporation of high-quality junctions into low-noise thin-film multilayers. The successful integration of a controllable, high-yield junction technology with a low-noise multilayer technology has still to be demonstrated.

V. dc SQUIDs

A. Practical devices

Early high-T_c dc SQUIDs were generally fabricated in the geometry of a square washer, following the most widely used configuration of low-T_c SQUIDs (Ketchen, 1981; Jaycox and Ketchen, 1981). Figure 11 shows a selection made at Berkeley. In these devices, it was implicitly assumed that ultimately the SQUIDs would be inductively coupled to flux transformers with planar, spiral input coils as is common practice with low-T_c magnetometers. Subsequently, various other magnetometer configurations emerged, in addition to the multiturn flux transformer (Sec. VI.C), and for reasons of minimizing the 1/f noise in ambient magnetic fields (Sec. IX.A) it is desirable to make SQUIDs with rather narrow linewidths. Thus a wide variety of SQUID configurations have been investigated, and we do not attempt to review them here; rather we shall describe some of the more useful types in Sec. VI in the context of magnetometers. Most SQUIDs are still made with either bicrystal or
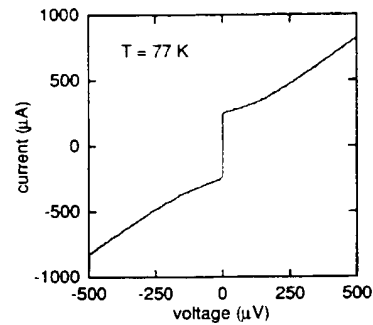

FIG. 12. *I-V* characteristics of bicrystal, type *B* dc SQUID at 77 K; L 41 pH, I_0 120 μA, R 1.28 Ω.

step-edge grain-boundary junctions, and these have yielded the highest performance to date.

With few exceptions, the SQUID is immersed directly in liquid nitrogen. To attenuate external magnetic-field fluctuations, above all the ubiquitous 50 or 60 Hz fields and their harmonics, one may surround either the dewar with a mu-metal shield or the SQUID with a high-T_c shield. Mu-metal shields have the advantage of reducing both the ambient static field and time-varying field substantially, while high-T_c shields generally offer greater attenuation of time-varying fields, but do not reduce the ambient field if they are cooled in it. Thus a combination of both types of shields is often desirable in evaluating the intrinsic noise of SQUIDs. It is also imperative to exclude radio-frequency interference, most commonly by running the measurement in a screened room.

Figure 12 shows a representative *I-V* characteristic for a YBCO SQUID, grown on a STO bicrystal, operated at 77 K. In Fig. 13 we have plotted the voltage V across the SQUID vs the applied flux Φ for a series of bias currents. As the current is increased, the amplitude of the oscillations increases smoothly to a maximum and then decreases. The SQUID is normally operated at the bias current that gives the maximum value of V_Φ.

B. Readout schemes

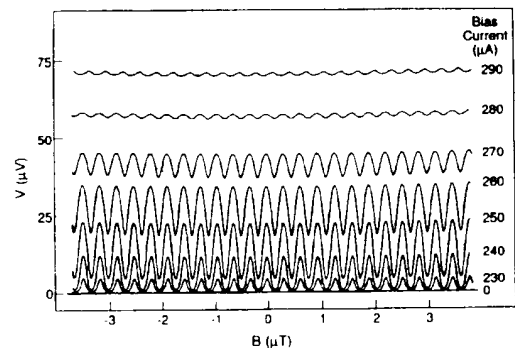In virtually all applications, SQUIDs are operated in a flux-locked loop in which the voltage change across the

FIG. 13. *V* vs Φ for dc SQUID of Fig. 12 for seven values of bias current.
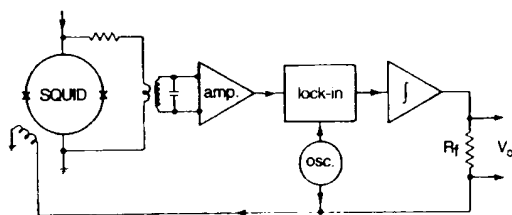
FIG. 14. Flux-locked loop for dc SQUID.

SQUID induced by an applied flux is amplified and fed back as an opposing flux. This feedback circuit linearizes the response of the SQUID, provides a straightforward means of measuring the intrinsic noise of the SQUID, and enables one to track inputs equivalent to many flux quanta. The input stage of the electronic circuitry is designed to add negligibly to the intrinsic noise of the SQUID. Drung (1996) has given a detailed review of a variety of schemes; here we review briefly the two most commonly used.

1. Flux modulation

In the widely used flux modulation scheme (Forgacs and Warnick, 1967), shown in Fig. 14, one applies a sinusoidal or square-wave flux modulation to the SQUID with a peak-to-peak amplitude of $\Phi_0/2$ and a frequency f_m of typically 100 kHz. The resulting alternating voltage across the SQUID is coupled to a room-temperature preamplifier via either a cooled LC series-resonant circuit (Clarke *et al.*, 1976) or a cooled transformer (Ketchen *et al.*, 1978). The voltage gain of either coupling circuit is usually chosen to transform the dynamic resistance of the SQUID at its operating point to the value required to optimize the noise temperature of the preamplifier. Since this noise temperature is typically a few kelvin, the preamplifier contributes negligible noise to a device operating at 77 K. After amplification, the signal is lock-in detected at the frequency f_m. If the quasistatic flux is $n\Phi_0$ (n is an integer), the V-Φ curve is symmetric about this local minimum and the voltage contains components only at the frequency $2f_m$. Thus the output of the lock-in detector is zero. On the other hand, if the flux is shifted away slightly from the local minimum, the voltage across the SQUID contains a component at frequency f_m and there will be an output from the lock-in detector. After integration (cf. Fig. 14), this signal is fed back as a current through a feedback resistor R_f to a coil inductively coupled to the SQUID; usually the same coil is used for both flux modulation and feedback. The flux fed back opposes the applied flux to keep the flux in the SQUID constant; the voltage developed across R_f is proportional to the applied flux. One can measure the intrinsic flux noise of the SQUID by connecting the output voltage to a spectrum analyzer in the absence of any input signal.

Ideally, the bandwidth for an optimized flux-locked loop extends to one half the modulation frequency. For unshielded applications in which the SQUID is exposed

to the magnetic noise of the environment, a more important figure of merit is often the slew rate, that is, the maximum rate of change of flux that the system is able to track without losing lock. For an ideal single-pole integrator, the slew rate is $2\pi f_1\Phi_0/4$, where f_1 is the frequency at which the open-loop gain of the feedback loop falls to unity (Drung, 1996). A considerable improvement in the slew rate at low frequencies can be achieved by means of a two-pole integrator (Giffard, 1980; Wellstood *et al.*, 1984). Using a high-T_c SQUID with a 500-kHz flux modulation and a single-pole filter, Dantsker *et al.* (1994) obtained a slew rate of $10^5\ \Phi_0\ \text{s}^{-1}$ at 900 Hz. Recently, Koch *et al.* (1996) described a flux-locked loop with a modulation frequency of 16 MHz, using a resonant matching circuit with a superconducting, thin-film transformer to match the SQUID to the amplifier. The system had a closed-loop bandwidth exceeding 2.5 MHz and a slew rate greater than $10^6\ \Phi_0\ \text{s}^{-1}$ at frequencies up to 1 MHz. Subsequently, Penny *et al.* (1997) used a transmission-line transformer feeding a matched transmission line to couple the SQUID to the amplifier. With a low-T_c SQUID they achieved a bandwidth of 5 MHz, a slew rate of $1.9\ 10^6\ \Phi_0\ \text{s}^{-1}$ at 200 Hz, and a flux noise of $5.5\mu\Phi_0\ \text{Hz}^{1/2}$. The performance with high-T_c SQUIDs has not yet been reported.

A further issue of particular importance when the outputs of SQUIDs are subtracted to form electronic gradiometers (Sec. VIII.A) is the linearity of the flux-locked loop. To investigate the nonlinearity, Nichols *et al.* (1996) measured the harmonic generation using a high-T_c SQUID with 130-kHz flux modulation and a single-pole integrator. For input signals at frequencies up to 248 Hz and rms amplitudes up to 20 Φ_0, 2nd, 3rd, and 4th harmonics were each 115 dB below the fundamental. At higher frequencies the harmonic content began to increase because of the reduction in the open-loop gain. It was also shown that the amplitudes of the even harmonics depended critically on the amplitude of the 130-kHz flux modulation, becoming zero when the peak-to-peak value was precisely $\Phi_0/2$.

The slew rate and linearity that have been achieved are likely to be adequate for most applications in which the magnetometer is static. For situations in which the magnetometer is moved in the earth's magnetic field—for example, in towed systems—the demands are substantially higher, and the performance may or may not be adequate.

As will be shown later (Sec. V.D), fluctuations in the critical current and resistance of the junctions are a major source of $1/f$ noise in dc SQUIDs. Fortunately, their contributions can be greatly reduced by a number of schemes (Koch *et al.*, 1983; Foglietti *et al.*, 1986; Dössel *et al.*, 1991), which have been successfully applied to high-T_c SQUIDs (Koch *et al.*, 1992; Miklich *et al.*, 1993; Grundler, Eckart *et al.*, 1993). At the operating point of SQUIDs, the critical-current noise dominates the resistance noise and contributes $1/f$ noise in two ways. Fluctuations at frequencies f_m that are in phase at the two junctions give rise to a voltage noise across the SQUID that is eliminated by flux modulation at frequency f_m.
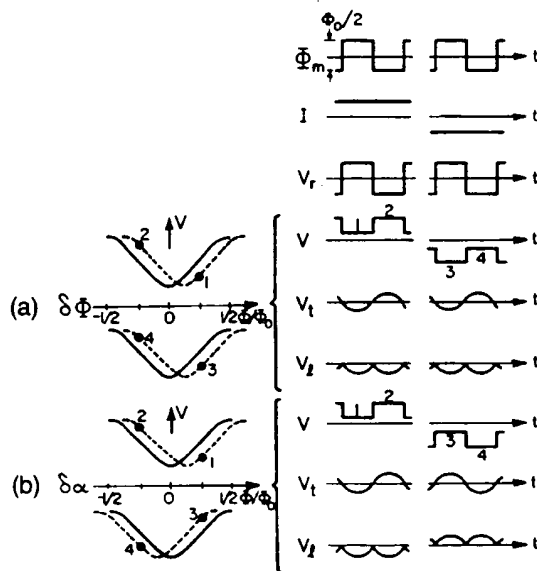
FIG. 15. Principle of bias-reversal scheme to reduce $1/f$ noise due to out-of-phase critical-current fluctuations. The left-hand column shows the V-Φ curves (solid lines), and the dashed lines indicate the effect of (a) an external flux change $\delta\Phi$ and (b) a flux change $\delta\alpha$ generated by out-of-phase critical-current fluctuations. The right-hand column shows, as a function of time t, (top to bottom) the flux modulation Φ_m, the bias current I, and the reference voltage V_r used to lock-in detect the signal from the SQUID; the next three rows are for an external flux change $\delta\Phi$, and show the voltage V across the SQUID, the voltage V_t across the secondary of the tuned transformer and the output V_l of the lock-in detector; the last three rows show the same voltages for an out-of-phase critical-current fluctuation (Koch *et al.*, 1983).

Fluctuations that are out-of-phase at the two junctions are equivalent to a flux noise that is not reduced by this scheme. Instead, one makes use of the fact that the apparent shift of the V-Φ characteristic along the flux axis changes polarity if one reverses the polarity of the bias current whereas the flux due to an input signal (or "flux noise") does not.

As an example of one of the bias-reversal schemes, we briefly describe that developed by Koch *et al.* (1983); the principle is illustrated in Fig. 15 and its implementation in Fig. 16. The SQUID is flux-modulated with a 100-kHz square wave of peak-to-peak amplitude Φ_m $\Phi_0/2$. Synchronously with the modulation, the bias current I through the SQUID is reversed, for example, at a frequency f_r 3.125 kHz. The resistance bridge shown in Fig. 16 minimizes the 3.125 kHz switching transients across the transformer. Simultaneously with the bias reversal, a flux $\Phi_0/2$ is applied to the SQUID. In Figs. 15(a) and (b) we see that the bias reversal changes the sign of the voltage across the SQUID while the flux shift ensures that the sign of the flux-to-voltage transfer function remains the same. The transformer coupling the SQUID to the preamplifier is often tuned at the modulation frequency with a Q of about 3, so that any 100-kHz signals at the secondary are approximately sinusoidal.

We assume that the SQUID is operated in the usual flux-locked loop, with the output from the lock-in detector integrated and fed back to the SQUID (Fig. 16). Thus the 100-kHz signal across the SQUID consists of just the error signal. Suppose now that we apply a small external flux $\delta\Phi$ to the SQUID at a frequency well below f_r. The V-Φ curves are shifted as in Figs. 15(a), and the 100-kHz flux modulation switches the SQUID between the points 1 and 2 for positive bias and 3 and 4 for negative bias. As a function of time, the voltage V across
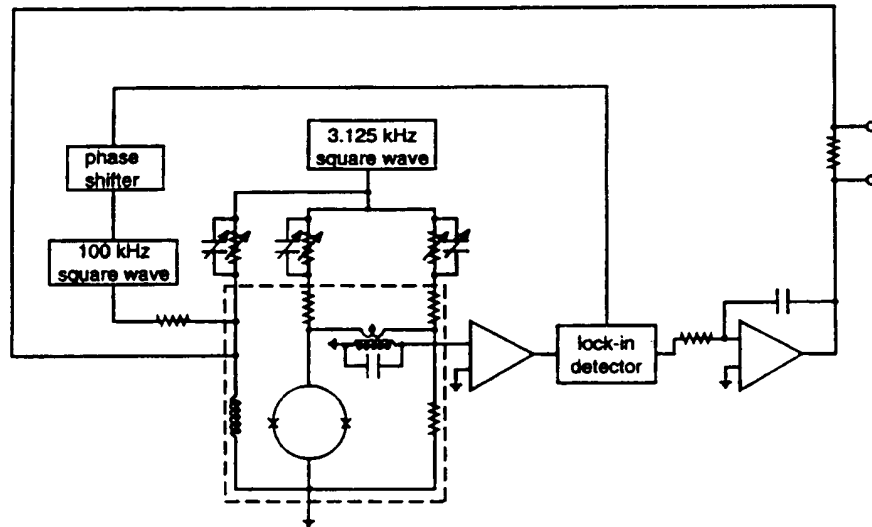

FIG. 16. Schematic for flux-locked loop with bias current reversal. Cryogenic components are enclosed in the dashed box (Koch *et al.*, 1983).
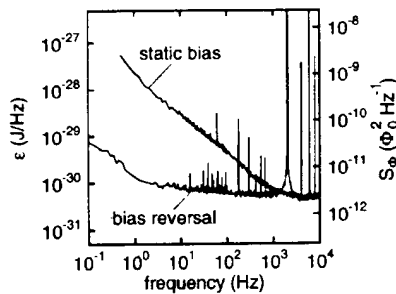
FIG. 17. Spectral density of flux noise of representative high-T_c dc SQUID with flux modulation and bias current reversal.

the SQUID is as shown in Fig. 15, and the signal across the tuned transformer V_t is at the fundamental frequency. When this signal is mixed with the reference voltage V_r, the output from the lock-in detector V_f will consist of a series of negative-going peaks for both polarities of the bias current. The average of this output produces a negative signal proportional to $\delta\Phi$ which is then used to cancel the flux applied to the SQUID. Thus, in the presence of bias reversal and flux shift, the SQUID responds to an applied flux in the usual way.

We consider now the effects of $1/f$ noise on the critical currents. The in-phase mode is eliminated by the 100-kHz flux modulation. Suppose, instead, we have an out-of-phase critical-current fluctuation at a frequency below f_r. Because the flux generated by this fluctuation *changes sign* when the bias current is reversed, the V-Φ curves are displaced in opposite directions. As a result, the voltage across the SQUID undergoes a phase change of π when the bias current is reversed, as shown in Fig. 15. Consequently, the voltage at the output of the lock-in due to the out-of-phase critical-current fluctuation changes sign each time the bias current is reversed, and the time average of the signal over periods much longer than $1/f_r$ is zero. Thus the $1/f$ noise due to both in-phase and out-of-phase critical-current fluctuations is eliminated by this scheme.

Figure 17 shows the spectral density of the flux noise of a representative SQUID operated with flux modulation and with and without bias reversal. Without bias reversal, $1/f$ noise is evident for frequencies below about 2 kHz. The application of bias reversal reduces the level of $1/f$ noise dramatically, by two orders of magnitude at 1 Hz, demonstrating that the $1/f$ noise indeed arose from critical-current fluctuations.

2. Direct readout

A "direct readout" scheme eliminates the need for a coupling network between the SQUID and the amplifier, and enables one to use particularly simple electronics for the flux-locked loop (Drung, 1994). In addition, it allows one to achieve bandwidths around 10 MHz relatively easily (Drung, 1996). The output of the current-biased SQUID is connected directly to one terminal of a low-noise, bipolar amplifier; an offset bias voltage is applied to the other terminal. After amplification, the sig-

nal is integrated and fed back via a resistor to a coil coupled to the SQUID. Since the preamplifier noise, typically 1 nV Hz$^{1/2}$, usually dominates the SQUID noise, typically 0.1 nV Hz$^{1/2}$ for low-T_c SQUIDs, it must be reduced to a tolerable level by increasing the transfer function. In the additional positive feedback (APF) scheme (Drung *et al.*, 1990) this increase is achieved by shunting the SQUID with an inductor L_a, with a mutual inductance M_a to the SQUID, in series with a resistor R_a. When the SQUID is current biased, a change in the voltage across the SQUID due to an applied flux generates a current through the shunting network and a flux in the SQUID. Thus the V-Φ characteristic becomes asymmetric, and the transfer function is enhanced by a factor $1/(1 \quad G_a)$ in the region of positive feedback; here

$$G_a \quad [M_a \quad (\partial\Phi/\partial I)_V]V_\Phi/R_a \tag{5.1}$$

is the APF gain. The maximum slew rate is concomitantly reduced by a factor $(1 \quad G_a)$. Thus for wideband systems G_a should be just high enough to make the effect of the preamplifier voltage noise negligible compared to the intrinsic SQUID noise. For a low-T_c SQUID and an effective APF gain of 0.57, a flux-locked bandwidth of 5 MHz was achieved with a white flux noise of $3.4\,\mu\Phi_0$ Hz$^{1/2}$, corresponding to a magnetic-field noise of 1.6 fT Hz$^{1/2}$. We note that the flux-to-current transfer coefficient of the SQUID at constant voltage, $(\partial\Phi/\partial I)_V$, is not affected by APF, so that the current noise of the amplifier may become important. If necessary, this contribution can be reduced by bias-current feedback (Drung and Koch, 1993).

To remove $1/f$ noise due to critical-current fluctuations, as for the flux-modulation scheme, one has to reverse the bias current (Drung, 1995); at the same time the bias voltage is reversed and a flux shift is applied to maintain the same polarity of the flux-to-voltage transfer function. Using this bias-reversal scheme, Ludwig *et al.* (1997) recently reported a modified, directly coupled flux-locked loop for high-T_c SQUIDs. Using a preamplifier with a voltage noise of 0.44 nV Hz$^{1/2}$, their high-T_c SQUIDs could be operated without APF with a total rms white noise typically 20% higher than the intrinsic rms noise of the SQUID. For an optimum bias-reversal frequency of around 100 kHz, it was demonstrated that $1/f$ noise due to critical-current fluctuations can effectively be suppressed without increasing the white-noise level (Drung, Ludwig *et al.*, 1996; Drung, Dantsker *et al.*, 1996; Ludwig *et al.*, 1997). In addition, a maximum bandwidth of about 1 MHz and slew rates close to $10^6\Phi_0$/s were achieved.

C. White noise

In this section, we present data on the white noise measured by a number of groups: Biomagnetic Technologies, Inc., San Diego, Philips, Hamburg, University

of California, Berkeley, University of Hamburg, University of Jena, and University of Twente. The SQUIDs were made with either grain-boundary or SNS ramp-edge junctions. For the devices discussed, L ranged from 10 to 210 pH, and I_0R from below 10 μV to 300 μV. Although values of I_0R of 300 μV or larger are desirable, such values are generally achieved only with high values of I_0. As a result, β_L is often well above unity, and sometimes greater than 10. Values of β_L near unity were achieved only for I_0R below 200 μV. One should bear in mind that some of the estimated values of L are likely to be rather uncertain, because of both the intricate geometries of the SQUID loops and the possible contributions of kinetic inductance (Töpfer and Uhlmann, 1994; Hildebrandt and Uhlmann, 1995).

We now compare the measured results with the theoretical predictions of Sec. II.C. Similar comparisons have been made by Enpuku (1993) and Enpuku *et al.* (1993, 1994), Enpuku, Tokita *et al.* (1995), Keene *et al.* (1995), and Koch (1997). To give an overview of SQUIDs with widely varying parameters, it is convenient to present the results in terms of the dimensionless parameters Γ, β_L, and $\Gamma\beta_L$. For the devices discussed, Γ ranges from 0.004 to 1.8, β_L ranges from 0.12 to 65, and $\Gamma\beta_L$ ranges from 0.03 to 0.65; the majority of the values of $\Gamma\beta_L$ are above the desirable upper limit of 0.15.

We begin by recalling from Sec. II that $v_\phi(\beta_L;\Gamma\beta_L)$ $f(\beta_L)g(\Gamma\beta_L)$, with $f(\beta_L)$ $v_\phi(\beta_L;\Gamma\beta_L \frac{1}{80})$ and $g(\Gamma\beta_L)$ $v_\phi(\beta_L;\Gamma\beta_L)/v_\phi(\beta_L;\Gamma\beta_L \frac{1}{80})$. We find $v_\phi(\beta_L,\Gamma\beta_L)$ and $v_\phi(\beta_L,\Gamma\beta_L \frac{1}{80})$ from Eqs. (2.5) and (2.6), respectively. In Figs. 18(a) and (b) the solid lines represent $v_\phi/f(\beta_L)$ and $v_\phi/g(\Gamma\beta_L)$ as functions of $\Gamma\beta_L$ and β_L, respectively. To compare the data with these predictions, we calculate the experimental values of $v_\phi/f(\beta_L)$ and $v_\phi/g(\Gamma\beta_L)$ and plot them as points in Fig. 18. The data show the same general trend as the theory, but relatively few points fall on or close to the predicted curves. Most of the data lie well below the predicted values, sometimes by as much as an order of magnitude. We note that not all authors measure the maximum value of V_ϕ directly, for example, by applying a small oscillating flux, but instead measure the peak-to-peak voltage swing ΔV and assume $V_\phi \approx \pi\Delta V/\Phi_0$. This estimate assumes that the voltage is sinusoidal in Φ, which is at best only an approximation.

We turn now to the dimensionless flux noise s_ϕ $S_\Phi(2\pi I_0R/\Phi_0)$ s_v/v_ϕ^2. In the simulations, we saw that s_ϕ can be factorized as $s_\phi(\beta_L;\Gamma\beta_L)$ $\approx f_\phi(\beta_L)g_\phi(\Gamma\beta_L)$, where we defined $f_\phi(\beta_L)$ $s_\phi(\beta_L;\Gamma\beta_L \frac{1}{80})$ and $g_\phi(\Gamma\beta_L)$ $s_\phi(\beta_L;\Gamma\beta_L)/$ $s_\phi(\beta_L;\Gamma\beta_L \frac{1}{80})$. In Figs. 19(a) and (b) we plot s_ϕ/f_ϕ vs $\Gamma\beta_L$ and s_ϕ/g_ϕ vs β_L, respectively, together with the theoretical curves. In both cases the reduced noise power is as much as two orders of magnitude too high. One can explain this discrepancy only partly by the reduced value of the transfer function, which enters as v_ϕ^2.

From Figs. 18 and 19 we see that the discrepancy between theory and experiment is roughly the same for all values of $\Gamma\beta_L$ and β_L. We also investigated whether
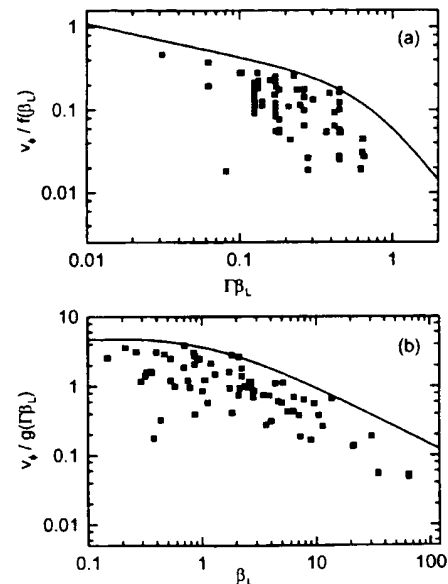

FIG. 18. Transfer function of dc SQUID: (a) Measured transfer function v_ϕ, normalized to the theoretical value $f(\beta_L)$, vs $\Gamma\beta_L$ for a wide selection of SQUIDs (solid squares); solid line corresponds to Eq. (2.5). (b) Measured transfer function normalized to the theoretical value $g(\Gamma\beta_L)$ vs β_L; solid line corresponds to Eq. (2.6).
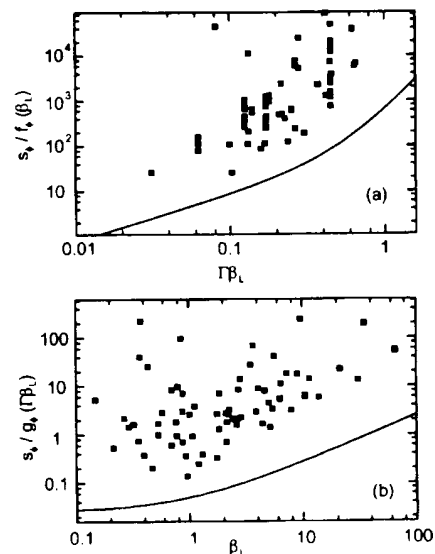

FIG. 19. Flux noise of dc SQUID: (a) Measured flux noise power, normalized to the theoretical value $f_\phi(\beta_L)$, vs $\Gamma\beta_L$ for the same SQUIDs as in Fig. 18 (solid squares); solid line corresponds to Eq. (2.8). (b) Measured flux noise power, normalized to the theoretical value $g_\phi(\Gamma\beta_L)$ vs β_L; solid line corresponds to Eq. (2.9).
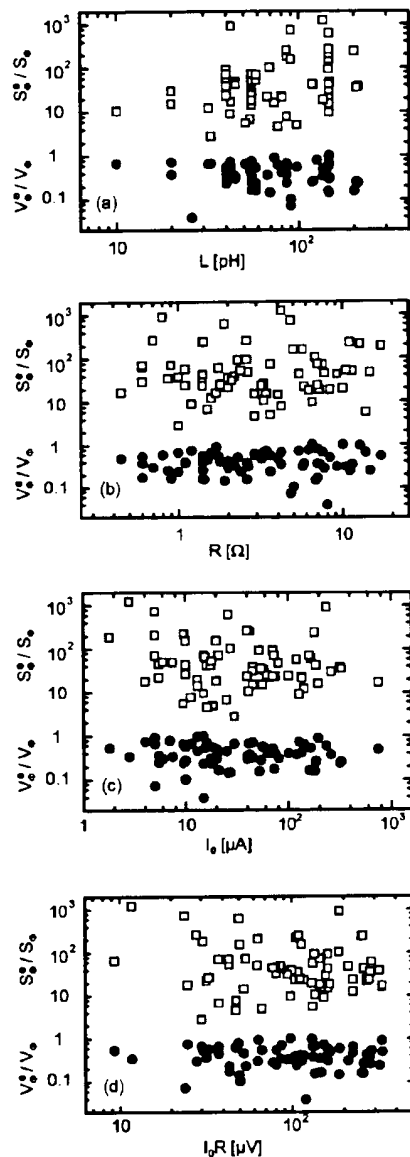
FIG. 20. For a wide selection of dc SQUIDs: ratio of measured and calculated transfer functions V_Φ^c/V_Φ (solid circles) and ratio of measured and calculated flux noise powers S_Φ^c/S_Φ (open squares) as a function of (a) SQUID inductance, (b) junction resistance, (c) junction critical current, and (d) I_0R.

systematic trends occur as functions of the absolute values of L, R, I_0, or I_0R by plotting V_Φ^c/V_Φ (solid circles) and S_Φ^c/S_Φ (open squares) versus these parameters in Fig. 20. The plots clearly show that there are no systematic trends throughout the ranges of parameters. However, for some devices V_Φ^c/V_Φ approaches unity; a similar result has been found by Koch (1997). Generally, the scatter in S_Φ^c/S_Φ is much greater than in V_Φ^c/V_Φ. We also calculated S_Φ by using the measured value V_Φ^c in-

stead of using its predicted value. The scatter was reduced, but no systematic trends became apparent.

What are the possible reasons for the high values of white noise that are almost universally observed? One explanation is that some measurements may have been taken with improperly set bias conditions; however, this is an unlikely explanation for most of the data. Second, experience with low-T_c SQUIDs suggests that environmental noise and noise from the readout electronics are improbable explanations. A third possibility is that the SQUID inductances are significantly underestimated, for example, because of a higher than anticipated kinetic inductance. Enpuku, Tokita *et al.* (1995) show that actual inductance values, 1.4 to 2 times higher than the estimated values, would explain much of the discrepancy; however, for some 40 pH devices, the actual value would have to be as much as 4 times higher, which is unreasonable. For example, Lee *et al.* (1995) estimated that the kinetic inductance for their devices was about 15% of the geometric inductance. Thus this explanation seems somewhat unlikely. A fourth explanation (Foglietti *et al.*, 1995) is that the junctions have a current-phase relation that is far from sinusoidal and that excess critical currents would lead one to overestimate the value of I_0R obtained from the I-V characteristics. Since I_0R enters v_ϕ and s_ϕ as a normalization factor, the high value would lead one to overestimate v_ϕ in the theory, and underestimate s_ϕ. A fifth explanation for the observed discrepancies between theory and experiment could be the presence of resonances. While the model in Sec. II ignores parasitic effects, the large dielectric constant of the commonly used $SrTiO_3$ substrates results in a substantial spurious capacitance. Transmission-line resonances (Enpuku *et al.*, 1996), as well as capacitive feedback effects (Enpuku *et al.*, 1997), have been demonstrated to influence the SQUID performance significantly. These possibilities cannot be entirely ruled out since the published noise data for dc SQUIDs are rarely accompanied by detailed measurements of the I-V characteristics. However, the reasonably good fit of a least some I-V characteristics to the RSJ model (for example, Gross and Chaudhari, 1992), the dependence of the amplitude of Shapiro steps on microwave power, and the reasonably good quality diffraction patterns of the critical current in a magnetic field suggest that they are not strong candidates. Finally, an effective bath temperature of roughly 2 T could explain the results (Enpuku, 1993). A twofold increase in temperature would double the value of $\Gamma\beta_L$ and reduce L_{th} to 160 pH. Thus one would have to shift the data in Figs. 18(a) and 19(a) to the right by a factor of 2 to account for the higher noise. This higher temperature could arise from some nonequilibrium process in the junction, for example, random telegraph signals from flux motion at characteristic frequencies well above the measurement bandwidth. The resulting Lorentzian power spectra would be white below the hopping frequencies. To our knowledge, there is no experimental evidence to support this notion, but it would be worth-

while to extend the measurements to much higher frequencies to see whether or not the noise decreased.

Finally, we note that, although they are significantly above theoretical predictions, impressive levels of noise have been achieved at 77 K, for example, $1.4\,\mu\Phi_0\,\mathrm{Hz}^{1/2}$ with L 13 pH (Kawasaki et al., 1991) and $2.2\,\mu\Phi_0\,\mathrm{Hz}^{1/2}$ with L 51 pH (Cantor et al., 1995); the corresponding noise energies were about 3×10^{-31} JHz^{-1} and $2\times10^{-31}\,\mathrm{JHz}^{-1}$, respectively.

D. Flicker (1/f) noise

For many applications, for example biomagnetism (Sec. X.A) and magnetotellurics (Sec. X.D), one requires the low level of noise to extend down to frequencies of 1 Hz or lower; if that were the case, high-T_c SQUIDs would be adequate for most purposes. Unfortunately, low-frequency $1/f$ noise, which is observed in low-T_c SQUIDs but is generally not a serious issue, is a severe problem in high-T_c SQUIDs and a great deal of effort has been expended in attempting to understand its origins and reduce its magnitude. Early high-T_c dc SQUIDs made from polycrystalline YBCO films (Koch et al., 1989) exhibited large levels of $1/f$ noise, which increased the noise energy at 1 Hz to above $10^{-26}\,\mathrm{JHz}^{-1}$. Since that time, there have been dramatic reductions in the level of $1/f$ noise, and the $1/f$ corner frequency f_c (the frequency at which the extrapolated values of the white noise and $1/f$ noise intersect) has been reduced from ~1 kHz to ~1 Hz.

Work on low-T_c dc SQUIDs (Koch et al., 1983) showed that there are generally two separate sources of $1/f$ noise. One arises from the motion of vortices in the body of the SQUID: even when the SQUID is cooled in zero field, some fraction of the vortices formed at T_c remain pinned at defects. The vortex hopping rate increases exponentially as the pinning energy is reduced, so that the microstructure of the film and the related pinning energies play an important role in determining the low-frequency noise (Ferrari et al., 1994). As we have seen in Sec. III, the microstructural quality of films is particularly crucial. When the SQUID is cooled in a nonzero magnetic field, in general the additional vortices so formed create high noise levels (Sec. IX.A). Unfortunately, one cannot relate the magnitude of the $1/f$ noise to any other measurable physical quantity, so that a direct noise measurement is the only means of characterizing the quality of a given film. It is important to note that $1/f$ noise due to vortex motion cannot be reduced by any bias reversal scheme.

The second source of $1/f$ noise is fluctuations in the critical current of the junctions which, as we saw in Sec. IV.C, can attain high levels. These fluctuations contribute in two independent ways: an "in-phase" mode, in which the critical currents of the two junctions fluctuate in phase to produce a voltage across the SQUID, and an "out-of-phase" mode in which the two fluctuating critical currents produce a current around the SQUID loop. Resistance fluctuations also contribute $1/f$ noise. However, at the low voltages where SQUIDs are operated

critical-current fluctuations dominate, and we shall not address resistance fluctuations further.

The first measurements of flux noise in high-T_c dc SQUIDs made from epitaxial YBCO films and with well-defined grain-boundary junctions were made by Gross et al. (1990a, 1990b). Measuring the voltage noise directly with a low-T_c SQUID preamplifier, they found similar levels of $1/f$ noise for both their SQUIDs and, after they had cut the loop, for the individual junctions. Furthermore, at temperatures well below T_c the $1/f$ voltage noise of the SQUIDs was constant, independent of V_Φ, providing strong evidence that in-phase critical-current fluctuations dominated the SQUID noise below 1 kHz. At temperatures just below T_c, however, they found that the $1/f$ noise power scaled with V_Φ^2, and attributed this to the rapid increase in the flux noise near T_c observed by Ferrari et al. (1989). Subsequently, Koch et al. (1992) measured the $1/f$ noise in bicrystal grain-boundary SQUIDs using flux modulation alone and also flux modulation combined with bias reversal. At 77 K, they found that bias reversal reduced the $1/f$ noise power by up to two orders of magnitude, demonstrating that critical-current fluctuations dominate the $1/f$ noise observed in SQUIDs with high-quality thin films, and that one needs to reduce both the in-phase and out-of-phase components.

In practice, the reduction of $1/f$ noise with bias reversal is optimized empirically, but nonetheless, there are predictions for the magnitudes of the in-phase and out-of-phase contributions (Koch et al., 1983; Foglietti et al., 1986). The in-phase mode produces a voltage noise with a spectral density $S_V \approx (\partial V/\partial I_0)^2 S_{I_0}/2 \approx (V/IR_d)^2 S_{I_0}/2I_0^2$, and the out-of-phase mode produces a term $S_v \approx L^2 S_{I_0} V_\Phi^2/2$. Here, R_d is the dynamic resistance. As mentioned in Sec. IV.C, one can write $s_I \equiv S_{I_0}(f)/I_0^2 \approx a^2/f$, where a is temperature independent and approximately equal to $10^{-4}(R/\Omega)^{1/2}$ for a wide variety of junctions. From these results, one can derive the approximate expressions

$$S_\Phi^{1/2}(\text{in-phase}) \approx s_I^{1/2}|V/IR_d|/V_\Phi$$
$$\approx (70\,\mu\Phi_0\,\mathrm{Hz}^{1/2})10^4 a\zeta v_\Phi^{-1}(f/\mathrm{Hz})^{-1/2},$$
$$(5.2a)$$

where $\zeta \equiv |V/IR_d|/I_0 R \sim 1$, and

$$S_\Phi^{1/2}(\text{out-of-phase}) \approx s_I^{1/2}\beta_L\Phi_0/2$$
$$\approx (35\,\mu\Phi_0\,\mathrm{Hz}^{1/2})10^4 a\beta_L(f/\mathrm{Hz})^{-1/2}.$$
$$(5.2b)$$

For optimized values of high-T_c dc SQUIDs at 77 K, β_L 1, Γ 0.2, and $I_0 R$ $100\,\mu V$, we estimate a flux noise of about 200 (100) $\mu\Phi_0$ $\mathrm{Hz}^{1/2}$ at 1 Hz for the in-phase (out-of-phase) contribution, substantially above measured levels of white noise. These estimates are in reasonable agreement with experimental observations, and emphasize the need for bias reversal with any high-T_c SQUID used for low-frequency measurements.
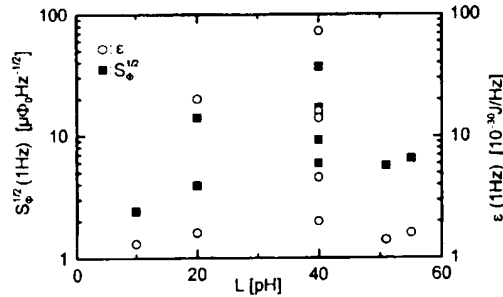
FIG. 21. $S_\Phi^{1/2}$ (1 Hz) and ε (1 Hz) of dc SQUIDs with various inductances, obtained at 77 K with flux modulation and bias reversal. (Data are from Koelle, Miklich, Ludwig et al., 1993; Koelle, Miklich, Dantsker et al., 1993; Koelle, Dantsker et al., 1993; Miklich et al., 1993; Cantor et al., 1995; Lee et al., 1995; Faley, Poppe, Urban et al., 1995; Friedl et al., 1992 and Grundler et al., 1995).

We conclude this discussion with examples of $1/f$ noise in dc SQUIDs cooled in nominally zero magnetic field. In Fig. 21 we plot $S_\Phi^{1/2}$(1 Hz) and ε (1 Hz) for ten SQUIDs, with L between 10 and 55 pH, obtained with flux modulation and bias reversal. In the best devices, the noise energies approach 10^{-30} JHz^{-1} at 1 Hz, a performance that is very adequate provided the SQUIDs can be coupled to appropriate pickup loops without further increases in the $1/f$ noise. However, as we discuss in Sec. IX.A, the level of $1/f$ noise in SQUIDs cooled in an ambient magnetic field such as that of the earth can be much higher than in zero field unless the linewidths are kept suitably narrow.

VI. dc SQUID MAGNETOMETERS

SQUIDs are mostly used as magnetometers or gradiometers. However, although SQUIDs are exquisitely sensitive to magnetic flux, their small area generally makes them relatively insensitive to magnetic field. An exception is the large square-washer design used for both dc and rf SQUIDs, which we discuss in Secs. VI.A and VII.A, respectively. Apart from these cases, one usually couples an additional superconducting structure to the SQUID to enhance its sensitivity to magnetic field; the magnetic-field noise is $S_B^{1/2}(f)$ $S_\Phi^{1/2}(f)/A_{\rm eff}$, where $A_{\rm eff}$ is the effective area of the magnetometer. Clearly, one endeavors to make $A_{\rm eff}$ as large as possible without increasing $S_\Phi(f)$ so as to produce high sensitivity to magnetic fields.

A. Square-washer designs

In this SQUID configuration (Ketchen 1981; Jaycox and Ketchen, 1981) a square washer with outer length D focuses flux into a square inner hole of length d. The effective area is dD (Ketchen et al., 1985), and the inductance is L_h $1.25 \mu_0 d$ for W $(D$ $d)/2$ d (Jaycox and Ketchen, 1981). In practice, however, the incorporation of the two Josephson junctions into the SQUID

loop modifies these expressions for $A_{\rm eff}$ and L. Five high-T_c dc SQUIDs grown on bicrystal substrates are shown in Fig. 11, and differ in the placement of the junctions intersecting the SQUID loop. In type A the junctions are outside the washer, and are thus far away from the region of strong field compression. The slit of length $l \approx W$ between the SQUID hole and the junctions can cause a significant increase in $A_{\rm eff}$ over the value dD, for example by a factor of 2.5 for D 250 μm and d

25 μm (Miklich et al., 1993). More importantly, it increases the inductance by $L_{\rm slit} \approx (0.3$ $0.4 l/\mu{\rm m})$pH (Wen, 1969). Thus, if one wishes to limit the total inductance to 40 pH, the maximum washer size is 200 μm even if there is no hole (d 0) as in type A/A. In contrast, for types B or C, the inductance is approximately L_h, independent of the washer size D. However, the effective area $A_{\rm eff}$ is significantly less than dD for D

d, because of the focusing of flux into the slits outside the SQUID loop (Miklich et al., 1993; Tanaka et al., 1994). The latter effect is minimized in type A/C: for example, for D 500 μm and L 40 pH one finds $A_{\rm eff}$ ≈ 0.015 mm^2, roughly a factor of two larger than for type B or C with the same values of D and L or for a 40-pH type A/A SQUID (Ludwig, Dantsker, Koelle, Kleiner, Miklich, Nemeth et al., 1995).

A general calculation of the SQUID inductance and effective area requires a numerical treatment, for example solving the London equations for the specific geometry. Several groups have performed such calculations (Chang, 1981; Hosoya et al., 1989; Sheen et al., 1991; Töpfer, 1991; Uhlmann and Töpfer, 1992; Hildebrandt and Uhlmann, 1995). More simply, one can estimate the SQUID inductance by summing the inductance of the hole L_h the inductance of the slit $L_{\rm slit}$ which may be modeled as two coplanar striplines, and the inductance of the junction striplines L_j $L_{j,g}$ $L_{j,k}$, which has a geometric and kinetic term. For a homogeneous current distribution the kinetic term is approximately $L_{j,k} \approx \mu_0(\lambda^2/t)2 l_j/w$, where λ is the London penetration depth, t the film thickness, w the junction width and l_j the length of the junction striplines (Meservey and Tedrow, 1969). The contribution of L_j should be small, typically a few pH, if l_j/w is kept close to unity. This estimate of L should be accurate to within 10%.

For most dc SQUIDs with these geometries, the relatively small effective area implies that $S_B^{1/2}$ is inadequate for most applications. For example, with $A_{\rm eff}$ 0.015 mm^2 and $S_\Phi^{1/2}$ 10 $\mu\Phi_0$/Hz$^{1/2}$ one finds $S_B^{1/2}$ 1.3 pT/Hz$^{1/2}$ well above the resolution of 10–100 fT/Hz$^{1/2}$ typically required. However, larger washers (Koelle, Miklich, Ludwig et al., 1993; Tanaka et al., 1994) have achieved a magnetic-field noise of about 150 fT/Hz$^{1/2}$ at 1 kHz and 500 fT/Hz$^{1/2}$ at 1 Hz with SQUID inductances of 40–100 pH and washers of 5 11 mm. Comparable performance has been achieved with flux-focusing plates of similar size coupled to washer SQUIDs 2 2 mm^2 in size (Tanaka et al., 1994; Itozaki et al., 1996). The $1/f$ noise in these devices tends to be high, and in some cases the motion of vortices trapped in the washer limits the effectiveness of bias reversal in
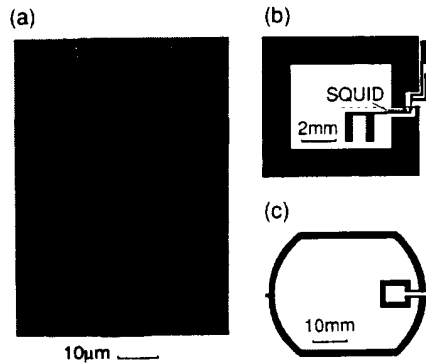
FIG. 22. Directly coupled magnetometer: (a) Photograph of 20 pH dc SQUID connected to the pickup loop shown in (b). Dashed line indicates grain boundary. (c) Configuration of single-layer YBCO flux transformer (Koelle, Miklich, Dantsker *et al.*, 1993).

reducing it (Koelle, Miklich, Ludwig *et al.*, 1993). Because of this limited performance, various alternative approaches for increasing the effective area have been pursued. There are two broad classes. The first is based on multilayer designs such as the flux transformer-coupled SQUID (Ketchen, 1981; Jaycox and Ketchen, 1981) (Sec. VI.C) or the fractional-turn SQUID (Zimmerman, 1971) (Sec. VI.D), which were successfully used for low-T_c magnetometers. However, the need for lower SQUID inductances and hence smaller SQUIDs for operation at 77 K has made optimum coupling of signal into the SQUID more challenging. Furthermore, multilayer high-T_c devices are more susceptible to excess $1/f$ noise and its reduction has been a major issue during the past years (Sec. III). As a result, single-layer designs have been developed which typically have less efficient coupling but benefit from straightforward fabrication, and lower levels of $1/f$ noise.

B. Directly coupled magnetometer

The directly coupled magnetometer (Matsuda *et al.*, 1991; Koelle, Miklich, Ludwig *et al.*, 1993) shown in Figs. 22(a) and (b) consists of a large pickup loop of inductance L_p and area A_p directly connected to the SQUID body of inductance L L_p. A magnetic field B applied to the pickup loop induces a screening current J $B A_p / L_p$, which in turn links a flux $(L$ $L_j)J$ to the SQUID. Here L_j is the parasitic inductance of the striplines incorporating the junctions, to which the current does not couple. The effective area is

$$A_{\text{eff}} \quad (L \quad L_j)A_p / L_p \quad A_s,\qquad(6.1)$$

where A_s A_{eff} is the effective area of the bare SQUID. The sign of A_s depends on the relative senses of the SQUID and the pickup loop. Koelle, Miklich, Ludwig *et al.* (1993) investigated devices grown on STO bicrystals. In their best device, a 20 pH SQUID with I_0 45 μA and R 3.4 Ω coupled to a 47 mm^2 pickup loop,

they achieved a flux noise of 93 fT Hz $^{1/2}$ at frequencies down to 1 Hz using bias reversal.

Subsequently, improvements in performance were achieved by reducing the large mismatch between L_p and L (Cantor *et al.*, 1995; Lee *et al.*, 1995). One can increase the ratio A_p / L_p by using a pickup loop with a large linewidth, $(d_1$ $d_2)/2$, where d_1 and d_2 are the outer and inner dimensions. In the limit $(d_1$ $d_2)$ $2d_2$ in which A_p $d_1 d_2$ and L_p 1.25 $\mu_0 d_2$, from Eq. (6.1) we find A_{eff} $4d_1(L$ $L_j)/5 \mu_0$; we have neglected A_s. Given the dependence of $S_\Phi(f)$ on L, I_0, and R discussed in Sec. II.C, one can then optimize $S_B(f)$.

Using Eq. (6.1) for A_{eff}, together with Eqs. (2.8) and (2.9) over the ranges 0.01 $\Gamma\beta_L$ 1 and 0.4 β_L 5.6, one finds

$$\frac{S_B^{1/2}}{(\text{fT Hz}^{1/2})} \quad \frac{262 \text{ pH}}{L_{\text{th}}} \quad \frac{1}{(d_1/\text{mm})(L \quad L_j)/L_j}$$
$$\left\{ \frac{1}{I_0 R/\text{mV}} \frac{\beta_L}{\left[\frac{80L}{L_{\text{th}}} \left(1 \quad \frac{4L}{L_{\text{th}}} \right)^{4.1} \quad 1 \right]} \right\}^{1/2}.$$
$$(6.2)$$

Clearly, $S_B^{1/2}$ scales with $1/d_1$. For a given value of L_j one can find a minimum in $S_B^{1/2}$ as a function of L/L_{th}, which depends on $I_0 R$ and β_L. As mentioned in Sec. II.C, the noise can be optimized in different ways: one way is to keep $I_0 R$ constant and to vary I_0 by changing the junction area A_j. However, this is difficult to achieve for practical reasons, since large $I_0 R$ products are associated with high critical-current densities and hence the smallest values of I_0 are determined by the smallest linewidth that can be patterned. Alternatively, according to the scaling relation $I_0 R \propto j_c^{1/2}$ found for many high-T_c junctions, one may keep $I_0 R^2$ constant with fixed A_j and vary I_0, for example, by changing the oxygen content in grain-boundary junctions. In this case $(1$ $\beta_L)/(I_0 R) \propto (1$ $\beta_L)/\beta_L^{1/2}$, which has a minimum at β_L 1. The result of this optimization procedure is shown in Fig. 23 where we plot $S_B^{1/2}$ vs L/L_{th} for the stated values of $I_0 R$, L_{th}, L_j, d_1, and A_j and for six values of β_L ranging from 0.4 to 5.0. There is a shallow minimum at $L/L_{\text{th}} \approx 0.3$, corresponding to $L \approx 100$ pH at 77 K. The dependence on β_L is weak, although β_L 1 is optimum: the minimum magnetic-field noise varies from 11 to 13 fT Hz $^{1/2}$ over the range of β_L plotted. Notice that the optimum value of L/L_{th}, about 0.3, is rather higher than that for the lowest noise energy found in Sec. II.C. The reason is that the coupling efficiency between L_p and L increases more rapidly in this range than V_Φ decreases. In an earlier analysis based on the work of Enpuku, Tokita *et al.* (1995), Cantor (1996) found a shallow minimum in $S_B^{1/2}$ vs L corresponding to $S_B^{1/2} \approx 32$ fT Hz $^{1/2}$ for β_L 1, d_1 9.3 mm, $I_0 R$ 100 μV, and L_j 8.4 pH; $S_B^{1/2}$ remained below 40 fT Hz $^{1/2}$ for 30 pH L L_j 170 pH. This result differs somewhat from the prediction of Eq. (6.2) because Enpuku *et al.* find a faster reduction in V_Φ for L/L_{th} 0.4 (Fig. 2).

The performance of directly coupled magnetometers with near optimum parameters can be appreciably bet-
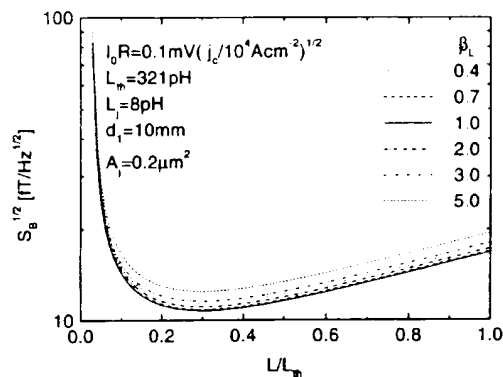
FIG. 23. Calculated rms magnetic-field resolution $S_B^{1/2}$ at 77 K vs normalized SQUID inductance L/L_{th} for directly coupled magnetometer in which the pick-up loop has an outer dimension d_1 10 mm. The curves were calculated for six values of β_L and fixed junction cross-section A_j 0.2 μm^2 by varying j_c and hence $(I_0 R)^2$.

ter than that of the earlier devices. For d_1 9.3 mm, d_2 3 mm, and L 50 pH, Lee *et al.* (1995) and Cantor (1996) achieved best results of about 40 fT Hz $^{1/2}$ at 1 kHz and 60 fT Hz $^{1/2}$ at 1 Hz (with bias reversal). Using a 19 19 mm^2 pickup loop on a 20 20 mm^2 bicrystal, the same group achieved 14 fT Hz $^{1/2}$ at 1 kHz and 26 fT Hz $^{1/2}$ at 1 Hz (Fig. 24) (Cantor *et al.*, 1995). In similar work, Glyantsev *et al.* (1996) reported a noise level as low as 20 fT Hz $^{1/2}$ at 1 kHz for a 150 pH SQUID coupled to a pickup loop with an outer diameter of 8 mm. However, they did not use bias reversal, and the noise was well above 100 fT Hz $^{1/2}$ at 1 Hz. Recently, using an STO bicrystal with a 30° misorientation angle and a pickup loop with d_1 9 mm and d_2 3 mm, Beyer *et al.* (1998) obtained 23 fT Hz $^{1/2}$ at 1 kHz and 67 fT Hz $^{1/2}$ at 1 Hz. These values were achieved with bias reversal in the PTB magnetically shielded room; the
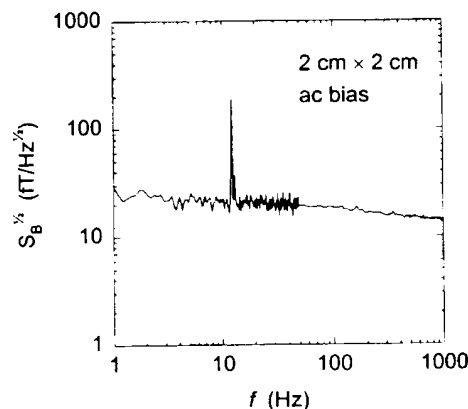

FIG. 24. Magnetic-field noise in a directly coupled magnetometer with bicrystal junctions and a 19 19 mm^2 pickup loop. The estimated inductance is 51 pH (Cantor *et al.*, 1995).
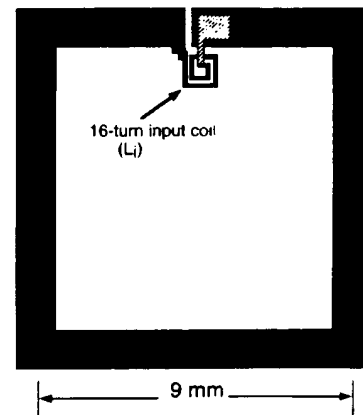

FIG. 25. Schematic layout of multilayer flux transformer (not to scale). Multiturn input coil (only two turns are shown) is either coupled to the SQUID in a flip-chip arrangement or deposited directly on top of it.

noise at low frequencies was dominated by environmental noise.

To complete this section, we note that the effective area of the directly coupled magnetometer can be further increased by coupling it in a flip-chip arrangement to a single-layer flux transformer [Fig. 22(c)] on a separate substrate (Koelle, Miklich, Dantsker *et al.*, 1993). The small loop of the transformer (which is inductively coupled to the magnetometer pickup loop) has inductance L_{ti} and area A_{ti} and is in series with the large loop of inductance L_{tp} and area A_{tp}. The effective area is

$$A_{eff} \approx \frac{L}{L_p} \frac{L_j}{} \left(A_p \quad \frac{A_{tp} \alpha_t (L_p L_{ti})^{1/2}}{L_{ti} \quad L_{tp}} \right), \quad (6.3)$$

where α_t is the coupling coefficient between L_{ti} and L_p. For the devices shown in Fig. 22, the transformer yielded a gain of 3.4 and the magnetic-field noise improved to 31 fT Hz $^{1/2}$ at 1 kHz and 39 fT Hz $^{1/2}$ at 1 Hz.

C. Flux transformer with multiturn input coil

The effective area of a SQUID may be efficiently enhanced by coupling it to a superconducting flux transformer with a multiturn input coil (Fig. 25). The transformer is a closed superconducting circuit consisting of a large-area pickup loop and a much smaller, multiturn input coil to couple flux into the SQUID. A magnetic field applied to the pickup loop induces a supercurrent that conserves the total magnetic flux and induces flux into the SQUID. The total effective area of the magnetometer is given by

$$A_{eff} \quad A_p M_i / (L_i \quad L_p) \quad A_s. \quad (6.4)$$

where A_s is the effective area of the bare SQUID (including flux focusing, see Sec. VI.A), A_p and L_p are the area and inductance of the pickup loop, $M_i \quad \alpha(L L_i)^{1/2}$ is the mutual inductance between the SQUID inductance L and the input-coil inductance L_i, and α is the

coupling coefficient. The sign of A_s depends on the sense of the winding of the coil relative to the pickup loop. Assuming that α does not depend on L_i and L and making certain approximations (Martinis and Clarke, 1985), one finds the effective area is maximum when $L_i \quad L_p$:

$$A_{\text{eff}} \quad \alpha A_p (L/L_p)^{1/2}/2; \qquad (6.5)$$

we have neglected A_s. In contrast to the directly coupled magnetometer (Sec. VI.B), the flux transfer into the SQUID can be optimized for a given value of L_p by varying the number of turns n on the input coil until $L_i \quad L_p$. For low-T_c SQUIDs integrated with multiturn input coils, the relations between M_i, L_i, L, and n (Ketchen, 1981) for the tightly coupled limit are usually in good agreement with experimental data (Jaycox and Ketchen, 1981). For high-T_c magnetometers on the other hand, there are only a few experimental studies on the coupling between the input coil and the SQUID (David *et al.*, 1995; Ludwig, Dantsker, Koelle, Kleiner, Miklich, Nemeth *et al.*, 1995; Kugai *et al.*, 1996), and the situation is less well understood. Ludwig, Dantsker, Koelle, Kleiner, Miklich, Nemeth *et al.* (1995) found that although α depends strongly on the SQUID design, being higher for type A/A and A/C than for type B and C devices (Fig. 11), it can be greater than 0.5 even for flip-chip magnetometers. Coupling the same transformer to different SQUID types, these authors showed that A_{eff} is proportional to A_s, that is, the magnetic-field gain is constant. According to Eq. (6.5), A_{eff} increases with increasing SQUID inductance L, but larger values of L do not necessarily produce lower magnetic-field noise. Using Eq. (6.5) one finds S_B $8(S_\Phi/2L)L_p/\alpha^2 A_p^2$, so that minimizing S_B with respect to L is equivalent to minimizing the noise energy $\varepsilon \quad S_\Phi/2L$. From Fig. 5 we know that for 77 K and β_L 1, the (effective) SQUID inductance should not exceed 40–50 pH, although one should bear in mind that Eq. (6.5) is valid only so long as α is independent of L and L_i. We note also that the flux transformer reduces the effective SQUID inductance to $L[1 \quad \alpha^2 L_i/(L_i$ $L_p)]$ (Zimmerman, 1971). However, this correction is small for $L_i \quad L_p$ and $\alpha \quad 0.5$.

1. Flip-chip magnetometers

The advantage of the flip-chip configuration over the integrated magnetometer is that problems related to the junction process can be separated from those related to the interconnect technology. One forms a flip-chip magnetometer by clamping the SQUID and the flux transformer chips together with either photoresist or a thin mylar sheet between them. The input coil and pickup loop of the transformer are usually patterned in one YBCO layer, and the crossover between the innermost turn of the coil and the pickup loop in the other. The first YBCO flux transformer with a multiturn input coil operating at 77 K was made by Wellstood *et al.* (1990) using shadow masks. The first multilayer flip-chip magnetometers were reported almost simultaneously by groups at Berkeley (Miklich *et al.*, 1991; Wellstood *et al.*,
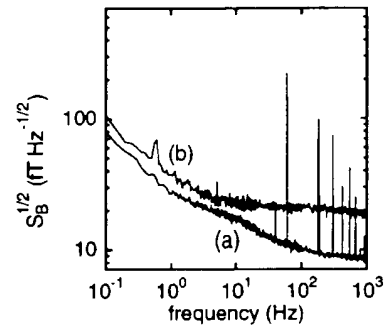

FIG. 26. Magnetic-field noise of (a) flip-chip magnetometer with a 9 9 mm^2 pickup loop and 16-turn input coil (Dantsker *et al.*, 1995), (b) the $\frac{1}{16}$-turn, 7-mm-diameter SQUID shown in Fig. 28 (Ludwig, Dantsker, Kleiner *et al.*, 1995).

1992) and IBM (Oh *et al.*, 1991). Since this early work, many groups have described the fabrication of multiturn flux transformers (Freltoft *et al.*, 1993; Hilgenkamp *et al.*, 1993) and the operation of flip-chip magnetometers at 77 K (Grundler, David *et al.*, 1993; Miklich *et al.*, 1993; Roas *et al.*, 1993; Keene, Goodyear *et al.*, 1994, Keene *et al.*, 1995; Dantsker *et al.*, 1995; Fife *et al.*, 1995; Ludwig, Koelle *et al.*, 1995; Scharnweber *et al.*, 1995; Schilling *et al.*, 1995; Kugai *et al.*, 1996).

The lowest magnetic-field noise was achieved by Dantsker *et al.* (1995), who used an 81 mm^2 pickup loop and a 16-turn input coil coupled to a 500 μm washer SQUID (type A/A in Fig. 11) with bicrystal junctions: 8.5 fT Hz $^{1/2}$ at 1 kHz and 27 fT Hz $^{1/2}$ at 1 Hz (Fig. 26). This performance depended critically on both the technology for fabricating multilayer structures with low levels of low-frequency flux noise and the use of a SQUID with a low flux noise. The uncoupled SQUID had a peak-to-peak modulation voltage V_{pp} 55 μV and a white flux noise of 7.3 $\mu\Phi_0$ Hz $^{1/2}$. The flux transformer was aligned so that the crossover covered about 90% of the length of the SQUID slit, reducing the SQUID inductance from 70 to about 30 pH, close to the optimum. As a result, V_{pp} increased to 108 μV, and the flux noise decreased to 4.9 $\mu\Phi_0$ Hz $^{1/2}$.

During the progressive reduction in $1/f$ magnetic-field noise from that in the first flip-chip magnetometer (Miklich *et al.*, 1991), 1.7 pT Hz $^{1/2}$ at 1 Hz, to that reported by Dantsker *et al.* (1995), it was important to understand the sources of excess flux noise in these multilayer structures. According to the model of Ferrari *et al.* (1991) and Wellstood *et al.* (1991), there are two distinct mechanisms by which this noise is coupled into the SQUID. First, the SQUID senses directly the magnetic flux produced by a vortex moving in the YBCO films of the flux transformer ("direct noise"). Second, a vortex moving perpendicularly to a YBCO line induces a screening current in the transformer to conserve the total magnetic flux, coupling flux into the SQUID ("indirect noise"). Together with flux-noise measurements on various components of transformers, the model has been used to analyze sources of excess flux noise (Lud-

FIG. 27. Photograph of 12-turn input coil and SQUID of an integrated magnetometer with 500-μm SQUID washer located in lower YBCO layer. Bicrystal junctions are outside the washer.

wig, Koelle et al., 1995; Ludwig, Dantsker, Koelle, Kleiner, Miklich, and Clarke, 1995), but it does not account for the degraded quality of YBCO films at the edges of crossovers and vias. To study the spatial distribution of critical-current densities and thus locate potential noise sources, several groups have successfully used such techniques as low-temperature scanning electron microscopy (Husemann et al., 1993; Hollin et al., 1994; Gerber et al., 1996), low-temperature laser scanning microscopy (Sivakov et al., 1994), magneto-optical imaging (Govorkov et al., 1997) and scanning micro-Raman spectroscopy (Dieckmann et al., 1996).

2. Integrated magnetometers

In an attempt to improve the inductive coupling between the SQUID and the input coil, several groups have integrated them on the same chip, thus reducing the spacing to the thickness of the insulating layer. Early monolithic SQUID magnetometers involving three YBCO layers and operating at 77 K (Lee et al., 1991; DiIorio, Yoshizumi, Yang, Maung, and Power, 1993) exhibited large levels of low-frequency flux noise. As a result, attention turned to a simplified design requiring only two superconducting layers (Kromann et al., 1993; Hilgenkamp et al., 1994; David et al., 1995; DiIorio et al., 1995; Ludwig, Dantsker, Koelle, Kleiner, Miklich, Nemeth et al., 1995; Shen et al., 1995). In all cases, the insulator was SrTiO$_3$. The SQUID washer is used as either a crossunder or crossover for the flux transformer, obviating the need for an extra superconducting layer. The input coil and SQUID of such a magnetometer are

shown in Fig. 27. The lowest magnetic-field noise was reported by Drung, Ludwig et al. (1996) using a magnetometer with 36° SrTiO$_3$ bicrystal junctions fabricated at NKT (Shen et al., 1995), namely 9.7 fT Hz$^{1/2}$ at 1 kHz and 53 fT Hz$^{1/2}$ at 1 Hz. Whereas the effective area $A_{\rm eff}$ 1.72 mm^2 for the 8.3 8.6 mm^2 pickup loop is comparable to that measured by others for their integrated devices, the SQUID parameters R 9 Ω and I_0 5.7 μA for an inductance of about 130 pH are close to optimum.

Despite this impressive performance, integrated magnetometers do have some disadvantages. One problem, reported by several groups, is that the V-Φ curves are often distorted by microwave resonances (Hilgenkamp et al., 1994; Ludwig, Dantsker, Koelle, Kleiner, Miklich, Nemeth et al., 1995; Drung, Ludwig et al., 1996). Such resonances have not been reported for flip-chip magnetometers. These resonances in the input-coil-washer structure are well known from low-T_c devices to degrade the SQUID performance (Ryhänen et al., 1989). Enpuku et al. (1997) and Minotani, Enpuku et al. (1997) recently reported the calculation of distorted V-Φ characteristics in good agreement with the data measured on high-T_c devices under the assumption that there is a parasitic capacitance between the input coil and the SQUID washer. Hilgenkamp et al. (1995) eliminated the resonances by means of a resistor between the SQUID and the input coil that shunted this parasitic capacitance. Another drawback is that the yield of high-performance integrated devices is well below that of flip-chip, multilayer devices. Finally, there is no compelling evidence that the coupling coefficient of integrated magnetometers is significantly higher than that for flip-chip devices (Ludwig, Dantsker, Koelle, Kleiner, Miklich, Nemeth et al., 1995).

D. Multiloop magnetometer

An alternative multilayer approach to achieving large effective areas is the multiloop magnetometer or fractional-turn SQUID, originally proposed and demonstrated by Zimmerman (1971) with a machined niobium device. The essential idea is to connect N loops in parallel, thus reducing the total inductance to a level acceptable for a SQUID, while keeping the effective area large. Drung et al. (1990, 1991) developed sensitive multiloop SQUID magnetometers, based on their niobium thin-film technology; with eight parallel loops and a diameter of 7.2 mm these devices have a typical noise of 1.5 fT Hz$^{1/2}$ down to a few Hz at 4.2 K. These devices have been used successfully for multichannel biomagnetic studies (Koch, Cantor et al., 1991; Drung and Koch, 1993).

In the thin-film multiloop magnetometer, shown schematically in Fig. 28(a), N loops (for clarity, only four are drawn) are connected in parallel with the connection made at the center via coplanar lines. The two junctions connect the upper and lower superconducting films of the central trilayer. Compared with a flux-transformer-coupled magnetometer, the multiloop magnetometer
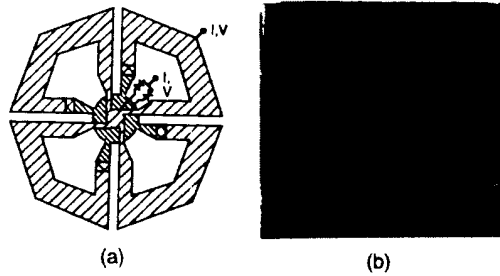
FIG. 28. Multiloop magnetometer: (a) Schematic layout of $\frac{1}{4}$-turn SQUID magnetometer. Cross-shaded regions indicate vias between upper and lower superconducting films. (b) Photograph of $\frac{1}{16}$-turn YBCO SQUID with outer diameter of 7 mm. Junctions are located close to the center (Ludwig, Dantsker, Kleiner *et al.*, 1995).

has the advantage that the current induced in each of the N loops when it is rotated in the earth's magnetic field is much smaller than that induced in a single loop of the same area. Furthermore, the device contains no closed superconducting loops, so that the maximum induced supercurrent is limited to the critical current of the junctions.

A comprehensive theory for thin-film multiloop SQUIDs and their performance at 77 K has been given by Drung *et al.* (1995). The effective area A_{eff} and inductance L_{eff} are given by

$$A_{\text{eff}} \quad A_p / N \quad A_s \tag{6.6}$$

and

$$L_{\text{eff}} \quad L_p / N^2 \quad L_s / N \quad L_j. \tag{6.7}$$

Here, A_p and L_p are the area and inductance of the large, outer loop, A_s and L_s are the average area and inductance of one spoke of the cartwheel, and L_j is the parasitic inductance of the connections from the pickup loops to the junctions. Calculation of the magnetic-field noise and transfer function as a function of N, based on the simulations of Enpuku *et al.* (1993) for $V_\Phi(L)$ and $S_\Phi^{1/2}$, shows that the optimum value of N for a minimum magnetic-field noise increases strongly with the overall size. For a diameter of 7 mm, the optimum number of loops is 15 to 20, considerably more than typically used in the low-T_c case. Using these calculations, Drung *et al.* (1995) designed a high-T_c multiloop SQUID with 16 parallel loops and an outer diameter of 7 mm. They estimated L_{eff} 145 pH, which is at the upper limit of acceptability for 77 K operation (Sec. II.C), and A_{eff} 1.77 mm^2.

In the first practical realization of this magnetometer, Ludwig, Dantsker, Kleiner *et al.* (1995) used their YBCO-SrTiO$_3$-YBCO multilayer technology and bicrystal junctions to make the magnetometer shown in Fig. 28(b). Most of the area of the pickup loops is patterned in the upper YBCO film, and each loop makes contact to the lower YBCO layer in the center (cross-shaded region). The two 24° bicrystal junctions are located in the lower YBCO film and also make contact to the up-

per and lower YBCO films in the central trilayer region. A voltage modulation as high as 20 μV was observed despite the relatively high inductance, and resulted from the nearly ideal junction parameters, I_0 13 μA and R 10 Ω. The effective area of 1.89 mm^2 was close to the predicted value. Using a flux-locked loop with 100 kHz flux modulation and bias reversal, the authors measured a magnetic-field noise of 18 fT Hz$^{1/2}$ at 1 kHz and 37 fT Hz$^{1/2}$ at 1 Hz (Fig. 26). Similar multiloop magnetometers based on the same design were subsequently made, using step-edge junctions (David *et al.*, 1996; Drung, Dantsker *et al.*, 1996) or PBCO ramp junctions (Reimer, Schilling *et al.*, 1995; Reimer, Ludwig *et al.*, 1995).

Two other high-T_c magnetometers involving multiloops differ from the design discussed above. Fife *et al.* (1995) coupled eight multiloop pickup coils with an outer diameter of 8.5 mm directly to a low-inductance washer SQUID with bicrystal junctions. The noise at 60 K with bias reversal was 100 fT Hz$^{1/2}$ above 3 Hz. Scharnweber and Schilling (1996, 1997) recently reported an integrated magnetometer in which a flux transformer with a multiturn input coil and a multiloop pickup coil is inductively coupled to a low-inductance washer SQUID. For their best magnetometer, with four parallel loops 8.5 mm in diameter, at 77 K they measured a magnetic field noise of 44 fT Hz$^{1/2}$ at 1 kHz with a static bias current and 100 fT Hz$^{1/2}$ at 1 Hz with bias reversal.

E. Comparison of magnetometers

Given the plethora of magnetometer designs, which should one choose for a particular application? Of course, integrated, multilayer magnetometers—the multiturn flux transformer grown on a square washer SQUID or the fractional-turn SQUID—are very appealing and offer the highest sensitivity for a given area, at least in the white noise. Unfortunately, the currently low yield of junctions with acceptable values of I_0 and R means that the yield of integrated magnetometers with high performance is correspondingly low. Consequently, on a commercial basis their price is correspondingly high, probably too high for most real-world applications. Thus one should examine the alternatives, namely single-layer and flip-chip, multilayer magnetometers.

The directly coupled magnetometer is appealing in its simplicity, requiring only a single layer in a bicrystal or step-edge junction technology. Noise levels below 30 fT Hz$^{1/2}$ have been achieved on 10 10 mm^2 bicrystals and below 20 fT Hz$^{1/2}$ on 20 20 mm^2 bicrystals; however, the larger bicrystals are currently very expensive. Fortunately, provided one can avoid an increase in the low-frequency noise in the presence of the earth's magnetic field (Sec. IX), the performance of the magnetometers on the smaller chip is adequate for geophysics, and probably also for magnetocardiology. Nonetheless, despite the simplicity of fabricating these single-layer devices, one has to accept the fact that the chip-to-chip variability in the junction parameters currently ensures

that the yield of high-performance magnetometers is less than 100%. Even though substrates can be repolished and reused two or three times, the cost of manufacturing a single magnetometer with low noise is likely to remain higher than desirable.

An alternative philosophy is to fabricate (say) ten square-washer SQUIDs on a 10   10 mm^2 chip, select the best and dice the chip accordingly. Experience suggests that one should obtain several SQUIDs with low noise with this procedure. One then couples each of these selected devices to a multiturn flux transformer in a flip-chip arrangement. Thus one separates the fabrication of the single-layer SQUIDs from the multilayer process for the flux transformer. As a further step towards lowering the cost of flux transformers dramatically, one should develop processes for depositing them in quantity on two-inch or preferably four-inch wafers using coevaporation (Berberich *et al.*, 1994; Matijasevic *et al.*, 1997). If one could develop such large-scale processing for flux transformers, for the currently available junction technologies this approach would appear to be the most economical, and could be used for all applications.

VII. rf SQUIDs

Although there has been substantially more effort to develop high-T_c dc SQUIDs, progress with rf SQUIDs has been excellent. Several groups have investigated rf SQUIDs (for example, Zani *et al.*, 1991; Tinchev and Hinken, 1992; Tinchev, 1997) but since the most concentrated effort has been made at FZ, Jülich, we shall largely focus on their work. We note that the main body of this work preceded the theory of Chesca (1998), and that a great deal of progress was made on largely empirical grounds. Furthermore, it is difficult to measure the critical current of the junction precisely without opening the loop, so that in at least some of the devices reported it is not clear whether β_L was greater or less than unity. It is possible that some of them were operated in a "mixed mode" in which the signal was produced by variations in both inductance and dissipation. For these reasons, it is often impracticable to compare the experimental results with theoretical predictions.

A. rf SQUIDs with lumped resonant circuits

The first rf SQUID magnetometers with high sensitivity (Zhang, Mück, Herrmann *et al.*, 1992; Zhang, Mück *et al.*, 1993) consisted of large YBCO square washers with step-edge, grain-boundary junctions [Fig. 29(a)], grown on 10   10 mm^2 SrTiO$_3$ substrates. The junctions were generally formed along the inner edge of the square washer to avoid the large parasitic inductance of the long slit. The SQUID was inductively coupled to the inductor of an LC tank circuit, which was resonant at 20 MHz in the early experiments. Subsequently, these authors increased the resonance frequency to about 150 MHz to increase the flux-to-voltage transfer coefficient and to reduce the level of white noise (see Sec. II). In addition to the rf excitation, the SQUID was flux modu-

lated in the usual way and operated in a flux-locked loop. The SQUIDs could be operated in both the hysteretic and nonhysteretic modes. For example, Zhang, Mück, Herrmann *et al.* (1992) reported a transfer function greater than $40 \,\mu V/\Phi_0$ for SQUIDs in either mode, operated at 150 MHz.

Zhang, Mück *et al.* (1993) varied both the outer and inner dimensions (d_1 and d_2) of the square washer to find the optimum magnetic-field sensitivity. The effective area $d_1 d_2$ increases with both d_1 and d_2, while the inductance L scales with d_2. Since $S_\Phi^{1/2}$ increases with L for both hysteretic and nonhysteretic modes, although with a different functional dependence, one expects to find a minimum. The optimum value, 170 fT Hz$^{-1/2}$, occurred for $d_2 \approx 150 \,\mu m$, and corresponded to a flux noise of 7   10^{-5} Φ_0 Hz$^{-1/2}$; the noise was white at frequencies down to 1 Hz. For larger inner dimensions the flux noise increased more rapidly than the effective area. At the time, this performance was the best obtained for a high-T_c magnetometer at 77 K.

There are several points to note about this result. First, the estimated inductance of this rf SQUID, about 240 pH, is larger than that of any useful dc SQUID. As a result, the effective area is substantially higher than for dc SQUIDs. In fact, the flux noise and noise energy of this rf SQUID are unremarkable by the standards of dc SQUIDs: it is the large effective area that produces the relatively low magnetic-field noise. The lack of $1/f$ noise is notable, and occurs for two reasons. In the first instance, as will be discussed in Sec. VII.C, the combination of rf and low-frequency flux modulation eliminates $1/f$ noise due to fluctuations in critical current. Of course, this scheme cannot reduce flux noise due to the motion of vortices in the square washer. Second, the relatively high level of white flux noise is now a virtue in that the $1/f$ knee is moved to a correspondingly low frequency.

Zhang, Mück *et al.* (1993) improved the performance of this device by coupling it to a flux concentrator, made of bulk YBCO, 43 mm in diameter. This magnetometer exhibited a white noise of 60 fT Hz$^{-1/2}$ at frequencies down to about 5 Hz; the additional $1/f$ noise was due to flux noise in the concentrator. Subsequently, Zhang *et al.* (1994) fabricated single-layer rf SQUIDs with several directly coupled pickup loops, improving the noise to 120 fT Hz$^{-1/2}$. They also fabricated a device in which the SQUID, in the form of a slit, was coupled to a 9   9 mm^2 pickup loop, and achieved 90 fT Hz$^{-1/2}$ down to about 4 Hz. They achieved their best performance, however, by coupling a 8   8 mm^2 square washer SQUID with a 200   200 μm hole to a single-layer flux transformer [inset, Fig. 30(a)] in a flip-chip arrangement. With a pickup loop of 40   40 mm^2 they achieved a magnetic-field noise of 24 fT Hz$^{-1/2}$ at frequencies down to 0.5 Hz [Fig. 30(a)].

More recently, Ockenfuß *et al.* (1997) made a systematic study of thin-film, single-layer flux transformers. The flux transformers were deposited on either 1   or 2   diameter substrates. Each transformer in turn was
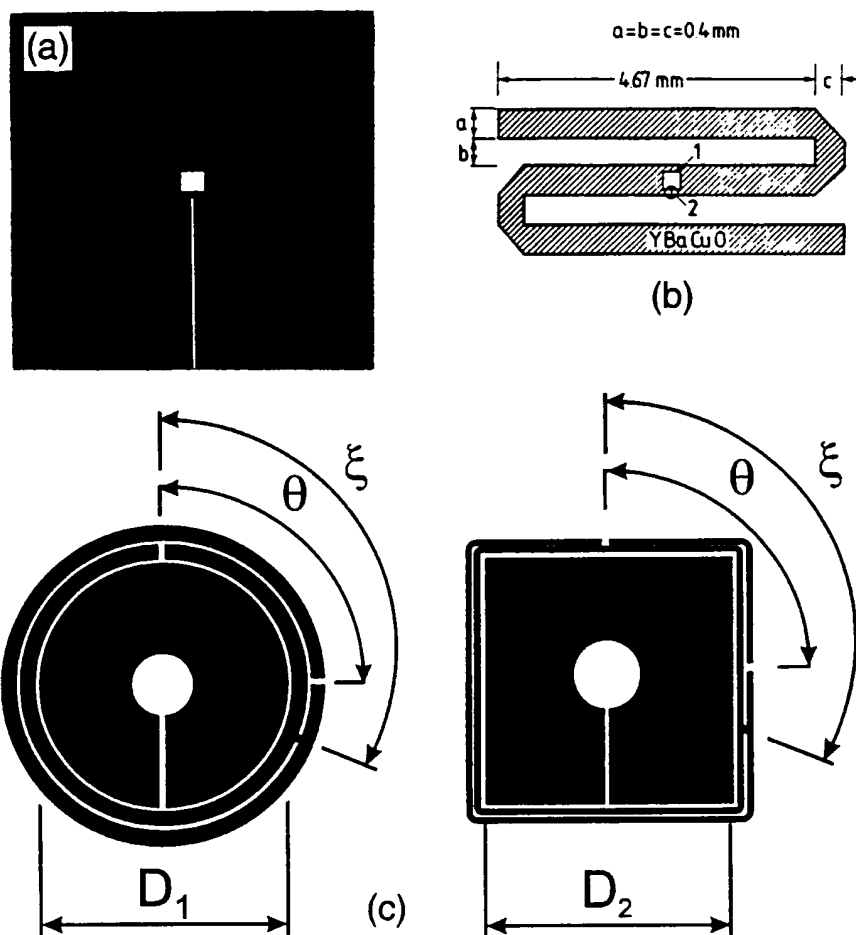
FIG. 29. Selection of rf SQUIDs from FZ, Jülich: (a) 6 6 mm² square-washer SQUID (Zhang, Mück, Hermann, *et al.*, 1993), (b) S-shaped microstrip SQUID (Zhang, Mück, Bode *et al.*, 1992). (c) coplanar microwave resonators (Zhang, Wolters *et al.*, 1997).

coupled in a flip-chip arrangement to an rf SQUID with a 200 200 μm² hole in an 8 8 mm² washer, operated at 200 MHz. The authors systematically reduced the width w_p of the pickup loop and measured the effective area and gain of the magnetometer. The maximum effective areas of 2.93 mm² and 4.94 mm² for the 1 and 2 transformers, respectively, were achieved for the maximum values of w_p, 8.2 and 19.0 mm; the corresponding magnetic field gains were 2.71 and 4.57. The magnetic-field noise above 10 Hz for these two cases was 52 fT Hz$^{1/2}$ and 30 fT Hz$^{1/2}$.

As a final remark, we note that all of the rf SQUIDs described above were at least somewhat undercoupled, that is, $\kappa^2 Q$ 1, so that the performance was less than optimum. Very recently, He *et al.* (1998) used a scheme in which they inductively coupled the lumped LC-resonant circuit to a coil that is connected to the 50 Ω transmission line supplying the rf signal. This approach, which was demonstrated at frequencies from 221 to 950 MHz, increases $\kappa^2 Q$ and reduces the flux noise compared with that obtained with conventional tank circuits.

B. rf SQUIDs with distributed element resonators

The devices described above involve lumped tank circuits consisting of a wire-wound coil and a capacitor. The flux noise achieved represents the limit of what can be achieved at 150–200 MHz As is evident from Eq. (2.15), further reductions in noise require high-frequency operation, but it then becomes difficult to achieve the required high values of Q with lumped circuits. As a result, devices operating at higher frequencies have involved various kinds of microwave resonators (Daly *et al.*, 1991; Zhang, Mück, Bode *et al.*, 1992, Zhang *et al.*, 1995, Zhang, Soltner, Wolters *et al.*, 1997, Zhang, Zander *et al.*, 1997, Zhang, Wolters *et al.*, 1997; Hein *et al.*, 1995). Zhang, Mück, Bode *et al.* (1992) described an S-shaped microstrip resonator with the 100 100 μm² SQUID loop in its central region [Fig. 29(b)]; subsequently, the loop was reduced to 100 100 μm² (Mück, 1993), with the longer side parallel to the edge of the resonator. The microstrip was formed by placing the
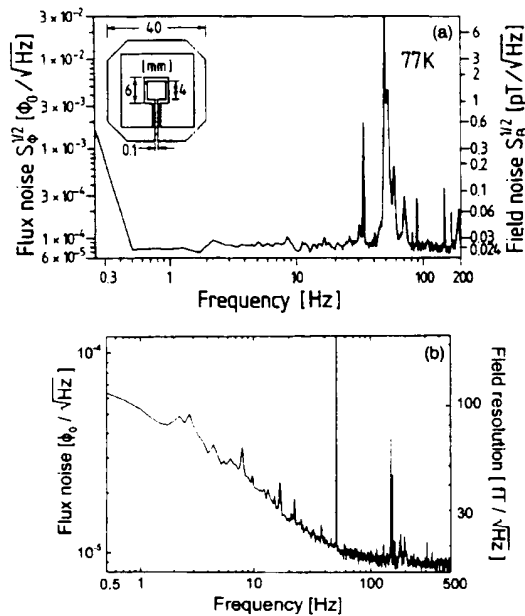
FIG. 30. Noise of rf SQUID magnetometers: (a) Magnetic flux and magnetic-field noise of 150-MHz SQUID with single-layer flux transformer with the configuration shown in the inset (Zhang *et al.*, 1994). (b) Magnetic-field noise of microwave resonator SQUID with 13-mm flux concentrator shown in Fig. 29(c) (Zhang, Wolters *et al.*, 1997).

0.5-mm-thick LaAlO$_3$ substrate on a copper ground-plane, and coupled to the room-temperature electronics via a 50 Ω coaxial cable. At 3 GHz, the best of these devices yielded a flux noise of $1.6 \times 10^{-5} \Phi_0$ Hz$^{1/2}$, corresponding to a noise energy of about 6×10^{-30} JHz^{-1}. However, the small effective area of the SQUID resulted in a relatively high magnetic-field noise, about 1 pT Hz$^{-1/2}$.

Subsequently, Zhang and coworkers improved the magnetic-field sensitivity of microwave SQUIDs operating at about 1 GHz. In their first design, Zhang *et al.* (1995) used a stack of $10 \times 10 \times 1$ mm^3 SrTiO$_3$ substrates, stacked face-to-face, as a dielectric resonator. The stack was placed above a 4×4 mm^2 washer SQUID with a $60 \times 60 \mu$m^2 inner hole. The stack was driven at resonance via a capacitively coupled line and the output voltage was also coupled out capacitively via a second line. With a frequency of 0.911 GHz and under optimum conditions, the flux noise was $10^{-5} \Phi_0$ Hz$^{-1/2}$ and the magnetic-field noise was 105 fT Hz$^{-1/2}$; the latter noise was improved to 30 fT Hz$^{-1/2}$ by means of a single-layer flux transformer with a 22 mm pickup loop.

In a later design, Zhang, Soltner, Wolters *et al.* (1997) used an integrated resonator in which the circular rf SQUID was surrounded by a line, patterned in the same YBCO film, containing a gap that provided the capacitance necessary for the resonant circuit. The signal from the resonator was coupled out either capacitively or inductively; inductive coupling has the advantage that the coil can also be used for both flux modulation and flux feedback. At frequencies from 0.511 to 1.1 GHz typical values of Q were around 5000, so that the requirement $\kappa^2 Q > 1$ was readily achievable. In the latest version of this device, Zhang, Zander *et al.* (1997) and Zang, Wolters *et al.* (1997) used the coplanar resonator designs shown in Fig. 29(c). Two coplanar lines surround the flux concentrator, which is coupled to the rf SQUID washer (2.5 or 3.5 mm in diameter) in a flip-chip configuration. The relative position of the gaps in the coplanar lines and the location of a short between them allows one to adjust the resonance frequency. For a SQUID with a $10 \times 500 \mu$m^2 inner hole ($L \approx 260$ pH) coupled to a resonator with a 13-mm-diameter flux concentrator, Zhang, Wolters *et al.* (1997) obtained a white flux noise of $8.5 \times 10^{-6} \Phi_0$ Hz$^{-1/2}$, corresponding to a noise energy of 6×10^{-31} JHz^{-1} and a magnetic-field noise of 16 fT Hz$^{-1/2}$ [Fig. 30(b)]. The noise at 1 Hz, however, was substantially higher, about 100 fT Hz$^{-1/2}$, and most likely arose from the motion of vortices in the resonator. This configuration is particularly appealing in its simplicity, enabling one to design the device with appropriate parameters very straightforwardly and offering simple fabrication with a minimum of additional cryogenic components.

In a further step towards higher sensitivity, very recently Zhang *et al.* (1998) described a new design in which a multiturn flux transformer is integrated with the coplanar resonator. The pickup loop is connected to two coils, a multiturn coil to couple in low-frequency signals and a single-turn coil to couple in rf currents. A two-hole SQUID is coupled to these coils in a flip-chip configuration to form a magnetometer. The separation of rf and low-frequency currents is a key factor that enables the authors to achieve a high quality factor.

C. 1/f noise

In the rf SQUIDs described above the onset of $1/f$ noise generally occurs at a relatively low frequency—1 Hz or less—provided one uses a flux-locked loop. This low $1/f$ knee frequency is due in part to the fact that the white flux noise is generally higher than for dc SQUIDs, but the major reason is the action of the readout scheme in eliminating $1/f$ noise arising from critical-current fluctuations (Giffard, 1980; Mück, Heiden, and Clarke 1994). We first describe this effect for hysteretic SQUIDs.

We first consider the effect on $V_T^{(0)}$ [Eq. (2.11)] of a fluctuation δI_0 in I_0 at a frequency much less than $\omega_{rf}/2\pi$. The value of Φ_c is increased to $L(I_0 + \delta I_0)$, so that the transitions from the $k = 0$ state to the $+1$ and -1 states occur at the flux values $L(I_0 + \delta I_0)$ and $-L(I_0 + \delta I_0)$, respectively. As a result, $V_T^{(0)}$ is increased to

$$\tilde{V}_T^{(0)} = \omega_{rf} L_T (\Phi_c + L \delta I_0)/M. \tag{7.1}$$

We see that $1/f$ noise in the critical current results in a $1/f$ noise component in the demodulated rf voltage.

However, when the SQUID is flux modulated and operated in a flux-locked loop, the effect of critical-current fluctuations is greatly reduced. Consider the effect of an applied flux $\delta\Phi$ $\Phi_0/2$ on the characteristics shown in Fig. 6. The asymmetry introduced into the hysteresis loops causes the SQUID to make its transition from the k 0 to the k 1 state at a lower rf flux, reducing the voltage across the tank circuit to

$$V_T^{(\delta)} \quad \omega_{rf}L_T(\Phi_c \quad \delta\Phi)/M \quad (0 \quad \delta\Phi \quad \Phi_0/2). \quad (7.2)$$

In the region DF of Fig. 6(c), the SQUID traverses only the k 0 k 1 hysteresis loop. Similarly, if we now change the flux to $\delta\Phi$ ($|\delta\Phi|$ $\Phi_0/2$), the voltage is

$$V_T^{(\ \delta)} \quad \omega_{rf}L_T|(\quad \Phi_c \quad \delta\Phi)|/M \quad (\quad \Phi_0/2 \quad \delta\Phi \quad 0). \quad (7.3)$$

The SQUID now traverses only the k 0 k 1 hysteresis loop; the modulus sign in Eq. (7.3) reflects the fact that the detection of the peak value of the rf voltage is insensitive to whether the transition occurs on a positive or negative peak of the rf current. Suppose now that I_0 undergoes a slow fluctuation to a new value I_0 δI_0. The peak voltage across the tank circuit changes to

$$\tilde{V}_T^{(\ \delta)} \quad \omega_{rf}L_T(\Phi_c \quad L\delta I_0 \quad \delta\Phi)/M \quad (0 \quad \delta\Phi \quad \Phi_0/2) \quad (7.4)$$

and

$$\tilde{V}_T^{(\ \delta)} \quad \omega_{rf}L_T| \quad (\Phi_c \quad L\delta I_0) \quad \delta\Phi|/M$$
$$(\quad \Phi_0/2 \quad \delta\Phi \quad 0). \quad (7.5)$$

We see that the effect of a (say) positive fluctuation δI_0 is to increase $\tilde{V}_T$ uniformly for all values of applied flux; correspondingly, the demodulated voltage vs flux curve will be shifted uniformly to a higher voltage. However, when the usual modulating flux at frequency f_m with a peak-to-peak amplitude of $\Phi_0/2$ is applied to the SQUID, the amplitude of the resulting voltage at f_m is unaffected by this shift. Thus, when this signal is mixed down with the same frequency f_m, the resulting quasistatic output voltage is unaffected by fluctuations in the critical current. Any slow fluctuations in the amplitude of the rf driving current are similarly suppressed.

Mück, Heiden, and Clarke (1994) examined the $1/f$ noise in Nb rf SQUIDs operated in the hysteretic mode at 4.2 K. For a SQUID at 3 GHz, operated in a flux-locked loop with conventional flux modulation, they found that the flux noise was white at frequencies down to below 0.5 Hz. However, when they operated the SQUID open loop in the absence of flux modulation, the spectral density of the noise was $1/f$ at frequencies below about 1 kHz, and three orders of magnitude higher at 1 Hz than in the previous measurement. These results show very clearly that the conventional operating mode of the rf SQUID eliminates the effects of critical-current fluctuations.

In the case of nonhysteretic rf SQUIDs (β_L 1), the critical current is small so that the amplitude of the $1/f$ noise fluctuations in the critical current, which scales as

I_0, is also correspondingly low. This factor contributes to the low level of $1/f$ flux noise observed in these devices (Chesca, 1998). In addition, flux modulation suppresses $1/f$ flux noise due to critical-current fluctuations (Mück, Clarke, and Heiden, 1994). The value of the tank circuit voltage V_T is proportional to I_0 [Eq. (2.19)], but in addition V_Φ also depends on I_0 [Eq. (2.20)]. As a result, a fluctuation in I_0 results in not only a fluctuation in the component of V_T at the same frequency but also in the amplitude of the component at the flux modulation frequency. Since, however, the feedback loop is (ideally) sensitive only to the phase of the flux modulation, these amplitude fluctuations will not contribute to the output of the phase-sensitive detector. Thus critical-current fluctuations are suppressed by modulation and feedback as in the hysteretic mode.

VIII. GRADIOMETERS

In Sec. VI we described magnetometers with a white noise level below 10 fT Hz $^{1/2}$, a sensitivity adequate for most practical applications. However, in many of these applications—good examples are magnetocardiology and nondestructive evaluation—one needs to detect weak signals against a background of magnetic noise that is many orders of magnitude higher. In urban environments, the dominant source of noise is the 50 or 60 Hz signals, and a large number of harmonics, from power lines: peak-to-peak amplitudes can range from 20 nT to 1 μT. Additionally, traffic (trains, subways, cars) can cause even stronger disturbances. For this reason, most sensitive measurements with low-T_c magnetometers—particularly of biomagnetic signals—are currently made in a magnetically shielded room. However, except for enclosures, such as that at the PTB, Berlin, with very high levels of attenuation, most shielded rooms do not reduce the 50 or 60 Hz fields sufficiently, and one requires a gradiometer to discriminate against distant noise sources with small gradients in favor of nearby signal sources. The traditional low-T_c gradiometer is wound from niobium wire: two pickup loops wound in opposition and mounted on a common axis with a baseline (separation) of typically 0.1 m are connected in series with an input coil inductively coupled to a SQUID (Zimmerman and Frederick, 1971). Such a device measures the first-derivative axial gradient $\partial B_z/\partial z$. The addition of a third coil midway between the two loops results in a second-derivative gradiometer measuring $\partial^2 B_z/\partial z^2$. In the case of axial gradiometers, the separation of one pickup loop and the signal source is generally made rather less than the baseline, so that the instrument effectively detects the magnetic field from the source. Thin-film gradiometers have also been made, measuring either an axial gradient (Hoenig *et al.*, 1991) or more usually planar devices measuring an off-diagonal gradient of the form $\partial B_z/\partial x$ (Hämäläinen *et al.*, 1993).

Early wire-wound gradiometers were balanced by adjusting the positions of small, superconducting pellets, sometimes to an accuracy of 1 part in 10^6. (We define

"balance" as the ratio of the output of the SQUID when a uniform magnetic field is applied to the gradiometer to the output when the same field is applied to one pickup loop.) However, a myriad of interacting, mechanically adjusted components becomes impractical for more than a few channels. Current practice is to use magnetometers and first-derivative gradiometers for the software generation of second or third derivatives (Vrba, 1996).

The lack of suitable wire eliminates the wire-wound, high-T_c gradiometer as an option, and two alternative approaches have been adopted. The first is an electronic gradiometer made by subtracting the signals from separate magnetometers: the gradiometer can be axial or planar, and the baseline can be chosen at will. The second is a planar gradiometer with thin-film pickup loops.

A. Electronic subtraction gradiometers

A high-T_c, axial gradiometer was demonstrated by Tavrin *et al.* (1993a), who mounted two rf SQUIDs one above the other, each with a bulk flux focuser (Zhang, Mück, Herrmann *et al.*, 1992). One sensor was mounted rigidly while the plane inclination of the second, placed 60 mm above, could be adjusted from outside the cryostat to achieve a balance of about 1 part in 10^3. This system was used to measure magnetocardiograms (MCG) (Sec. X.A) in an unshielded environment, against a 50 Hz background of 1 to 20 nT, although the quality of the cardiograms was limited by $1/f$ noise in the magnetometers, about 1 pT Hz $^{1/2}$. Subsequently, Tavrin *et al.* (1994) added a third, vertically stacked sensor to form a second-derivative gradiometer. The lowest sensor was rigidly mounted, while the inclination of the other two, 60 and 120 mm above it, could be adjusted. The three channels, A, B, and C could be added electronically to generate two first-derivatives, A B and B C, and the second derivative, A $2B$ C. The system could be balanced to achieve a common mode rejection ratio of 1 part in 3000 and a gradient rejection of 1 part in 100. The magnetic-field noise referred to SQUID A or C was below 300 fT Hz $^{1/2}$. Once balanced, the unit required no readjustment after thermal cycling and after transporting it over long distances in the course of examining some 200 human subjects. A similar electronically formed axial gradiometer was recently reported by Borgmann *et al.* (1997) who used a set of adjustable superconducting plates, similar to those in early low-T_c gradiometers, to achieve the final balance. The authors achieved a balance better than 10^4 for uniform background fields and better than 200 for gradient fields. Electronic gradiometers have also been constructed with the magnetometers in the same plane (David *et al.*, 1997; ter Brake, Janssen *et al.*, 1997).

The balance of an electronic gradiometer is limited by the linearity of the flux-locked magnetometers and by the common mode rejection ratio of the subtraction system. In the presence of high background noise, the dynamic range and slew rate of the magnetometers may be challenged. None of these difficulties arises with superconducting gradiometers, which thus have an inherent
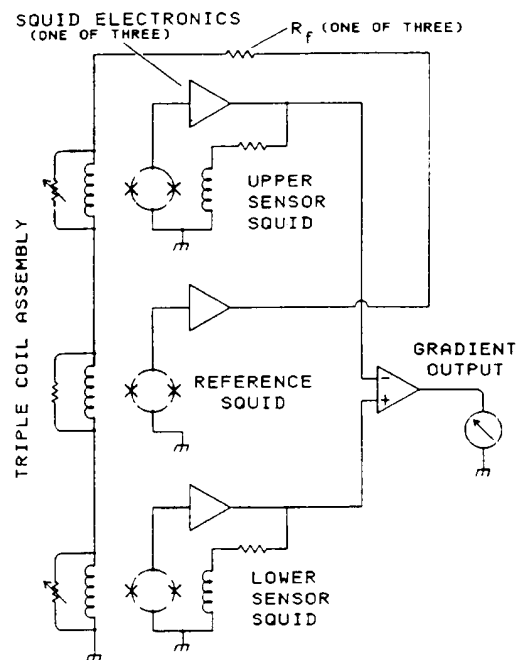

FIG. 31. Configuration of three-SQUID gradiometer (Koch *et al.*, 1993).

advantage over electronic cancellation. However, the three-SQUID gradiometer (TSG) of Koch *et al.* (1993), shown in Fig. 31, also circumvents these problems by using electronic cancellation and subtraction. The center, reference magnetometer operates in a flux-locked loop and applies its output also to a coil coupled to each of the outer magnetometers. Thus the environmental noise at each of the two sensing magnetometers is greatly attenuated, reducing their linearity and slew-rate requirements. The signals from the outer two sensors are then subtracted to form a first-derivative gradiometer. Koch and co-workers demonstrated several versions of the TSG, with baselines of 0.1 to 0.25 m and using both low-T_c and high-T_c SQUIDs. The balance can be adjusted to about 1 part in 4000 by adjusting the feedback currents with room-temperature resistors. A key advantage of this approach is that any noise generated by the central sensor is applied equally to the two outer magnetometers and eliminated in the subtraction. As a result, one can use less sensitive SQUIDs to generate the canceling fields or even a total-field magnetometer, such as a flux gate, which can be used to cancel not only the fluctuating fields but also the static field. However, one difficulty with most flux gates is that their bandwidth is typically limited to 100 Hz, so that they cannot be used to cancel harmonics of the 50 or 60 Hz signal. In their original publication, Koch *et al.* reported a white gradient noise of 6 pT m ^{1} Hz $^{1/2}$ for SQUIDs with 3 $\times$ 3 mm^2 flux-focusing washers. For a baseline of 0.1 m, this result corresponds to a magnetic-field noise of 600 fT Hz $^{1/2}$ referred to one sensor.

B. Gradiometric flux transformers

Electronic subtraction enables one to choose an arbitrary baseline and to adjust the balance externally. Experience with low-T_c devices, however, shows that it is notoriously difficult to operate such systems in the harsh environment of a laboratory or a hospital and to achieve an adequate signal-to-noise ratio for clinical applications. Low-T_c systems intended for unshielded operation invariably have a gradiometric flux transformer to bear the brunt of the large level of background noise; even then, an adequate signal-to-noise ratio in unfavorable situations may not be possible (Vrba, 1996). Thus there are strong incentives to develop high-T_c equivalents, albeit in planar geometries. An early gradiometer fabricated from a YBCO-STO-YBCO multilayer (Eidelloth *et al.*, 1991) employed a multiturn input coil coupled to two pickup loops of opposite senses in the same plane. The baseline was about 5 mm. The multiturn coil was coupled to a square-washer SQUID in a flip-chip arrangement. At the time, multilayer technology was still in its infancy and the device exhibited substantial levels of $1/f$ noise. The best reported gradient noise at 10 Hz was 400 pT m^{-1} Hz$^{-1/2}$. A similar flip-chip gradiometer with improved $1/f$ noise was reported later by Keene, Chew *et al.* (1994). However, both gradiometers exhibited poor balance because of the unbalanced SQUID. The balance was improved by two orders of magnitude to about 1 part in 1000 by means of gradiometrically configured SQUIDs (Keene, Chew *et al.*, 1994; Keene *et al.*, 1995).

An alternative gradiometer configuration (Ketchen *et al.*, 1978) consists of two pickup loops in parallel with a SQUID measuring the current induced along the common line [(Fig. 32(a)]. This configuration has the disadvantage that large supercurrents are induced around the perimeter when the device is rotated in an ambient field. Knappe *et al.* (1992), Zakosarenko *et al.* (1994), Daalmans *et al.* (1995), Schultze, Stolz *et al.* (1997), Schmidl, Wunderlich, Dörrer, Specht *et al.* (1997) and Dörrer *et al.* (1997) have all made single-layer, first-derivative gradiometers of this kind, using dc SQUIDs with either step-edge or bicrystal junctions. The baselines are limited by the size of the substrate to about 5 mm, and the best gradient sensitivities are about 50 pT m^{-1} Hz$^{-1/2}$. All the dc SQUID-based gradiometers described above have the disadvantage that the SQUID itself has a non-zero response to magnetic field, producing an intrinsic imbalance. This problem is circumvented in the rf SQUID-based gradiometer by Zhang, Soltner, Krause *et al.* (1997), resembling the configuration of Fig. 32(a), with a single, step-edge junction intersecting the central strip. This structure is a re-creation of the Nb "two-hole" rf SQUID (Zimmerman *et al.*, 1970). The device had a baseline of about 5 mm and was balanced to 1 part in 1000. The gradient field noise was about 100 pT m^{-1} Hz$^{-1/2}$ above 10 Hz. One of these gradiometers was used to perform eddy-current measurements of cracks in aluminum in an unshielded environment.
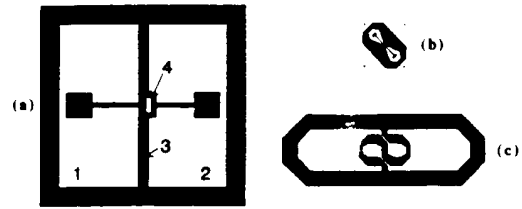

FIG. 32. Gradiometers: (a) Principle of single-layer, planar gradiometer with parallel inductances 1 and 2. A gradient $\partial B_z/\partial_x$ induces a current in the central strip 3 that links flux to the SQUID 4 (Daalmans, 1995). (b) First-derivative planar gradiometer on a 10 × 10 mm^2 chip that is coupled to (c) the gradiometric structure on a two-inch substrate (Faley *et al.*, 1997).

Several attempts have been made to extend the baseline using single-layer gradiometers in a flip-chip arrangement (Daalmans, 1995; Faley *et al.*, 1997). The concept is illustrated in Figs. 32(b) and (c) (Faley *et al.*, 1997), which shows a dc SQUID with quasiplanar PBCO junctions on a 10 × 10 mm^2 chip that is inductively coupled to a gradiometric flux transformer on a 50 mm substrate. The central strip in the transformer is intended to reduce the inductance and pickup area of the SQUID by screening. The baseline was 20 mm, the balance about 1 part in 1800 and the noise 5 pT m^{-1} Hz$^{-1/2}$ at 1 kHz. A comparable sensitivity was reported by Daalmans (1995).

It should be noted that all the single-layer, thin-film gradiometers lose substantial sensitivity because the inductances of the pickup loops are mismatched to the input coil coupling them to the SQUID. This drawback, together with the relatively short baseline of even the largest devices (20 mm) implies that none of them is practicable for applications such as magnetocardiology. However, as demonstrated already, they may be well-suited to nondestructive evaluation (NDE). To achieve high enough sensitivity and a long enough baseline for magnetocardiology with this approach would require a multiturn input coil fabricated on a substrate at least 50 mm and preferably 100 mm in length. This somewhat daunting prospect has yet to be tackled.

A new approach to single-layer, thin-film gradiometers was recently demonstrated by Dantsker, Froehlich *et al.* (1997) who fabricated the asymmetric, planar gradiometer shown schematically in Fig. 33(a). The gradiometer consists of a directly coupled SQUID magnetometer with a pickup loop of inductance L_m and area A_m, and a superconducting flux transformer with an input loop of inductance L_i and area A_i connected to a pickup loop of inductance L_p and area A_p. The mutual inductance between the magnetometer and input loop is $M_i = \alpha(L_m L_i)^{1/2}$. With a suitable choice of these parameters, one attains the balance condition

$$\alpha = [A_m/(A_p - A_i)](L_p - L_i)/(L_i L_m)^{1/2} \tag{8.1}$$

for which the directly coupled magnetometer produces zero response to a uniform magnetic field B_z. On the other hand, a magnetic field δB_z applied only to the
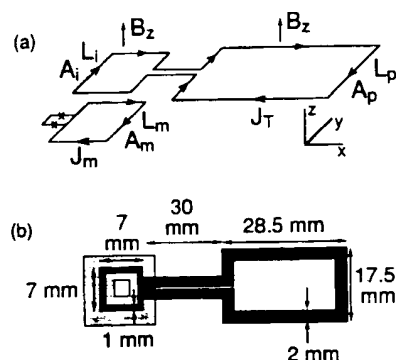
FIG. 33. Configuration of asymmetric, planar gradiometer coupled to a directly coupled magnetometer: (a) schematic, (b) experimental (shaded square represents magnetometer) (Dantsker, Froehlich *et al.*, 1997).

magnetometer and the input loop induces a current δJ_m $\eta \delta B_z A_m / L_m$ in the magnetometer loop, where

$$\eta \quad [L_p/L_i \quad 1 \quad \alpha(L_m/L_i)^{1/2}A_i/A_m]/(L_p/L_i \quad 1 \quad \alpha^2)$$

(8.2)

represents the screening effect of the flux transformer.

The physical configuration of the gradiometer is shown in Fig. 33(b). The single-layer directly coupled magnetometer was patterned in a 150-nm-thick YBCO film laser-deposited on a 10 10 mm^2 SrTiO$_3$ bicrystal. The outer and inner dimensions of the magnetometer loop are 10 and 2 mm, respectively, yielding an estimated inductance L_m 4 nH and area A_m 20 mm^2. The flux transformer was fabricated from a 260-nm-thick YBCO film coevaporated on a 100 mm *r*-plane sapphire wafer. For these dimensions, balance is predicted to occur for α 0.43 0.04. The corresponding value η 0.95 implies that the flux transformer reduces the intrinsic sensitivity of the magnetometer by only 5%. The baseline—the separation between the midpoints of the two loops—is 48 mm.

The gradiometer was balanced by sliding the flux transformer over the magnetometer, immersed in liquid nitrogen, thereby varying the coupling coefficient α. A balance of about 1 part in 3000 was achieved with respect to magnetic fields perpendicular to the plane of the gradiometer, while the intrinsic balance with respect to in-plane fields was about 1 part in 1400. Operated in an unshielded environment, the gradiometer reduced the 60 Hz peak by a factor of 1600 compared with the bare magnetometer.

This approach to gradiometers has several advantages. The fact that the intrinsic magnetic-field sensitivity of the magnetometer is reduced by only a few percent by the presence of the transformer is particularly appealing for high-T_c devices, for which resolution is at a premium. It should not be necessary to use particularly high quality films, since vortex motion in a flux transformer with a relatively large area and inductance does not contribute significantly to the overall $1/f$ magnetic-field noise (Koelle, Miklich, Dantsker *et al.*, 1993). The

general principle can be extended to other derivatives of the magnetic field: for example, the addition of a second, identical pickup loop on the opposite side of the input loop would produce a gradiometer sensitive to $\partial^2 B_z / \partial x^2$. The high degree of balance and long baseline make this gradiometer eminently suitable for multichannel arrays for biomagnetic measurements. However, it would be impracticable to balance these gradiometers mechanically—a more realistic approach might be to mount the transformer permanently on the magnetometer and to achieve the final balance by laser trimming.

Finally, which of these gradiometers should one use? Currently, the two major applications are biomagnetism and NDE (Secs. X.A and X.B). For NDE, one generally does not require particularly high sensitivity, and a relatively compact, single-layer gradiometer with a baseline of 5–10 mm is likely to be adequate. For biomagnetism, the situation is more complex. Good results have been achieved with electronic subtraction of magnetometers, but limitations of slew rate, linearity and CMRR present difficulties for unshielded operation. Still, this approach is the only one that can measure an axial gradient. For the immediate future, at least, gradiometric flux transformers are limited to planar configurations. Ideally, one would like to fabricate a long-baseline gradiometer with a multiturn, multilayer input coil, with an inductance to match that of the pick-up loops, inductively coupled to the SQUID. In practice, the cost of manufacturing such structures on large substrates—say, four inch—is likely to be prohibitive. The best alternative would seem to be the asymmetric, planar gradiometer, provided it can be balanced adequately without recourse to mechanical adjustment.

IX. SQUID'S IN UNSHIELDED ENVIRONMENTS

Sections VI and VII illustrate the low levels of magnetic flux and field noise achieved with high-T_c SQUIDs and magnetometers. All these results, however, were obtained with the devices cooled and operated inside magnetic shields which attenuate the ambient static and time-varying fields by large factors. In this section, we discuss the operation of high-T_c SQUIDs in the ambient environment, without magnetic shielding, as is essential for some applications. For example, it is obviously impractical to shield an airplane wing undergoing nondestructive evaluation. In the case of geophysical applications, one measures fluctuating magnetic fields generated either naturally or by man-made sources, and has no option other than to operate the magnetometer unshielded. In biomagnetic measurements, magnetically-shielded rooms large enough to enclose a patient and multiple SQUID sensors are commercially available and have been widely used with low-T_c SQUIDs, but their price—as high as \$0.5 M—adds substantially to the overall cost of the system. This is particularly true for systems with a relatively small number of channels, for example, for magnetocardiology, and the elimination of the MSR would do much to make such techniques more financially accessible.

A SQUID exposed to the ambient environment is adversely affected by a variety of sources. These can be categorized into sources that are extrinsic—arising directly from the environment—and sources that are intrinsic to the SQUID. Examples of environmental noise sources are nearby power lines (typical amplitudes are 20 nT-1 μT at 50 or 60 Hz), computer displays (40 to 80 Hz), lasers, elevators, and automobiles. These extrinsic noise sources and their harmonics and intermodulation products obscure the signal of interest such as a magnetocardiogram, and their reduction requires gradiometers (Sec. VIII) or active cancellation. One possible intrinsic effect is the reduction of the critical current, resulting in a decrease in the transfer function and an increase in the white noise. For example, Miklich *et al.* (1994) found that the critical current of their 3-μm-wide bicrystal junctions decreased by 15% when they were cooled in a 100 μT field. However, this problem can be largely eliminated by reducing the width of the junctions: Dantsker, Tanaka, and Clarke (1997) found an insignificant reduction in the critical current of 1-μm-wide junctions cooled in 130 μT. We note that ramp-edge junctions are intrinsically shielded and also suffer a negligible critical current reduction in comparable fields (Faley, Poppe, Urban *et al.*, 1995).

A. 1/f noise

The low-frequency flux noise power of most high-T_c SQUIDs increases when they are cooled in the earth's field, by as much as a factor of 50. This increase is caused by the thermally activated hopping of weakly pinned vortices which penetrate the YBCO film during cooling. Ferrari *et al.* (1994) used a low-T_c dc SQUID to measure the noise in YBCO films cooled in static fields B_0 and found that at low frequencies $S_\Phi(f)$ scaled as $1/f$ for cooling fields above a few μT. Furthermore, $S_\Phi(f)$ scaled linearly with B_0 [Fig. 34(a)], as expected for the uncorrelated hopping of vortices since $S_\Phi(f)$ is expected to be proportional to the number of vortices and hence to B_0. Miklich *et al.* (1994) found similar increases for a dc SQUID [Fig. 34(b)] and a directly coupled magnetometer, although $S_\Phi(f)$ did not always scale linearly with B_0. Other authors (Faley, Poppe, Urban *et al.*, 1995; Tanaka *et al.*, 1995; Glyantsev *et al.*, 1996) confirmed these findings, in SQUIDs, and Keene *et al.* (1996) found that the low-frequency noise of their planar gradiometers increased substantially for cooling fields above 15 μT. The flux noise for the SQUID in Fig. 34(b) at B_0 50 μT is about 200 $\mu\Phi_0$/Hz$^{1/2}$ at 1 Hz. Even coupled to the best flux transformer described in Sec. VI.C, this excess noise would limit the magnetic-field resolution to about 400 fT/Hz$^{1/2}$, an order of magnitude greater than that of the most sensitive sensors in zero field. Recently, however, Schmidt *et al.* (1996) showed that the flux noise in one of their directly coupled magnetometers, about 10 $\mu\Phi_0$ Hz$^{1/2}$ at 1 Hz, was nearly independent of magnetic field up to 100 μT, but gave no details of the fabrication process or geometry.
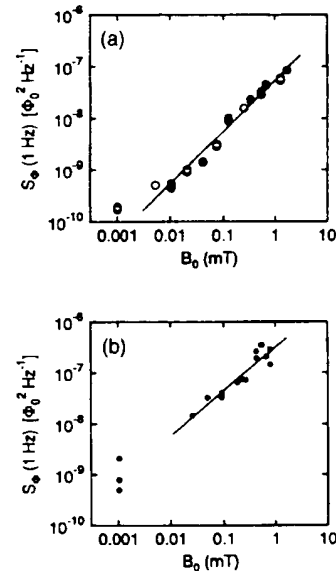

FIG. 34. Flux noise S_Φ (1 Hz) vs cooling field B_0: (a) for a YBCO film at 77 K, measured with a low-T_c SQUID. Filled and open circles indicate reversed direction of B_0, line is least-squares fit. (b) for YBCO dc SQUID with bicrystal junctions and 250-μm washer, measured with bias reversal (Miklich *et al.*, 1994).

Reduction of the excess $1/f$ noise in SQUIDs operated in unshielded environments is clearly essential. One must eliminate either the motion or the presence of flux vortices, and we now examine the approaches that have been investigated.

To reduce the motion of a given density of vortices, one has to create strong pinning sites. Shaw *et al.* (1996) showed that proton or heavy-ion irradiation of single crystals of YBCO not only increased the critical-current density but also reduced the $1/f$ noise substantially. However, the critical-current densities were still substantially lower and the $1/f$ noise in ambient fields still substantially higher than the values in thin films. Furthermore, heavy-ion irradiation at doses up to the level at which T_c starts to degrade does not increase the critical current of thin films that already have high critical-current densities (Barbour *et al.*, 1992), implying that pinning in these films as grown is already close to optimum. Thus it seems unlikely that this approach will materially reduce the level of $1/f$ noise in thin YBCO films cooled in an ambient magnetic field.

One method of eliminating the excess $1/f$ noise is to cancel the static field that causes it. For medical applications, some groups, for example Aarnink *et al.* (1995), have used a three-axis flux-gate magnetometer as a reference sensor that controls the current through three orthogonal sets of cancellation coils surrounding the dewar. This technique can reduce the ambient field to about 1%, but the flux-gate magnetometers themselves generate excess noise. This noise can be reduced if one
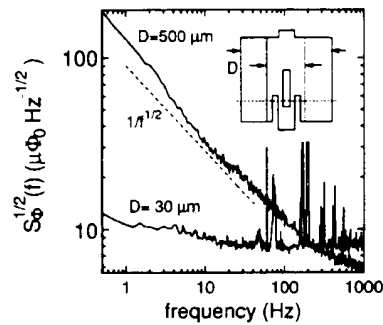
FIG. 35. $S_\Phi^{1/2}(f)$ for dc SQUID shown in the inset cooled in a field of 24 μT. Upper trace is for device with outer dimension D 500 μm, lower trace is after repatterning to a width D 30 μm (dotted lines). Inset not to scale. Dashed line indicates grain boundary (Dantsker *et al.*, 1996).

uses SQUID gradiometers. A simpler and perhaps more practical version of this method is the three-SQUID gradiometer (Koch *et al.*, 1993, see Sec. VIII.A) with the reference SQUID replaced with a flux-gate magnetometer. Of course, none of these methods is appropriate for geophysical measurements in which one is interested in fluctuations in the ambient magnetic field.

The most practical method of eliminating the excess $1/f$ noise is to design the superconducting components of the magnetometer so that flux vortices do not enter. For a film of width w cooled in a perpendicular field B_0, Clem(1996) has shown that it is energetically unfavorable for flux to penetrate provided $w \leq (\pi\Phi_0/4B_0)^{1/2}$. Dantsker *et al.* (1996) studied the $1/f$ noise produced by SQUIDs with various film widths as a function of the magnetic field in which they were cooled. The upper trace of Fig. 35 is the flux noise $S_\Phi^{1/2}(f)$ of a square-washer bicrystal SQUID with outer dimensions of 500 μm and a slit 100 μm long and 4 μm wide, cooled in 24 μT. The observed $1/f$ spectrum is typical for such devices. The SQUID was subsequently repatterned to reduce the outer dimension to 30 μm and the linewidth to 13 μm, as indicated by dotted lines in the inset. The lower trace shows that the low-frequency noise is dramatically lower, by two orders of magnitude in power at 1 Hz. Similar measurements on SQUIDs with linewidths ranging from 4 to 13 μm showed that the flux noise at 1 Hz, typically 8–20 $\mu\Phi_0$ Hz $^{1/2}$, was independent of the cooling field up to a threshold B_T, above which the noise increased rapidly, indicating that vortices begin to penetrate the film. Although B_T increased with decreasing linewidth, the increase was slower than Clem's model predicts. For example, in the first batch of devices B_T was about 33 μT for w 4 μm, a field about three times less than the predicted value $\pi\Phi_0/4w^2 \approx 100$ μT. It was suggested that poor-quality edges, which offer low-energy sites where vortices tend to nucleate, were the most likely cause of the lower threshold. However, subsequent work (see below) showed that threshold fields of over 100 μT could be achieved with more carefully patterned edges. We note that edges should be vertical
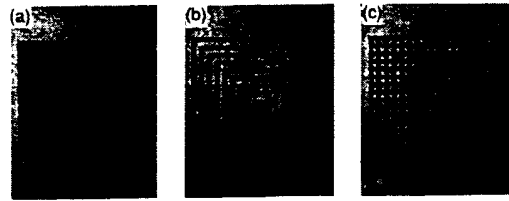

FIG. 36. Photographs of (a) a solid, thin-film dc SQUID, (b) a SQUID with eight slots and (c) with 248 holes. The outer dimensions of each device are 186 μm 204 μm (Dantsker, Tanaka, and Clarke, 1997).

to give the highest threshold field, a requirement that is the antithesis of the smoothly beveled edges needed for multilayer structures.

We now discuss the implications of this result to directly coupled magnetometers in which we use a SQUID with a narrow linewidth. We show that the pickup loop is expected to add negligible $1/f$ noise even though its linewidth is often several millimeters wide and thus the film is penetrated by vortices even in low cooling fields. The motion of the vortices generates screening currents which couple an indirect flux noise $S_\Phi^{in}(f)$ to the SQUID. For a square pickup loop of outer and inner dimension d_1 and d_2 and inductance L_p, this indirect noise is given by (Dantsker *et al.*, 1996)

$$S_\Phi^{in}(f) \approx S_\Phi^U(f)\alpha_d^2(L/L_p)^2(d_1 \quad d_2)/(d_1 \quad d_2). \quad (9.1)$$

Here, $S_\Phi^U(f)$ is the spectral density of the flux noise of an unpatterned YBCO film measured by a SQUID placed directly over it, typically 10 ^{9} Φ_0^2/Hz at 1 Hz for high-quality films cooled in B_0 50 μT (Ferrari *et al.*, 1994). Taking the typical values $L \approx 20$ pH, $\alpha_d \approx 1$ and $L_p \approx 5$ nH for a magnetometer pickup loop with $d_1 \approx 10$ mm and $d_2 \approx 2$ mm, we find S_Φ^{in} (1 Hz) $\approx 10^{-14} \Phi_0^2$/Hz. This value is several orders of magnitude below the flux noise of the SQUID (for example, Fig. 35). The best directly coupled magnetometers on a 10 10 mm^2 substrate have a noise of about 50 fT Hz $^{1/2}$ (Lee *et al.* 1995; Beyer *et al.*, 1998), and with appropriate SQUID design it should be possible to achieve this result in the earth's field at frequencies down to (say) 1 Hz. This would be adequate for most geophysical applications.

We turn next to a discussion of multilayer devices. In the case of the multiloop magnetometer (Sec. VI.D), at least in principle, it should be possible to reduce all the linewidths to (say) 4 μm, so that the $1/f$ noise should not increase in ambient fields up to about 100 μT. For a square-washer SQUID coupled to a multiturn flux transformer, however, it is clearly out of the question to reduce the outer dimensions of the SQUID. Dantsker, Tanaka, and Clarke (1997) tackled this problem using SQUIDs with the configurations shown in Figs. 36(b) and (c). Once again, the key is to maintain narrow linewidths. In the first design [Fig. 36(b)] the SQUID washer is interpenetrated by eight slots, each 8 μm wide, separating nine YBCO strips, each 4 μm wide. In the second design [Fig. 36(c)] 248 holes, each 8 8 μm, di-
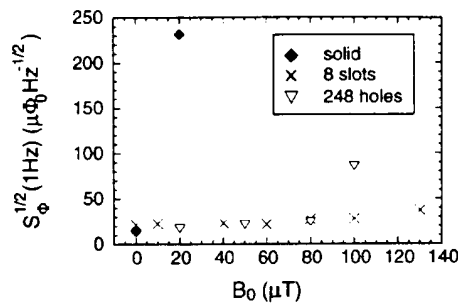
FIG. 37. $S_\Phi^{1/2}$ (1 Hz) vs cooling field B_0 for the three SQUIDs shown in Fig. 36 (Dantsker, Tanaka, and Clarke, 1997).

vide the washer into a grid of 4-μm-wide lines. Figure 37 compares $S_\Phi^{1/2}(1\,\text{Hz})$ for three devices made on a single chip in the configurations of Fig. 36, cooled in static magnetic fields B_0. The noise of the solid SQUID increases rapidly with B_0, much like the device in Fig. 34(b). The SQUID with slots, on the other hand, shows no significant increase in the noise for fields up to at least 100 μT. At 130 μT the noise has increased somewhat, suggesting that vortex entry occurred just below this field. For the device with 248 holes $S_\Phi^{1/2}$ (1 Hz) also shows no increase for cooling fields up to at least 80 μT. Furthermore, measurements of the mutual inductance M_i between each of the SQUIDs in Fig. 36 and a seven-turn input coil revealed that the presence of slots or holes reduces M_i by no more than 14%. Since the flux noise generated by the pickup loop is expected to be unimportant, these results suggest that it should be possible to operate magnetometers with multiturn input coils in the earth's magnetic field with no increase in $1/f$ noise.

However, it should be stressed that when a device is moved in an ambient magnetic field, the induced supercurrents are very likely to generate vortices and increase the noise. For example, Keene *et al.* (1996) rotated a planar gradiometer in static fields as high as 70 μT and measured a monotonic increase in the $1/f$ noise as they turned the device through 90°; furthermore they observed large random telegraph signals (RTS) over some narrow angular ranges. Thus, after any such devices are moved in a static field, it is likely to be necessary to raise their temperature briefly above T_c to release the induced currents.

Earlier, Koch *et al.* (1995) had investigated the effect of cooling a directly coupled magnetometer inside a magnetic shield which they subsequently removed, exposing the device to an ambient field. They showed that the current generated in the pickup loop by the field caused vortices to enter the material. Exposure to a field of 50 μT, for example, caused a substantial increase in the level of $1/f$ noise. We note that, according to our discussion concerning Eq. (9.1), the density of vortices generated by these currents must far exceed the density produced by the ambient field itself. If this were not the case, the $1/f$ noise contribution of the loop would be negligible. Koch *et al.* (1995) demonstrated that this flux

entry and ensuing $1/f$ noise could be prevented by means of a "flux dam"—a weak link in the pickup loop that limits the circulating current to its critical current. With the flux dam in place, exposing the magnetometer to 50 μT after a zero-field cool resulted in a considerably smaller increase in the $1/f$ noise. More recently, Milliken, Brown, and Koch (1997) reported a directly coupled magnetometer containing a flux dam in which the noise of several hundred fT Hz$^{-1/2}$ at 1 Hz did not increase significantly when the device was exposed to fields as high as 34 μT following a zero-field cool. Thus for magnetometers that are subject to being moved, the lowest levels of $1/f$ noise are likely to be achieved with a combination of narrow linewidths and a flux dam.

B. Hysteresis

Magnetic hysteresis in a SQUID-based instrument manifests itself as a shift of the voltage-flux characteristics along the flux axis after the magnetic field is cycled. This effect is undesirable if one wishes to keep track of the absolute value of the magnetic field or to measure gradients in large fluctuating background fields. Magnetic hysteresis is observed for low-T_c and high-T_c SQUIDs and is related to vortex entry and pinning near the edges of thin films (Koch *et al.*, 1989, Sun *et al.*, 1992; Sun, Gallagher, and Koch, 1993; Sun *et al.*, 1994; Clem *et al.*, 1993; Purpura *et al.*, 1993; Keene *et al.*, 1996). The degree of hysteresis is expressed by the hysteresis parameter $h \quad \delta\Phi/\Delta\Phi$, where $\delta\Phi$ is the flux error caused by sweeping the applied flux between $\Delta\Phi$. For integrated thin-film low-T_c gradiometers operated at 4.2 K in the ambient magnetic field, a magnetic hysteresis as low as 10^{-9}–10^{-11} (Koch, Ketchen *et al*, 1991) has been measured. Initial studies on high-T_c dc SQUIDs based on polycrystalline films showed high levels of nonlinear hysteresis (Foglietti *et al.*, 1989; Koch *et al.*, 1989). For grain-boundary dc SQUIDs involving epitaxial YBCO films on bicrystals, Gross and Chaudhari (1992) reported $h \quad 10^{-6}$ at 77 K for $\Delta\Phi \leq \Phi_0$.

Sun and co-workers made systematic studies of the hysteresis in low-T_c and high-T_c dc SQUIDs using cycling fields ranging from 10 μT to 1 mT peak to peak. In each case they found both time-independent and time-dependent hysteresis. The time-independent hysteresis appeared above a threshold field of a few hundred microtesla. The threshold field had a similar temperature dependence to the critical-current density of the thin films, suggesting a relation between this hysteresis and flux pinning. Sun *et al.* (1994) developed a quantitative model involving the Lorentz force on vortices due to screening currents, the surface barrier to flux entry, and the pinning force of defects in the superconducting film. Within this model they showed that the observed threshold field corresponds to the value at which the Lorentz force equals the sum of the surface barrier and the pinning force. Since the screening currents and hence the Lorentz force on a vortex are maximum at the edges of the film and decay into film, the vortices are swept into the film until the Lorentz force becomes smaller than
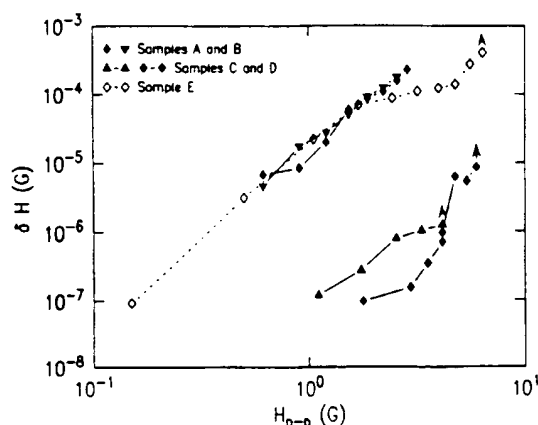
FIG. 38. Hysteresis of YBCO dc SQUIDs with a 240-μm square washer. Lower traces are for devices prepared with higher edge quality and show a significant reduction in hysteresis (Sun *et al.*, 1994).

the pinning force. The distance over which the vortices penetrate into the washer and the ensuing degree of hysteresis are predicted to depend crucially on the local pinning force near the film edges, in agreement with the dramatic reduction of the hysteresis achieved by improving the quality of the film edges (Sun, Gallagher, Callegari *et al.*, 1993). This improvement is illustrated in Fig. 38. Clearly, to obtain small hysteresis one requires a high average critical-current density in the films. However, the hysteresis is dominated by the local properties close to the edges: for example, a single grain boundary cutting across the edge of a SQUID washer increased the hysteresis by several orders of magnitude (Sun *et al.*, 1994). Keene *et al.* (1996) made similar measurements of hysteresis in a gradiometric, high-T_c SQUID coupled to a gradiometric flux transformer with multiturn input coils. For cycling fields up to 70 μT, the hysteresis parameter averaged 3   10^{-6}. When the measurements were repeated on the SQUID without the flux transformer, the hysteresis was little changed for cycling fields below 40 μT but increased dramatically for higher fields. The authors attribute this behavior to the pinning of the radial motion of vortices in the SQUID by the input coils. It is particularly important to note that high edge-pinning forces are a key to producing low levels of both 1/f noise and hysteresis, and imply steep film edges. This requirement is, unfortunately, not compatible with the need for gently sloping edges on all but the last film of a multilayer structure.

C. rf interference

Environmental rf fields may have a major effect on SQUIDs. In their simulations, Koch *et al.* (1994) coupled rf signals to dc SQUIDs as both a flux and a bias current, via the input and output circuitry of the SQUID. They showed that rf interference distorts the V-Φ characteristic by both reducing its amplitude and

creating an asymmetry about the $\Phi_0/2$ point. The first effect increases the white noise of the SQUID but, when conventional flux modulation is used, does not create a shift in the output of the flux-locked loop. The second effect can lead to a large increase in the level of low-frequency noise; however Koch and co-workers showed that this problem can largely be eliminated by using bias current reversal.

One can often effectively eliminate rf interference by means of appropriate shielding. However, this may not be possible in certain situations, notably for systems that are required to move in the earth's field; such motion induces eddy currents in the shield. In these situations, the combined use of flux modulation and bias reversal greatly reduces the effects of rf interference. Koch *et al.* (1994) emphasize that the rf coupling is reduced by making the superconducting structure small so as to decrease their antenna gain and, especially, by making the input and output circuits and the SQUID itself as balanced as possible. A high degree of balance prevents common mode rf fields, which have no effect on the SQUID, from creating differential signals that couple to the current and flux biases.

D. Temperature fluctuations

The effects of temperature fluctuations or drifts on the output of a high-T_c SQUID have been largely ignored until recently. However, these effects can be substantial (Milliken, Koch *et al.*, 1997; ter Brake *et al.*, 1997). Such fluctuations can be induced, for example, by changes in the ambient pressure above the liquid nitrogen bath. A change in temperature modifies the penetration depth and hence the effective sensing area of a SQUID, producing a flux change in the presence of an ambient magnetic field. For typical devices in the earth's magnetic field, the change in flux can be as high as 0.5 Φ_0/K. To achieve a noise level of (say) $10\,\mu\Phi_0\,\mathrm{Hz}^{-1/2}$ with this temperature coefficient would require a temperature stability of a few tens of μK Hz$^{-1/2}$ at frequencies above 1 Hz. The effect of temperature fluctuations can be reduced by appropriate design of the SQUID and flux transformer, stabilizing the ambient pressure, providing a long thermal time constant between the bath and the device, and reducing the ambient field. These are complicated issues that require further attention.

X. APPLICATIONS

The first practical measurement with a high-T_c SQUID was probably the use of a bulk rf SQUID by Likhachev *et al.* (1990) to detect the magnetocardiogram of a human subject. Since then, as the sensitivity of SQUIDs has progressively improved, the range of applications has grown rapidly. Currently, there is most interest in magnetocardiology and, to a lesser extent, magnetoencephalography, nondestructive evaluation (NDE), and SQUID "microscopes." Geophysical instrumentation is receiving growing attention and appears to

have an important future. We shall review each of these topics in turn. Of the various other applications, we mention just two. One is the SQUID picovoltmeter, in which the voltage to be measured is coupled in series with a resistor and a multiturn, single-layer film that is inductively coupled to a directly coupled magnetometer (Miklich *et al.*, 1995; Faley *et al.*, 1997). The other is the spinner magnetometer, in which a geophysical sample is rotated, typically at 10 rev/sec, just below the bottom of a dewar containing a high-T_c SQUID (Tinchev, 1997). The resulting oscillating magnetic field enables one to determine the static magnetization of the sample.

A. Biomagnetism

Biomagnetism refers quite generally to the measurement of magnetic fields produced by any living organism but, apart from experiments on magnetotactic bacteria mentioned in Sec. X.C, it appears that high-T_c magnetometers have been used only to detect signals from the human body. These fields range from several tens of picotesla from the human heart down to a few tens of femtotesla from the spinal cord (Wikswo, 1995). The majority of the commercial low-T_c SQUIDs ever made are employed in multichannel systems for magnetoencephalography (MEG)—measurements of signals from the human brain. This application demands a magnetic-field resolution of a few fT Hz $^{1/2}$ at frequencies down to about 1 Hz. As discussed in Sec. VI, the best high-T_c SQUID magnetometers have a white noise below 10 fT Hz $^{1/2}$, but at 1 Hz the noise is about a factor of 3 higher. Thus high-T_c magnetometers are not yet quite good enough for clinical MEG, although there have been several demonstrations of neuromagnetic measurements (Zhang, Tavrin *et al.*, 1993; DiIorio *et al.*, 1995; Curio *et al.*, 1996; Drung, Ludwig *et al.*, 1996). On the other hand, the requirements for magnetocardiology (MCG)—measurements of signals from the human heart—are somewhat more relaxed, and as a result most biomagnetic measurements with high-T_c SQUIDs have focused on this application.

Although the peak signal amplitudes in MCG are several tens of picotesla, there is fine structure of clinical interest with a mean amplitude of about 2 pT (David *et al.*, 1997). The base-to-peak amplitude of a biomagnetic signal to be identified in a single measurement in a bandwidth Δf is given by B_p $c_R S_B^{1/2}(\Delta f)^{1/2}$. The crest factor c_R is determined by the probability that an observed magnetic field is signal rather than noise, and a value of about 4 is used under the assumption that the noise is white throughout the measurement bandwidth (Ott, 1988). Thus for the typical values Δf 200 Hz and B_p 2 pT, the sensor should have a noise below 35 fT Hz $^{1/2}$. Although magnetocardiograms measurements have been obtained by a number of groups to illustrate the performance of their magnetometers, only a few such recordings, obtained in a well-shielded environment, are of sufficient quality to yield diagnostically useful information. The best data were obtained in the magnetically shielded room of the PTB in Berlin with
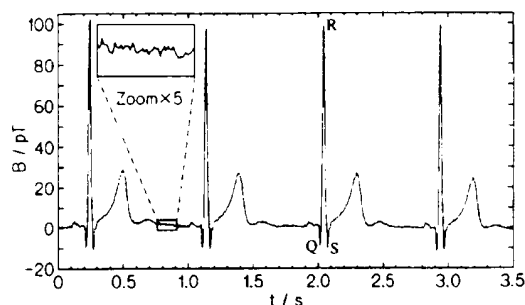

FIG. 39. Real-time trace of magnetocardiogram recorded with NKT integrated magnetometer in magnetically shielded room at PTB in Berlin. The measurement was performed in a bandwidth of 0.016–200 Hz without power line filter. Inset illustrates very low peak-to-peak noise (Drung, Ludwig *et al.*, 1996).

several kinds of multilayer magnetometers (Drung, Ludwig *et al.*, 1996; Drung, Dantsker *et al.*, 1996). The highest signal-to-noise ratio was obtained with an integrated magnetometer involving a multiturn input coil, fabricated at NKT, which had a noise of 10 fT Hz $^{1/2}$ at 1 kHz and 53 fT Hz $^{1/2}$ at 1 Hz (Drung, Ludwig *et al.*, 1996). An unfiltered, real-time MCG measurement with this device is illustrated in Fig. 39. The measurement bandwidth was 200 Hz, resulting in a base-to-peak noise amplitude of 0.75 pT and a signal-to-noise ratio of 130 for the peak value. The latter value is considered acceptable for MCG with low-T_c systems. The sensitivity of this particular high-T_c magnetometer was adequate to detect wide-band MEG signals produced by both the central and peripheral nervous systems, with amplitudes of 100 fT or less (Curio *et al.*, 1996; Drung, Ludwig *et al.*, 1996).

Subsequently, Burghoff *et al.* (1996) used a high-T_c rf SQUID magnetometer in the Berlin shielded room to record the MCG of both a healthy subject and a subject with arrhythmia. The noise of the sensor was 35–40 fT Hz $^{1/2}$ at 200 Hz. To assess the performance of the high-T_c magnetometer, the PTB 37-channel, low-T_c system (Koch, Cantor *et al.*, 1991) was used as a reference. Although the rms noise of the high-T_c sensor was a factor of 4 higher than the low-T_c sensors, one half of this disadvantage was regained from the shorter distance between the high-T_c magnetometer and the thorax. The ability to place high-T_c SQUIDs closer to the signal source clearly relaxes their sensitivity requirement somewhat compared with their low-T_c counterparts. A further potential advantage of liquid nitrogen-cooled sensors is that the cryogenic package can be made quite compact. Schilling *et al.* (1996) measured a MCG with a cryostat containing only 0.1 liter of liquid nitrogen.

The systems we have just described have only a single channel. However, most applications require a multichannel system to enable one to map fields from the heart at different locations. The most elaborate high-T_c systems have been built at the Superconducting Sensor Laboratory in Japan: 4 channels (Tanaka *et al.*, 1994), 16 channels (Itozaki *et al.*, 1994), and 32 channels (Itozaki

et al., 1996). Their sensors were 5-mm-washer dc SQUIDs with a noise of 70–250 fT Hz $^{1/2}$ at 1 kHz and 300–800 fT Hz $^{1/2}$ at 1 Hz; to protect them from moisture, the SQUIDs were sealed in an epoxy resin package. The 32 SQUIDs were in a flat 6 × 6 array, with each corner location unoccupied, with 40 mm separation. Magnetocardiogram recordings were obtained in a small magnetic shield, with inner dimensions 0.8 × 0.8 × 2 m^3. Although the noise specifications did not fulfill the requirements listed earlier, Itozaki and co-workers were able to obtain magnetocardiac isofield contour maps of the *R*, *S*, and *T* waves.

To our knowledge, the only multichannel system using multilayer technology is the four-channel system of DiIorio *et al.* (1995), who used integrated, multiturn magnetometers. The noise levels were 70 fT Hz $^{1/2}$ at 1 kHz and 280 fT Hz $^{1/2}$ at 1 Hz. These authors obtained both MCG's and MEG's in a magnetically shielded room.

All the systems described so far involved magnetometers, and can thus be used only in a magnetically shielded room, which, as pointed out in Sec. IX, is expensive. If one hopes to see SQUIDs in widespread use, one is required not only to replace liquid ^{4}He with liquid N$_2$ but also to eliminate the need for expensive shielding. This requirement has driven extensive development of gradiometers: since the separation of the sensor and the source is only a few tens of millimeters, even high-order gradiometers behave as magnetometers for the signal source, provided the baseline is sufficiently long (Vrba, 1996).

Tavrin *et al.* (1994) and Borgmann *et al.* (1997) used second-order electronic gradiometers to record good-quality MCG's in unshielded environments. However, the bandwidth was only 0–30 Hz, which is insufficient for some of the high-frequency information of clinical interest. Weidl *et al.* (1997) used a single-layer, planar gradiometer with a 4-mm baseline to record MCG's in an unshielded environment with a bandwidth of 250 Hz. The *R* peak was just resolved in a real-time trace. The authors demonstrated that the signal-to-noise ratio could be significantly improved by averaging, by using notch filters, and by triggering the recording with the peak of the electrocardiogram (Seidel *et al.*, 1997).

Progress towards the development of multichannel systems for unshielded operation has been reported by Woeltgens *et al.* (1997), David *et al.* (1997), ter Brake, Janssen *et al.* (1997), and ter Brake, Karunanithi *et al.* (1997). David *et al.* fabricated a nine-channel system based on directly coupled dc SQUID magnetometers, each of which was enclosed in a fiberglass module to protect it from moisture. Each module contained a resistive heater so that the SQUID could be driven into the normal state to release trapped magnetic flux. To reduce the environmental noise David *et al.* (1997) used a copper coil around the dewar as a reference magnetometer that fed compensating currents into a coil surrounding the planar magnetometer array. They also used digital subtraction to form first-derivative gradiometers. The combination of these techniques reduced the

noise at 30 Hz from about 30 pT Hz $^{1/2}$ to about 1 pT Hz $^{1/2}$ for each channel, an order of magnitude above the intrinsic noise of the sensors. This performance made it possible to obtain contour maps after 80 averages, with the aid of a template matching technique. Compensating the component of the earth's static magnetic field perpendicular to the plane of the magnetometers did not reduce the noise any further. The excess noise was believed to arise from gradients in the environmental noise or the motion of vortices in the YBCO films. The latter effect could presumably be eliminated by reducing the linewidths of the superconducting films sufficiently (Sec. IX.A).

Ter Brake, Janssen *et al.* (1997), and ter Brake, Karunanithi *et al.* (1997) made a similar seven-channel system, also encapsulating their directly coupled magnetometers to exclude moisture. They used groups of three neighboring magnetometers in the planar array to form electronic first- and second-order gradiometers. Noise rejection was limited to about 2% by lack of planarity and by variations in the transfer functions of the individual SQUIDs, which resulted in varying gains and phase shifts in the flux-locked loops.

The five-channel system of Woeltgens *et al.* (1997) makes use of the TSG (Koch *et al.*, 1993). Three magnetometers were stacked in the z direction to form the TSG, and two more magnetometers were used to cancel residual x and y components of the noise. In addition, the outputs from a three-axis flux-gate magnetometer were coupled to three sets of external coils to provide active noise cancellation. The lowest noise achieved was about 400 fT Hz $^{1/2}$ at 1 Hz (Koch, 1997).

We have seen that single-channel, multilayer magnetometers operating in a magnetically shielded environment have sufficient resolution to obtain clinically meaningful MCG's. Packages to protect the sensors and to enable excess flux to be expelled have been developed. However, no multichannel system has yet been demonstrated that even approaches the performance of the best single-channel devices, suggesting that such high-T_c sensors are not yet routinely available. With regard to unshielded systems, a good deal of progress has been made, but substantially more will have to be made before the noise levels approach that of high-T_c directly coupled magnetometers, about 100 fT Hz $^{1/2}$, let alone the much lower noise levels of low-T_c systems. One might hope some of the recent progress reported in Secs. VIII and IX will lead to lower noise in unshielded systems in the near future.

B. Nondestructive evaluation

Nondestructive evaluation (NDE) is the noninvasive identification of structural or material flaws in a specimen. Examples are the imaging of surface and subsurface cracks or pits due to corrosion or fatigue in aging aircraft and reinforcing rods in concrete structures (Wikswo, 1995). While there is a variety of acoustic, thermal, and electromagnetic techniques currently used in NDE, these methods are often not entirely adequate for de-

tecting flaws at an early enough stage, usually because of a lack of spatial or depth resolution.

An important application of high-T_c SQUIDs in NDE is to replace induction coils in eddy-current imaging, a widely used method for the detection of subsurface damage in metallic structures such as aircraft (Wikswo, 1995). In this technique, one applies an alternating magnetic field produced by a drive coil and lock-in detects the fields generated by the induced eddy currents in the structure. The eddy currents are diverted by structural flaws resulting in distortions of the magnetic field. Since the eddy currents flow over a skin depth, which is inversely proportional to the square root of the frequency, deep defects require correspondingly low frequencies. Thus the flat frequency response of SQUIDs is a distinct advantage over the response of coils which falls off with decreasing frequency. Furthermore, high-T_c SQUIDs are distinctly preferable to low-T_c SQUIDs because their associated dewars or cryocoolers can be lighter and more compact. The insertion of SQUIDs into the NDE market is largely contingent on one's ability to retain high sensitivity in a mobile unit capable of operating in the magnetically unfriendly environment of an aircraft maintenance hangar or a factory.

Demonstrations of eddy-current NDE using high-T_c SQUIDs have been reported by a number of groups, especially during the past two years. Both dc and rf SQUIDs have been used in a variety of magnetometer and gradiometer configurations. The drive coil is mounted on the cryostat and typically has a double-D configuration to minimize the excitation field at the SQUID, which is mounted at the point where the field changes sign. For most realistic applications, one scans the SQUID and drive coil over the sample.

In one such system Tavrin et al. (1995) used an electronic SQUID gradiometer consisting of two high-T_c SQUIDs in a dewar of liquid nitrogen suspended over a sample that was scanned linearly at about 7 mm/s in an unshielded laboratory environment. The authors successfully imaged a series of slots cut into a copper plate as well as a 6-mm hole in a 1-mm-thick sheet of aluminum situated beneath two additional sheets of the same material. In a similar unshielded system Carr et al. (1977) used an electronic gradiometer consisting of two dc SQUIDs that was scanned above three 3-mm-thick layers of aircraft-grade aluminum held together by rivets and containing simulated defects 2–4 mm long radiating from the rivet centers in all three layers. Excitation fields were applied at two discrete frequencies and the resulting signals were lock-in detected and subtracted in an appropriate manner to distinguish the defects in the deeper layer from those in the surface layer.

In a step towards practical development of this technology, Hohmann et al. (1997) reported NDE measurements of structures in an unshielded environment using dc and rf SQUID-based magnetometers and monolithic gradiometers cooled by a commercial Joule-Thomson cryocooler. Either the sample or the sensor was scanned on a mobile x-y stage; the latter mode was aimed at
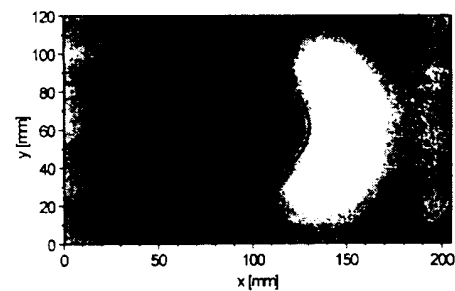

FIG. 40. Eddy-current image of a corrosion pit in an aluminum sheet (1.5 200 400 mm) situated beneath four aluminum sheets of equal size (Hohmann et al., 1997).

investigating the possibility of a mobile SQUID system. Among the flaws analyzed were a corrosion pit and a simulated fatigue crack in an aluminum sheet; both were hidden underneath four intact 1.5-mm-thick aluminum plates. Figure 40 shows the image of a corrosion pit detected at a drive frequency of 20 Hz with the cryocooler in motion.

Kreutzbruck, Tröll et al. (1997), Mück et al. (1997), and Kreutzbruck et al. (1998) developed two NDE systems, one with the sensors cooled by liquid nitrogen and the other with them cooled by a miniature Stirling refrigerator, which chills neon gas to about 50 K. Each system contained up to four rf SQUIDs operated at 3 GHz, with a noise of about 1 pT Hz$^{1/2}$ above 1 Hz and a high slew rate and dynamic range to allow unshielded operation. This group reported an impressive demonstration of one of their systems in an aircraft hangar to detect flaws in felloes that were rotated close to the dewar at 6–20 rpm. The felloe consists of a hollow steel cylinder containing six ferromagnetic steel bars, at 60° intervals, for heat dissipation, and three venting holes, 10 mm in diameter, at 120° intervals. Thus, in searching for cracks in the felloe, it is necessary to distinguish their signature from the signals produced by the bars and holes. Figure 41 shows the amplitude and phase of the magnetic field detected by the SQUID as the felloe is rotated through 360°. A 4-mm-long crack is easily distinguished from the periodic signals from the bars and holes. The authors developed an algorithm that combines the amplitude and phase data to make the periodic signals vanish, leaving a prominent signal from the crack [Fig. 41(c)]. Similar work has been reported by Krause et al. (1997), who tested aircraft wheels with a mobile SQUID system in the Lufthansa maintenance facility at Frankfurt airport. Although still at the prototype stage, these techniques have considerable promise as an NDE tool for the aircraft industry.

Historically, much of the early research on NDE with low-T_c SQUIDs was concerned with the detection of magnetic fields generated by specimens containing magnetized components (Donaldson et al., 1990; Banchet et al., 1995), and several groups are now using high-T_c devices for this approach. Schmidl, Wunderlich, Dörrer, Specht, Linzen et al. (1997) and Kasai et al.
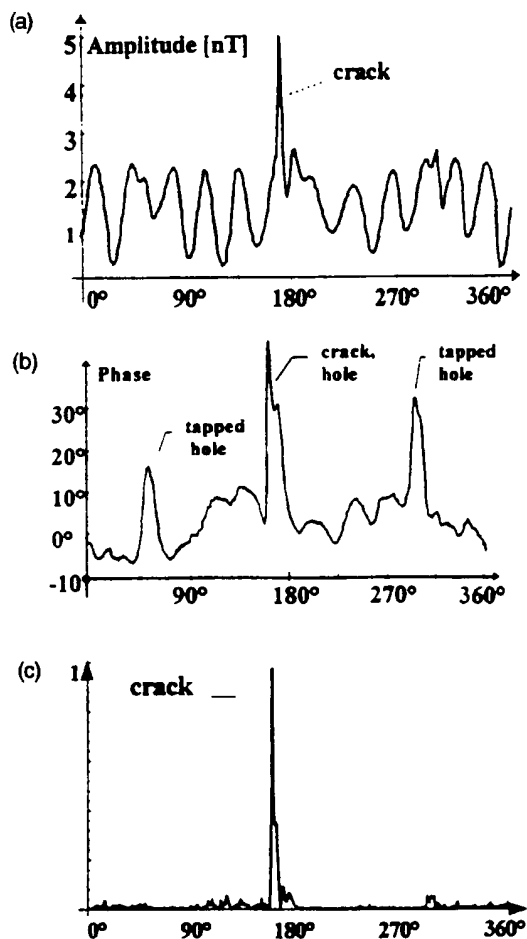
(a)

(b)

(c)

FIG. 41. Crack detection in an aircraft felloe: (a) Amplitude and (b) phase of gradiometer signal produced by eddy currents during one rotation of the felloe. The crack is indicated. The periodic signal is due to ferromagnetic steel bars located in the felloe at 60° intervals and three tapped holes at 120° intervals. (c) Result of algorithm to suppress signals from the steel bars and holes. (Mück *et al.*, 1997).

(1997) used a planar dc SQUID gradiometer and a magnetometer, respectively, to scan samples of steel to explore the correlation between mechanical stress and magnetic-field distribution. The latter group imaged the magnetic field contours resulting from different degrees of residual stress in the material. This method is a unique probe of the mechanical or thermal stress to which a sample has been subjected. We have recently become aware of work by Tavrin *et al.* (1999), under contract with a manufacturer of turbine engines. These authors detect ferrous inclusions in the disks of turbine engine rotors using a high-T_c, second-order electronic SQUID gradiometer in an unshielded environment. This work represents an important step beyond "proof-of-concept" in introducing high-T_c SQUIDs into the NDE market. In a very different application Nagaishi *et al.*

(1997) used a high-T_c dc SQUID magnetometer to detect fine magnetic particles in a rapidly moving copper wire. In their arrangement, the nitrogen-cooled SQUID was surrounded by a magnetic shield and the wire was pulled through holes in the shield about 15 mm below the SQUID at speeds of 10 to 500 m/min. Iron particles as small as 50 μm in diameter were detected. The goal of this technique is to locate impurities that make the wire brittle, causing it to break.

Although some of the measurements we have just described are at the prototype stage, there have been impressive demonstrations on aircraft components. Fortunately, these techniques do not require the highest sensitivity, since the Nyquist noise generated by the sample can be on the order of 1 pT Hz$^{1/2}$. This noise level is much lower than that of coils conventionally used for eddy current NDE. Thus, although some development remains, the future of NDE based on high-T_c SQUIDs is very promising indeed.

C. Scanning SQUID microscopy

Magnetic microscopes based on low-T_c dc SQUIDs have been used to image static magnetic fields with a combination of high field and spatial resolution (for example, Mathai *et al.*, 1993; Vu and Van Harlingen, 1993; Tsuei *et al.*, 1994). This development led, shortly afterwards, to the development of high-T_c SQUID microscopes (Black *et al.*, 1993; Black, 1995; Lee *et al.*, 1996, 1997), in which the sample may be at either 77 K or at room temperature. Most often, the sample is scanned over the SQUID in a two-dimensional raster to produce an image. The scanning stage, made from nonmagnetic composite material, is driven by threaded rods turned by stepper motors. The frequency at which the image is obtained ranges from near zero, where one simply measures the static magnetic field produced by the sample, to beyond 1 GHz.

Figure 42 shows a microscope in which the sample is maintained at room temperature. The SQUID is mounted in vacuum at the upper end of a sapphire rod, the lower end of which is cooled by liquid nitrogen. Superinsulation surrounding the rod ensures that the temperature gradient along it is negligible. The SQUID is separated from room temperature and atmospheric pressure by a window, which may be either a 75-μm-thick sapphire disk or a 3-μm-thick Si$_x$N$_y$ window fabricated on a Si chip. In the first case, the SQUID-to-sample separation is typically 150 μm, whereas in the latter, the separation can be as low as 15 μm. The entire system is surrounded by a mu-metal shield to exclude spurious magnetic field fluctuations, and the SQUID is operated in a flux-locked loop.

A novel application of the microscope, in which the sample is held fixed, is the detection of the motion of magnetotactic bacteria (Lee *et al.*, 1997). Each bacterium contains a series of magnetite particles giving it a magnetic moment of about 5 10^{16} A cm^2. As an example of such measurements, Fig. 43 shows the spectral density of the magnetic-field fluctuations produced by an
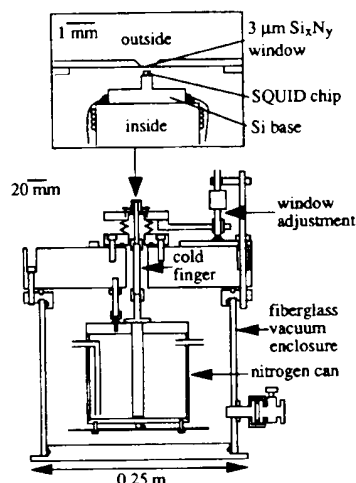
FIG. 42. Sectional side view of scanning SQUID microscope, without *X-Y* scanner (Chemla *et al.*, 1997).

ensemble of dead bacteria in water. The bacteria undergo Brownian rotation, producing a Lorentzian power spectrum of the form $1/[1 \; (\omega\tau_0)^2]$, where τ_0 $\alpha_r/k_B T$ is the characteristic rotation time of the bacteria and α_r is the rotational damping coefficient. The fitted value of τ_0, 15 9 s, is in good accord with predictions assuming a bacterial diameter of 1 μm and a length of 4 μm. Measurements underway include the dynamics of living bacteria (Chemla *et al.*, 1997), the effects of an applied magnetic field, and the migration of bacteria through porous media.

We turn now to higher-frequency operation. In the frequency range from 1 kHz to 1 MHz, Black *et al.* (1994) operated the SQUID open loop and used a drive coil to apply a sinusoidal magnetic field to induce eddy currents in the sample and modulate the flux in the SQUID. The magnetic response of the sample is determined by measuring the amplitude and phase of the output from the SQUID: the out-of-phase component corresponds to the eddy current in the sample. This approach resembles the eddy current technique described in Sec. X.B, but enables one to operate at substantially higher frequencies.
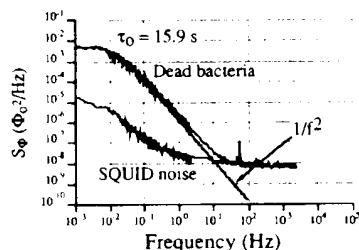

FIG. 43. Spectral density of dead magnetotactic bacteria with fitted Lorentzian (solid line). Lower power spectrum represents the SQUID noise (Lee *et al.*, 1997).
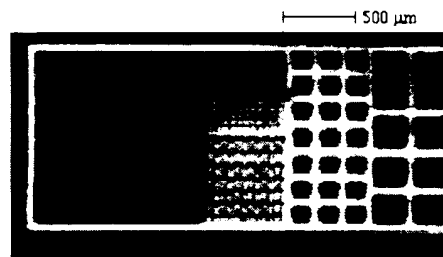

FIG. 44. Image of patterned thin film of Cu scanned over SQUID with 9 GHz Josephson frequency (Black *et al.*, 1995).

Black *et al.* (1995b, 1995) extended the imaging frequency from 1 MHz to 1 GHz by applying a rf field to the sample, which, in turn, couples an rf flux Φ_{rf} into the SQUID. The rf flux smoothes out the V-Φ curve of the SQUID, reducing the modulation depth. Thus, when the SQUID is also flux-modulated at a low frequency, f_m 25 kHz, one can show that the modulation depth is given by

$$V(\Phi_{rf}) \quad V_0 J_0(2\pi\Phi_{rf}/\Phi_0), \tag{10.1}$$

where V_0 is the value with no rf field and J_0 is the zero-order Bessel function of the first kind. Equation (10.1) can be inverted to find Φ_{rf} provided it is sufficiently small. This technique was used to image a wire in the shape of a meander pattern.

For frequencies higher than 1 GHz, one can use the SQUID itself as the source of the field excitation (Black *et al.*, 1995a, 1995). The oscillating magnetic fields at the Josephson frequency corresponding to the bias voltage induce eddy currents in the nearby sample which couple fields back into the SQUID. The essential effect is to reduce the inductance of the SQUID, thereby increasing the voltage modulation depth measured at low frequencies. Thus by monitoring the modulation depth as the sample is scanned over the SQUID one can obtain images at microwave frequencies. Figure 44 shows an image of a 500-nm-thick Cu film that had been patterned into a series of grids of various sizes. The SQUID was 40 μm from the grid, and the Josephson frequency was about 9 GHz. The brightest regions correspond to an increase in modulation depth of about 2%.

In concluding this section, we note that the best scanning SQUID microscopes with cold samples have a spatial resolution of perhaps 5 μm, while those with room-temperature samples have a resolution that is more like 30-50 μm. A recent innovation (Pitzius *et al.*, 1997), however, has dramatically improved the spatial resolution for cold samples, albeit at the price of magnetic-field sensitivity. These authors use a soft magnetic tip to focus the flux from the sample into the SQUID, and were able to achieve a spatial resolution of the order of 0.1 μm. A similar principle has been used by Tavrin and Siegel (1997) to examine room-temperature samples.

D. Geophysics

A particularly appealing application of high-T_c SQUID magnetometers is in geophysical surveying

(Clarke, 1983), for example, magnetotellurics, controlled-source electromagnetics, and cross-borehole sounding. In magnetotellurics, one measures simultaneously the fluctuating horizontal components of the electric and magnetic fields at the earth's surface; these fluctuating fields originate in the magnetosphere and ionosphere. From these frequency-dependent fields one calculates the impedance tensor of the ground and hence estimates the spatial variation of the resistivity of the ground. Frequencies of interest are typically $10^{-3}-10^2$ Hz, and the corresponding skin depths, assuming a resistivity of 10 Ωm, are 50 km to 150 m. To eliminate the effects of local noise sources, one cross-correlates the fluctuating fields with those measured with a remote reference magnetometer 5–10 km away. Applications of magnetotellurics include surveying for oil and gas, and locating subsurface fault lines. In controlled-source electromagnetics, one uses a transmitter to supply large current or magnetic pulses to the ground, and determines the magnetic response. The naturally occurring fluctuating fields are now a source of noise, and a remote magnetometer is used to cancel them. In cross-borehole sounding, a receiver in one borehole is used to detect magnetic pulses from a transmitter in a second borehole. From the real and imaginary parts of the received signal one deduces the susceptibility of the ground between the two boreholes, and models the porosity.

Currently, these magnetic measurements are made with induction coils. In fact, in the late 1970s and early 1980s, low-T_c SQUID magnetometers were used very successfully in magnetotellurics (Clarke *et al.*, 1983) and exploited commercially. However, the inconvenience of using liquid helium, particularly in remote areas of the world, coupled with the drop in the price of oil which severely curtailed oil prospecting, led to the abandonment of cryogenic sensors. The advent of liquid nitrogen-cooled magnetometers, on the other hand, has renewed interest in this application Below about 1 Hz, the spectral density of the noise in coils increases as $1/f^3$, whereas that of SQUIDs increases as $1/f$, giving the latter magnetometer a substantial advantage at low frequencies. Furthermore, coils for use below 1 Hz can be as long as 1.5 m. and the deployment of three such coils orthogonally, buried in the ground for stability, is a tedious undertaking. Thus a three-axis high-T_c magnetometer in a compact dewar with a long hold time becomes very competitive.

Dantsker *et al.* (1994) constructed a three-axis magnetometer based on directly coupled magnetometers, and showed that it had sufficient slew rate for use in the field. Wang *et al.* (1997) reported preliminary experiments using a high-T_c magnetometer for magnetotellurics and transient electromagnetics. Matzander *et al.* (1997) deployed a system with a white noise of 200 fT Hz$^{1/2}$ and a $1/f$ knee of 10 Hz, and used it successfully to demonstrate controlled-source electromagnetic measurements. A system for shallow borehole sounding is under development (Drung *et al*, 1997; Radic *et al.*, 1997).

What sensitivity does one require, for example, for magnetotellurics? A white noise of 20–30 fT Hz$^{1/2}$ and a $1/f$ knee of 1 Hz would be competitive; needless to say, these noise levels must be attained with the magnetometer operating in the earth's magnetic field, so that elimination of low-frequency noise due to vortex motion is imperative (Sec. IX.A). The fabrication of such a system is eased by the fact that there are no tight space constraints, and one could almost certainly use single-layer components, for example, a dc or rf SQUID coupled to a large-area flux transformer in a flip-chip arrangement.

XI. CONCLUDING REMARKS

The performance of high-T_c dc and rf SQUIDs and of magnetometers based upon them has progressed to the point where, in principle, it is adequate for many practical applications. One notable exception is magnetoencephalography, where the magnetic-field noise of a few fT Hz$^{1/2}$ at frequencies down to below 1 Hz routinely achieved with low-T_c devices is still somewhat beyond the reach of their high-T_c counterparts. What, then, are the major issues remaining in the fabrication and operation of the high-T_c devices and what are the most likely uses of them in the next few years?

Many groups can routinely deposit high-quality thin films of YBCO with low levels of $1/f$ flux noise in zero magnetic field. Very few, however, have anything like the same capability to deposit a YBCO-STO-YBCO structure, with each layer patterned to form a flux transformer, with guaranteed electrical integrity let alone low levels of $1/f$ noise. The multilayer magnetometers with the lowest white magnetic-field noise all exhibit $1/f$ noise at 1 Hz, even when cooled in zero magnetic field. Since unpatterned trilayers can be made with negligible excess noise, the noise in patterned structures is presumably associated with edges. It is likely—but not assured—that sufficiently careful engineering of these edges, perhaps accompanied by more transmission electron microscopy, will reduce the flux noise power at 1 Hz by the required order of magnitude. With regard to junctions, despite enormous progress with artificial barriers, the workhorse for SQUIDs remains the grain-boundary junction. Even bicrystal grain-boundary junctions are not entirely routine: although one often can produce, say, a dozen SQUIDs on a bicrystal that all exhibit quantum interference, not all of them have optimum characteristics and correspondingly low noise. The degree of irreproducibility represents the variability in the bicrystal substrates, and it is not obvious that a great deal of improvement can be made. Thus the field still awaits the invention of a new junction technology that offers both high yield and high $I_0 R$ product. For the moment, at least from an economic standpoint, the best philosophy is probably to fabricate relatively large numbers of SQUIDs, select the best, and couple them to a suitable input circuit in a flip-chip arrangement.

Most research has been focused on dc SQUIDs, probably because their performance at 4.2 K has been much superior to rf SQUIDs. However, the advantage

of the dc SQUID over the rf SQUID at 77 K is much narrower, in part because one can use a somewhat larger inductance for the latter so that the effective area and intrinsic magnetic-field sensitivity are higher. To date, magnetometers based on dc SQUIDs have achieved lower noise than those of comparable size based on rf SQUIDs, particularly at low frequencies. However, this advantage has been due largely to the use of multilayer flux transformers coupled to dc SQUIDs, and may not persist now that such transformers are being used with rf SQUIDs. On the other hand, the fact that the white noise in dc SQUIDs is generally higher than predicted remains an important issue. If this problem is eventually resolved, for example, by the introduction of a more "perfect" type of junction, the performance of dc SQUIDs may well improve substantially. Furthermore, the possibility of significant crosstalk between rf SQUIDs in a multichannel system may prove to be a significant challenge. Thus the question of whether to choose dc or rf SQUIDs is still open, and may ultimately depend on the application at hand.

We have emphasized issues of operating SQUIDs in an unshielded environment. The fact that the $1/f$ noise can increase dramatically when a high-T_c SQUID is cooled in the earth's field is peculiar to high-T_c superconductors: because they are operated at much lower temperatures and have much higher flux-pinning energies, low-T_c SQUIDs do not suffer from this drawback. Hopefully, the introduction of narrow linewidths has solved the problem for high-T_c devices cooled in a static field, although this has yet to be demonstrated for a SQUID coupled to a multilayer, multiturn flux transformer. The use of a "flux dam" offers the possibility of maintaining low $1/f$ noise even after the ambient field is changed. In common with low-T_c SQUIDs, for most applications the operation of high-T_c SQUIDs without shielding generally raises the issue of ambient magnetic-field noise. The solution—the gradiometer—is the same for both techniques. However, 4.2 K systems have an inexpensive "low tech" approach based on niobium wire that is not available to 77 K systems. In high-T_c systems, the current options are to subtract the outputs of two or more magnetometers or to make planar, thin-film gradiometers. The former approach requires no new thin-film components and can be easily implemented with diagonal or off-diagonal first- or second-order gradients, arbitrarily long baselines, and in ingenious configurations such as the three-SQUID gradiometer. The thin-film gradiometers have the advantage of substantial rejection of uniform magnetic-field noise—say, by three orders of magnitude—by a passive, linear, noise-free device. It is straightforward to make gradiometers with short baselines—a few millimeters—that are very adequate for nondestructive evaluation. On the other hand, a baseline of, say, 50 mm is more of a challenge. Single-layer, symmetric flux transformers have been used successfully but lose sensitivity because the inductance of their large-area pickup loops cannot be matched to the much lower inductance of the SQUID. The solution, of course, is to use multiturn input coils, but the cost of

making multilayer structures on large substrates is likely to be prohibitive. An alternative solution is the asymmetric gradiometer which requires only a single-layer flux transformer and does not significantly reduce the intrinsic sensitivity of the magnetometer to which it is coupled. The choice of gradiometers is another area that remains to be resolved.

Turning briefly to applications of high-T_c SQUIDs, we have seen impressive demonstrations of both MEG and MCG. However, as already noted, the sensitivity of high-T_c sensors is marginal for the former systems and while these systems are confined to relatively few centers and to a magnetically shielded room, the cost and higher boil-off rate of liquid ^{4}He are not overriding issues. On the other hand, one might hope that MCG will become a more widespread modality over the next few years, for example, in the assessment of damage to heart muscle following a cardiac infarction, for the diagnosis of heart arrhythmia and for locating the source of certain kinds of arrhythmia. Here, the benefits of liquid nitrogen as a cryogen—or indeed of a cryocooler in the longer term—combined with unshielded operation are highly desirable. Although clinical trials on large numbers of patients have yet to be performed, MCG currently appears to be the largest potential application of high-T_c SQUIDs. Whether or not this field materializes depends not only on the development of suitable, low-noise gradiometers for unshielded operations but also on the availability of funding for suitable trials.

A second application, nondestructive evaluation (NDE), is the one where the most "real world" progress has been made, for example, for the evaluation of aircraft components. Techniques involving both eddy currents and remanent magnetization have been successfully implemented. This is an area in which the ultimate sensitivity of SQUIDs is not required—generally 1 pT Hz$^{1/2}$ is more than sufficient—and in which short-baseline gradiometers are adequate. The ability of the SQUID to operate in a static field and over a very wide range of frequencies gives an advantage over flux-gate magnetometers, and the fact that the sensitivity is maintained at arbitrarily low frequencies offers a distinct advantage over coils. This area seems poised for rapid growth.

Novel "SQUID microscopes" can be used in either a scanning or a static mode. The potential of these microscopes for biology is intriguing. One novel example is in immunoassay (Kötitz *et al.*, 1997). Here, one labels an antibody with a tiny magnetic particle and exposes it to an appropriate antigen in the solid phase. The binding of the antibody with the antigen is detected by means of the remanent magnetization imparted to the immobilized particle. Another potential use of the microscope is to detect low-frequency nuclear magnetic resonance (NMR) and nuclear quadrupole resonance of room-temperature samples, for example, NMR of hyperpolarized ^{129}Xe (TonThat *et al.*, 1997).

The use of high-T_c SQUIDs in geophysics is "straightforward" now that low levels of $1/f$ noise can be realized in the earth's magnetic field. One should not

underestimate the sensitivity of commercially available coils in these applications, but since the space constraints on a three-axis magnetometer are not severe, one should be able to achieve 10 fT Hz $^{1/2}$ at 1 Hz, with a $1/f^{1/2}$ increase at lower frequencies, using a single-layer flux transformer. Such a system, packaged with suitably rugged dewar and electronics, would be very competitive for low-frequency applications at the earth's surface. In the longer term, the use of SQUID magnetometers for cross-borehole sounding would offer a distinct advantage over coils.

What will it take to foster this wide range of applications? Currently, most of these techniques continue to be practiced by people who are experts in SQUIDs and, indeed, who have made the devices themselves. Clearly, this situation must change if high-T_c SQUIDs are to be widely deployed. This change will require not only more user-friendly packaging but also lower pricing. Lower costs imply larger-scale manufacturing, and it is to be hoped that one or more companies will soon see fit to adopt the necessary processing technologies. However, one should recognize that the total system price is often dominated by the cost of the cryogenics, be it liquid nitrogen or a cryocooler. This additional expense must be justified in terms of improved performance compared with competing technologies if SQUID-based instruments are to be widely adopted.

Note added in proof. Chesca (1998b, 1999) developed an analytic theory for dc SQUIDs operating in the presence of large thermal fluctuations, similar to his approach for rf SQUIDs. This work is based on solving the two-dimensional Fokker-Planck equation, which is equivalent to the coupled Langevin equations. Chesca finds analytical solutions for the dc SQUID in the limit β_L $1/\pi$. The noise energy ε scales as $\varepsilon \propto \Gamma^4$, for fixed L, and the optimum SQUID inductance is found to be L L_{th}/π (≈ 10 pH at T 77 K) for Γ 1.

In a systematic study of the transfer function and thermal noise of YBCO dc SQUIDs, Barthel *et al.* (1999) compare both numerical simulations and Chesca's analytical approach with experimental results obtained for a wide range of noise parameters up to Γ 5. Several predictions of the analytical theory could be verified experimentally, and a good qualitative agreement with both theories is observed. Furthermore, the numerical simulations performed in the limit of large thermal fluctuations show excellent agreement with the analytic theory.

Zhang *et al.* (1999) demonstrated a design of a planar multiturn flux transformer integrated with a superconducting labyrinth resonator serving as the planar tank circuit for a YBCO thin film rf SQUID magnetometer. When coupled to a 210 pH double-hole washer SQUID in flip-chip configuration the magnetometer showed a white magnetic field noise as low as 11.5 fT Hz $^{1/2}$ (above $f \approx 3$ kHz). However, the noise at 10 Hz was more than one order of magnitude above the white noise level, presumably due to $1/f$ noise from poor film quality.

Kittel *et al.* (1998) have fabricated and tested a planar, thin-film, second-derivative gradiometer. The flux transformer consisted of two identical pickup loops placed one on each side of a smaller loop that was inductively coupled to a directly coupled magnetometer; this configuration can be envisioned as a second pickup loop coupled to the left-hand side of the smaller loop in Fig. 33(b). The overall length of the flux transformer was 80 mm, and the baselines for the first- and second-derivatives were 62 mm and 31 mm, respectively. By mechanically adjusting the separation between the magnetometer and the flux transformer, the authors achieved a typical rejection of uniform magnetic fields of 50 ppm. The residual first-order gradient response was at most 1.4% relative to the second-order gradient response.

Fleet *et al.* (1999) have described a high T_c scanning SQUID microscope for detecting flaws in computer chips. The room-temperature sample could be brought to within 30 μm of the SQUID, which was cooled by a cryocooler. A 3 kHz current was passed through the circuit, which was on the far side of the chip from the SQUID, and the magnetic field images obtained by the SQUID were inverted to generate two-dimensional current density distributions. This technique enabled the authors to achieve a spatail resolution of 75 μm, substantially less than the SQUID-circuit separation of 340 μm. A short-circuit on the chip was located.

ACKNOWLEDGMENTS

REFERENCES

Aarnink, W. A. M., P. J. van den Bosch, T.-M. Roelofs, M. Verbiesen, H. J. Holland, H. J. M. ter Brake, and H. Rogalla, 1995, IEEE Trans. Appl. Supercond. **5**, 2470.

Alff, L., G. M. Fischer, R. Gross, F. Kober, A. Beck, K. D. Husemann, T. Nissel, F. Schmidl, and C. Burckhardt, 1992, Physica C **200**, 277.

Alff, L. S., S. Kleefisch, U. Schoop, M. Zittartz, T. Kemen, T. Bauch, A. Marx, and R. Gross, 1998, Eur. Phys. J. B **5**, 423.

Ambegaokar, V., and B. I. Halperin, 1969, Phys. Rev. Lett. **22**, 1364.

Aminov, B A., A. A. Golubov, and M. Y. Kupriyanov, 1996, Phys. Rev. B **53**, 365.

Banchet, J., J. Jouglar, P.-L. Vuillermoz, P. Waltz, and H. Weinstock, 1995, IEEE Trans. Appl. Supercond. **5**, 2486.

Barbour, J. C., E. L. Venturini, D. S. Ginley, and J. F. Kwak, 1992, Nucl. Instrum. Methods Phys. Res. B **65**, 531.

Barone, A., and G. Paterno, 1982, *Physics and Applications of the Josephson Effect* (Wiley, New York).

Barth, R., B. Spangenberg, C. Jäckel, H. G. Roskos, H. Kurz, and B. Holzapfel, 1993, Appl. Phys. Lett. **63**, 1149.

Barthel, K., D. Koelle, B. Chesca, A. I. Braginski, A. Marx, R. Gross, and R. Kleiner, 1999, Appl. Phys. Lett. (in press).

Beck, A., O. M. Froehlich, D. Koelle, R. Gross, H. Sato, and M. Naito, 1996, Appl. Phys. Lett. **68**, 3341.

Beck, A., A. Stenzel, O. M. Froehlich, R. Gerber, R. Gerdemann, L. Alff, B. Mayer, R. Gross, A. Marx, J. C. Villegier, and H. Moriceau, 1995, IEEE Trans. Appl. Supercond. **5**, 2192.

Bednorz, J. G., and K. A. Müller, 1986, Z. Phys. B **64**, 189.

Berberich, P., B. Utz, W. Prusseit, and H. Kinder, 1994, Physica C **219**, 497.

Beyer, J., D. Drung, F. Ludwig, T. Minotani, and K. Enpuku, 1998, Appl. Phys. Lett. **72**, 203.

Black, R. C., 1995, Ph.D. thesis, University of Maryland.

Black, R. C., A. Mathai, F. C. Wellstood, E. Dantsker, A. H. Miklich, D. T. Nemeth, J. J. Kingston, and J. Clarke, 1993, Appl. Phys. Lett. **62**, 2128.

Black, R. C., F. C. Wellstood, E. Dantsker, A. H. Miklich, J. J. Kingston, D. T. Nemeth, and J. Clarke, 1994, Appl. Phys Lett. **64**, 1.

Black, R. C., F. C. Wellstood, E. Dantsker, A. H. Miklich, D. Koelle, F. Ludwig, and J. Clarke, 1995, IEEE Trans. Appl Supercond. **5**, 2137.

Black, R. C., F. C. Wellstood, E. Dantsker, A. H. Miklich, D. T. Nemeth, D. Koelle, F. Ludwig, and J. Clarke, 1995a, Appl. Phys. Lett. **66**, 99.

Black, R. C., F. C. Wellstood, E. Dantsker, A. H. Miklich, D. T. Nemeth, D. Koelle, F. Ludwig, and J. Clarke, 1995b, Appl. Phys. Lett. **66**, 1267.

Bode, M., M. Grove, M. Siegel, and A. I. Braginski, 1996, J. Appl. Phys. **80**, 6378.

Borgmann, J., P. David, G. Ockenfuß, R. Otto, J. Schubert, W. Zander, and A. I. Braginski, 1997, Rev. Sci. Instrum. **68**, 2730.

Braginski, A. I., 1993, in *The New Superconducting Electronics*, NATO ASI series, edited by H. Weinstock and R. W. Ralston (Kluwer Academic, Dordrecht), p. 89.

Braginski, A. I., 1996, in *SQUID Sensors: Fundamentals, Fabrication and Applications*, NATO ASI Series, edited by H. Weinstock (Kluwer Academic, Dordrecht), p. 235.

Bruines, J. J. P., V. J. de Waal, and J. E. Mooij, 1982, J. Low Temp. Phys. **46**, 383.

Burghoff, M., L. Trahms, Y. Zhang, H. Bousack, and J. Borgmann, 1996, J. Clin. Eng. **21**, 62.

Cantor, R., 1996, in *SQUID Sensors: Fundamentals, Fabrication and Applications*, NATO ASI Series, edited by H. Weinstock (Kluwer Academic, Dordrecht), p. 179.

Cantor, R., L. P. Lee, M. Teepe, V. Vinetskiy, and J. Longo, 1995, IEEE Trans. Appl. Supercond. **5**, 2927.

Carr, C., D. McA. McKirdy, E. J. Romans, and G. B. Donaldson, 1997, IEEE Trans. Appl. Supercond. **7**, 3275.

Chang, W. H., 1981, IEEE Trans. Magn. **MAG-17**, 764.

Char, K., M. S. Colclough, L. P. Lee, and G. Zaharchuk, 1991, Appl. Phys. Lett. **59**, 2177.

Chaudhari, P., J. Mannhart, D. Dimos, C. C. Tsuei, C. C. Chi, M. M. Oprysko, and M. Scheuermann, 1988, Phys. Rev. Lett. **60**, 1653.

Chemla, Y. R., T. S. Lee, J. Clarke, M. Adamkiewicz, and B. Buchanan, 1997, in *Extended Abstracts of the 6th International Superconductive Electronics Conference (ISEC'97)*, Berlin, edited by H. Koch and S. Knappe (Physikalisch-Technische Bundesanstalt, Braunschweig), Vol. 1, p. 140.

Chen, J., T. Yamashita, H. Suzuki, K. Nakajima, H. Kurosawa, Y. Mutoh, Y. Hirotsu, H. Myoren, and Y. Osaka, 1991, Jpn. J. Appl. Phys., Part 1 **30**, 1964.

Chen, Y. F., Z. G. Ivanov, E. A. Stepantsov, A. Ya. Tzalenchuk, S. Zarembinski, T. Claeson, and L.-G. Johansson, 1996, J. Appl. Phys. **79**, 9221.

Chesca, B., 1998a, J. Low Temp. Phys. **110**, 963

Chesca, B., 1998b, J. Low Temp. Phys. **112**, 165.

Chesca, B., 1999, IEEE Trans. Appl. Supercond. (in press).

Clarke, J., 1983, IEEE Trans. Magn. **MAG-19**, 288.

Clarke, J., 1996, in *SQUID Sensors: Fundamentals, Fabrication and Applications*, NATO ASI Series, edited by H. Weinstock (Kluwer Academic, Dordrecht), p. 1.

Clarke, J., T. D. Gamble, W. M. Goubau, R. H. Koch, and R. F. Miracky, 1983, Geophys. Pros. **31**, 149.

Clarke, J., W. M. Goubau, and M. B. Ketchen, 1976, J. Low Temp. Phys. **25**, 99.

Clem, J., 1996, unpublished.

Clem, T. R., J. W. Purpura, R. F. Wiegert, and W. L. Goodman, 1993, IEEE Trans. Appl. Supercond. **3**, 1848.

Colclough, M. S., C. E. Gough, M. Keene, C. M. Muirhead, N. Thomas, J. S. Abell, and S. Sutton, 1987, Nature (London) **328**, 47.

Curio, G., D. Drung, H. Koch, W. Müller, U. Steinhoff, L. Trahms, Y. Q. Shen, P. Vase, and T. Freltoft, 1996, Neurosci. Lett. **206**, 204.

Daalmans, G. M., 1995, Appl. Supercond. **3**, 399.

Daalmans, G. M., L. Bär, M. Kühnl, D. Uhl, M. Selent, and J. Ramos, 1995, IEEE Trans. Appl. Supercond. **5**, 3109.

Daly, K. P., J. Burch, S. Coons, and R. Hu, 1991, IEEE Trans. Magn. **MAG-27**, 3066.

Danilov, V. V., K. K. Likharev, and O. V. Snigirev, 1980, in *SQUID'80. Superconducting Quantum Interference Devices and their Applications*, edited by H. D. Hahlbohm and H. Lübbig (Walter de Gruyter, Berlin), p. 473.

Dantsker, E., O. Froehlich, S. Tanaka, K. Kouznetsov, J. Clarke, Z. Lu, V. Matijasevic, and K. Char, 1997, Appl. Phys. Lett. **71**, 1712.

Dantsker, E., D. Koelle, A. H. Miklich, D. T. Nemeth, F. Ludwig, J. Clarke, J. T. Longo, and V. Vinetskiy, 1994, Rev. Sci. Instrum. **65**, 3809.

Dantsker, E., F. Ludwig, R. Kleiner, J. Clarke, M. Teepe, L. P. Lee, N. McN. Alford, and T. Button, 1995, Appl. Phys. Lett. **67**, 725.

Dantsker, E., S. Tanaka, and J. Clarke, 1997, Appl. Phys. Lett. **70**, 2037.

Dantsker, E., S. Tanaka, P.-Å. Nilsson, R. Kleiner, and J. Clarke, 1996, Appl. Phys. Lett. **69**, 4099.

David, B., O. Dössel, V. Doormann, R. Eckart, W. Hoppe, J. Krüger, H. Laudan, and G. Rabe, 1997, IEEE Trans. Appl. Supercond. **7**, 3267.

David, B., D. Grundler, R. Eckart, K. Fanghänel, J. P. Krumme, V. Doormann, and O. Dössel, 1994, Supercond. Sci. Technol. **7**, 287.

David, B., D. Grundler, S. Krey, V. Doormann, R. Eckart, J. P. Krumme, G. Rabe, and O. Dössel, 1996, Supercond. Sci. Technol. **9**, A96.

David, B., D. Grundler, J.-P. Krumme, and O. Dössel, 1995, IEEE Trans. Appl. Supercond. **5**, 2935.

Delin, K. A., and A. W. Kleinsasser, 1996, Supercond. Sci. Technol. **9**, 227.

Deutscher, G., and K. A. Müller, 1987, Phys. Rev. Lett. **59**, 1745.

de Waal, V. J., P. Schrijner, and R. Llurba, 1984, J. Low Temp. Phys. **54**, 215.

Dieckmann, N., A. Bock, and U. Merkt, 1996, Appl. Phys. Lett. **68**, 3626.

DiIorio, M. S., K.-Y. Yang, and S. Yoshizumi, 1995, Appl. Phys. Lett. **67**, 1926.

DiIorio, M. S., S. Yoshizumi, K.-Y. Yang, M. Maung, and B. Power, 1993, in *Advances in Superconductivity V*, edited by Y Bando and H. Yamauchi (Springer, Tokyo), p. 1161.

DiIorio, M. S., S. Yoshizumi, K.-Y. Yang, M. Maung, J. Zhang, and B. Power, 1993, IEEE Trans. Appl. Supercond. **3**, 2011.

DiIorio, M. S., S. Yoshizumi, K.-Y. Yang, J. Zhang, and M. Maung, 1991, Appl. Phys. Lett. **58**, 2552.

Dillmann, F., V. N. Glyantsev, and M Siegel, 1996, Appl. Phys. Lett. **69**, 1948.

Dimos, D., P. Chaudhari, and J. Mannhart, 1990, Phys. Rev. B **41**, 4038.

Dimos, D., P. Chaudhari, J. Mannhart, and F. K. LeGoues, 1988, Phys. Rev. Lett. **61**, 219.

Dömel, R., C. Horstmann, M. Siegel, A. I. Braginski, and M. Y. Kupriyanov, 1995, Appl. Phys. Lett. **67**, 1775.

Donaldson, G., S. Evanson, M. Otaka, K. Hasegawa, T. Shimizu, and K. Takaku, 1990, Br. J. Non-Destr. Test. **32**, 238.

Dörrer, L., S. Wunderlich, F. Schmidl, H. Schneidewind, U. Hübner, and P. Seidel, 1997, Appl. Supercond. (in press).

Dössel, O., B. David, M. Fuchs, W. H. Kullmann, and K.-M. Lüdeke, 1991, IEEE Trans. Magn. **MAG-27**, 2797.

Drung, D., 1994, IEEE Trans. Appl. Supercond. **4**, 121.

Drung, D., 1995, Appl. Phys. Lett. **67**, 1474.

Drung, D, 1996, in *SQUID Sensors: Fundamentals, Fabrication and Applications*, NATO ASI Series, edited by H. Weinstock (Kluwer Academic, Dordrecht), p. 63.

Drung, D., R. Cantor, M. Peters, T. Ryhänen, and H. Koch, 1991, IEEE Trans. Magn. **MAG-27**, 3001.

Drung, D., R. Cantor, M. Peters, H.-J. Scheer, and H. Koch, 1990, Appl. Phys. Lett. **57**, 406.

Drung, D, E. Dantsker, F. Ludwig, H. Koch, R. Kleiner, J. Clarke, S. Krey, D. Reimer, B. David, and O. Doessel, 1996, Appl. Phys. Lett. **68**, 1856.

Drung, D., S. Knappe, and H. Koch, 1995, J. Appl. Phys. **77**, 4088.

Drung, D. and H. Koch, 1993, IEEE Trans. Appl. Supercond. **3**, 2594.

Drung, D., F. Ludwig, W. Müller, U. Steinhoff, L. Trahms, Y. Q. Shen, M B. Jensen, P. Vase, T. Holst, T. Freltoft, and G. Curio, 1996, Appl. Phys. Lett. **68**, 1421.

Drung, D., T. Radic, H. Matz, H. Koch, S. Knappe, S. Menkel, and H. Burkhardt, 1997, IEEE Trans. Appl. Supercond. **7**, 3283.

Ehnholm, G. J., 1977, J. Low Temp. Phys. **29**, 1.

Eidelloth, W., B. Oh, R. P. Robertazzi, W. J. Gallagher, and R. H. Koch, 1991, Appl. Phys. Lett. **59**, 3473.

Enpuku, K., 1993, Jpn. J. Appl. Phys., Part 2 **32**, L1407.

Enpuku, K., H. Doi, G. Tokita, and T. Maruo, 1995, IEEE Trans. Appl. Supercond. **5**, 2762.

Enpuku, K., T. Maruo, and T. Minotani, 1996, J. Appl. Phys. **80**, 1207.

Enpuku, K., T. Maruo, and T. Minotani, 1997, IEEE Trans. Appl. Supercond. **7**, 3355.

Enpuku, K, T. Muta, K. Yoshida, and F. Irie, 1985, J. Appl. Phys. **58**, 1916.

Enpuku, K., Y. Shimomura, and T. Kisu, 1993, J. Appl. Phys. **73**, 7929.

Enpuku, K., K. Sueoka, K. Yoshida, and F. Irie, 1985, J. Appl. Phys. **57**, 1691.

Enpuku, K., G. Tokita, and T. Maruo, 1994, J. Appl. Phys. **76**, 8180.

Enpuku, K., G. Tokita, T. Maruo, and T. Minotani, 1995, J. Appl. Phys. **78**, 3498.

Erné, S. N., H.-D. Hahlbohm, and H. Lübbig, 1976, J. Appl. Phys. **47**, 5440.

Falco, C. M. and W. H. Parker, 1975, J. Appl. Phys. **46**, 3238.

Faley, M. I., U. Poppe, C. L. Jia, U. Dähne, Yu. Goncharov, N. Klein, K. Urban, V. N. Glyantsev, G. Kunkel, and M. Siegel, 1995, IEEE Trans. Appl. Supercond. **5**, 2091.

Faley, M. I, U. Poppe, K. Urban, H. Hilgenkamp, H. Hennes, W. Aarnink, J. Flokstra, and H. Rogalla, 1995, Appl. Phys. Lett. **67**, 2087.

Faley, M. I, U. Poppe, K. Urban, H.-J. Krause, H. Soltner, R. Hohmann, D. Lomparski, R. Kutzner, R. Wördenweber, H. Bousack, A. I. Braginski, V. Y. Slobodchikov, A. V. Gapelyuk, V. V. Khanin, and Y. V. Maslennikov, 1997, IEEE Trans. Appl. Supercond. **7**, 3702.

Ferrari, M. J., M. Johnson, F. C. Wellstood, J. Clarke, A. Inam, X. D. Wu, L. Nazar, and T. Venkatesan, 1989, Nature (London) **341**, 723.

Ferrari, M. J., M. Johnson, F. C. Wellstood, J. Clarke, P. A. Rosenthal, R. H. Hammond, and M. R. Beasley, 1988, Appl. Phys. Lett. **53**, 695.

Ferrari, M. J., M. Johnson, F. C. Wellstood, J. J. Kingston, T. J. Shaw, and J. Clarke, 1994, J. Low Temp. Phys. **94**, 15.

Ferrari, M. J., J. J. Kingston, F. C. Wellstood, and J. Clarke, 1991, Appl. Phys. Lett. **58**, 1106.

Fife, A. A., G. Anderson, V. Angus, C. Backhouse, K. Betts, M. B. Burbank, R. A. Cragg, K. Ferguson, F. Habib, P. R. Kubik, J. Nomura, M. Smith, P. Spear, W. Westera, Hu Zhou, S. Govorkov, B. Heinrich, J. C. Irwin, and W. B. Xing, 1995, IEEE Trans. Appl. Supercond. **5**, 3113.

Fleet, E. H., S. Chatraphorn, F. C. Wellstood, S. M. Green, and L. A. Knauss, 1999, IEEE Trans. Appl. Supercond. (in press).

Foglietti, V., W. J. Gallagher, M. B. Ketchen, A. W. Kleinsasser, R. H. Koch, S. I. Raider, and R. L. Sandstrom, 1986, Appl. Phys. Lett. **49**, 1393.

Foglietti, V., R. H. Koch, W. J. Gallagher, B. Oh, B. Bumble, and W. Y. Lee, 1989, Appl. Phys. Lett. **54**, 2259.

Foglietti, V., R. H. Koch, J. Z. Sun, R. B. Laibowitz, and W. J. Gallagher, 1995, J. Appl. Phys. **77**, 378.

Forgacs, R. L., and A. F. Warnick, 1967, Rev. Sci. Instrum. **38**, 214.

Freltoft, T., Y. Q. Shen, and P. Vase, 1993, IEEE Trans. Appl. Supercond. **3**, 2937.

Friedl, G., M. Vildić, B. Roas, D. Uhl, F. Bömmel, M. Römheld, B. Hillenbrand, B. Stritzker, and G. M. Daalmans, 1992, Appl. Phys. Lett. **60**, 3048.

Gao, J., W. A. M. Aarnink, G. J. Gerritsma, and H. Rogalla, 1990, Physica C **171**, 126.

Gao, J., Y. Boguslavskij, B. B. G. Klopman, D. Terpstra, D. Wijbrans, G. J. Gerritsma, and H. Rogalla, 1992, J. Appl. Phys. **72**, 525.

Gerber, R., D. Koelle, R. Gross, R. P. Huebener, F. Ludwig, E. Dantsker, R. Kleiner, and J. Clarke, 1996, Appl. Phys. Lett. **68**, 1555.

Giffard, R. P., 1980, in *Superconducting Quantum Interference Devices and Their Applications*, edited by H. D. Hahlbohm and H. Lübbig (de Gruyter, Berlin), p. 445.

Giffard, R. P., J. C. Gallop, and B. N. Petley, 1976, Prog. Quantum Electron. **4**, 301.

Glyantsev, V. N., Y. Tavrin, W. Zander, J. Schubert, and M. Siegel, 1996, Supercond. Sci. Technol. **9**, A105.

Golubov, A. A., and M. Y. Kupriyanov, 1996, Physica C **259**, 27.

Govorkov, S., A. A. Fife, G. Anderson, V. Haid, Hu Zhou, B. Heinrich, and J. Chrzanowski, 1997, IEEE Trans. Appl. Supercond. **7**, 3235.

Gross, R., in *Interfaces in High-T_c Superconducting Systems*, edited by S. L. Shinde and D. A. Rudman (Springer, New York), p. 176.

Gross, R., L. Alff, A. Beck, O. M. Froehlich, R. Gerber, R. Gerdemann, A. Marx, B. Mayer, and D. Koelle, 1995, in *Proceedings of the 2nd Workshop on HTS Applications and New Materials*, edited by D. H. Blank (University of Twente, The Netherlands), p. 8.

Gross, R., L. Alff, A. Beck, O. M. Froehlich, D. Koelle, and A. Marx, 1997, IEEE Trans. Appl. Supercond. **7**, 2929.

Gross, R., and P. Chaudhari, 1992, in *Principles and Applications of Superconducting Quantum Interference Devices*, edited by A. Barone (World Scientific, Singapore), p. 419.

Gross, R., P. Chaudhari, D. Dimos, A. Gupta, and G. Koren, 1990, Phys. Rev. Lett. **64**, 228.

Gross, R., P. Chaudhari, M. Kawasaki, and A. Gupta, 1990, Phys. Rev. B **42**, 10735.

Gross, R., P. Chaudhari, M. Kawasaki, and A. Gupta, 1991, IEEE Trans. Magn. **MAG-27**, 3227.

Gross, R., P. Chaudhari, M. Kawasaki, M. B. Ketchen, and A. Gupta, 1990a, Appl. Phys. Lett. **57**, 727.

Gross, R., P. Chaudhari, M. Kawasaki, M. B. Ketchen, and A. Gupta, 1990b, Physica C **170**, 315.

Gross, R., and B. Mayer, 1991, Physica C **180**, 235.

Grove, M., R. Dittmann, M. Bode, M. Siegel, and A. I. Braginski, 1996, Appl. Phys. Lett. **69**, 696.

Grundler, D., B. David, R. Eckart, and O. Dössel, 1993, Appl. Phys. Lett. **63**, 2700.

Grundler, D., B. David, and O. Dössel, 1995, in *Proceedings of the Second European Conference on Applied Superconductivity (EUCAS'95)*, Institute of Physics Conference Series No. **148**, Edinburgh, edited by D. Dew-Hughes (Institute of Physics, Bristol/Philadelphia), p. 1625.

Grundler, D., R. Eckart, B. David, and O. Dössel, 1993, Appl. Phys. Lett. **62**, 2134.

Gupta, A., J. Z. Sun, and C. C. Tsuei, 1994, Science **265**, 1075.

Gurvitch, M., M. A. Washington, and H. A. Huggins, 1983, Appl. Phys. Lett. **42**, 472.

Hagerhorst, J. M., J. D. Mannhart, M. M. Oprysko, M. R. Scheuermann, and C. C. Tsuei, 1989, *Laser and Particle-Beam Modification of Chemical Processes on Surfaces*, edited by A. W. Johnson, G. L. Loper and T. W. Sigmon, Mat. Res. Soc. Symp. Proc. Vol. 129, 347.

Hämäläinen, M., R. Hari, R. J. Ilmoniemi, J. Knuutila, and O. V. Lounasmaa, 1993, Rev. Mod. Phys. **65**, 413.

Hansma, P. K., 1973, J. Appl. Phys. **44**, 4191.

He, D. F., X. H. Zeng, H.-J. Krause, H. Soltner, F. Rüders, and Y. Zhang, 1998, Appl. Phys. Lett. **72**, 696.

Hein, M. A., S. Schmöe, M. Strupp, H. Piel, Y. Zhang, and A. I. Braginski, 1995, IEEE Trans. Appl. Supercond. **5**, 2501.

Herrmann, K., Y. Zhang, M. Mück, J. Schubert, and A. I. Braginski, 1991, Supercond. Sci. Technol. **4**, 583.

Herrmann, K., G. Kunkel, M. Siegel, J. Schubert, W. Zander, A. I. Braginski, C. L. Jia, B. Kabius, and K. Urban, 1995, J. Appl. Phys. **78**, 1131.

Hildebrandt, G., and F. H. Uhlmann, 1995, IEEE Trans. Appl. Supercond. **5**, 2766.

Hilgenkamp, J. W. M., G. C. S. Brons, J. G. Soldevilla, R. P. J. Ijsselsteijn, J. Flokstra, and H. Rogalla, 1994, Appl. Phys. Lett. **64**, 3497.

Hilgenkamp, J. W. M., R. P. J. Ijsselsteijn, A. J. H. M. Rijnders, P. A. C. Tavares, J. Flokstra, and H. Rogalla, 1993, J. Alloys Compd. **195**, 707.

Hilgenkamp, H., J. Mannhart, and B. Mayer, 1996, Phys. Rev. B **53**, 14586.

Hilgenkamp, J. W. M., F. J. G. Roesthuis, S. Hoogeveen, L. D. Vargas Llona, J. Flokstra, and H. Rogalla, 1995, in *Proceedings of the 2nd Workshop on HTS Applications and New Materials*, edited by D. H. A. Blank (Enschede, The Netherlands), p. 117.

Hoenig, H. E., G. M. Daalmans, L. Bär, F. Bömmel, A. Paulus, D. Uhl, H. J. Weisse, S. Schneider, H. Seifert, H. Reichenberger, and K. Abram-Fuchs, 1991, IEEE Trans. Magn. **MAG-27**, 2777.

Hohmann, R., H.-J. Krause, H. Soltner, Y. Zhang, C. A. Copetti, H. Bousack, and A. I. Braginski, 1997, IEEE Trans. Appl. Supercond. **7**, 2860.

Hollenhorst, H. N., and R. P. Giffard, 1980, J. Appl. Phys. **51**, 1719.

Hollin, C. A., J. S. Abell, S. W. Goodyear, N. G. Chew, and R. G. Humphreys, 1994, Appl. Phys. Lett. **64**, 918.

Hosoya, M., E. Goto, N. Shimizu, and Y. Harada, 1989, IEEE Trans. Magn. **MAG-25**, 1111

Humphreys, R. G., J. S. Satchell, N. G. Chew, J. A. Edwards, S. W. Goodyear, and M. N. Keene, 1991, Mater. Sci. Eng., B **10**, 293.

Husemann, K.-D., R. Gross, R. P. Huebener, and B. Roas, 1993, Appl. Phys. Lett. **62**, 2871.

Il'ichev, E., V. Zakosarenko, V. Schultze, H.-G. Meyer, H. E. Hoenig, V. N. Glyantsev, and A. Golubov, 1998, Appl. Phys Lett. **72**, 731.

Itozaki, H., S. Tanaka, T. Nagaishi, and H. Kado, 1994, IEICE Trans. Electron. **E77-C**, 1185.

Itozaki, H., S. Tanaka, H. Toyoda, T. Hirano, Y. Haruta, M. Nomura, T. Saijou, and H. Kado, 1996, Supercond. Sci. Technol. **9**, A38.

Ivanov, Z. G., P. Å. Nilsson, D. Winkler, J. A. Alarco, T. Claeson, E. A. Stepantsov, and A. Ya. Tzalenchuk, 1991, Appl. Phys. Lett. **59**, 3030.

Jackel, L. D., and R. A. Buhrman, 1975, J. Low Temp. Phys. **19**, 201.

Jaklevic, R. C., J. Lambe, A. H. Silver, and J. E. Mercereau, 1964, Phys. Rev. Lett. **12**, 159.

Jaycox, J. M., and M. B. Ketchen, 1981, IEEE Trans. Magn. **17**, 400.

Jia, C. L., B. Kabius, K. Urban, K. Herrmann, G. J. Cui, J. Schubert, W. Zander, A. I. Braginski, and C. Heiden, 1991, Physica C **175**, 545.

Jia, C. L., B. Kabius, K. Urban, K. Herrmann, J. Schubert, W. Zander, and A. I. Braginski, 1992, Physica C **196**, 211.

Josephson, B D., 1962, Phys. Lett. **1**, 251.

Josephson, B D., 1965, Adv. Phys. **14**, 419.

Kang, D.-J., W. E. Booij, M. G. Blamire, and E. J. Tarte, 1997, in *Extended Abstracts of the 6th International Superconductive Electronics Conference (ISEC'97)*, Berlin, edited by H. Koch and S. Knappe (Physikalisch-Technische Bundesanstalt, Braunschweig), Vol. 3, p. 40

Kasai, N., N Ishikawa, H. Yamakawa, K. Chinone, S. Nakayama, and A. Odawara, 1997, IEEE Trans. Appl. Supercond. **7**, 2315.

Kawasaki, M., P. Chaudhari, and A. Gupta, 1992, Phys. Rev. Lett. **68**, 1065.

Kawasaki, M., P. Chaudhari, T. H. Newman, and A. Gupta, 1991, Appl. Phys. Lett. **58**, 2555.

Kawasaki, M., E. Sarnelli, P. Chaudhari, A. Gupta, A. Kussmaul, J. Lacey, and W. Lee, 1993, Appl. Phys. Lett. **62**, 417.

Keene, M. N., N. G. Chew, S. W. Goodyear, J. A. Edwards, R. G. Humphreys, K. Lander, and J. S. Satchell, 1994, Physica C **230**, 110.

Keene, M. N., N. J. Exon, R. G. Humphreys, and N. G. Chew, 1996, J. Appl. Phys. **79**, 8783.

Keene, M. N., S. W. Goodyear, N. G. Chew, R. G. Humphreys, J. S. Satchell, J. A. Edwards, and K. Lander, 1994, Appl. Phys. Lett. **64**, 366.

Keene, M. N., S. W. Goodyear, J. S. Satchell, J. A. Edwards, N. G. Chew, and R. G. Humphreys, 1993, IEEE Trans. Appl. Supercond. **3**, 2430.

Keene, N. M., J. S. Satchell, S. W. Goodyear, R. G. Humphreys, J A. Edwards, N. G. Chew, and K. Lander, 1995, IEEE Trans. Appl. Supercond. **5**, 2923.

Ketchen, M. B., 1981, IEEE Trans. Magn. **17**, 387.

Ketchen, M. B., W. J. Gallagher, A. W. Kleinsasser, S. Murphy, and J. R. Clem, 1985, in *SQUID'85, Superconducting Quantum Interference Devices and their Applications*, edited by H. D. Hahlbohm and H. Lübbig (Walter de Gruyter, Berlin), p. 865.

Ketchen, M. B., W. M. Goubau, J. Clarke, and G. B. Donaldson, 1978, Appl. Phys. **49**, 4111.

Kittel A., K. A. Kouznetsov, R. McDermott, B. Oh, and John Clarke, 1998, Appl. Phys. Lett. **73**, 2197.

Kleiner, R., 1996, unpublished.

Kleiner, R., and P. Müller, 1994, Phys. Rev. B **49**, 1327.

Kleiner, R., F. Steinmeyer, G. Kunkel, and P. Müller, 1992, Phys. Rev. Lett. **68**, 2394.

Kleinsasser, A. W., and K. A. Delin, 1995, Appl. Phys. Lett **66**, 102.

Knappe, S, D. Drung, T. Schurig, H. Koch, M. Klinger, and J. Hinken, 1992, Cryogenics **32**, 881

Koch, H., R. Cantor, D. Drung, S. N. Erne, K. P. Matthies, M. Peters, T Ryhänen, H. J. Scheer, and H. D. Hahlbohm, 1991, IEEE Trans. Magn. **MAG-27**, 2793.

Koch, R. H. 1994, unpublished.

Koch, R. H. 1997, private communication.

Koch, R. H., J. Clarke, W. M. Goubau, J. M. Martinis, C M. Pegrum, and D. J. Van Harlingen, 1983, J. Low Temp. Phys. **51**, 207.

Koch, R. H., W. Eidelloth, B. Oh, R. P. Robertazzi, S. A. Andrek, and W. J. Gallagher, 1992, Appl. Phys. Lett. **60**, 507.

Koch, R. H., V. Foglietti, J. R. Rozen, K. G. Stawiasz, M. B. Ketchen, D. K. Lathrop, J. Z. Sun, and W J Gallagher, 1994, Appl. Phys. Lett. **65**, 100

Koch, R. H., W. J. Gallagher, B. Bumble, and W. Y. Lee, 1989, Appl. Phys. Lett. **54**, 951

Koch, R. H., M. B. Ketchen, W. J. Gallagher, R. L. Sandstrom, A. W. Kleinsasser, D. R. Gambrel, T. H. Field, and H. Matz, 1991, Appl. Phys. Lett. **58**, 1786.

Koch, R. H., J. R. Rozen, J. Z. Sun, and W J Gallagher, 1993, Appl. Phys. Lett. **63**, 403

Koch, R. H., J. R. Rozen, P. Wöltgens, T. Picunko, W. J. Goss, D. Gambrel, D. Lathrop, R. Wiegert, and D. Overway, 1996, Rev. Sci. Instrum. **67**, 2968.

Koch, R. H., J. Z. Sun, V. Foglietti, and W J Gallagher, 1995, Appl. Phys. Lett. **67**, 709

Koch, R. H., C. P. Umbach, G. J. Clark, P. Chaudhari, and R. B. Laibowitz, 1987, Appl. Phys. Lett. **51**, 200.

Koelle, D., E. Dantsker, D. T. Nemeth, F Ludwig, and J. Clarke, 1993, unpublished.

Koelle, D., A. H. Miklich, E. Dantsker, F. Ludwig, D. T. Nemeth, J. Clarke, W. Ruby, and K. Char, 1993, Appl. Phys. Lett. **63**, 3630.

Koelle, D., A. H. Miklich, F. Ludwig, E. Dantsker, D. T. Nemeth, and J. Clarke, 1993, Appl. Phys. Lett. **63**, 2271.

Kötitz, R., H. Matz, L. Trahms, H. Koch, W. Weitschies, T. Rheinländer, W. Semmler, and T. Bunte, 1997, IEEE Trans. Appl. Supercond. **7**, 3678.

Krause, H.-J. Y. Zhang, R. Hohmann, M. Grüneklee, M. I. Faley, D. Lomparski, M. Maus, H. Bousack, and A. I. Braginski, 1997, in *Proceedings of the Third European Conference on Applied Superconductivity (EUCAS'97)*, Ueldhoven Institute of Physics Conference Series No. 158, edited by H. Rogalla and D. H. A. Blank (Institute of Physics, Philadelphia), p. 775.

Kreutzbruck, M. v., M. Mück, U. Baby, and C. Heiden, 1998, in *Studies in Applied Electromagnetics and Mechanics* (IOS Press Amsterdam, The Netherlands), Vol. 13, p. 345.

Kreutzbruck, M. v., J. Tröll, M. Mück, C. Heiden, and Y. Zhang, 1997, IEEE Trans. Appl. Supercond. **7**, 3279.

Kromann, R., J. J. Kingston, A. H. Miklich, L. T. Sagdahl, and J. Clarke, 1993, Appl. Phys. Lett. **63**, 559

Kugai, H., T. Nagaishi, and H. Itozaki, 1996, in *Advances in Superconductivity VIII*, edited by H. Hayakawa and Y. Enomoto (Springer, Tokyo), p. 1145.

Kupriyanov, M. Y., and K. K. Likharev, 1990, Sov. Phys. Usp. **160**, 49.

Kurkijärvi, J., 1972, Phys. Rev. B **6**, 832.

Kurkijärvi, J., 1973, J Appl. Phys. **44**, 3729.

Kuzmin, L. S., K. K. Likharev, V. V. Migulin, E. A. Polunin, and N. A. Simonov, 1985, in *SQUID'85, Superconducting Quantum Interference Devices and their Applications*, edited by H.-D. Hahlbohm and H. Lübbig (Walter de Gruyter, Berlin), p. 1029.

Lee, L. P., K. Char, M. S. Colclough, and G. Zaharchuk, 1991, Appl Phys. Lett. **59**, 3051.

Lee, L. P., J. Longo, V. Vinetskiy, and R. Cantor, 1995, Appl. Phys. Lett. **66**, 1539.

Lee, T. S., Y. R. Chemla, E. Dantsker, and J. Clarke, 1997, IEEE Trans. Appl. Supercond. **7**, 3147.

Lee, T. S., E. Dantsker, and J. Clarke, 1996, Rev. Sci. Instrum. **67**, 4208.

Likhachev, A. G., V. N. Polushkin, S. V. Uchaikin, and B. V. Vasiliev, 1990, Supercond. Sci. Technol. **3**, 148.

Likharev, K. K., 1986, *Dynamics of Josephson Junctions and Circuits* (Gordon and Breach, New York).

Likharev, K. K. and B. T. Ulrich, 1978, *Dynamics of Josephson Junction Circuits: Basic Theory* (Moscow University, Moscow; in Russian).

Ludwig, F., J. Beyer, D Drung, S. Bechstein, and Th. Schurig, 1997, Appl. Supercond. **5**, 345.

Ludwig, F., E. Dantsker, R. Kleiner, D. Koelle, J. Clarke, S. Knappe, D. Drung, H. Koch, N. McN. Alford, and T. W. Button, 1995, Appl. Phys. Lett. **66**, 1418.

Ludwig, F., E. Dantsker, D. Koelle, R. Kleiner, A. H. Miklich, and J. Clarke, 1995, Appl. Supercond. **3**, 383.

Ludwig, F., E. Dantsker, D. Koelle, R. Kleiner, A. H. Miklich, D. T. Nemeth, J. Clarke, D. Drung, J. Knappe, and H. Koch, 1995, IEEE Trans. Appl. Supercond. **5**, 2919.

Ludwig, F., E. Dantsker, D. T. Nemeth, D. Koelle, A. H. Miklich, J. Clarke, S. Knappe, H. Koch, and R. E. Thomson, 1994, Supercond. Sci. Technol. **7**, 273.

Ludwig, F., D. Koelle, E. Dantsker, D. T. Nemeth, A. H. Miklich, J. Clarke, and R. E. Thomson, 1995, Appl. Phys. Lett. **66**, 373.

Mannhart, J., P. Chaudhari, D. Dimos, C. C. Tsuei, and T. R. McGuire, 1988, Phys. Rev. Lett. **61**, 2476.

Martinis, J. M., and J. Clarke, 1985, J. Low Temp. Phys. **61**, 227.

Marx, A., L. Alff, and R. Gross, 1995, Appl. Phys. Lett. **67**, 1929.

Marx, A., U. Fath, W. Ludwig, R. Gross, and T. Amrein, 1995, Phys. Rev. B **51**, 6735.

Marx, A., and R. Gross, 1997, Appl. Phys. Lett. **70**, 120.

Mathai, A., D. Song, Y. Gim, and F. C. Wellstood, 1993, IEEE Trans. Appl. Supercond. **3**, 2609.

Matijasevic, V., Z. Lu, T. Kaplan, and C. Huang, 1997, in *Proceedings of the Third European Conference on Applied Superconductivity (EUCAS'97)*, Veldhoven Institute of Physics Conference Series No. 158, p. 189.

Matsuda, M., Y. Murayama, S. Kiryu, N. Kasai, S. Kashiwaya, M. Koyanagi, and T. Endo, 1991, IEEE Trans. Magn. **MAG-27**, 3043.

Matzander, U., U. Kalberkamp, V. Rath, K.-D. Husemann, G. Panaitow, E. Zimmermann, and Y. Zhang, 1997, in *Extended Abstracts of the 6th International Superconductive Electronics Conference (ISEC'97)*, Berlin, edited by H. Koch and S. Knappe (Physikalisch-Technische Bundesanstalt, Braunschweig), Vol. 3, p. 355.

Mayer, B., L. Alff, T. Träuble, R. Gross, P. Wagner, and H. Adrian, 1993, Appl. Phys. Lett. **63**, 996.

McCumber, D. E., 1968, J. Appl. Phys. **39**, 3113.

McDaniel, E. B., S. C. Gausephohl, C.-T. Li, M. Lee, J. W. P. Hsu, R. A. Rao, and C. B. Eom, 1997, Appl. Phys. Lett. **70**, 1882.

Mercereau, J. E., 1970, Rev. Phys. Appl. **5**, 13.

Meservey, R., and P. M. Tedrow, 1969, J. Appl. Phys. **40**, 2028.

Miklich, A. H., J. Clarke, M. S. Colclough, and K. Char, 1992, Appl. Phys. Lett. **60**, 1899.

Miklich, A. H., J. J. Kingston, F. C. Wellstood, J. Clarke, M. S. Colclough, K. Char, and G. Zaharchuk, 1991, Appl. Phys. Lett. **59**, 988.

Miklich, A. H., D. Koelle, E. Dantsker, D. T. Nemeth, J. J. Kingston, R. F. Kroman, and J. Clarke, 1993, IEEE Trans. Appl. Supercond. **3**, 2434.

Miklich, A. H., D. Koelle, F. Ludwig, D. T. Nemeth, E. Dantsker, and J. Clarke, 1995, Appl. Phys. Lett. **66**, 230.

Miklich, A. H., D. Koelle, T. J. Shaw, F. Ludwig, D. T. Nemeth, E. Dantsker, and J. Clarke, 1994, Appl. Phys. Lett. **64**, 3494.

Milliken, F. P., S. L. Brown, and R. H. Koch, 1997, Appl. Phys. Lett. **71**, 1857.

Milliken, F. P., R. H. Koch, S. L. Brown, R. A. Altman, W. J. Gallagher, S. G. Haupt, and D. K. Lathrop, 1997, J. Appl. Phys. **82**, 6301.

Minotani, T., K. Enpuku, and Y. Kuroki, 1997, J. Appl. Phys. **82**, 457.

Minotani, T., S. Kawakami, T. Kiss, Y. Kuroki, and K. Enpuku, 1997, Jpn. J. Appl. Phys., Part 2 **36**, L1092.

Missert, N., T. E. Harvey, and R. H. Ono, 1993, Appl. Phys. Lett. **63**, 1690.

Moeckley, B. H., D. K. Lathrop, and R. A. Buhrman, 1993, Phys. Rev. B **47**, 400.

Mück, M., 1993, IEEE Trans. Appl. Supercond. **3**, 2003.

Mück, M., J. Clarke, and C. Heiden, 1994, Proc. SPIE **2160**, p. 180.

Mück, M., C. Heiden, and J. Clarke, 1994, J. Appl. Phys. **75**, 4588.

Mück, M., M. v. Kreutzbruck, U. Baby, J. Tröll, and C. Heiden, 1997, Physica C **282-287**, 407.

Nagaishi, T., H. Kugai, H. Toyoda, and H. Itozaki, 1997, IEEE Trans. Appl. Supercond. **7**, 2886.

Nakane, H., Y. Tarutani, T. Nishino, H. Yamada, and U. Kawabe, 1987, Jpn. J. Appl. Phys., Part 2 **26**, L1925.

Nichols, D. G., E. Dantsker, R. Kleiner, M. Mück, and J. Clarke, 1996, J. Appl. Phys. **80**, 6032.

Nisenoff, M., 1970, Rev. Phys. Appl. **5**, 21.

Ockenfuß, G. J., J. Borgmann, M. Reese, and R. Wördenweber, 1997, IEEE Trans. Appl. Supercond. **7**, 3698.

Ockenfuß, G. J., R. Wördenweber, T. A. Scherer, R. Unger, and W. Jutzi, 1995, Physica C **243**, 24.

Oh, B. D., R. H. Koch, W. J. Gallagher, R. P. Robertazzi, and W. Eidelloth, 1991, Appl. Phys. Lett. **59**, 123.

Ono, R. H., J. A. Beall, M. W. Cromar, T. E. Harvey, M. E. Johansson, C. D. Reintsema, and D. A. Rudman, 1991, Appl. Phys. Lett. **59**, 1126.

Ono, R. H., L. R. Vale, K. R. Kimminau, J. A. Beall, M. W. Cromar, C. D. Reintsema, T. E. Harvey, P. A. Rosenthal, and D. A. Rudman, 1993, IEEE Trans. Appl. Supercond. **3**, 2389.

Ott, H. W., 1988, *Noise Reduction Techniques in Electronic Systems*, Second Edition (Wiley, New York), p. 233.

Penny, R. D., D. K. Lathrop, E. E. Magnuson, B. D. Thorson, B. R. Whitecotton, R. H. Koch, and J. R. Rosen, 1997, IEEE Trans. Appl. Supercond. **7**, 2323.

Pettiette-Hall, C. L., J. A. Luine, J. Murduck, J. F. Burch, R. Hu, M. Sergant, and D. St. John, 1995, IEEE Trans. Appl. Supercond. **5**, 2087.

Phillips, J., 1993, in *The New Superconducting Electronics*, NATO ASI series, edited by H. Weinstock and R. W. Ralston (Kluwer Academic, Dordrecht), p. 59.

Phillips, J., 1996, J. Appl. Phys. **79**, 1829.

Pitzius, P., V. Dworak, and U. Hartmann, 1997, in *Extended Abstracts of the 6th International Superconductive Electronics Conference (ISEC'97)*, Berlin, edited by H. Koch and S. Knappe (Physikalisch-Technische Bundesanstalt, Braunschweig), Vol. 3, p. 395.

Purpura, J. W., T. R. Clem, and R. F. Wiegert, 1993, IEEE Trans. Appl. Supercond. **3**, 2445.

Quincey, P. G., 1994, Appl. Phys. Lett. **64**, 517.

Radic, T. D. Drung, S. Knappe, and S. Menkel, 1997, in *Extended Abstracts of the 6th International Superconductive Electronics Conference (ISEC'97)*, Berlin, edited by H. Koch and S. Knappe (Physikalisch-Technische Bundesanstalt, Braunschweig), Vol. 3, p. 352.

Reimer, D , F. Ludwig, M. Schilling, S. Knappe, and D. Drung, 1995, in *Proceedings of the Second European Conference on Applied Superconductivity (EUCAS'95)*, Edinburgh, edited by D. Dew-Hughes (Institute of Physics, Bristol, Philadelphia) Institute of Physics Conference Series No. 148, p. 1605.

Reimer, D., M. Schilling, S. Knappe, and D. Drung, 1995, IEEE Trans. Appl. Supercond. **5**, 2342.

Reintsema, C. D., R. H. Ono, G. Barnes, L. Borcherdt, T. E. Harvey, G. Kunkel, D. A. Rudman, L. R. Vale, N. Missert, and P. A. Rosenthal, 1995, IEEE Trans. Appl. Supercond. **5**, 3405.

Roas, B., L. Bär, M. Kühnl, G. Daalmans, and F. Bömmel, 1993, in *Proceedings of European Conference on Applied Superconductivity (EUCAS'93)*, edited by H. C. Freyhardt (DGM Informationsgesellschaft, Oberursel), p. 1335.

Rosenthal, P. A., E. N. Grossman, R. H. Ono, and L. R. Vale, 1993, Appl. Phys. Lett. **63**, 1984.

Russek, S. E., D. K. Lathrop, B. H. Moeckly, R. A. Buhrman, D. H. Shin, and J. Silcox, 1990, Appl. Phys. Lett. **57**, 1155.

Russek, S. E., S. C. Sanders, A. Roshko, and J. W. Ekin, 1994, Appl. Phys. Lett. **64**, 3649.

Russek, S. E., S. C. Sanders, C. C. Clickner, and J. W. Ekin, 1996, Applied Superconductivity Conference (ASC'96), Pittsburgh, PA (unpublished).

Ryhänen, T., H. Seppä, R. Ilmoniemi, and J. Knuutila, 1989, J. Low Temp. Phys. **76**, 287.

Satoh, T., M. Y. Kupriyanov, J. Tsai, M. Hidaka, and H. Tsuge, 1995, IEEE Trans. Appl. Supercond. **5**, 2612.

Savo, B., F. C. Wellstood, and J. Clarke, 1987, Appl. Phys. Lett. **50**, 1757.

Scharnweber, R., and M. Schilling, 1996, Appl. Phys. Lett. **69**, 1303.

Scharnweber, R., and M. Schilling, 1997, IEEE Trans. Appl. Supercond. **7**, 3485.

Scharnweber, R., K.-O. Subke, and M. Schilling, 1995, in *Proceedings of the Second European Conference on Applied Superconductivity (EUCAS'95)*, Edinburgh, edited by D. Dew-Hughes (Institute of Physics, Bristol/Philadelphia) Institute of Physics Conference Series No. 148, p. 1609.

Scheel, H. J., M. Berkowski, and B. Chabotes, 1991, J. Cryst. Growth **115**, 19.

Schilling, M., 1997, IEEE Trans. Appl. Supercond. **7**, 2960.

Schilling, M., S. Krey, and R. Scharnweber, 1996, Appl. Phys. Lett. **69**, 2751.

Schilling, M., R. Scharnweber, and S. Völkl, 1995, IEEE Trans. Appl. Supercond. **5**, 2346.

Schmidl, R., S. Wunderlich, L. Dörrer, H. Specht, J. Heinrich, K.-U. Barholz, H. Schneidewind, U. Hübner, and P. Seidel, 1997, in *Proceedings of the Third European Conference on Applied Superconductivity (EUCAS'97)*, Veldhoven, edited by H. Rogalla and D. H. A. Blank (Institute of Physics, Philadelphia), Vol. 158, p. 651.

Schmidl, R., S. Wunderlich, L. Dörrer, H. Specht, S. Linzen, H. Schneidewind, and P. Seidel, 1997, IEEE Trans. Appl. Supercond. **7**, 2756.

Schmidt, J. M., L. P. Lee, A. Matlashov, M. Teepe, V. Vinetskiy, and R. Cantor, 1996, Biomag'96, Santa Fe, New Mexico, Abstracts p. 340.

Schneider, J., H. Kohlstedt, and R. Wördenweber, 1993, Appl. Phys. Lett **63**, 2426.

Schneidewind, H., F. Schmidl, S. Linzen, and P. Seidel, 1995, Physica C **250**, 191.

Schultze, V., R. Ijsselsteijn, V. Zakosarenko, F. Thrum, E Il'ichev, and H. G. Meyer, 1997, in *Extended Abstracts of the 6th International Superconductive Electronics Conference (ISEC'97)*, Berlin, edited by H. Koch and S. Knappe (Physikalisch-Technische Bundesanstalt, Braunschweig), Vol. 3, p. 71.

Schultze, V., R. Stolz, R. Ijsselsteijn, V. Zakosarenko, L Fritzsch, F. Thrum, E. Il'ichev, and H.-G. Meyer, 1997, IEEE Trans. Appl. Supercond. **7**, 3473.

Seidel, P., R. Weidl, S. Brabetz, F. Schmidl, H. Nowak, and U Leder, 1997, in *Extended Abstracts of the 6th International Superconductive Electronics Conference (ISEC'97)*, Berlin, edited by H. Koch and S. Knappe (Physikalisch-Technische Bundesanstalt, Braunschweig), Vol. 3, p. 321.

Shaw, T J., J. Clarke, R. B. van Dover, L. F. Schneemeyer, and A. E. White, 1996, Phys. Rev. B **54**, 15411.

Sheen, D. M., S. M. Ali, D. E. Oates, R. S. Withers, and J. A Kong, 1991, IEEE Trans. Appl. Supercond. **1**, 108.

Shen, Y. Q., Z. J. Sun, R. Kromann, T. Holst, P. Vase, and T. Freltoft, 1995, Appl. Phys. Lett. **67**, 2081.

Simon, R., J. B. Bulman, J. F. Burch, S. B. Coons, K. P. Daly, W. D. Dozier, R. Hu, A. E. Lee, J. A. Luine, C. E. Platt, and M. J. Zani, 1991, IEEE Trans. Magn. **MAG-27**, 3209.

Sivakov, A. G., A. P. Zhuravel, O. G. Turutanov, I. M. Dmitrenko, J. W. M. Hilgenkamp, G. C. S. Brons, J. Flokstra, and H. Rogalla, 1994, Physica C **232**, 93.

Somekh, R. E. and Z. H. Barber, 1992, in *Physics and Materials Science of High Temperature Superconductors, II*, edited by R. Kossowsky, B. Raveau, D. Wohlleben, and S. K. Patapis (Kluwer Academic, Dordrecht), p. 443.

Stewart, W. C., 1968, Appl. Phys. Lett. **12**, 277.

Strikovskiy, M. D., and A. Engelhardt, 1996, Appl. Phys. Lett. **69**, 2918.

Sun, J. Z., W. J. Gallagher, A. C. Callegari, V. Foglietti, and R. H. Koch, 1993, Appl. Phys. Lett. **63**, 1561.

Sun, J. Z., W. J. Gallagher, and R. H. Koch, 1992, Appl. Phys Lett. **61**, 3190

Sun, J. Z., W. J. Gallagher, and R. H. Koch, 1993, IEEE Trans Appl. Supercond. **3**, 2022.

Sun, J. Z., W. J. Gallagher, and R. H. Koch, 1994, Phys. Rev. B **50**, 13664.

Tanaka S., H. Itozaki, and H. Kado, 1995, in *Proceedings of the 7th International Symposium on Superconductivity (ISS '94)*, Advances in Superconductivity VII, edited by K. Yamafuji and T. Morishita (Springer, Tokyo), p. 1117.

Tanaka, S., H. Itozaki, H. Toyoda, N. Harada, A. Adachi, K Okajima, and H. Kado, 1994, Appl. Phys. Lett. **64**, 514.

Tavrin, Y., H.-J. Krause, W. Wolf, V. Glyantsev, J. Schubert, W. Zander, and H. Bousack, 1995, Cryogenics **36**, 83.

Tavrin Y., and M. Siegel, 1997, in *Proceedings of the Third European Conference on Applied Superconductivity (EUCAS'97)*, Veldhoven, edited by H. Rogalla and D. H. A. Blank (Institute of Physics, Philadelphia), No. 158, p. 719.

Tavrin, Y., M. Siegel, and J. Hinken, 1999, IEEE Trans. Appl. Supercond. (in press).

Tavrin, Y., Y. Zhang, M. Mück, A. I. Braginski, and C. Heiden, 1993a, IEEE Trans. Appl. Supercond. **3**, 2477.

Tavrin, Y., Y. Zhang, M. Mück, A. I. Braginski, and C. Heiden, 1993b, Appl. Phys. Lett. **62**, 1824.

Tavrin, Y., Y. Zhang, W. Wolf, and A. I. Braginski, 1994, Supercond. Sci. Technol. **7**, 265.

ter Brake, H. J. M., W. A. M. Aarnink, P. J. van den Bosch, J. W. M. Hilgenkamp, J. Flokstra, and H. Rogalla, 1997, Supercond. Sci. Technol. **10**, 512.

ter Brake, H. J. M., N. Janssen, J. Flokstra, D. Veldhuis, and H. Rogalla, 1997, IEEE Trans. Appl. Supercond. **7**, 2545.

ter Brake, H. J. M., R. Karunanithi, H. J. Holland, J. Flokstra, D. Veldhuis, L. Vargas, J. W. M. Hilgenkamp, W. Jaszczuk, N. Janssen, F. J. G. Roesthuis, and H. Rogalla, 1997, Meas. Sci. Technol **8**, 927.

Tesche, C. D., and J. Clarke, 1977, J. Low Temp. Phys. **29**, 301.

Tesche, C. D., and J. Clarke, 1979, J. Low Temp. Phys. **37**, 397.

Tinchev, S. S., 1997, in *Microwave Physics and Technique* (Kluwer Academic, Dordrecht), p. 173.

Tinchev, S. S., and J. H. Hinken, 1992, in *Superconducting Devices and their Applications*, edited by H. Koch and H. Lübbig, Springer Proceedings in Physics, (Springer, Berlin/Heidelberg), Vol. 64, p. 102.

TonThat, Dinh M., M. Ziegeweid, Y.-Q. Song, E. J. Munson, S. Appelt, A. Pines, and J. Clarke, 1997, Chem. Phys. Lett **272**, 245.

Töpfer, H., 1991, in *Superconductivity and Cryoelectronics*, edited by W. Krech, P. Seidel, and H. G. Meyer (World Scientific, Singapore), p 170.

Töpfer, H., and F. H. Uhlmann, 1994, in *Proceedings of the Seventh International Symposium on Weak Superconductivity*, Smolenice, p 336

Tsuei, C. C., J. R Kirtley, C. C. Chi, L. S. Yu-Jahnes, A. Gupta, T. Shaw, J. Z. Sun, and M. B. Ketchen, 1994, Phys. Rev. Lett. **73**, 593.

Tsuei, C. C., J. Mannhart, and D. Dimos, 1989, in *Proceedings of the Topical Conference on High T_c Superconducting Thin Films, Devices and Applications*, Atlanta, GA, 1988, edited by G. Mararitondo, R. Joint, and M. Onellion (AIP, New York), p. 194.

Uhlmann, H., H. Töpfer, F. Verwiebe, and J. Uhlig, 1992, in *Superconducting Devices and their Applications*, edited by H. Koch and H. Lübbig, Springer Proceedings in Physics (Springer, Berlin/Heidelberg), Vol. 64, p. 292.

Vale, L. R., R. H. Ono, and D. A. Rudman, 1997, IEEE Trans. Appl. Supercond. **7**, 3193.

van der Harg, A. J. M., E. van der Drift, and P. Hadley, 1995, IEEE Trans. Appl. Supercond. **5**, 1448.

Voss, R. F., 1981, J. Low Temp. Phys. **42**, 151.

Vrba, J., 1996, in *SQUID Sensors: Fundamentals, Fabrication and Applications*, NATO ASI Series, edited by H. Weinstock (Kluwer Academic, Dordrecht), p. 117.

Vu, L. N., and D. J. Van Harlingen, 1993, IEEE Trans. Appl. Supercond. **3**, 1918.

Wang, S. G., L. H. Zhang, C. J. Wang, and Y. D. Dai, 1997, M2S-HTSC-V, *Fifth International Conference, Materials and Mechanisms of Superconductivity, High-Temperature Superconductors*, Beijing, China, p. 31.

Weidl, R., S. Brabetz, F. Schmidl, F. Klemm, S. Wunderlich, and P. Seidel, 1997, Supercond. Sci. Technol. **10**, 95.

Weinstock H, 1996, Ed., *SQUID Sensors: Fundamentals, Fabrication and Applications* (Kluwer Academic, Dordrecht).

Wellstood, F., C. Heiden, and J. Clarke, 1984, Rev. Sci. Instrum. **55**, 952.

Wellstood, F. C., J. J. Kingston, and J. Clarke, 1994, J. Appl. Phys. **75**, 683.

Wellstood, F. C., J. J. Kingston, M. J. Ferrari, and J. Clarke, 1990, Appl. Phys. Lett. **57**, 1930.

Wellstood, F. C., J. J. Kingston, M. J. Ferrari, and J. Clarke, 1991, IEEE Trans. Magn. **27**, 2569.

Wellstood, F. C., A. H. Miklich, J. J. Kingston, M. J. Ferrari, J. Clarke, M. S. Colclough, K. Char, and G. Zaharchuk, 1992, in *Superconducting Devices and their Applications*, edited by H. Koch and H. Lübbig, Springer Proceedings in Physics (Springer, Berlin/Heidelberg), Vol. 64, p. 162.

Wen, C. P., 1969, IEEE Trans. Microwave Theory Tech. **MTT-17**, 1087.

Wikswo, Jr., J. P., 1995, IEEE Trans. Appl. Supercond. **5**, 74.

Woeltgens, P. J. M., R. H. Koch, R. Matthews, S. L. Brown, R. A. Altman, W. J. Gallagher, S. G. Haupt, and D. K. Lathrop, 1996, Applied Superconductivity Conference (ASC'96), Pittsburgh (unpublished).

Wu, M. K., J. R. Ashburn, C. J. Torng, P. H. Hor, R. L. Meng, L. Gao, N. Z. Huang, Y. Q. Wang, and C. W. Chu, 1987, Phys. Rev. Lett. **58**, 908.

Yanamoto, K., B. M. Lairson, J. C. Bravman, and T. H. Geballe, 1991, J. Appl. Phys. **69**, 7189.

Yi, H. R., M Gustafsson, D. Winkler, E. Olsson, and T. Claeson, 1996, J. Appl. Phys. **79**, 9213.

Zakosarenko, V., F. Schmidl, H. Schneidewind, L. Dörrer, and P. Seidel, 1994, Appl. Phys. Lett. **65**, 779.

Zani, M. J., J. A. Luine, G. S. Lee, J. M. Murduck, R. Ha, M. J. Levis, R. A. Davidheiser, and L. R. Eaton, 1991, IEEE Trans. Magn. **MAG-27**, 2557.

Zhang, Y., M. Gottschlich, H. Soltner, E. Sodtke, J. Schubert, W. Zander, and A. I. Braginski, 1995, Appl. Phys. Lett. **67**, 3183.

Zhang, Y., U. Krüger, R. Kutzner, R. Wördenweber, J. Schubert, W. Zander, E. Sodtke, and A. I. Braginski, 1994, Appl. Phys. Lett. **65**, 3380.

Zhang, Y., M. Mück, M. Bode, K. Herrmann, J. Schubert, W. Lander, A. I. Braginski, and C. Heiden, 1992, Appl. Phys. Lett. **60**, 2303.

Zhang, Y., M. Mück, K. Herrmann, J. Schubert, W. Zander, A. I. Braginski, and C. Heiden, 1993, IEEE Trans. Appl. Supercond. **3**, 2465.

Zhang, Y., M. Mück, K. Herrmann, W. Zander, J. Schubert, A. I. Braginski, and Ch. Heiden, 1992, Appl. Phys. Lett. **60**, 645.

Zhang, Y., H. Soltner, H.-J. Krause, E. Sodtke, W. Zander, J. Schubert, M. Grüneklee, D. Lomparski, M. Banzer, H. Bousack, and A. I. Braginski, 1997, IEEE Trans. Appl. Supercond. **7**, 2866.

Zhang, Y., H. Soltner, N. Wolters, W. Zander, J. Schubert, M. Banzet, and A. I. Braginski, 1997, IEEE Trans. Appl. Supercond. **7**, 2870.

Zhang, Y., Y. Tavrin, M. Mück, A. I. Braginski, C. Heiden, S. Hampson, C. Pantev, and T. Elbert, 1993, Brain Topography **5**, 379.

Zhang, Y., N. Wolters, X. H. Zeng, J. Schubert, W. Zander, H. Soltner, M. Banzet, F. Ruders, and A. I. Braginski, 1997, Appl. Supercond. (in press).

Zhang, Y., W. Zander, J. Schubert, F. Rüders, H. Soltner, M. Banzet, N. Wolters, X. H. Zeng, and A. I. Braginski, 1997, Appl. Phys. Lett. **71**, 704.

Zhang, Y., H. R. Yi, J. Schubert, W. Zander, M. Banzet, and A. I. Braginski, 1998, Appl. Phys. Lett. **72**, 2029.

Zhang, Y., H. R. Yi, J. Schubert, W. Zander, H.-J. Krause, H. Bousack, and A. I. Braginski, 1999, IEEE Trans. Appl. Supercond. (in press).

Zimmerman, J. E., 1971, J. Appl. Phys. **42**, 4483.

Zimmerman, J. E., J. A. Beall, M. W. Cromar, and R. H. Ono, 1987, Appl. Phys. Lett. **51**, 617.

Zimmerman, J. E., and N. V. Frederick, 1971, Appl. Phys. Lett. **19**, 16.

Zimmerman, J. E., P. Thiene, and J. T. Harding, 1970, J. Appl. Phys. **41**, 1572.

Wavefunction symmetry and its influence on superconducting devices

J Mannhart and H Hilgenkamp

Augsburg University, Experimentalphysik VI, D-86135 Augsburg, Germany

Abstract. It has been shown that the symmetry of the order parameter in the high-T_c cuprates is dominated by a $d_{x^2-y^2}$-component. In this contribution, the implications of the unconventional symmetry on devices and on large-scale applications of high-T_c superconductors are discussed.

1. Introduction

In recent years several ingenious experiments have been conducted to identify the symmetries of the wavefunctions characterizing the superconducting condensates of the high-T_c cuprates. Reviews of these studies can be found in [1–5]. The results of these experiments, of which the IBM tricrystal-ring experiments [6] are especially compelling and elegant, give evidence for at least one [7] $d_{x^2-y^2}$-wave-dominated order parameter of the superconducting cuprates, with the possible exception of $Nd_{1-x}Ce_xCuO_4$ and related compounds. For orthorhombic superconductors such as $YBa_2Cu_3O_{7-x}$, the order parameter symmetry cannot be purely $d_{x^2-y^2}$, but must have an admixture of a real s-wave component ($s + \alpha d_{x^2-y^2}$). The mixing ratio α is a function of temperature, doping concentration and distance to the surface or to other interfaces [3, 7–9]. As shown in figure 1, an order parameter with $d_{x^2-y^2}$ symmetry is characterized by a vanishing gap function along the four $\langle 110 \rangle$ directions, as well as by phase changes of π for rotations of $90°$ around the z-axis. As basically all superconducting devices rely on the magnitude of the superconducting gap or on the phase of the order parameter it is crucial to consider the question 'given a $d_{x^2-y^2}$-wave-dominated symmetry for most cuprates, what are the implications for devices?'.

2. Surface resistance

The disappearance of the gap along the $\langle 110 \rangle$ directions puts a lower limit on the high-frequency surface resistance R_s, which obviously is undesirable for rf devices such as resonators or filters. The value of R_s also depends on the parameters characterizing quasiparticle scattering and thus cannot be determined from first principles. Experimentally, large values of R_s have been observed even in high-quality single crystals and films [10] and it has been shown that these values can accurately be fitted in a $d_{x^2-y^2}$-wave-based model [11]. However, because of uncertainties in the determination of the scattering parameters, it cannot be ruled out that part of the surface resistance is caused by other mechanisms [10].

3. Abrikosov vortices

As described in [12], the $s + \alpha d_{x^2-y^2}$ symmetry gives rise to a vortex-core structure with a fourfold symmetry and furthermore leads to a distorted square vortex lattice, tilted by $45°$ from the a-axis. The latter has been found in neutron-scattering experiments [13] and in STM measurements [14]. No strong effects on pinning have been identified and implications of a $d_{x^2-y^2}$-wave-modified vortex behaviour on applications have to our knowledge not been reported yet.

4. Josephson junctions and grain boundaries

As the characteristics of Josephson junctions are highly sensitive to the density of states of the electrodes and to the phase of the order parameter, they are strongly influenced by the unconventional symmetry component. As will be demonstrated below with a few examples, basically all relations known from conventional junctions are altered for junctions connecting electrodes with a $d_{x^2-y^2}$-wave order parameter ($d_{x^2-y^2}$-wave junctions). Consequently, most properties of $d_{x^2-y^2}$-wave junctions will differ from those of s-wave junctions, and the design rules valid for s-wave junctions are not necessarily applicable.

The current–voltage $I(V)$ characteristic of Josephson junctions, for example, is affected by the $d_{x^2-y^2}$-wave symmetry of the electrodes in several respects. The critical current I_c is controlled by the $d_{x^2-y^2}$-wave specific density of states, as modelled for tunnel junctions [15] and for Sharvin contacts [16]. Apart from I_c, because of the $d_{x^2-y^2}$-wave-type quasiparticle spectrum, the voltage branch of the $I(V)$ characteristics is strongly influenced by the unconventional symmetry. This part of the $I(V)$ characteristics has been calculated by several groups [17–20] who find considerable deviations from the textbook RSJ behaviour, subject to the orientation of the $d_{x^2-y^2}$-wave lobes with respect to the junction barrier and being a function of junction roughness and barrier height. Depending on the junction type and geometrical
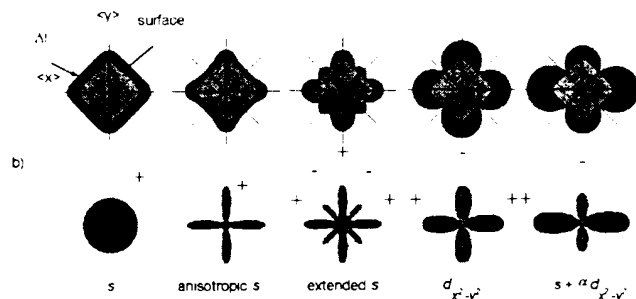
Figure 1. Illustration of symmetry functions relevant for the high-T_c superconductors showing (a) the Fermi surface and the superconducting gap $|\Delta|$ and (b) the magnitude and the phase of the order parameter.

configuration, a variety of $I(V)$ characteristics have been derived theoretically, with $I_{qp} \propto V^2$ and $I_{qp} \propto V^3$ representing the most prominent dependences for $|V| < 2\Delta$ [17, 18, 20]. Experimentally, $I_{qp} \propto V^2$ dependences are found indeed for bicrystal grain boundary junctions in nominally fully oxidized $YBa_2Cu_3O_{7-x}$ films [21, 22]. However, as the junction parameters used in the models differ from the experimental ones, it remains to be seen whether the $d_{x^2-y^2}$-wave symmetry is the prime cause of the observed $I(V)$ characteristics.

Quasiparticles scattered at interfaces and at surfaces of $d_{x^2-y^2}$-wave superconductors experience a phase shift of π along their paths for a variety of interface orientations and trajectories. If the phase of the order parameter undergoes a sign change during the scattering process, quasiparticle states will form at the Fermi level (zero-energy states) [23–25] which may also affect the critical current density J_c [26–28]. Furthermore, they can lead to unconventional temperature dependences $I_c(T)$ [25, 26, 28] and cause zero-bias anomalies in the $I(V)$ characteristic [19]. In many experiments zero-bias anomalies have been observed for various types of high-T_c Josephson junctions [29]. Studies confirming a direct relationship between the anomalies and $d_{x^2-y^2}$-wave superconductivity were recently performed for films [30–32] and single crystals [33].

Josephson junctions based on large-angle grain boundaries, in particular junctions with a misorientation of $45°$, the geometry typically obtained with biepitaxial processes, show highly anomalous dependences of their critical current on an applied magnetic field H, with the maxima of the symmetric $I_c(H)$ patterns occurring at fields of several gauss [34–37]. Such dependences have never been reported for junctions between conventional superconductors and directly prove the existence of areas in the junctions with a negative J_c. Here, even for $H = 0$, the Josephson current flows backward across the junction. It was suggested [34–37] that this effect is caused by the $d_{x^2-y^2}$-wave symmetry and grain boundary faceting [38–41]. This mechanism is sketched in figure 2, which illustrates for an asymmetric $45°$ grain boundary junction that the π phase shift between the positive and negative lobes of the $d_{x^2-y^2}$-wave order parameter may cause additional local phase differences of π, which for the Josephson current $J = J_c \sin(\varphi + \pi)$ is equivalent to a negative J_c. This model is able to account for all experimental observations concerning the
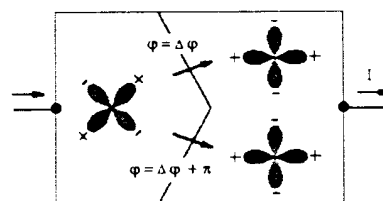

Figure 2. Sketch of a faceted (100)(110), [001] tilt grain boundary. As shown in the lower half of the drawing, faceting may cause an additional phase difference of π, leading to areas in which the Josephson current flows backward across the junction.

$I_c(H)$ characteristics of grain boundaries, such as their misorientation dependence and their insensitivity to oxygen concentration [42].

Based on this understanding it was predicted that asymmetric $45°$ [001] tilt boundaries will spontaneously produce circulating currents and generate unquantized magnetic flux, which subsequently was observed directly by scanning SQUID microscopy [43]. Because of the areas with negative J_c, the global critical current density measured across a grain boundary junction may be much smaller than the local current density, which in fact is not known. Therefore one is also required to distinguish between a local and a global Josephson penetration depth. The fractional area characterized by a negative J_c increases with grain boundary misorientation, and it has been estimated that negative critical current densities account for a reduction of the grain boundary I_c by an order of magnitude for an increase of the grain boundary angle from $0°$ to $45°$ [37]. Furthermore, for large-angle boundaries, the washboard-type dependence of the Josephson energy on phase difference is distorted, which enhances phase-slip processes, critical current fluctuations and noise. Theoretical treatments of the $I_c(H)$ dependence of $d_{x^2-y^2}$-wave junctions have been given by Mints who derived startling predictions, such as the existence of two types of Josephson vortices in long $d_{x^2-y^2}$-wave junctions, each having a flux content smaller than a flux quantum, quantization only applying to their sum [44].

In junctions between misoriented superconductors, even without the presence of an artificial barrier, the order
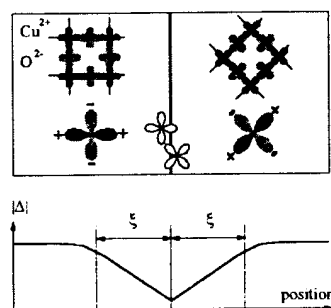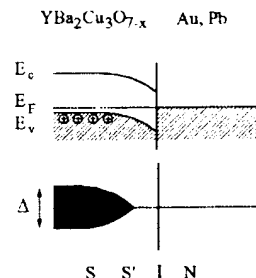
Figure 3. Schematic representation of a contact between two $d_{x^2-y^2}$-wave superconductors. In the boundary region with a width of several times the coherence length ξ the order parameter is depressed owing to the misalignment of the two crystal lattices (after [45]). For simplicity, in this sketch mixing of additional symmetry terms at the interface has been neglected.

Figure 4. Illustration of the band bending possibly occurring in heterostructures involving high-T_c materials. In the band diagram shown at the top, an insulating depletion layer is formed at the interface between $YBa_2Cu_3O_{7-x}$ and a conventional metal, increasing the interface resistance and turning the contact into a superconductor–insulator–normal metal (SS'IN) junction. Bottom: spatial dependence of the order parameter.

parameter is suppressed at the interface owing to the finite size of the coherence length ξ [45]. As illustrated in figure 3, up to distances of the order of ξ from the boundary, the order parameter is affected by the orientation of the adjacent grain and thus is reduced by frustration effects. We suggest that this intrinsic effect is one of the mechanisms limiting the critical current of grain boundaries in the high-T_c cuprates.

All of these mechanisms affecting J_c alter the junction's normal state resistance R_n (measured at $|V| \gg 2\Delta$) only indirectly and weakly. Consequently, for $d_{x^2-y^2}$-wave junctions a universal Ambegaokar–Baratoff-type scaling law [46] cannot hold for the $I_c R_n$ product [22, 28, 37]. Instead, one is led to the conclusion that various weak and configuration-dependent scaling behaviours have to apply for different sample geometries and that in general reduced $I_c R_n$ products have to be expected ($I_c R_n < \Delta$). Because of boundary inhomogeneities and $d_{x^2-y^2}$-wave effects, macroscopically measured transport properties of grain boundaries do not directly reflect their microscopic transport mechanisms.

Another property of Josephson junctions relevant for various device applications is the relation $I(\varphi)$ between the Josephson current and the phase difference. The $d_{x^2-y^2}$ symmetry of the order parameter can affect this relation in several respects. First, the proximity effect between misoriented $d_{x^2-y^2}$ superconductors or the presence of zero-energy quasiparticle states can cause nonharmonic $I(\varphi)$ dependences [18, 25, 28]. Second, it has been predicted for highly misoriented grain boundaries that some facets have to be characterized by an $I(\varphi)$ characteristic with doubled periodicity [47], which in combination with the other facets will deform the global $I(\varphi)$ dependence. Third, if such boundaries form large junctions, facets with a negative J_c will cause deviations from a sinusoidal $I(\varphi)$ relation and lead to enhanced noise and phase slip processes [37, 48].

In conclusion, for Josephson junctions between $d_{x^2-y^2}$-wave superconductors, the orientation of the superconductors with respect to the junction and also

that with respect to each other are important parameters controlling the junction properties. Likewise, the roughness of the barrier is a much more important parameter than in conventional junctions. Most principles and relations known from conventional s-type junctions do not hold for $d_{x^2-y^2}$-wave junctions which needs to be taken into account for junction design, fabrication and analysis. Because of their misorientation [45] and their faceting [37], grain boundaries are in particular affected by the $d_{x^2-y^2}$ symmetry, which, in addition to the other mechanisms caused by the grain boundary microstructure (see for example [49]), is expected to control the grain boundary critical current to a large extent. For devices, depending on the specific application, relatively small angles such as $20°$ seem to be the misorientations of choice, as boundaries with larger misorientations suffer from a larger fractional area with a negative J_c and thus from aggravated noise.

5. Additional phenomena

As has been shown, the unconventional symmetry component, which a short time ago was discussed on a rather abstract level only, strongly affects the operation of superconducting devices. Therefore one may ask whether, apart from the $d_{x^2-y^2}$-wave symmetry, there are other fundamental properties of the high-T_c cuprates which are unknown from conventional superconductors and which are of concern for devices. This is indeed the case. We point out that in particular along the c-axes the high-T_c materials behave like semiconductors, rather than like conventional metals. Compared with metals their carrier densities are low and their dielectric constants are high, causing Debye lengths of the order of a nanometre. Therefore, at interfaces band bending will take place over distances of several nanometres, analogously to the band bending in standard Schottky contacts. Accordingly, depletion or accumulation layers form in the high-T_c materials, the properties of which are drastically altered from the bulk behaviour [50–52].

Further, intrinsic or extrinsic interface states have to be expected in such structures, which will also affect the band bending and at high densities may even pin the Fermi level. It is noted that interface states with areal charge densities as small as 300 μC cm^{-2} are sufficient to turn an adjacent unit cell of YBa$_2$Cu$_3$O$_{7-x}$, into an insulator. Figure 4 illustrates that band-bending effects have to be considered for an understanding of surface properties, interface resistances and the effective superconducting gap of a wide variety of devices, such as SNS-type junctions, grain boundaries (the argument also applies to [001] tilt boundaries in epitaxial films, as they also meander in the c-direction) or metallic contacts.

Acknowledgments

References

[1] Scalapino D 1995 *Phys. Rep.* **250** 329–65
[2] van Harlingen D J 1995 *Rev. Mod. Phys.* **67** 515–35
[3] Müller K A 1995 *Nature* **377** 133–5
[4] Annett J, Goldenfeld N and Leggett T 1996 *Physical Properties of High Temperature Superconductors* vol 5, ed D M Ginsberg (Singapore: World Scientific) pp 375–461
[5] Maki K and Won H 1996 *J. Phys. I France* **6** 1–14
[6] Tsuei C C *et al* 1994 *Phys. Rev. Lett.* **73** 593–6
Kirtley J R *et al* 1995 *Nature* **373** 225–8
Tsuei C C *et al* 1996 *Science* **271** 329–32
[7] Müller K A 1997 *Nature* **377** 133–5
[8] Buchholtz L J *et al* 1995 *J. Low Temp. Phys.* **101** 1079–98
[9] Bahcall S R 1996 *Phys. Rev. Lett.* **76** 3634–7
[10] Hein M A *et al* 1996 *Studies of High-Temperature Superconductors* vol 18, ed A Narlika (New York: Nova Science) pp 141–216
[11] Hensen S, Müller G, Rieck C T and Scharnberg K 1997 *Phys. Rev.* B **56** 6237–64
[12] Maki K, Schopohl N and Won H 1995 *Physica* B **204** 214–21
[13] Keimer B *et al* 1994 *Phys. Rev. Lett.* **73** 3459–62
[14] Maggio-Aprile I *et al* 1995 *Phys. Rev. Lett.* **75** 2754–77
[15] Sigrist M and Rice T M 1995 *Rev. Mod. Phys.* **67** 503–13

[16] Deutscher G and Maynard R 1995 *Europhys. Lett.* **30** 361–6
[17] Bruder C, van Otterlo A and Zimanyi G T 1995 *Phys. Rev.* B **51** 12 904 7
[18] Barash Yu S, Galaktionov A V and Zaikin A D 1995 *Phys. Rev.* B **52** 665–82
[19] Kashiwaya S *et al* 1996 *Phys. Rev.* B **53** 2667–76
[20] Hurd M 1997 *Phys. Rev.* B **55** R11 993–6
[21] Mannhart J *et al* 1990 *Cryogenics* **30** 397–400
[22] Ivanov Z G *et al* 1996 *Czech. Journ. Phys.* **46** 1311–12
[23] Buchholtz L J and Zwicknagel G 1981 *Phys. Rev.* B **23** 5788–96
[24] Hu C R 1994 *Phys. Rev. Lett.* **72** 1526–9
[25] Tanaka Y and Kashiwaya S 1995 *Phys. Rev. Lett.* **74** 3451–4
Tanaka Y and Kashiwaya S 1996 *Phys. Rev.* B **53** R11 957–60
[26] Barash Yu S, Burkhardt H and Rainer D 1996 *Phys. Rev. Lett.* **77** 4070–3
[27] Tang H X, Wang Z D and Zhu J-X 1996 *Phys. Rev.* B **54** 12 509–16
[28] Burkhardt H, to be published
[29] Walsh T 1992 *Int. J. Mod. Phys.* B **6** 125 70
[30] Kashiwaya S *et al* 1995 *Phys. Rev.* B **51** 1350–3
[31] Alff L *et al* *Phys. Rev.* B, to be published
[32] Covington M *et al* 1997 *Phys. Rev. Lett.* **79** 277–80
[33] Wei J and Yeh N C, to be published
[34] Humphreys R G *et al* 1995 *Proc. 2nd Workshop on HTS Applications and New Materials* ed D H A Blank pp 16–21
[35] Copetti C A *et al* 1995 *Physica* C **253** 63–70
[36] Mannhart J, Mayer B and Hilgenkamp H 1996 *Z. Phys.* B **101** 175–9
[37] Hilgenkamp H, Mannhart J and Mayer B 1996 *Phys. Rev.* B **53** 14 586–93
[38] Alarco J A *et al* 1993 *Ultramicroscopy* **51** 239–46
[39] Marshall A F and Eom C B 1994 *Physica* C **207** 129–246
[40] Traeholt C *et al* 1994 *Physica* C **230** 425–34
[41] Kabius B *et al* 1994 *Physica* C **231** 123–30
[42] Hilgenkamp H *et al* 1997 *IEEE Trans. Appl. Supercond.* **7** 3670–3
[43] Mannhart J *et al* 1996 *Phys. Rev. Lett.* **77** 2782–5
[44] Mints R G and Kogan V G 1997 *Phys. Rev.* B **55** R8681–4
Mints R G, to be published
[45] Hilgenkamp H and Mannhart J 1997 *Appl. Phys.* A **64** 553–4
[46] Ambegaokar V and Baratoff A 1963 *Phys. Rev. Lett.* **10** 486–9
Ambegaokar V and Baratoff A 1963 *Phys. Rev. Lett.* **11** 104
[47] Tanaka Y 1994 *Phys. Rev. Lett.* **72** 3871–4
[48] Il'ichev E *et al*, to be published
[49] Dimos D, Chaudhari P and Mannhart J 1990 *Phys. Rev.* B **41** 4038–49
[50] Mannhart J 1996 *Supercond. Sci. Technol.* **9** 49 67
[51] Mannhart J, Kleinsasser A, Ströbel J and Baratoff A 1993 *Physica* C **216** 401–16
[52] Emig T, Samokhin K and Scheidl S 1997 *Phys. Rev.* B **56** 8386–95

EXHIBIT I

MANNHART AND HILGENKAMP, 1997, SUPERCONDUCTOR SCIENCE AND TECHNOLOGY 10, PP. 880–883